Investigating Chemical and Microstructural Evolution at Dissimilar Metal Welds

John William Gordon Clark

Thesis submitted for the degree of

Doctor of Engineering (EngD)

EFET EngD Centre,

University of Nottingham,

UK,

NG7 2RD,

December 2015

Abstract

Dissimilar metal welds (DMWs) are widely used in steam vessels in thermal power stations to join low-temperature alloys, such as steels, to high temperature alloys, such as nickel-based alloys. This provides a cost-effective manufacturing solution. However, there is a history of DMWs failing due to creep in service environments. Many investigations have been performed on weld systems and failures in the traditional 2.25Cr-1Mo (P22) steels, but fewer have been performed on newer 9Cr-1Mo steels, such as P91 and P92. Failures involving these newer steels continue to occur, for reasons which are not thoroughly understood. The factors involved are believed to include system stresses, differences in thermal expansion and microstructural evolution due to interdiffusion across the weld interface. The overall aim of this research was to investigate the chemical and microstructural stability of a range of DMWs involving P91 and P92 steels.

Much of the work is centred on a 3-bead manual metal arc weld of nickel alloy 625 onto a P92 substrate. This was subjected to tempering (760 $^{\circ}C$ for 2 hours) and furnace ageing (625 $^{\circ}C$ for 32 and 125 days). The as-welded and aged states were characterised by a range of techniques, including SEM, TEM, EDX and microhardness testing. Site-specific TEM samples were extracted from the weld interfaces using focussed ion beam (FIB) methods.

EDX measurements show iron-enrichment in the weld metal (WM) up to 30 wt%, and a partially mixed zone (PMZ) up to 50 μm from the weld. TEM analysis of the as-welded state reveals the presence of a 1 – 2 μm wide band separating the two alloys, and of different crystallographic orientation to both. Following ageing, diffusion of carbon takes place from the P92 to the WM, leading to a carbon denuded zone (CDZ) in the former and an enriched zone (CEZ) in the latter. Precipitates in the CDZ ($M_{23}C_6$ and MX) dissolve to supply this diffusion, while

Nb-rich MX phases have formed on grain boundaries in the CEZ. Additionally, carbides are found to form along the interface between the band and the P92. EDX measurements confirm that the aged WM is enriched in carbon near the interface. Microhardness measurements reveal slight softening of the P92 in response to ageing, and pronounced hardening of the WM. The thermodynamics of the alloys were modelled using the software *Thermo-Calc*, while diffusion across the interface was modelled using *DICTRA*. The findings support the trends of the experimental results in terms of diffusion behaviour and phase changes.

An industrial case study, ex-service P91 – alloy 625 pressure vessel welds exposed to c. 565 $^{\circ}C$ for c. 40,000 hours, has also been undertaken. Creep failure occurred during service near the weld interface. SEM showed that the creep crack tip was advancing through the CDZ. Microstructural changes were similar to those in the P92 – alloy 625 system, only more pronounced; the CDZ was found to be almost entirely devoid of standard $M_{23}C_6$ and MX precipitates, having been replaced by a band of carbonitrides (either $M_{23}X_6$ or M_6X) of unusual chemistry, parallel to the weld interface.

A second industrial case study involved a weld between P91 and P92 steels using the P87 filler metal, recently developed by EPRI, which is designed to minimise interdiffusion. This system, in contrast to those involving alloy 625, shows evidence for only minimal interdiffusion after ageing at 649 $^{\circ}C$ for 131 days, with no CDZ being observed. These observations are supported by *Thermo-Calc* and *DICTRA* calculations. Therefore, systems of this type may be resistant to creep failure in long-term service.

Acknowledgements

First and foremost, I would like to thank my principal supervisors: Professor Graham McCartney, my academic supervisor, and Dr Chris Bullough, my industrial supervisor from Alstom Power. Their support, advice, feedback and technical input at all stages of the research have been crucial, and without them I surely would not have progressed to this stage. My other industrial contacts, David Allen (formerly of E.On), John Shingledecker and John Siefert (both of EPRI), have also provided valuable technical insight and research materials.

I am indebted to the sponsoring organisations that have funded my research: the EPSRC, through the Efficient Fossil Energy Technologies doctoral training centre, and the Biomass and Fossil Fuels Research Alliance (BF2RA).

I would also like to extend my thanks to the technical staff in the Wolfson building at the University of Nottingham for their support and assistance in experimental work. This includes Keith Dinsdale, Thomas Buss, Jason Greaves, Max Mason and Graham Malkinson for their roles in sample preparation, and Martin Roe, Nigel Neate, Nikki Weston and Julie Thompson for their assistance with SEM and TEM work. Nigel in particular deserves my gratitude for the long hours spent operating the TEM.

Additionally, I must extend my gratitude to two members of staff at the University of Loughborough, Dr Geoff West and Dr Zhaoxia Zhou, for their assistance with FIB sample preparation, TEM/STEM analysis, and EDX analysis. The data gathered by these methods has proved invaluable to this thesis.

Finally, I must thank my family and close friends for their enduring love and support.

Publications

During this research period, the following conference papers have been published:

- J.W.G. Clark and D.G. McCartney, Modelling Chemical and Microstructural Evolution at Dissimilar Ferritic-Ferritic Interfaces, 11th International EPRI Conference on Welding and Repair Technology for Power Plants, June 25 – 27 2014, Naples, Florida, USA.

- J.W.G. Clark, D.G. McCartney, H. Saghafifar and P.H. Shipway, Modelling Chemical and Microstructural Evolution Across Dissimilar Metal Interfaces in Power Plant Welds, Proceedings of the ASME 2014 Power Conference (Paper No. Power 2014-32242), July 28 – 31 2014, Baltimore, Maryland, USA.

Table of Contents

List of Figures

List of Tables

List of Abbreviations

Item	Description
BCC	Body-centred Cubic
BCT	Body-centred Tetragonal
BSE	Backscattered Electrons
CALPHAD	Calculation of Phase Diagrams
CCT	Continuous Cooling Transformation diagram
CDZ	Carbon Denuded Zone
CNDZ	Carbon and Nitrogen Denuded Zone
CEZ	Carbon Enriched Zone
CNEZ	Carbon and Nitrogen Enriched Zone
CGHAZ	Coarse-grained Heat Affected Zone
CSEF	Creep-strength Enhanced Ferritic (steel)
DMW	Dissimilar Metal Weld
EBSD	Electron Backscatter Diffraction
EDM	Electrical Discharge Machining
EDX	Energy Dispersive X-ray (analysis/spectroscopy)
EPMA	Electron Probe Microanalysis
EPRI	Electric Power Research Institute
FCC	Face-centred Cubic
FEG	Field Emission Gun
FGHAZ	Fine-grained Heat Affected Zone
FIB	Focussed Ion Beam
HAZ	Heat Affected Zone
ICHAZ	Inter-critical Heat Affected Zone
PAGB	Prior Austenite Grain Boundary
PMZ	Partially Mixed Zone
PWHT	Post-weld Heat Treatment
SADP	Selected Area Diffraction Pattern
SEM	Scanning Electron Microscope/Microscopy
SE	Secondary Electrons
STEM	Scanning Transmission Electron Microscopy
TEM	Transmission Electron Microscope/Microscopy

Nomenclature

Symbol	Description	Units
a	Lattice parameter	Å
A	Activity	-
C	The concentration of an atomic species	m^{-3}
c_M	Composition of metal M (parent, filler or weld metal)	-
d	Weld dilution	-
$\bar{d}$	Mean type I carbide diameter as a function of time	m
$\bar{d}_i$	Initial type I carbide diameter	m
D	Interdiffusivity	$m^2 s^{-1}$
$D_{i,j}$	Intrinsic diffusivity	$m^2 s^{-1}$
D^n	Reduced diffusivity	$m^2 s^{-1}$
$f(z,t)$	A generic function of z and t	-
f^i	Local volume fraction of phases	-
F	Number of degrees of freedom	-
F_{kVa}	Kinetic factor describing vacancy exchange	-
G	Gibbs free energy	$Jmol^{-1}$
ΔH_M	Activation enthalpy associated with atom movement	$Jmol^{-1}$
ΔH_V	Activation enthalpy associated with vacancy movement	$Jmol^{-1}$
i, j, k	Labels identifying atomic species	-
J^L	Diffusion flux in the lattice-fixed reference frame	$mol\ m^{-2} s^{-1}$
J^V	Diffusion flux in the volume-fixed reference frame	$mol\ m^{-2} s^{-1}$
k	A material constant describing carbide coarsening	$m^3\ s^{-1}$
L	Kinetic factor in the lattice-fixed frame	m^{-3}
$L\prime$	Kinetic factor in the volume-fixed frame	m^{-3}
M	Mobility	-
M^{eff}	Effective mobility	-
Mo_{eq}	Equivalent amount of Mo in a Mo-W steel	-
n	Integer label for number of components	-
N	Number of moles	-
Q_c	Activation energy for coarsening	$Jmol^{-1}$
Q_I	Activation energy for an interstitial diffusion jump	$Jmol^{-1}$
Q_S	Activation energy for a substitutional diffusion jump	$Jmol^{-1}$
R	Gas constant	$JK^{-1}mol^{-1}$

S	Entropy	JK^{-1}
t	Time	s
T	Thermodynamic temperature	K
u	An arbitrary value of z	m
U	Internal energy	J
v	An arbitrary value of t	s
V	Volume	m^3
W_i	Mass of component i	kg
x	Mole fraction of an atomic species	-
y_{Va}	Fraction of vacancies	-
z	Distance	m
$\Delta\tilde{z}$	Distance between two planes/sources	m
γ	Activity coefficient	-
ϵ_2^1	Chemical interaction parameter between elements 1 and 2	-
μ	Chemical potential	$Jmol^{-1}$
$\mu^\star$	Chemical potential under reference conditions	$Jmol^{-1}$
ν_L	Velocity of the lattice-fixed frame	ms^{-1}
ν_z	Velocity of an inert marker	ms^{-1}
χ	Number of components in a system	-
ϕ	Number of phases in equilibrium	-

Chapter 1

Introduction

Owing to concerns of limited fuel reserves and climate change, there is a strong drive for thermal power plant operators to increase the efficiency of their facilities. Increasing efficiency allows more energy to be generated per unit of fuel, while simultaneously emitting less CO_2. This is done by setting the peak temperature and pressure of the steam cycle as high as possible. Old steam-raising plants are pushed to their limits, while new plants (such as ultra-supercritical, or USC, plants) are being designed specifically for such operation [1]. The alloys used to contain the steam need to have acceptable service life under these extreme conditions, whilst being economically feasible to manufacture.

There is not one single alloy that meets all of these requirements. Classic low alloy steels, such as 2.25Cr-1Mo steels, may be suitable for relatively low temperature parts of the steam vessel, but will experience corrosion, oxidation and mechanical failure far too rapidly under peak conditions. Steels containing high concentrations of alloying elements, particularly chromium and nickel, such

as 9Cr-1Mo steels, may be more suitable for exposure to higher temperatures. Stronger still are austenitic stainless steels and nickel-based alloys, but these are too expensive to use ubiquitously. A compromise may be reached whereby different grades of alloy are welded together to form the steam vessel in thermal power plant.

Dissimilar metal welds (DMWs) are therefore commonplace in power plants. While this solution appears to present the best trade-off between performance and affordability, such welded joints introduce new issues. Atomic interdiffusion between the alloys often has a profound impact on the microstructure of the weld region, and hence on the mechanical properties. There is also the effect of heat input during the welding process, which can lead to microstructural changes and the formation of undesirable phases. These effects, among others, have been observed to cause premature failure of steam containers at the joints.

The microstructural evolution of DMWs involving 2.25Cr-1Mo steels (grade T/P22) has been reasonably well-documented, and a number of contributing factors to service failures have been proposed [2]. This is possible in part due to the long history of this alloy and the extensive industrial familiarity with it. However, far less is known of the evolution and failure modes of DMWs involving the newer 9Cr-1Mo family of steels, such as T/P91 and T/P92. This presents a gap in the knowledge in an important area.

The work presented in this thesis to address these issues will cover three distinct ferritic-austenitic DMWs:

1. P92 steel - Alloy 625 filler metal
2. P91 steel - Alloy 625 filler metal
3. P91/P92 steel - P87 filler metal

The first of these systems is a laboratory-aged, 3-pass bead-on-plate weld of the nickel-based Alloy 625 on P92 steel, a relatively recently-developed steel which

is seeing increasing use in the manufacture of new power plant. The second case is a failed ex-service weld of P91 steel, an older alloy than P92, with wide usage over a number of years in modern power plants. The third system is a laboratory-aged groove weld between the two aforementioned steels and nickel alloy P87, a new filler metal which has been developed by the Electric Power Research Institute (EPRI) specifically to mitigate DMW failures at P91 and P92 steel welds. To serve as a comparison with the these cases, some select novel data from an otherwise well-known 2.25Cr-1Mo – alloy 625 weld system is presented in an appendix.

These systems, in a range of aged states, have been investigated experimentally by measuring variations in microhardness, by characterising their microstructures (from macroscopic scales by optical microscopy to sub-micron scales by transmission electron microscopy) and by measuring chemical variations in electron microscopes. Additionally, computational modelling of selected cases was undertaken using the thermodynamic modelling tool *Thermo-Calc* and the diffusion modelling tool *DICTRA* to provide insight into diffusion behaviour and associated microstructural evolution.

The thesis comprises the following chapters:

2. **Literature Review**, in which the findings of prior research in this area are covered, highlighting the gaps to be filled by the present work.

3. **Modelling Methods**, in which the principles and operating procedures underpinning the computational tools *Thermo-Calc* and *DICTRA* are outlined.

4. **Experimental Methods**, in which the sample preparation and characterisation methods are described.

5. **Experimental Analysis of the P92 – Alloy 625 System**, in which the results of the work undertaken to characterise the various states of this weld system are presented.

6. **Computational Investigation of the P92 – Alloy 625 System**, in which results of the predictions made by *Thermo-Calc* and *DICTRA* are presented.

7. **Discussion of the P92 – Alloy 625 System**, in which the results from the previous two chapters are brought together so as to explain the evolution of this weld interface and the two base alloys.

8. **Industrial Case Studies 1**, which contains results of the characterisation of a failed P91 – alloy 625 ex-service weld. The failure mechanism and possible causes are proposed, analysed and discussed.

9. **Industrial Case Studies 2**, which contains results of the characterisation of a laboratory-aged P91 – P87 – P92 weld. The properties of this weld, particularly its potential role in DMW failure mitigation, are discussed and evaluated.

10. **Conclusions & Future Work**, in which aspects of the preceding chapters are brought together to form a set of conclusions about DMW evolution and failure mechanisms. Directions for future research activities are also suggested.

Chapter 2

Literature Review

This chapter will provide an overview of the scientific theory and published work in relevant areas, including the relevant metallurgical aspects of power plant steels and phenomena that occur at dissimilar metal interfaces. This will provide context for the work presented in this thesis, and illustrate the gaps in the present knowledge that are to be addressed.

2.1 Metallurgy of Power Plant Alloys

Alloys used for steam vessels in power plant must meet a number of key criteria. They must have, at their predicted operating temperature:

- Good strength (resistance to mechanical overload).
- Good toughness (resistance to brittle failure).
- Good resistance to creep (time-dependent plastic deformation under constant stress at elevated temperature).

- Good resistance to corrosion and oxidation.
- Predicted lifetimes comparable to the lifespan of the plant, or be easily replaceable.

These criteria must be met whilst simultaneously minimising capital cost. Due to the natural abundance of iron, and the convenient, well-known properties of its alloys, the most commonly used metals are steels of various grades. Concentrations of other elements are included to ensure that the resultant alloy meets the required physical properties. What follows is an outline of some of the common power plant alloys, and the importance of their compositions.

2.1.1 Plain Carbon Steel

The simplest form of steel contains only carbon as an alloying element. It has a body centred cubic (BCC) structure at low temperature, and undergoes a phase transition to face centred cubic (FCC) at higher temperature. These structures are named α-ferrite and γ-austenite respectively. In certain steels, the BCC phase will reform close to the melting point, in a form named δ-ferrite. From a crystallographic standpoint, α-ferrite and δ-ferrite are indistinguishable.

Carbon has a very low solubility in ferrite, so under equilibrium (i.e. slow) cooling from the austenite phase field to the ferrite phase field it precipitates as alternating lamellae of cementite (iron carbide, Fe_3C) and ferrite, a structure known as pearlite. The phase behaviour of the system is illustrated in the iron – iron carbide phase diagram (figure 2.1).

The phase diagram in figure 2.1 applies only to systems that have been allowed to evolve to their equilibrium state (strictly cementite is a metastable phase, but it is sufficiently stable to be considered as a pseudo-equilibrium phase). If an alloy sample is cooled quickly (i.e. quench cooled) from the austenite phase field then the diffusion processes that form the equilibrium lamellar structure will not have

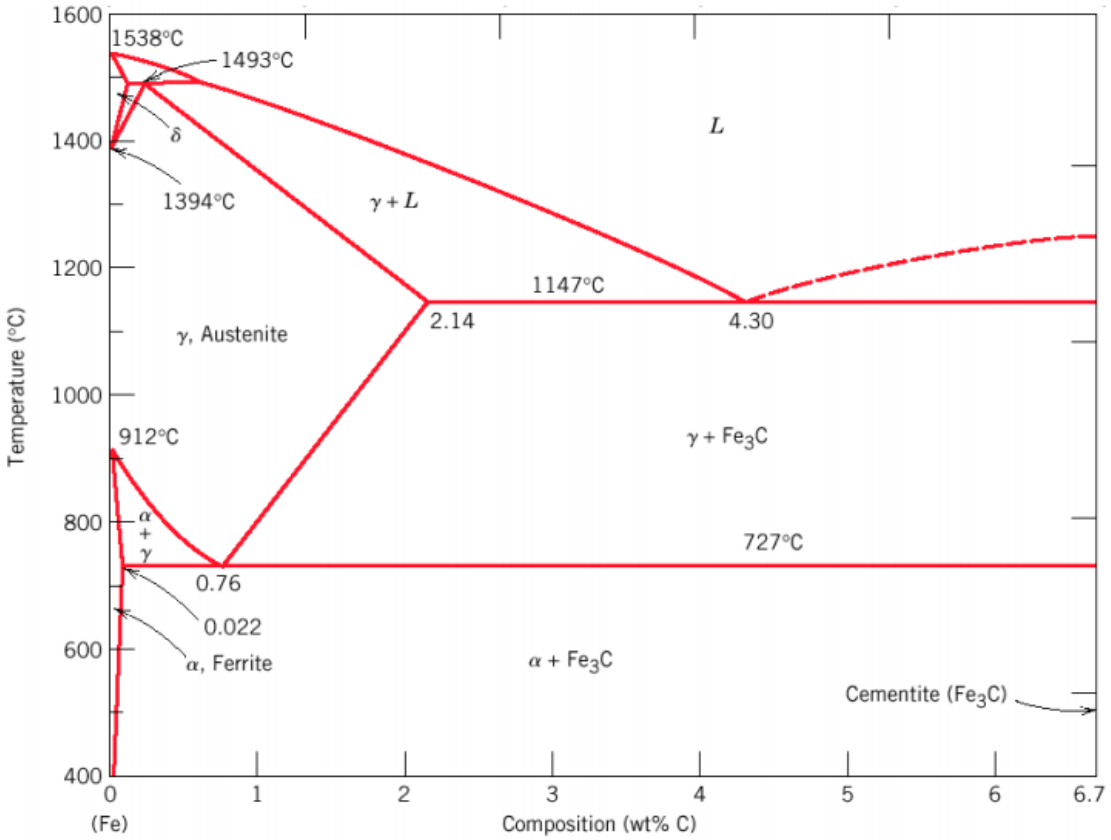

Figure 2.1: Equilibrium phase diagram for the iron-iron carbide system. From Callister [3].

time to take place. Instead, a martensitic transformation will take place. Carbon atoms will be locked into the ferrite matrix, forcing it to undertake a body centred tetragonal (BCT) structure with a high dislocation density. In the BCT structure, one of the axes in the cubic crystal is distorted; the extent of distortion is called tetragonality, which will vary based on a number of parameters (cooling rate, composition, etc.).

The final structure consists of martensite laths forming within prior austenite grains, the boundaries of which ('PAGBs') are retained. In the case of steel this phase, known as martensite, is strong but has poor ductility. It is a possible product of welding processes due to the input of heat and subsequent rapid cooling. Suitable heat treatments can relax some of the stresses associated with the martensite structure, and allow some diffusion of carbon to occur to reduce the supersaturation. The martensite is hence softened to the extent that it becomes

useful; this process is known as tempering. Tempered martensite in specific steels, P91 and P92, will be discussed in more detail in section 2.1.3.2.

A further non-equilibrium microstructure in steels is known as bainite [4]. It shares some characteristics with martensite, namely the BCT structure and high dislocation density, though it forms at slower cooling rates. The microstructure is formed of sheaf-like or plate-like areas of dislocation-rich ferrite, with iron carbide forming around the edges of the plates. It is generally softer than martensite, often to the extent that a tempering treatment is not required. An example bainitic steel, P22, will be described in section 2.1.3.1.

2.1.2 The Role of Alloying Elements

Pure iron is extremely soft, and hence of limited value for most industrial applications. The presence of other elements can lead to a significant increase in strength and hardness. This is achieved through solid solution strengthening, precipitate strengthening and dispersion strengthening. Certain elements are also good for other properties; corrosion and/or oxidation resistance, for instance. Carbon is a universal addition, and a wide range of other species (metals and non-metals) can be added to various levels depending on the required properties [5].

2.1.2.1 Carbon and Nitrogen

Carbon is present in all grades of steel as a result of the smelting process; iron oxide is reduced with coke to form iron and carbon dioxide, and some carbon will inevitably be left in solution. It occupies an interstitial site in the metal matrix up to its solubility limit, and the remainder precipitates into carbides. Carbon is an extremely effective solid solution strengthener; even small additions can have a dramatic effect on mechanical properties by introducing lattice strains which act to impede the movement of dislocations. Carbides, meanwhile, can strengthen

an alloy by pinning the dislocations and grain boundaries (and, in the case of martensite, laths) on which they tend to form (though excessively coarse carbides can be detrimental to mechanical properties due to their brittle nature).

Carbides are ordered chemical compounds of one or more metals and carbon. These are hard, brittle phases that are distinct from the non-stoichiometric metal matrix. The most familiar example, cementite, bestows high-carbon grades of steel with their characteristic hardness. Other types of carbide can form in the presence of certain alloying elements, such as chromium. Due to the embrittling effect these phases have on their host matrix, it is generally desirable to keep their volume fraction low. As such, power plant steels typically have very low carbon contents (around 0.1 wt%).

Nitrogen behaves in a similar way to carbon in steel [6]. Atoms occupy interstitial sites on the lattice, and can form precipitates (nitrides and carbo-nitrides) with certain alloying elements. These precipitates generally have similar properties to carbides. As such, nitrogen is effective at both solid solution and precipitation strengthening. It is a much less common addition than carbon, generally being reserved for advanced alloy systems where elements such as vanadium, niobium and titanium (strong nitride formers) are present.

There are several carbides and carbonitrides that may be found in the steels investigated in this thesis. They are commonly described by general formulae, in which 'M' refers to a metal atom and 'X' refers to carbon or nitrogen. These phases, full crystallographic data for some of which are given in appendix C, are:

- M_3C, or cementite. This carbide is standard in plain carbon steels, and so is usually of the form Fe_3C, but is generally not an equilibrium carbide in steels that contain chromium. It has an orthorhombic crystal structure.

- MX, where 'M' is most often vanadium and/or niobium. MX precipitates are FCC in crystal structure. They are a staple of advanced creep-resistant

steels, such as P91 and P92, which will be described later in this chapter.

- M_2X, another possible carbo-nitride. It has been observed to have several possible structures, depending on its composition [7].

- M_6C, which is also known as η-carbide. M in this case may stand for a number of elements, including iron, molybdenum, chromium, nickel and silicon, though the dominant component is usually molybdenum. This phase is FCC, with a lattice parameter $a = 11.1$ Å. It is an equilibrium carbide in some low-chromium steels, such as 2.25Cr-1Mo steel.

- $M_{23}C_6$, a chromium-rich phase which may also contain iron and other elements. This is an equilibrium carbide in most common steels that contain chromium, such as those of the 9Cr-1Mo steel family. Like M_6C it is FCC, but with a lattice parameter $a = 10.6$ Å. This similarity in structure can make determination between these two phases problematic based on crystallographic data alone.

2.1.2.2 Chromium

Pure iron and plain carbon steels have very poor oxidation resistance. An oxide layer (rust) will readily be formed which flakes off the surface, exposing more metal to oxidation. These oxides can be of the form FeO, Fe_2O_3 or Fe_3O_4. One remedy to this problem is to include chromium in the steel. When present in sufficient quantities, chromium will preferentially oxidise at the surface, forming a protective layer of chromium-iron oxide. This oxide is slow-growing and adheres to the surface, hence acting as a barrier to further oxidation. Chromium is also important as a carbide former, most commonly precipitating as $M_{23}C_6$. As such, chromium is present to some extent in all common steam vessel alloys, with the exact amount typically depending on operating temperature and desired properties.

2.1.2.3 Nickel and Manganese

The main reason to add nickel as an alloying element is that it causes the austenite crystal structure to be retained to lower temperatures. Chromium, while on its own a ferrite stabiliser, adds to this effect by retarding the austenite to ferrite transformation, hence permitting steels that are fully austenitic at room temperature. Manganese has much the same effect, although higher quantities are required to achieve the same results. Additionally, both elements are effective as solid solution strengtheners. Although neither are strong carbide formers, their presence has been shown to accelerate the coarsening of carbides [8] [9].

2.1.2.4 Molybdenum and Tungsten

Molybdenum is a common addition in low alloy steels because it is a highly effective solid solution strengthener. It is also known to enhance the corrosion resistance of stainless steels, particularly in chloride-like environments [10], and it may form stable carbide phases (typically of form M_6C) or intermetallic phases (most notably Laves phase of composition A_2B, where A is iron or chromium and B is molybdenum or tungsten) under the right conditions.

Tungsten can be used alongside or instead of molybdenum in some alloy systems, performing much the same role but with better high temperature stability [11], the trade-off being increased production cost. The combined effect of molybdenum and tungsten can be described in terms of a molybdenum equivalent, Mo_{eq}, defined as: [12]

$$Mo_{eq} = wt\%Mo + 0.5wt\%W \tag{2.1}$$

2.1.2.5 Vanadium and Niobium

Both vanadium and niobium strongly favour precipitate formation, with both carbon and with nitrogen. The resulting precipitates (most commonly MX-type carbonitrides) are important for the mechanical properties, particularly creep strength, of many high performance steels [13]. Due to the expense of adding these elements, and the detriment to mechanical properties resulting from excessive volume fractions of precipitates, these elements are usually only included in small quantities (i.e 0.2 wt% or less).

2.1.3 Ferritic Power Plant Steels

Ferritic steels are the 'workhorse' metals of most industries, the power industry included, due largely to their good mechanical properties (strength, toughness, etc.) in common operating conditions. Concentrations of alloying elements are typically low and processing methods are well-refined, meaning that capital costs are also relatively low. The compositions of three relevant ferritic steels are given in table 2.1.

Table 2.1: Nominal compositions of common ferritic steels designed for use in power plant.

	Element (wt %)											
	B	C	Cr	Fe	Mn	Mo	N	Nb	Ni	Si	V	W
T/P22	-	0.12	2.25	bal.	0.45	1.0	-	-	-	0.3	-	-
T/P91	-	0.1	9.0	bal.	0.45	1.0	0.05	0.08	0.3	0.4	0.2	-
T/P92	0.004	0.07	9.0	bal.	0.45	0.5	0.06	0.05	-	0.06	0.2	1.8

These steels have the α-ferrite crystal structure up to and beyond their maximum operating temperatures. They will undergo an allotropic phase transformation to γ-austenite over a range of temperatures that depend upon composition (usually around $800 - 900°C$). The start temperature for this transformation is labelled A_{e1} (in equilibrium conditions) or A_{c1} (in non-equilibrium conditions), and the finish temperature is labelled A_{e3} or A_{c3}. These steels undergo a second

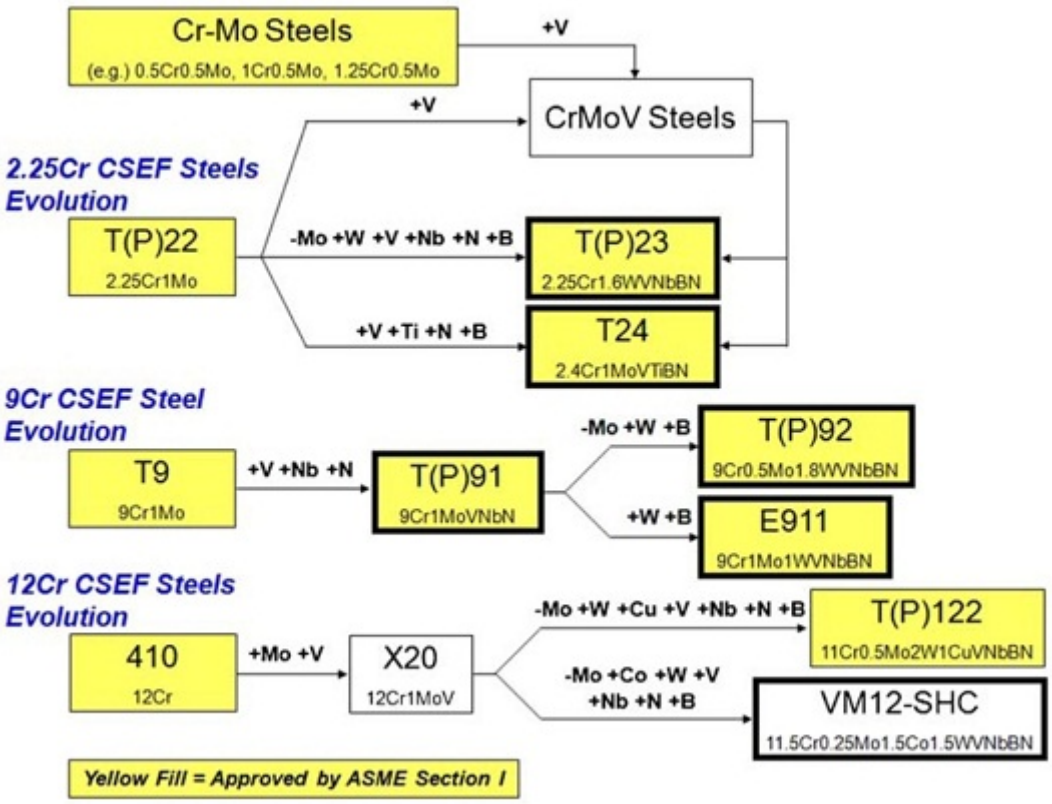

Figure 2.2: Schematic chart showing the evolution of power plant steels. The steels of direct relevance to this thesis are T(P)22, T(P)91 and T(P)92. [14].

allotropic phase transformation back to BCC (δ-ferrite) at some point close to their melting temperature.

There has been extensive research over a number of years in the development of steels for power plant applications. New generations have been introduced, while those in older generations have been modified to improve their mechanical properties. An overview of this evolution process is shown in figure 2.2.

2.1.3.1 T/P22

P/T22 steel, sometimes known as 2.25Cr-1Mo, is a classic bainitic high strength low alloy steel. Chromium endows some oxidation resistance, while creep resistance is provided primarily by the molybdenum content. This alloy has been used extensively for steam vessels operating up to $560°C$ for a number of decades. The properties of this alloy in service-type conditions have been described thoroughly

[15]. It is reported to be stable, with a reasonably good resistance to creep damage.

In addition to the basic alloy shown in table 2.1, there are also modified versions. Building upon the experience of newer high alloy steels, elements such as tungsten, vanadium, niobium and nitrogen are sometimes added [16] [17]. The resultant precipitates (most significantly MX) improve high temperature creep strength.

2.1.3.2 T/P91

In the 1970s, research was performed into advanced steels for nuclear reactors. The steels that emerged from these programs have since seen widespread use in fossil fuel plants, as operators seek steels that can contain steam at higher temperature and pressure so as to increase plant efficiency. The steels that emerged from these research efforts contain 9 - 12 wt% chromium. One of the most successful and widely used CSEF steels is T/P91, more generically referred to as grade 91 [18]. The nominal composition of this steel is given in table 2.1.

The ideal microstructure of grade 91 steels is that of tempered martensite. This is achieved though controlled heat treatments. The steel is first heated up to 1050 - 1100 $°C$, so that the microstructure transforms entirely to austenite; this step is known as normalising. It is then quench-cooled to room temperature in oil so that martensite forms. Finally, the steel is tempered at 730 - 780 $°C$ for 2 hours to relax stresses and drive precipitate formation, making the properties suitable for service [19]. The processing sequence can be understood with reference to a CCT diagram, as shown in figure 2.3.

P91 steel is reported to have good welding properties when a suitable PWHT is applied (to re-temper the martensite). This treatment is usually a repeat of the standard tempering treatment. This increases the toughness and reduces the hardness to more desirable values [21] [22]. However, problems have been noted to arise in and around the heat-affected zone (HAZ) [23] [24]; such issues will be

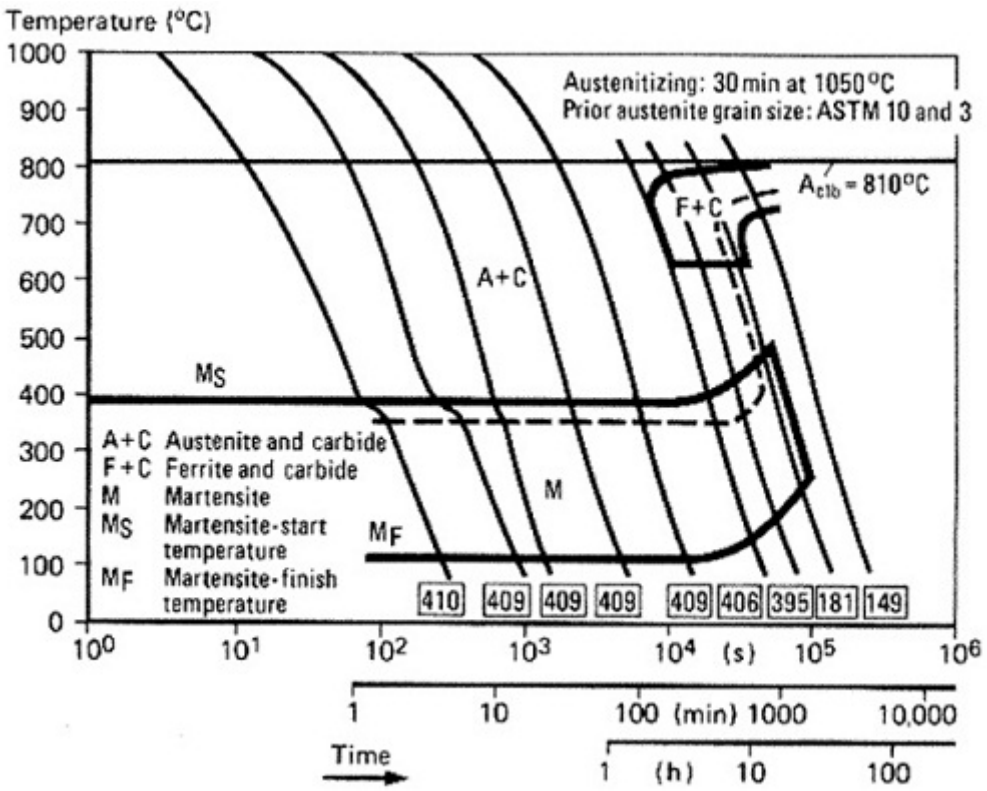

Figure 2.3: CCT diagram for P91 steel [20]. The numbers in square boxes (410, 409, etc.) are the Vickers hardness numbers at the end of the cooling process.

discussed in depth later in section 2.2.4.

The tempered martensite structure and precipitate distribution provides grade 91, and its derivatives, with good long-term creep strength, generally superior to that of traditional 2.25Cr-1Mo steels. Additonally, these alloys have superior oxidation resistance (in steam and in air) due to their higher chromium contents. As such, they can be used at temperatures up to $595°C$ [25] [26].

The improved creep strength of this steel over 2.25Cr-1Mo means that it can either contain fluid at higher pressures, or a thinner pipe can be used in the same conditions; the latter option allows a plant operator to minimise capital cost (by reducing material requirements and welding time) and reduce system stress. The requisite pipe thicknesses for a number of steels in a given system are shown in figure 2.4, which shows that a P91 pipe need only be 37 % of the thickness of a P22 pipe in the same conditions.

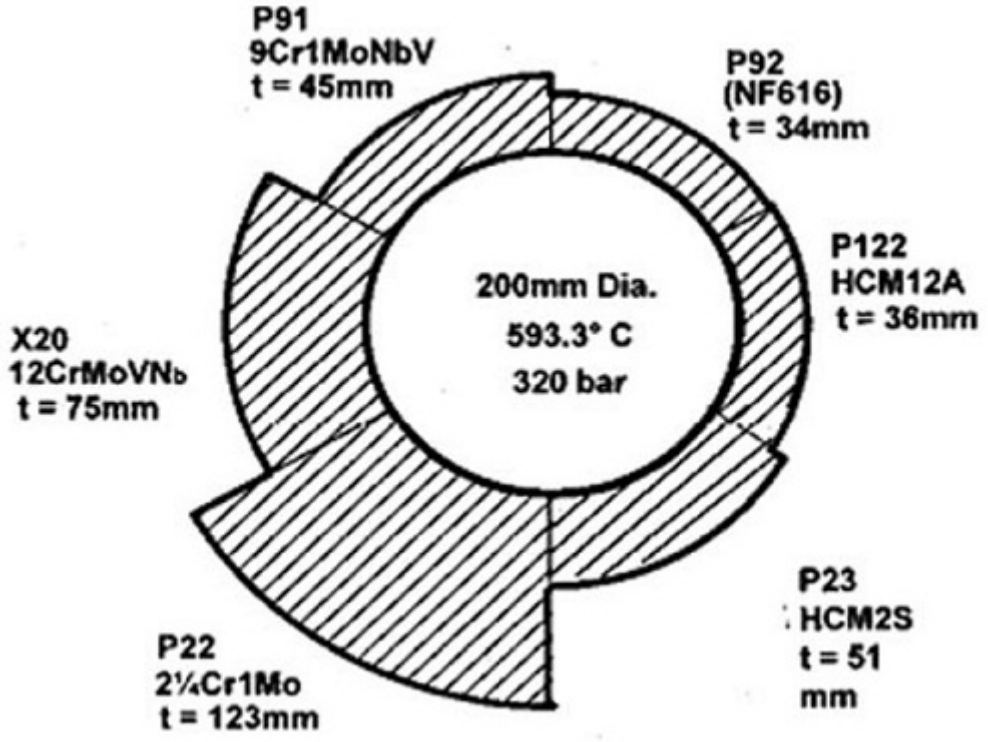

Figure 2.4: An illustration of equivalent wall thicknesses for various steels necessary to contain high pressure steam [14].

While the reported properties of this steel are good, it has recently been found that its creep life is less than originally predicted, due to unforeseen microstructural evolution during long term service brought on by large precipitates and inclusions [27] and by the reformation of ferrite from martensite [28].

The phases that form in P91 have been studied by various authors [29] [30] [31]. It is generally recognised that $M_{23}C_6$ and MX phases precipitate during the tempering treatment. From this point, a precipitation sequence can be defined:

$$M_{23}C_6 + MX \rightarrow M_{23}C_6 + MX + Laves \rightarrow M_{23}C_6 + modified\ Z + Laves \quad (2.2)$$

Laves is an intermetallic precipitate of hexagonal structure, in this case of the form $(Fe,Cr)_2Mo$. Modified Z-phase, of the form Cr(Nb,V)N, grows at the expense of MX [32]. The ideal stage of this precipitation sequence is the second

stage, with the three phases existing as a large population of fine precipitates on PAGBs and lath boundaries (though Laves phase is not entirely beneficial, since it removes some molybdenum from the metal matrix, hence reducing solid solution strengthening). It is desirable for the $M_{23}C_6$ and Laves phases to be between 200 and 300 nm in size, and no larger than 400 nm, while the MX particles are ideally between 10 and 50 nm; this results in a large population of dispersed particles, which act to pin microstructural features. Z-phase is hence problematic because it rapidly coarsen once it forms, replacing the distribution of fine particles with occasional coarse particles and removing the pinning effect. This makes Z-phase precipitation strongly detrimental to creep strength.

However, the amount of Z-phase that forms in grade 91 in relevant time scales is reported to be small. It is a more significant issue in CSEF steels of higher chromium content, since the presence of chromium accelerates Z-phase growth [33]. Recent work has shown that tantalum (which behaves similarly to niobium) may be included in CSEF steels to stabilise Z-phase against coarsening, making it beneficial for creep strength [34]

Coarsening of the other three phases must still be controlled to ensure long-term creep strength. The process, as a form of Ostwald ripening, is described in detail by Abe et al. [35]. It is reported that vanadium aids in coarsening resistance of $M_{23}C_6$, as does Laves phase by virtue of taking up molybdenum (though Laves phase itself can coarsen significantly in grade 91). MX phase is intrinsically resistant to coarsening [36].

Though P91 has a high Cr content, it will oxidise at service temperatures in steam or in air (the latter being less rapid). The scale that forms has been found by Laverde et al. [37] as having three distinct layers:

- An inner layer of $(Cr,Fe)_3O_4$ spinel-type oxide.
- A layer of Fe_3O_4 magnetite. This and the spinel layer are the two major

layers, constituting the majority of the scale thicknes.

- A thin outer layer of Fe_2O_3 hematite.

The oxide scale thickness has been found to increase with both temperature and pressure, and is more pronounced when the steel is exposed to wet conditions [38]. The growth dynamics are parabolic, with growth rate decreasing as a function of time. The scale is relatively brittle, and as such is vulnerable to fracturing under stress and/or being damaged by spallation. The distinctive three-layer structure allows one to determine if the oxide of an examined cross-section is intact.

2.1.3.3 T/P92

A modified version of grade 91, known as grade 92 or T/P92, has seen increasing use in recent years. The most significant difference between the two alloys is the addition of tungsten, which further increases creep strength [39] [40] [41]. At a temperature of $600°C$, this alloy is reported to have 30 % greater creep strength than grade 91, and it can operate in service conditions up to $620°C$; beyond this temperature, oxidation becomes an untenable drawback. The improved strength is illustrated in figure 2.4, in that less P92 is required than P91 for the given condition.

Like its sister steel, the ideal microstructure of P92 is tempered martensite, and the ideal phase balance is the same [42] [43]. The composition of the Laves phase is different due to the presence of tungsten; it can now be described as $(Fe,Cr)_2(Mo,W)$. This variant of Laves phase is reported to be more thermally stable than the tungsten-free variant, resulting in larger populations of particles [44].

In P92, the $M_{23}C_6$ phase is stabilised against coarsening by the presence of small amounts of boron. The total amount of boron must be limited so that hot working properties are not affected, and the boron/nitrogen ratio must be

carefully controlled so that BN particles do not form [45]. There is some evidence that boron may improve the welding properties of this alloy by allowing grain growth in the normally fine-grained area of the HAZ [46]; welding procedures are otherwise similar to those concerning P91 [47].

The rate of formation of oxide on P92 has been found to be faster than on P91 due in large part to the rapid oxidation of tungsten, which is taken up in the inner oxide layer [48].

2.1.4 Austenitic Steels

When nickel and chromium are included in a steel in appropriate proportions the austenitic crystal structure, ordinarily only seen at high temperatures, can be preserved down to room temperature and below. Steels of this type were originally designed to be resistant to corrosion and oxidation, but have since been found to have excellent mechanical properties at both high temperature (creep resistance) and low temperature (ductility). The capital cost, however, is higher than that of ferritic steels due to the higher concentration of alloying elements. As such, they are typically only used for the parts of power plants that are exposed to particularly high steam temperatures. The constitution of the Fe-Cr-Ni system (the basis of austenitic steels) has been reviewed in detail by Rivlin and Raynor [49]. The compositions of some common austenitic steels are given in table 2.2.

Table 2.2: Nominal compositions of three common austenitic steels used in power plant engineering.

	Element (wt %)									
	Al	C	Cr	Fe	Mn	Mo	Nb	Ni	Si	Ti
Type 304	-	0.08	18.0	bal.	1.6	-	-	8.0	0.6	-
Type 316	-	0.08	16.0	bal.	1.6	2.5	-	12.0	0.6	-
Alloy 800	0.4	0.08	21.0	bal.	1.2	-	-	32.0	0.5	0.5

2.1.5 Nickel-based alloys

Certain critical applications in industry call for the use of nickel-based alloys, which generally have superior mechanical properties and oxidation resistance to steels, particularly at high temperatures. These alloys have the FCC crystal structure at all temperatures up to their melting point; the lack of an allotropic phase transformation means that martensite cannot form. The high cost of these alloys prevents their widespread use in the power industry, but they are sometimes used as corrosion resistant layers on steels (as a coating or cladding), or as the filler metal at welded joints. The nominal compositions of relevant nickel-based alloys are given in table 2.3.

Table 2.3: Nominal compositions of relevant nickel-based alloys that may be used in power plant as weld fillers. Note that the Nb figure may also include Ta, due to the similarity and frequent co-existence of these two elements.

	Element (wt %)									
	Al	C	Cr	Fe	Mn	Mo	Nb+Ta	Ni	Si	Ti
Alloy 82	-	≤ 0.1	18-22	≤ 3	2.5-3.5	-	2-3	bal.	≤ 0.5	≤ 0.75
Alloy 182	-	≤ 0.1	13-17	≤ 10	5-9.5	-	1-2.5	bal.	≤ 1	≤ 1
Alloy 625	≤ 0.4	≤ 0.1	20-23	≤ 5	m. 0.5	8-10	3.15-4.15	bal.	≤ 0.5	≤ 0.4
EPRI P87	0.15	0.11	9	40	1.5	2	1.2	bal.	0.15	0.1

2.1.5.1 Inconel 625

Also known generically as Alloy 625 (or ERNiCrMo-3 when used as a filler metal), this is one of the most widely used nickel-based alloys. It was originally developed in the 1950s as a strong high-temperature material [50], but it has also proven itself to have good corrosion resistance. The niobium content is a key factor in the former property, chromium in the latter. The molybdenum content contributes strongly to both properties [51]. Alloy 625 has been used in the power industry due to its good thermal stability, excellent oxidation resistance and low diffusivity to carbon.

A range of possible secondary phases may form in Alloy 625, depending on

processing and ageing conditions [52]. These are:

- NbC carbide, which is a specific form of the MX phase described in section 2.1.2.1. This phase, and the other two carbides described below, generally form on grain boundaries.
- M_6C carbide, similar to that which occurs in steels (i.e. Mo-rich).
- $M_{23}C_6$ carbide, also similar to that found in steels (i.e. Cr-rich).
- Laves phase, in this case of the form $(Cr,Fe,Ni)_2(Nb,Mo,Si)$. This phase, and the three other intermetallic phases described below, generally form in the interdentritic areas of the microstructure (i.e. areas rich in Nb and Mo).
- γ'', an ordered intermetallic phase of form $Ni_3(Nb,Al,Ti)$. It is body-centred tetragonal in structure, and it precipitates coherently with the FCC matrix, hence making it highly useful for strengthening. However, it is metastable, and may evolve into δ-phase during long-term ageing. It usually precipitates in a plate-like morphology.
- δ-phase, of form Ni_3Nb, a phase known to evolve from γ''. It is orthorhombic in structure, and is not coherent with the matrix, making it less effective than γ'' at providing strength. It precipitates in a distinctive needle-like morphology.

When Alloy 625 is deposited as a weld material, its solidification behaviour will have a significant impact on its final microstructure. Being a multicomponent alloy, 625 solidifies over a range (nominally 1290 $°C$ to 1350 $°C$). Solidification begins with the formation of Ni-rich FCC dendrites. The elements Mo, Nb and C will tend to segregate to the remaining liquid. As a result, the final solidified structure is generally dentritic, with the crystallographic FCC-<100> direction of the dendrites being oriented along the direction of maximum thermal gradient,

usually near-perpendicular to the weld line. The dendrites are a substructure within larger columnar grains, which are elongated in the same direction as the dendrites [53] [54] [55].

The interdendritic regions, being enriched in Mo, Nb and C, are usually reported to be rich in secondary phases. These phases have been variously reported as NbC, M_6C and/or Laves phase [56] [57]. Floreen et al. [58], in a comprehensive study of the metallurgy of Alloy 625, have described the phases that form during the solidification process as follows:

$$Liquid \rightarrow Liquid + \gamma FCC \rightarrow \gamma FCC + NbC + Laves \tag{2.3}$$

The relative proportions of NbC and Laves phases in the final state will depend upon the ratio of C to Nb in the initial composition (with NbC being dominant at higher C/Nb ratios). Floreen et al. then describe the phases that can form following elevated temperature exposure, with their findings summarised in a time-temperature-transformation diagram (presented in figure 2.5).

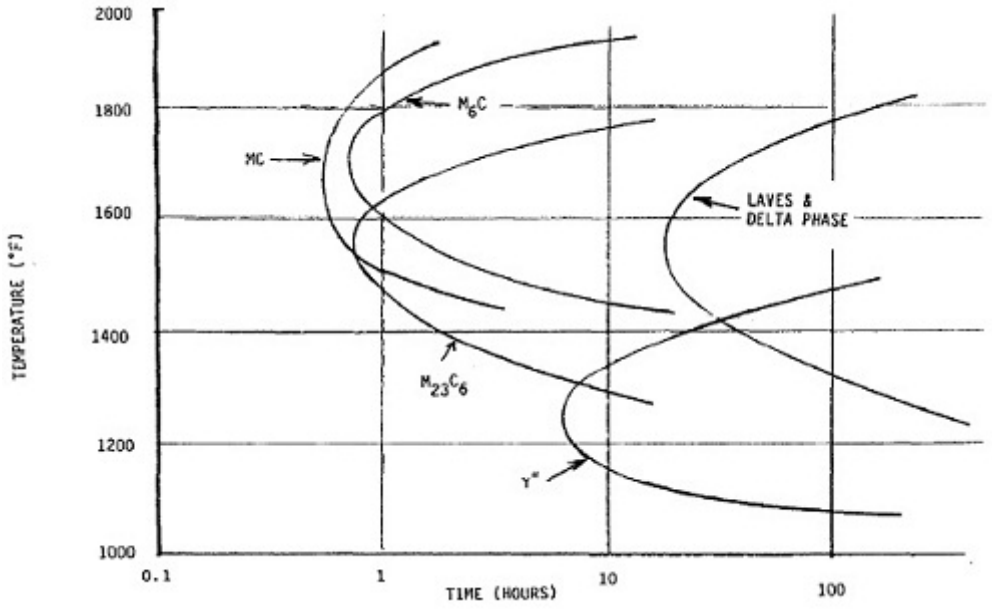

Figure 2.5: TTT diagram for welded Alloy 625, showing the phases that may form following high-temperature exposure [58].

Figure 2.5 indicates a strong tendency for the formation of the γ'' at tempera-

tures around $1200°F$ (c. $650°C$). The formation of this phase in these conditions has been reported by other authors [59] [60] (these authors also reported additional phases, but their findings were on wrought Alloy 625 and thus may not be entirely applicable to welded Alloy 625). The Laves and δ phases, in contrast to γ'', are solely detrimental (due to their own mechanical properties, their incoherence with the matrix, and the fact that they reduce the level of niobium, a solid solution strengthener, in the surrounding metal matrix).

The carbide phases in Alloy 625 do not have particularly significant benefits, but they have been noted to strengthen the grain boundaries on which they form in wrought alloys. Carbides do not form as readily in this alloy as in the ferritic steels described earlier due to the lower nominal carbon concentration of Alloy 625.

2.1.5.2 EPRI P87 Filler Metal

This alloy, the composition of which is given in table 2.3, has been recently developed by the Electric Power Research Institute (EPRI) as a bespoke DMW filler metal, in response to the relative inadequacy of stainless steels and conventional nickel alloys in this role [61]. It was designed specifically with the welding of grade 91/92 steels in mind, either to one another or to other alloys. Its carbon and chromium contents are closely matched to these steels, with the intended effect of reducing carbon interdiffusion when compared with other filler metals due to lesser chemical potential gradients. The other benefit of this alloy is that its thermal expansion coefficient is more closely matched to those of power plant steels than conventional filler metals, hence reducing stress build up as a result of thermal cycling [62]. Since this alloy is newly developed, there is minimal published work investigating its long-term evolution in service conditions, although initial results have shown promising properties [63].

2.2 Dissimilar Interfaces between Power Plant Alloys

Welds between dissimilar metals (DMWs) are an inevitable part of power plants, for reasons outlined previously. Their evolution under service conditions must therefore be understood, so that their behaviour can be predicted and potential failures avoided. What follows is an outline of phenomena relating to diffusion and microstructural evolution that occur at dissimilar interfaces in metals.

2.2.1 Welding and the Effect of Heat

Welding is a necessary joining process in power plant metals. Fusion welding, where the components are melted together by the application of heat, is most commonly used in this field due to its versatility and the reliability of joints produced. However, this process adversely affects the properties of the base metals in various ways.

The heat source used for welding, usually an electric arc in industrially relevant cases, must be sufficiently hot and concentrated so as to only cause localised melting at the intended fusion zone. Metals, though, are excellent conductors of heat, and so the thermal energy introduced by the heat source will diffuse into the base materials, resulting in solid state heat-affected zones (HAZs). The typical layout of these zones is shown schematically in figure 2.6, and will be discussed in more detail in section 2.2.2. The HAZ usually experiences microstructural changes, making welds a common area of weakness in power plants, since mechanical behaviour generally depends upon the microstructure and chemistry of the alloy.

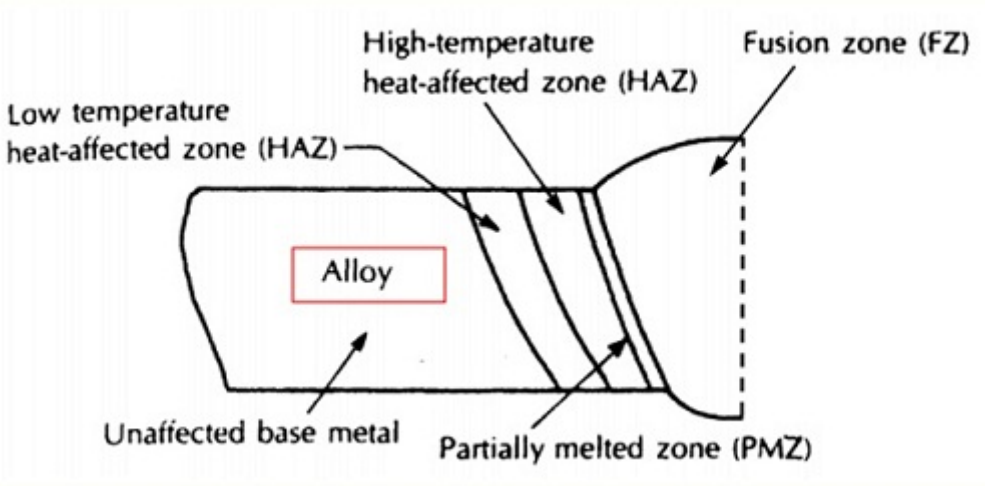

Figure 2.6: Schematic representation of the regions that may be present at a weld. Adapted from Messler [64].

2.2.2 Properties of the As-Welded State

In the cases investigated in this thesis, the nickel-based weld metals (e.g. Alloy 625) have been applied to the base steels (P91/92) by fusion welding processes. The weld metal microstructures form during the welding process, while the steel is modified from its base state by the input of heat. Industrial welding processes almost always involve multiple passes (as illustrated in figure 2.7), the effects of which must be taken into account.

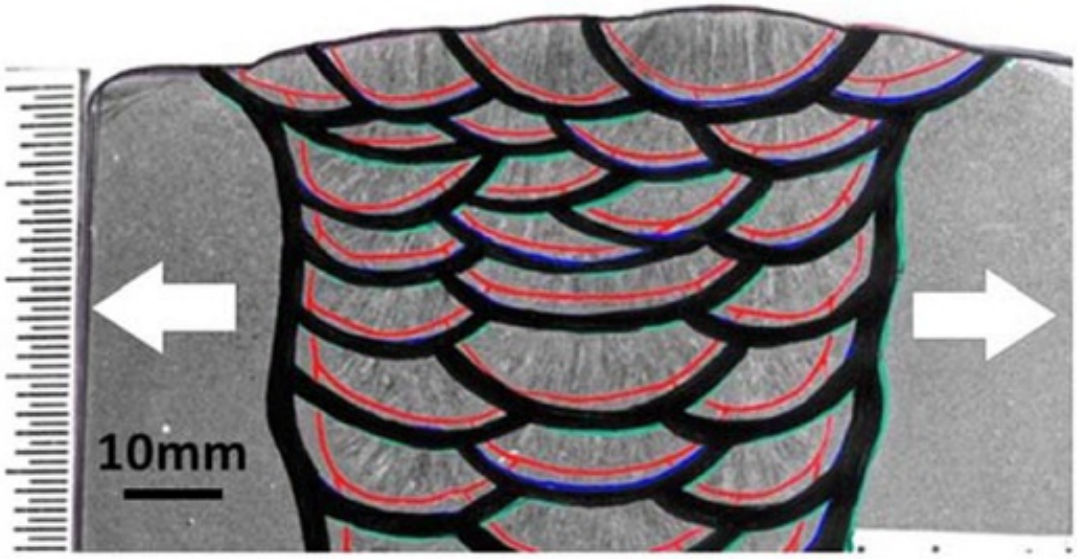

Figure 2.7: Macrostructural overview of section of a multi-pass weldment between two alloys. Each of the areas separated by black lines is a single weld pass [65].

2.2.2.1 Properties of the Weld Metal

During the welding process, the weld metal (Alloy 625 in most of the cases of relevance to this thesis) is applied to the base steel in the liquid state. Contact with the surface of the base steel causes some of this material to melt, and the arc welding process causes this melted steel to be mixed into the weld pool by convective flow. This phenomenon is called dilution. The extent of dilution will be different in each weld pass, with the first pass having the highest dilution level. The most significant consequence of this is that the iron level in the weld metal will increase, with the concentrations of other alloying elements decreasing to compensate. This may cause the behaviour of the alloy to deviate to some degree from the description in section 2.1.5. The extent to which dilution occurs can be limited through careful control of welding parameters, but it must always be expected to some degree [66] [67]. The extent of dilution, in terms of the compositions of the base metal (c_B), the nominal filler metal (c_F) and the diluted weld metal (c_W), can be described as follows:

$$c_W = c_F + \frac{d}{100}(c_B - c_F) \tag{2.4}$$

where d is dilution as a percentage.

However, not all of the weld pool is so well mixed. There is generally a stagnant boundary layer at the interface of the un-melted steel which does not engage in convective flow. As the weld metal solidifies, so does this layer, and it becomes part of the final structure. Its composition usually varies smoothly between that of the base metal and that of the diluted weld metal. This area is known as the partially mixed zone (PMZ), and has been reported by a number of authors [68] [69] [54]. The PMZ can be quite large, depending on the alloys involved and the nature of the welding process, but in fusion arc welds between steels and nickel-based alloys it is generally no more than 50 μm in width.

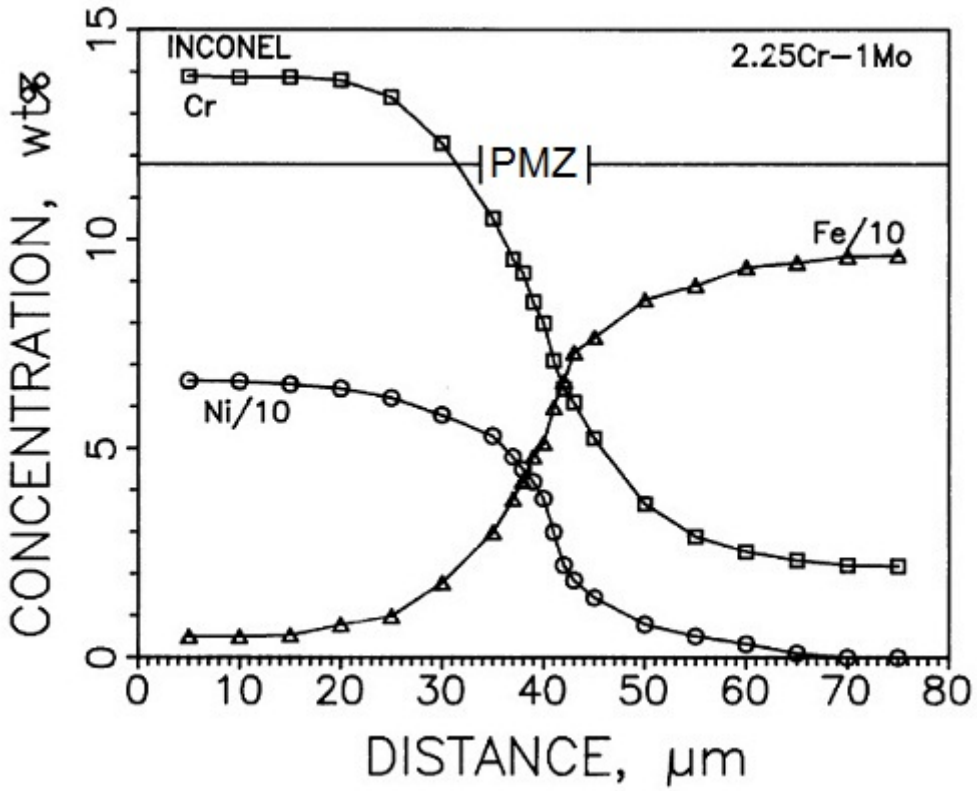

Figure 2.8: Composition profiles across a 2.25Cr-1Mo steel – Inconel 182 arc welded interface in the as-welded state, showing the location of the PMZ. The zero point on the horizonal axis is arbitrary [70].

The composition profile of the PMZ layer is of great significance, since this will determine its microstructure and mechanical properties. The compositions of Fe, Cr and Ni across a typical PMZ in a 2.25Cr-1Mo steel – Inconel 182 (a nickel-based alloy similar to Inconel 625, the composition of which is given in table 2.3) weld are shown in figure 2.8. This shows the smooth transition between compositions, and indicates that much of the PMZ area has a composition closer to that of an austenitic stainless steel than a nickel-based alloy. By comparison with a Schaeffler diagram, shown in figure 2.9, which gives the predicted matrix phase based on concentrations of ferrite-stabilising elements (chromium equivalent) and austenite stabilising elements (nickel equivalent), it can be seen that welding Alloy 625 to either 2.25Cr-1Mo or 9Cr-1Mo steel is most likely to result in an austenitic or austenitic/martensitic PMZ (as the composition of the PMZ will lie on the straight lines connecting the nominal alloy compositions). However, the precipitate distribution and mechanical strength of the PMZ will be different to those of the bulk weld metal due to the higher iron content.

The nature of solidification at ferritic-austenitic DMWs has been studied in depth by Nelson et al. in a pair of reports [72] [73], and later published in a text book by Lippold et al. [74] (who was a contributing author in the aforementioned reports). They found solidification of the austenitic weld metal to be largely directional, with dendritic growth taking place along the FCC <100> direction (as described in section 2.1.5.1). However, the area adjacent to the fusion boundary, initial solidification was found to be less simple due to the base metal having been heated into the δ-ferrite (BCC) range. Heterogeneous solidification was found to occur, with new FCC crystals being misoriented with respect to the underlying BCC crystals due to the differences in structure and lattice parameter. However, once the base steel was cooled into the γ-austenite range, the boundary between the base and weld metals was found to be mobile. It would tend to migrate into the weld metal, leading to an apparent region of planar material (later observed in

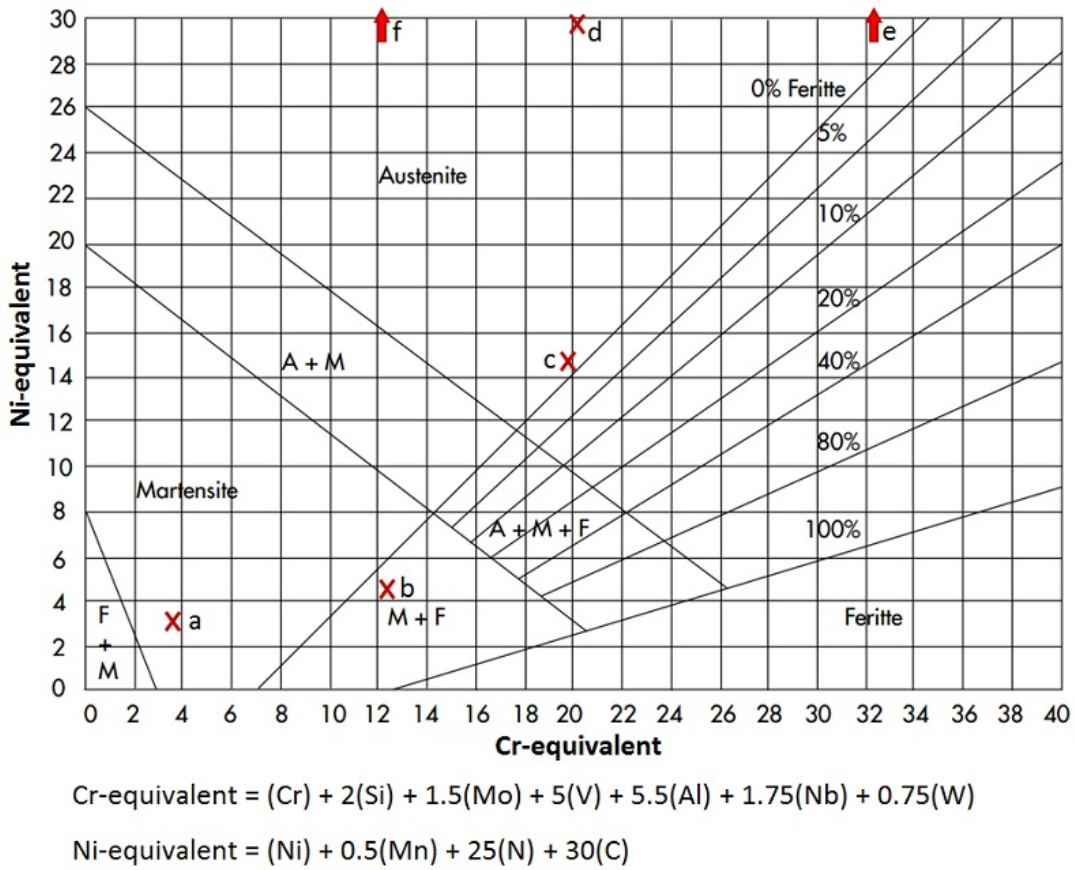

Figure 2.9: A Schaeffler diagram for steels, which gives the expected microstructure for a range of compositions. The expressions for Cr- and Ni-equivalents are given, where the element labels stand for compositions in wt%. The labelled points correspond to the approximate positions of: a) 2.25Cr-1Mo steel; b) P91/P92 steels; c) Type 304 stainless steel; d) Alloy 800 stainless steel; e) The position of Alloy 625 on the horizontal axis - its Ni equivalent is around 60; f) The position of EPRI P87 filler on the horizontal axis - its Ni equivalent is around 52. [71]

a related study by one of the original authors [75]) and a grain boundary parallel to the weld line, which was associated with the possibility of weld failure.

2.2.2.2 Properties of the Solid-state Heat-affected Steel

Since the mechanical properties of power plant steels are so critically dependent on fine microstructural details, the condition of the as-welded steel has a great effect on subsequent performance. The heat that is applied to the system during the welding process will cause some of the steel to melt (as described above), and will expose the adjoining solid steel to high temperatures. Much research has

hence been done on the welded states of common steels, including the 2.25Cr-1Mo and 9Cr-1Mo families.

The microstructural properties of the HAZ in power plant steels may perhaps be best understood with reference to a diagram. Figure 2.10 shows this in great detail for the P91 system by matching the local peak temperature experienced as a function of distance from the weld with the equilibrium phase diagram for the system. 2.25Cr-1Mo steels behave in much the same way, though the relative sizes of the zones may vary. The metallurgical impacts of fusion welding have been described in detail by other authors [76] [77] [78] [79], but for the reader's sake they will be reiterated here.

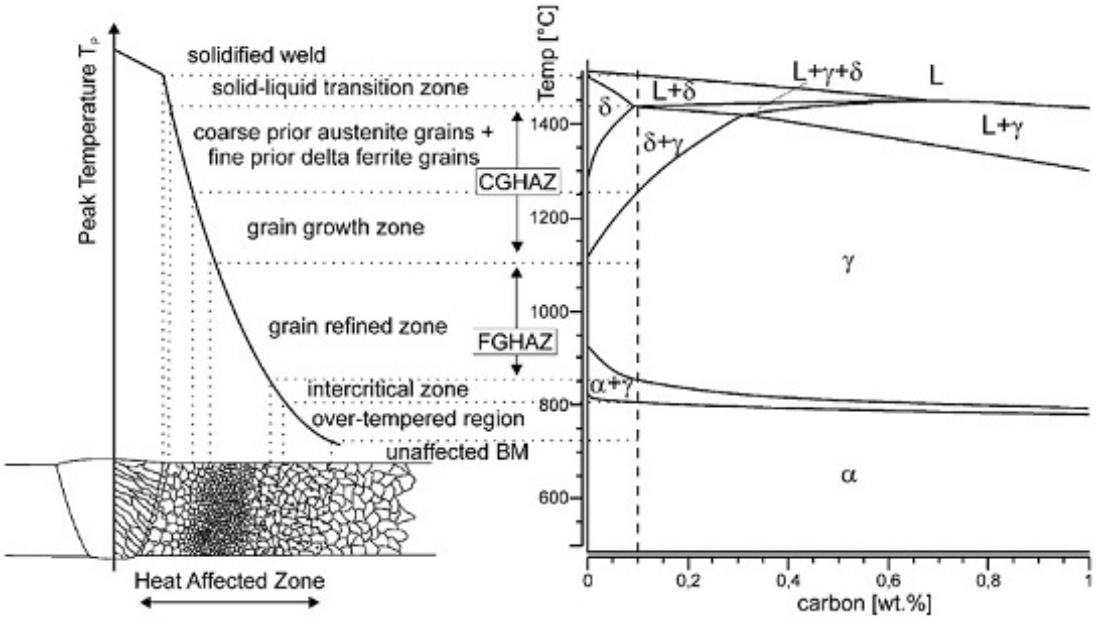

Figure 2.10: Detailed overview of the microstructural impacts of welding upon P91 steel [80].

The first major part of the HAZ is the coarse-grained heat affected zone, or CGHAZ. This part of the steel has been exposed to the highest temperatures during welding, placing it in the $\delta + \gamma$ region of the phase diagram or the the upper part of the γ region. This part of the HAZ will have been exposed to high enough temperatures for γ -austenite grains to form and grow to significant sizes. This grain growth is aided by the local dissolution of carbide phases, removing

their inhibiting influence. During the fast cooling that follows the welding process, these features are locked into the microstructure, becoming the PAGBs between which martensite laths form. The part of the CGHAZ exposed to the $\delta + \gamma$ phase field may also exhibit small retained δ -ferrite grains; δ -ferrite formation is undesirable, since it cannot contain martensite (it does not undergo an allotropic transformation on fast cooling) and is hence weaker than the surrounding material [81].

Adjacent to the CGHAZ is the fine-grained HAZ, or FGHAZ. In this region, the peak temperature experienced during welding was sufficient to cause the local microstructure to transform to austenite, but insufficient to completely dissolve carbide phases. New austenitic crystals grow within the existing grains, but are prohibited from coarsening to any significant degree. The result is a region of relatively fine austenite grains. As this region is cooled down, the martensite laths that form will hence be smaller than in either the CGHAZ or the base metal. The fact that carbides do not dissolve in this area means there is minimal carbon in solid solution, which in turn affects the morphology of the martensite laths; their tetragonality (the extent to which the cubic lattice is distorted) is lower than in the CGHAZ or base material. There is generally a smooth transition from CGHAZ to FGHAZ, so the exact boundary between them is difficult to define.

Adjacent to the FGHAZ sits the area which was exposed to the $\alpha + \gamma$ two-phase field (the temperature between A_{C1} and A_{C3}). This results in partial transformation to austenite, with small grains precipitating within the progenitor structure (i.e. tempered martensite). These grains are poor in carbon since carbides are not dissolved, so the final martensitic structure formed upon cooling shares similarities with that of the FGHAZ, the difference being that the resultant martensite sits within areas of over-tempered base martensite. This region is called the intercritical HAZ, or ICHAZ.

The final region of the HAZ is the area exposed to the part of the α phase

field above the tempering range (usually 760 $°C$ for P91/92 steels). This area will have hence been over-tempered, resulting in higher than ideal ferrite recovery, dislocation annihilation and carbide coarsening. This area will hereby be known as the transition zone (TZ).

2.2.2.3 Interfacial Martensite Formation

In general, the welded interface between austenitic and ferritic materials will not show a sudden microstructural transition from one to the other. Several authors have reported the existence of a band of martensite at the weld line. This band appears to be distinct from either base metal. This has been observed by Nicholson [82] in welds between 2.25Cr-1Mo steel and Inconel 182. The band was observed in the as-welded state, and was described to be, on average, 1 μm in width. It was associated with the precipitation of carbides, a phenomenon which will be discussed later in this section.

This band has also been observed by other authors. Bhaduri et al. [83] observed it at an interface between the same alloys as used by Nicholson, while Ayer et al. [54] observed it when welding Alloy 625 to a low-alloy steel; a TEM micrograph of this band as observed by the latter authors is shown in figure 2.11. Both groups observed narrow bands, typically 1 μm or less in width. Gittos and Gooch [69] observed this band at the welded interfaces between 2.25Cr-1Mo steel and various austenitic alloys (stainless steels and alloy 82, another nickel-based alloy). They observed a large variation in band width depending on the alloy and the welding process, ranging from 1 μm when welding with nickel alloy 82 to 301 μm when welding with grade 308 stainless steel. It was noted that the band was, on average, narrower when welding with the nickel-based alloy.

In a more recent study, DuPont and Kusko [68] have investigated this band by looking at the interfaces made by the welding of Alloy 625 and type 309 stainless steel onto a plain carbon steel using optical and scanning electron microscopes.

They found the band width to be larger in the stainless steel case (35 – 40 μm) than in the nickel case (2 – 3 μm), matching the trend observed by Gittos and Gooch.

Pan and Zhang [84] observed the interfaces between plain carbon steels of varying carbon contents and a 25% -Cr13% -Ni weld metal. In low-carbon joints, they found the interfacial region to consist of a martensite band, with an adjoining region of sawtooth-like morphology between the martensite band and the steel. This sawtooth-like morphology was previously identified by Savage et al. [85] in other welds between low-alloy steels and austenitic alloys.

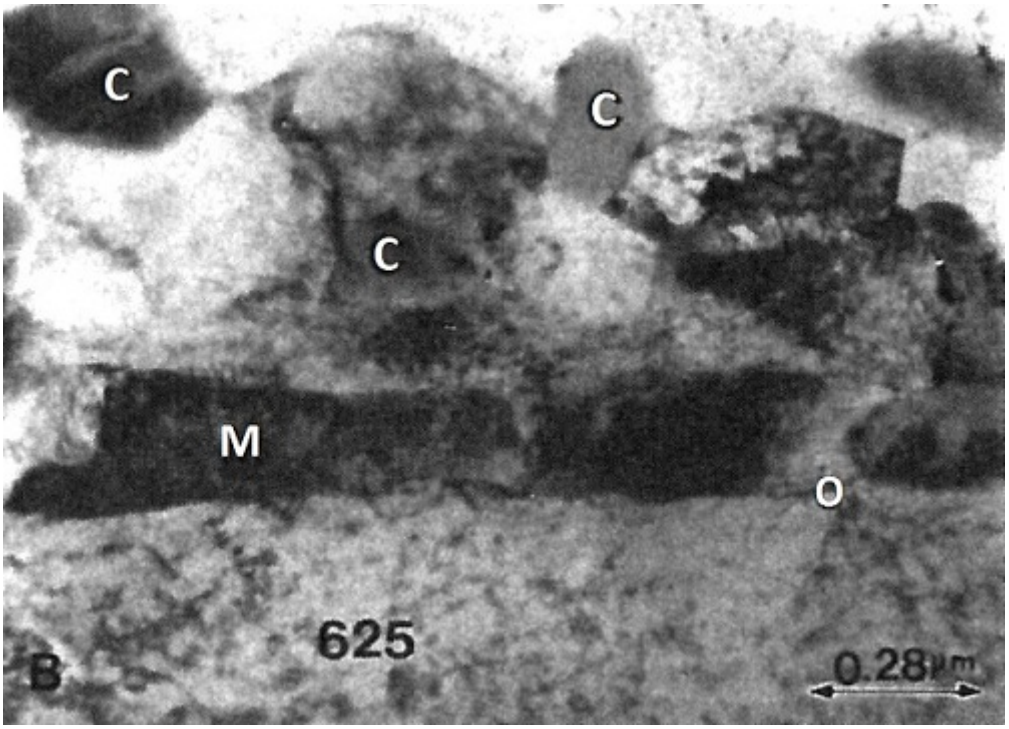

Figure 2.11: A TEM micrograph of interfacial martensite formation at a weld between a low-alloy steel and Alloy 625 as observed by Ayer et al. [54]. The labels are: (C) carbide; (M) martensite band; (O) weld interface.

Ayer et al. claim that this band formed during PWHT, although their analysis may have been limited in that they did not investigate an as-welded sample. Bhaduri and DuPont both explain the band in terms of local composition variation, and the effect thereof on martensite formation after welding (i.e. the local variation in start and finish temperatures, M_S and M_F). Gittos and Gooch explain the

band as being a region of heavily diluted weld metal that falls in the austenite + martensite region of the Schaeffler diagram ('A + M' on figure 2.9), a theory supported by their measurements of the composition of the band.

2.2.3 Experimental Observation of Evolution during Ageing

In a dissimilar weld there are discontinuities in one or more of the elemental concentrations at the weld line. This means there are chemical potential (or activity) gradients, which serve as driving forces for atomic diffusion across the interface. This is referred to as interdiffusion, a well known phenomenon that has been widely reported in many systems. The rate of diffusion increases exponentially with increasing temperature, and thus is observed most prominently during high-temperature ageing. Diffusion may lead to microstructural changes by altering the local equilibrium phase balance. The mathematics underpinning interdiffusion will be outlined in detail in chapter 3; this section is devoted largely to the experimental observations of this phenomenon and the resulting effects.

2.2.3.1 Carbon Migration

With regards to the alloy systems of relevance to this research, carbon diffusion has been studied most extensively. This is because of its faster diffusion rate compared to other common alloying elements and because of the profound impact it has on the microstructure and mechanical properties of metals (for reasons outlined earlier in this chapter).

In general, chemical potential gradients are roughly proportional to concentration gradients (which may be the intuitive driving force for diffusion). However, this is not universally true, since the chemical potential of an atomic species depends upon the concentrations of all species in the system. The impact is minimal

in most cases, but small atoms such as carbon can have their chemical potentials significantly altered by the presence of certain alloying elements. This effect was first demonstrated by Darken [86] in his 'uphill diffusion' experiment, in which carbon was found to diffuse against its own concentration gradient between two low alloy steels of varying silicon level. Experiments were performed at 1050 $^{\circ}C$, causing both steels to be in the austenite phase field. The conclusion drawn was that silicon increases the chemical potential of carbon, causing it to diffuse to the lower-silicon steel. It was also found that manganese and molybdenum reduce this quantity. Darken's work was an important milestone in the development of multicomponent diffusion theory, which will be discussed in depth in chapter 3.

Perhaps the element with the most significant impact on the diffusion dynamics of carbon is chromium. This was shown by Christoffel and Curran [87], who found that the extent of decarburisation in a low-alloy steel joined to a high-alloy steel depends upon the amount of chromium in the high-alloy steel. This is due to the fact that chromium, like molybdenum and manganese, reduces the local chemical potential of carbon. These studies were carried out on a range of dissimilar interfaces, some being ferritic-ferritic and others being ferritic-austenitic, with the same trends observed in both cases. Evidence for the diffusion of carbon across an interface into a steel of higher chromium content has since been observed elsewhere in ferritic-ferritic systems [88] and ferritic-austenitic systems [89] [90] [91] [92] [93]. This is significant in that it indicates that a discontinuity in crystal structure at a weld interface is not a barrier to diffusion, and that high chromium content results in a low chemical potential of carbon regardless of crystal structure.

Foret et al. [94] have shown that nitrogen displays similar diffusion characteristics to carbon in a ferritic-ferritic system. This is something which may have been intuitively assumed, but could not be taken for granted. It is an important consideration when dealing with CSEF steels, the mechanical properties of which depend so critically upon the presence of MX carbo-nitrides.

It is generally found that the diffusion distances in FCC metals are shorter than those in BCC metals, particularly when the FCC metal is rich in nickel. In recent studies by Anand et al. [95] [96] [97] it has been shown that carbon diffusion is far slower in nickel-based alloys than in steels. This is ascribed to reduced atomic mobility within the nickel alloy. It is clear from these results that nickel-based alloys are beneficial if one wishes to suppress carbon diffusion.

2.2.3.2 Carbon Enriched and Denuded Zones

The diffusion of carbon away from a low-alloyed steel results in the formation of a carbon denuded/depleted zone (CDZ). This zone is characterised by the dissolution of carbides (since carbon must flow to satisfy the potential gradient, but it is only mobile when in an interstitial lattice site; carbides are immobile). Meanwhile, the higher-alloyed steel or nickel-based alloy will take on an excess of carbon (in a carbon enriched zone, or CEZ), which will generally manifest itself in the form of carbide precipitation if the concentration exceeds the local solubility limit.

The carbon enriched and denuded zones of various ferritic-ferritic steel welds have been studied at length in a thesis and subsequent papers by Race and Bhadeshia [98] [99] [100]. In these studies it was found that the diffusion of carbon away from low-alloy steels generally reduced the local volume fraction of carbide to essentially zero over relatively large areas - a CDZ of approximately 1 mm was reported at a 9Cr-1Mo – 2.25Cr-1Mo steel weld interface after ageing for 64 hours at 730 $^{\circ}C$. The CDZ was in the 2.25Cr-1Mo steel, and clearly visible under an optical microscope due to the significant changes in microstructure. These changes manifested as a significant, but not total, dissolution of carbide phases, and the growth of ferrite grains. The carbides dissolved in order to supply the diffusion of carbon, while the grain growth occurred due to the loss of the grain boundary pinning effect of the carbides. Conversely, the CEZ on the 9Cr-1Mo side of the

interface was observed to have a higher density of carbides than the bulk.

The growth rate of the carbon enriched and denuded zones was investigated by studying samples aged for different amounts of time. It was found that zone growth did not follow the expected parabolic behaviour, but rather began to tail off after long times. This was found to be caused by changes in phase balance of the steels, causing a reduction in the diffusion driving force, and the decarburisation of the 2.25Cr-1Mo steel reducing the amount of carbon available for diffusion.

Other studies by Albert et al. [101] and Sudha et al. [102] have confirmed the existence of a CEZ and CDZ in aged 9Cr-1Mo – 2.25Cr-1Mo steel joints. The qualitative microstructural changes they observed were very similar to those observed by Race and Bhadeshia, although covering shorter length scales due to shorter heat treatment times. A micrograph of their system is shown in figure 2.12. The relatively high carbon concentration in the CEZ was conclusively confirmed (though not fully quantified) by the latter authors using X-ray analysis. In a later study by Sudha et al. [103] the types of carbides present in the various zones were identified using TEM methods. The predominant carbide in the CEZ was Cr-rich $M_{23}C_6$, accompanied at short ageing times by small Mo-rich M_2C phase. The latter was replaced by Mo-rich M_6C at longer ageing times. The CDZ was found to be almost devoid of carbides, apart from occasional particles of M_6C, an equilibrium carbide in 2.25Cr-1Mo steels.

There has been less work on decarburisation of 9Cr-1Mo steels than 2.25Cr-1Mo steels. In a study by Sireesha et al. [104] a weld between 9Cr-1Mo steel and Inconel 182 was investigated in various aged conditions. It was found that, even after long term ageing (625 $^{\circ}C$ for 5000 hours), decarburisation of the steel was significantly less pronounced than a 2.25Cr-1Mo steel would have been in the same conditions. This was ascribed to the lesser carbon activity gradient in the 9Cr-1Mo case, itself a result of higher chromium content and microalloying with niobium and vanadium. Bhaduri et al. [105] also observed minimal changes in

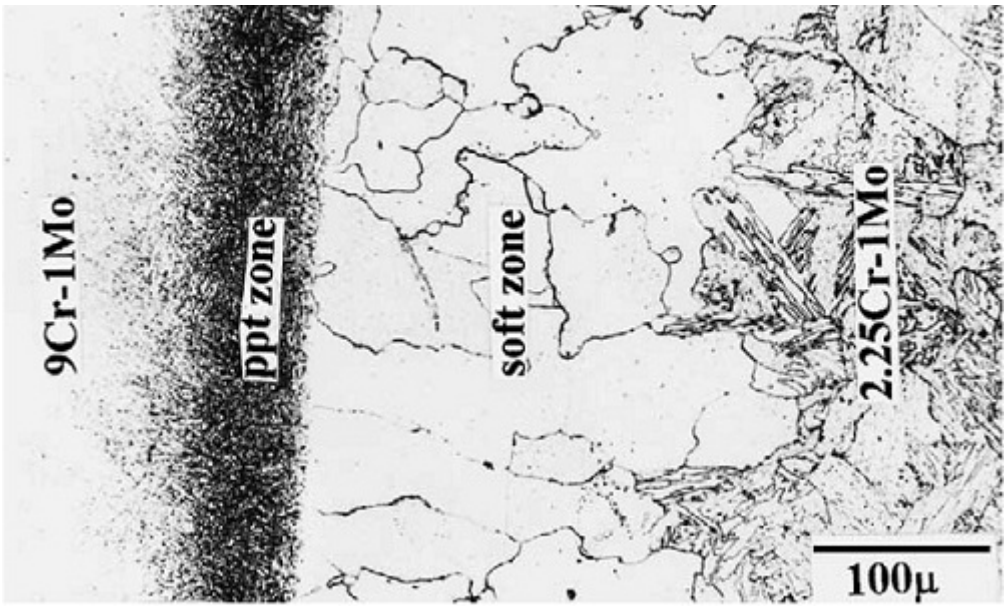

Figure 2.12: Microstructural variation around a 2.25Cr-1Mo steel – 9Cr-1Mo steel weld, showing the CEZ ('hard zone') and CDZ ('soft zone') [102].

precipitation levels around a similar interface (in this case aged at 572 $^{\circ}C$).

The properties of the carbon enriched zones in FCC alloys have also been investigated. Gittos and Gooch [69], reporting on a 2.25Cr-1Mo steel weld clad with nickel alloy Inconel 82 (an alloy very similar to Inconel 182), observed carbide precipitation in the weld metal up to 200 μm from the weld line after a PWHT at 690 $^{\circ}C$ for 30 hours. Lopez et al. [106] have reported extensive carbide precipitation in Alloy 625 after being joined to a low alloy ferritic steel by various solid state bonding techniques. The principal carbide type found by both groups of authors was $M_{23}C_6$. Huang et al. [93], reporting on the CEZ in an austenitic stainless steel, observed primarily $M_{23}C_6$ along with small amount of M_6C.

2.2.3.3 Weld Line Precipitation

A feature of aged welded interfaces between ferritic low-alloy steels and stainless steels / nickel alloys that has been reported is a band of carbides in the steel, immediately adjacent to the weld line. The existence of such particles will depend critically on the compositions of both alloys in the weld pair, the manner of the

welding process and the thermal exposure conditions. Their formation has not been observed in welds between dissimilar grades of ferritic steel.

TEM studies of these particles were carried out by Nicholson [82] [107]. The system in question was a 2.25Cr-1Mo base steel with Inconel 182 welded to it; indeed, most of the literature on interfacial carbides of this sort is reported on 2.25Cr-1Mo steels. These particles were found solely in the 2.25Cr-1Mo steel, on the edge of the martensite band described in section 2.2.2.3. There have been found to be two distinct precipitate morphologies: [108] [109]

- Type I particles, which are blocky precipitates up to 0.6 μm in diameter. They exist in a single line running parallel to the weld line. These are the predominant precipitate type in welds prepared with nickel-based alloys. Examples of this type of particle are shown in figure 2.13(a).

- Type II particles, which are individually much finer, and exist as a band up to 15 μm wide. This type of carbides are predominant in welds prepared with stainless steel, but are uncommon when nickel-based alloys are used. This is because type II carbide formation is more favourable on wider interfacial martensite bands, and wider bands are usually associated with stainless steel welds. Examples of this type of particle are shown in figure 2.13(b).

In a study on ex-service 2.25Cr-1Mo steel – type 316 stainless steel welds, Nicholson [111] found type I particles have been found to exist as two chemically distinct families: an $M_{23}C_6$ phase, which is rich in chromium, and an M_6C phase, which is rich in molybdenum. These phases have been identified by elemental analysis (EDX) and electron diffraction. The former is more abundant than the latter, since chromium is more abundant than molybdenum in systems of this type. However, Ayer et al. [54], in a weld system between 2.25Cr-1Mo steel with Alloy 625, found only $M_{23}C_6$ carbide by the same methods.

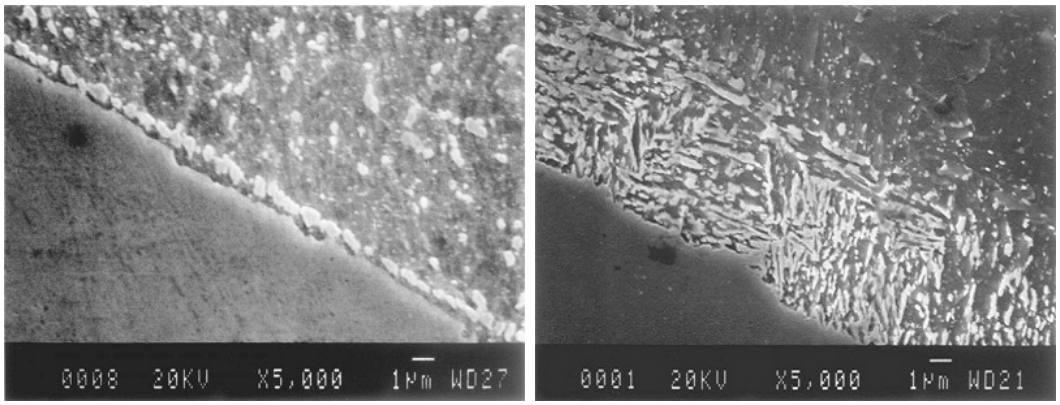

(a) Type I carbide band **(b)** Type II carbide array

Figure 2.13: SEM image of **(a)** a band of Type I carbides in 2.25Cr-1Mo steel, and **(b)** an array of type II carbides, at the weld interface with alloy 182 [110].

Type I carbides have been observed to form following high temperature ageing, from service temperatures up to 700 $°C$. Their growth is enabled by diffusion flux of carbon from the steel into the adjoining weld metal. Nicholson reported that at temperatures approaching 700 $°C$ the carbides initially grew rapidly, but begin to dissolve after 100 - 500 hours. This was explained in terms of carbon flux; at high temperatures, depletion of carbon in the steel would reduce the available flux, so that carbides would begin to dissolve to satisfy the chemical potential gradient. The implication is that these particles are in fact transient non-equilibrium features that only exist while carbon flux is ongoing.

Nicholson described the growth kinetics of type I carbides by the following Ostwald ripening equation:

$$\bar{d}^3 - \bar{d}_i^3 = kt \cdot exp\left(\frac{-Q_c}{RT}\right) \tag{2.5}$$

where $\bar{d}$ is the mean carbide size as a function of time, $\bar{d}_i$ is the initial precipitate size, k is a material constant, Q_c is activation energy for growth, R is the gas constant and T is absolute temperature. By assuming $\bar{d}_i$ to be much smaller than $\bar{d}$, and by assuming spherical carbide growth, Nicholson estimated that $Q_c = 316\ kJmol^{-1}$. By means of equation 2.5, and by measuring carbide sizes in a

variety of samples, Nicholson was able to determine a relationship between service conditions and higher-temperature laboratory tests, so as to calculate equivalent service times in accelerated ageing tests.

Building upon this work, Parker and Stratford [110] discovered that type I particles in fact displayed axial growth, with major and minor axes, and growth being more favourable along the former. The major axis was found to be parallel to the plane of the weld line. The spherical approach was found to tend to over-estimate particle size. By measuring the major and minor axes after different ageing treatments, independent activation energies and growth rates were determined. Type II carbides were also observed in some isolated areas, but they were found to disperse and eventually dissolve completely after prolonged heat treatments (up to 6000 hours at 625 $°C$). Examples of the type I and II carbides observed by Parker and Stratford are shown in figure 2.13.

There has been little published work on type I carbides in 9Cr-1Mo steels, though they have been observed by Laha et al. [112] in welds with alloy 182. Their size was reported to be smaller than the equivalent particles in 2.25Cr-1Mo steels after the same ageing condition, and the only type observed were Cr-rich $M_{23}C_6$. Additionally, type I carbides are a known feature of ex-service ferritic-austenitic welds involving P91 steel [113].

2.2.4 Mechanical Properties and Failure Modes

As one might expect, the phenomena discussed above (microstructural changes during welding and carbon migration during ageing) can have a significant impact on the mechanical properties of welded joints. It is mechanical properties that are of most interest from an industrial perspective, since they are the factors that affect service performance and ultimately component failure. The general trend, as might be expected, is that weldments demonstrate mechanical weakness relative to unaffected alloys [114] [115] [116].

The changes in hardness in the CEZ and CDZ are a consequence of the changes in local volume fraction of carbide phases, since these phases are harder than the surrounding metal matrix and act to inhibit dislocation movement. These hardness changes are well known; in a series of studies, Albert et al. [101] and Sudha et al. [102] [103] demonstrated the hardness variations across a heat treated 2.25Cr-1Mo – 9Cr-1Mo steel interface. The CDZ in the 2.25Cr-1Mo steel was softer than the bulk metal, while the CEZ in the 9Cr-1Mo steel was harder than the bulk. These changes in hardness corresponded directly with visible microstructural changes (i.e. differences in precipitate fractions). Care must be taken when interpreting hardness data in terms of the CEZ/CDZ, since hardness changes can also be caused by other effects - for instance, the microstructural changes brought on by welding, as shown by Sireesha et al. [117].

The mechanisms that cause damage and failure in weld components can be complex, and are generally inter-related. The primary damage mechanism is usually creep, i.e. plastic deformation (strain accumulation) under constant stress at elevated temperature. In systems undergoing cyclic loading (increasingly common in modern power plants), fatigue may become an issue; in such cases, the final damage mechanism may be identified as creep-fatigue. Damage is almost always in the base steel or at the fusion line, very rarely in the weld metal. Damage can be classified into four different types (not to be confused with type I/II carbides):

- Type I, which refers to cracking in the weld metal. This is rare when proper welding practices are observed.
- Type II, which is on or near the fusion line (within a few microns).
- Type III, which occurs in the CGHAZ.
- Type IV, which is located in the FGHAZ/ICHAZ.

From the comprehensive literature surveys on this matter performed by Lundin

[2], DuPont [118], and David et al. [14], a set of possible mechanisms leading to failure can be collated:

- Carbon diffusion across the weld can lead to extreme local variations in mechanical properties (most notably hardness) by changing the local phase balance. This will not in itself cause failure, but does make the weld (the CDZ in particular) vulnerable.

- Stresses acting on the vessel can lead to creep damage. Stresses can come from many sources (residual stress from welding, pressure stress, cyclic stress from thermal expansion/contraction, system stress from bending or vibration) and may act parallel and/or perpendicular to the weld. Thermal expansion stresses are noted to be less of an issue in welds between nickel-based filler metals and ferritic steels than those between austenitic stainless steels and ferritic steels due to the closer thermal expansion coefficients in the former case [119].

- The base and weld metals are generally designed to cope with these stresses, but the soft CDZ may not be able to. This is exacerbated by the adjacent CEZ, which is hard and resistant to strain; additional accumulation of strain therefore occurs in the CDZ as a result.

- The interfacial type I carbides discussed earlier may act as stress concentrators, as well as sites for void formation. Type II carbides are generally less detrimental in this regard, due to their smaller size.

- The oxide scale which naturally forms on the surface of the steel may grow inwards at the weld line. This is known as an oxide 'notch', and it acts to further concentrate the stresses on the system by reducing the load-bearing area. This mechanism is most prevalent in thin-walled tubes, since the notch size and growth rate do not depend on pipe diameter.

- The strain accumulation in the steel eventually leads to void formation, and hence failure. In welds prepared with nickel-based filler metals, type II cracking is most common. Welds with a stainless steel filler are more likely to experience type III cracking, often along PAGBs [120]. The creep crack then advances along the weld line in the manner reported by Budden and Curbishley [121].

- Alternatively, strain accumulation and subsequent cracking may occur in the type IV area. It appears that CSEF steels are most prone to failure of this type, though it may happen to any ferritic steel.

Nicholson and Williams [122] [123] have measured the creep strength of welds on 2.25Cr-1Mo steels in accelerated laboratory tests. They observed low-ductility creep failures in the steels, whether the weld metal was stainless steel or nickel-based (though they did note better durability, by a factor of 2.5 - 3, in nickel-based weldments). With nickel-based filler metal, failures that happened after relatively short times occurred by type III cracking. However, failures after long term ageing were caused by creep void formation at type I carbides. In either case, it is clear that carbon diffusion and the resultant phase changes (the softening of the steel, precipitate dissolution in the CGHAZ and formation of type I carbides at the weld line) play a part in the failure mechanism. This would appear to be supported by the findings of Laha et al. [70], who investigated the same systems as Nicholson, as well as similar welds between two identical grades of 2.25Cr-1Mo steel. They found the similar welds, in which no diffusion would have occurred, to exhibit exclusively type IV damage, while the dissimilar welds also showed damage in the type II and III areas.

Other authors, such as Klueh and King [124], Ryder et al. [125] and Roberts et al. [126], have investigated failures in ex-service welds between 2.25Cr-1Mo steels and nickel alloys. They observed similar type II failures to those observed

previously, but additional importance was placed on oxide notching as the initiator of cracking. This was proposed to be enabled as a result of the difference in oxidation resistances of the two alloys. It was observed to be a more significant issue in thin-walled tubes for geometric reasons (i.e. a fixed reduction in load-bearing area is proportionately more significant in a thin tube) - with reference to figure 2.4, it may be inferred that oxide notch-assisted failure will a more significant issue in P91/92 pipes more than 2.25Cr-1Mo pipes. It should, however, be noted that oxide notching does not necessarily cause cracking; all samples examined by the above authors had notches, but not all had experienced failure.

Parker and Stratford, in a series of studies [127] [128] [129], have investigated the interfacial failures in the same systems as mentioned above, with particular attention being paid to the role of type I carbides. They found the failure mechanism to be low-ductility cracking caused by link-up of creep voids forming at type I carbides, confirming the previous observations. These failures happened after 7 - 10 years of service operation. It was also found that interfaces fabricated with a pre-existing array of type I carbides failed after similar lengths of time to ordinary interfaces. While this does not necessarily mean that these carbides are unrelated to type II failure, it does suggest that the life-limiting factor is not the time it takes for them to form, but rather the time taken for creep strain to accumulate.

There has been less published work on the mechanical properties of 9Cr-1Mo welds than on those of 2.25Cr-1Mo steel. In a study by Laha et al. [112], in which welds between Inconel 182 and the two aforementioned steels were compared, it was found that welds of 9Cr-1Mo steel displayed superior creep resistance, as well as greater resistance to decarburisation. In the cases where type II cracking occured in the 9Cr-1Mo welds, the cause was found to be creep cavitation at interfacial particles (the same mechanism as observed in 2.25Cr-1Mo steel welds).

It was also observed by these authors that the failure position would switch to the ICHAZ (i.e. the type IV position) at increased stress. This location was con-

firmed to be weaker in 9Cr-1Mo steel than the corresponding position in 2.25Cr-1Mo steel, implying that the former is more susceptible to type IV failure - this is compounded by the greater strength of the type II/III areas due to lesser decarburisation. Such failures in various systems have also been studied by other authors; in low-Cr steels [130] [131], and in 9Cr-1Mo steels [77] [132].

There is some disagreement concerning the exact location of type IV failure; Zhang et al. [133] contend that it occurs in the FGHAZ, while Divya et al. [76] and Chandravathi et al. [81] place it in the ICHAZ. The findings of Laha et al. [134] indicate that it may occur in either area, depending on the stress state; failure location was observed to move from the FGHAZ the ICHAZ with increasing stress.

In a comprehensive review of type IV cracking in high-Cr steels by Francis et al. [135] it was found that the area of minimum hardness, as well as the point of creep failure in accelerated high-stress tests, was the ICHAZ. However, at lower stresses, more typical of service conditions, failure occurred in the FGHAZ. This supports the findings of Laha et al., and indicates that hardness cannot necessarily be used as an indicator for type IV failure location. It was suggested that type IV failure was enabled by grain boundary sliding, to which these regions are susceptible because of their small prior austenite grain size; this theory is supported by Abe et al. [136]. This allows for the accumulation of creep strain, eventually leading to void formation and failure. This also confirms that type IV failure does not occur as a result of diffusion, and is entirely a consequence of the welding process.

2.2.5 Industrial Conditions

When performing welding operations in an industrial setting, it is necessary to carefully control the practices and procedures so as to ensure optimal joint integrity, whilst simultaneously operating in a practical and economical manner. There are a multitude of codes, varying between regions, that define the welding standards for different alloys so as to minimise common mechanical failures.

The application of a PWHT is strongly recommended when welding to grade 91/92 steels to minimise the impact of the HAZ. However, it may not be possible to perform such a treatment on site to particularly large pipe sections, or to pipe sections in hard to reach places. In such cases, a 'buttering' treatment may be performed in the workshop before the pipe section is sent to the plant. In this treatment, a layer of weld filler metal (up to a few millimetres thick) is deposited to the end of the pipe, and a PWHT is then applied. The part is then sent to the site and welded without need for a PWHT (since the butter layer protects the steel from the heat of welding).

Another way in which the integrity of a weld can be protected is by preheating the base steel before performing the welding operation, usually up to 100 to 200 $^{\circ}C$. This has the effect of reducing the cooling rate in the steel by lowering the thermal gradients, which reduces the amount of fresh martensite that forms (which can be understood with reference to the CCT diagram in figure 2.3). This reduces the tendency for hard microstructures to form in the HAZ, as well as lessening effects such as restraint cracking and weld distortion, hence reducing the likelihood of subsequent failure.

Based on the effects that have been outlined thus far in this chapter, a schematic overview of the conditions experienced by a weld in an industrial setting, and some of the phenomena it may display, can be constructed. This is shown in figure 2.14. The range of temperatures to which a DMW is exposed, and the lengths of the exposures, is a critical factor to consider when analysing evolution phenomena.

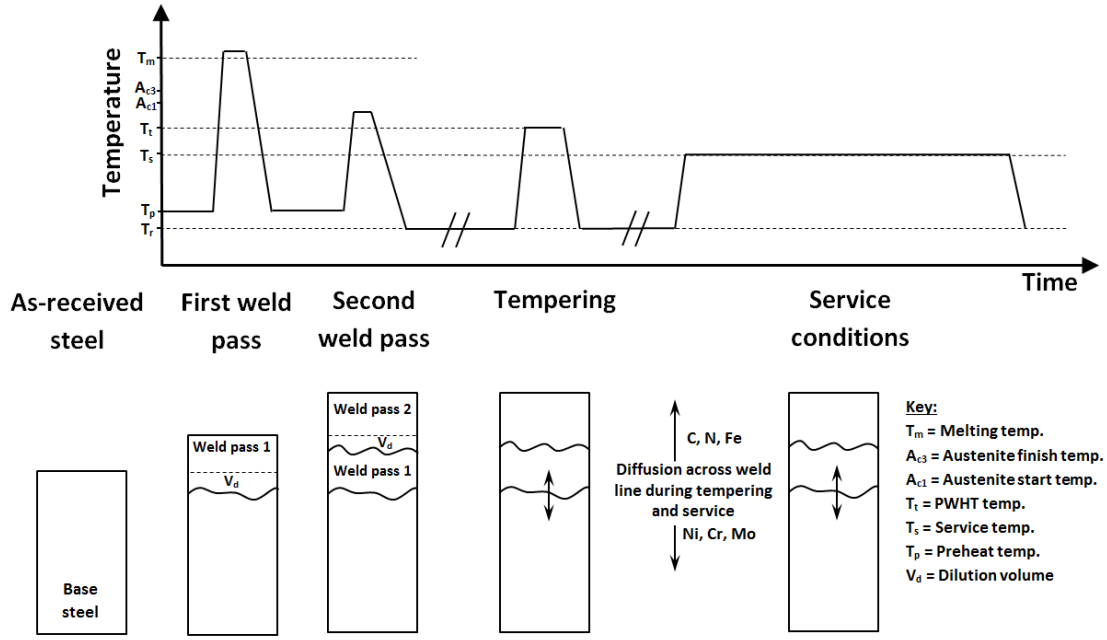

Figure 2.14: An overview of the thermal life of a weld, and the progressive build-up of material during the welding process. The normalising treatment, were it to be performed, would precede the tempering treatment.

2.2.6 Modelling of Diffusion at Dissimilar Interfaces

It has long been desirable to be able to model the carbon diffusion process, so that the evolution of dissimilar interfaces can be predicted. In general, this requires the application of diffusion theory, which will be discussed in detail in the following chapter. Simple analytical models have been constructed by various researchers, such as Buchmayr et al. [88], who used a ternary Fe-Cr-C model to predict diffusion across a welded interface between two ferritic steels during PWHTs (at 680 and 730 $°C$). The model assumes that chromium does not migrate, allowing the interaction between chromium and carbon to be expressed by an interaction parameter ϵ_C^{Cr}. Chromium and other carbide formers have negative ϵ-values, lowering the local chemical potential of carbon and hence creating a driving force; elements such as nickel have positive ϵ-values, hence having the opposite effect. Reasonable agreement was observed between the results of the model and measurements of carbon concentration by electron probe microanalysis

(EPMA).

In three loosely related studies, Pavlovský et al. [91], Million et al. [92] and Foret et al. [94] constructed models between different grades of steel by estimating carbon diffusivities based on empirical carbon concentration data. The approach used was in some respects similar to that applied by Buchmayr et al., in that the effect of chromium (and nickel, where necessary) was taken into account using interaction parameters ϵ. The results of these studies, which show good agreement with experimental data, reveal several important characteristics about carbon diffusion across dissimilar interfaces:

- The diffusivity of carbon in an FCC matrix is lower than that in a BCC matrix, by at least two orders of magnitude. This causes carbon to 'pile up' in the FCC alloy near the interface.
- The extent of carbon diffusion between two dissimilar steels depends to some degree on their relative chromium levels, with the most extensive diffusion taking place when the chromium gradient is greatest.
- The diffusion distances of carbon increase non-linearly with time, confirming the observations by Race reported in section 2.2.3.2.

These analytical expressions are only truly applicable for simple cases, becoming exponentially more complicated as more components are included. Models including more than four components are not practicable. Additionally, by these methods it is difficult to account for the evolution of secondary phases, and the effects that such phases have on diffusion (i.e. their physical impediment on diffusing species and their impact on local chemical potentials). More complete models that combine thermodynamic and kinetic properties have been derived using numerical methods, enabled by the processing power of modern computers and the availability of commercial software packages. A summary of work that has been

published on computational modelling of diffusion at dissimilar metal interfaces is given in table 2.4.

One such tool is a closely linked pair of packages, called *Thermo-Calc* and *DICTRA* [137]. The former is used for thermodynamic calculations, the latter for kinetics. Using these tools, Helander et al. [138] [139] (members of the software development team) have been able to successfully simulate the carbon diffusion and resultant phase changes across an interface between two four-component Fe-Cr-Ni-C steels; one similar to type 304 austenitic stainless steel, and one low-alloy steel. Simulations were carried out in the high temperature regime, in which both steels were fully austenitic, and in the low temperature regime, in which the low alloy steel was ferritic. These two cases are subtly different, with the latter being difficult to implement due to the difficulties in describing diffusion though multiple matrix phases. Two approaches were hence used: the dispersed phase approach for the austenite-austenite case and the cell model for the ferrite-austenite case (the cell model consisting of two conjoined simulations). The results were reasonable in both cases, with the models predicting the correct diffusion distances and resultant phases.

Engström et al. [140] have also used these software tools to separately model carburisation of nickel-based alloys and interdiffusion at a ferritic-ferritic steel weld. Carburisation was simulated using a boundary condition, while the weld system was simulated by effectively the same means as used by Helander et al. for their austenite-austenite simulations. Both sets of calculations were performed in *DICTRA* using the dispersed phase approach. Again, satisfactory agreement was observed between simulations and experiments, with regards to both diffusion distances and phases.

Other independent researchers have also carried out computational studies of dissimilar interfaces. Anand et al. [97], building upon the earlier works on 2.25Cr-1Mo – 9Cr-1Mo steel interfaces outlined in section 2.2.3.2, applied the *DICTRA*

dispersed phase model with good results. They also simulated the effect of a nickel-based diffusion barrier at the interface, using a similar approach (the cell model) to that used by Helander et al. The latter model has been successfully used to demonstrate the effectiveness of the diffusion barrier, and its optimal thickness.

Meanwhile, an alternative numerical model within *DICTRA*, called the 'homogenisation model' has proven to have applications in the simulation of dissimilar interfaces. This model, which will be described in more detail in section 3.2.9, calculates the local average of the kinetic properties of all present phases, hence eliminating the complications involved with multiple matrix phases. Larsson et al. [141] [142] have described the method and demonstrated its applicability to Fe-Cr-Ni diffusion couples (not involving carbon). Alexandrov et al. [75] have used this same scheme to simulate the diffusion of carbon from a low-alloy steel to Alloy 625, with good agreement with their experimental data.

Kozeschnik et al. [143] [144] used a different software package, *MatCalc*, to simulate diffusion across various ferritic-ferritic steel interfaces. Again, they observed good agreement with experimental results (both measured carbon concentrations and precipitate identification).

Table 2.4: A summary of the results of prior works involving the computational modelling of dissimilar metal interfaces.

Report	Alloys	Joining Method	Ageing Temp.	Modelling Method	Validation
Engström et al., 1994 [140]	12-% Cr steel 1-% Cr steel	Fusion welding	680 – 730 $°C$ (BCC – BCC)	*DICTRA*, Dispersed phase model	EPMA
Helander & Ågren, 1997 [138]	18Cr-10Ni steel Low alloy steel	Diffusion bonding	835 – 1200 $°C$ (FCC – FCC)	*DICTRA*, Dispersed phase model	–
Helander & Ågren, 1997 [138]	18Cr-10Ni steel Low alloy steel	Diffusion bonding	600 – 725 $°C$ (FCC – BCC)	*DICTRA*, Cell model	Micrographs
Kozeschnik et al., 2002 [143] [144]	P91 steel 2.25Cr-1Mo	Fusion welding	565 – 730 $°C$ (BCC – BCC)	*MatCalc*	WDX and TEM
Foret et al., 2006 [145]	P91 steel 1.9 % Cr steel	Diffusion bonding	600 – 700 $°C$ (BCC – BCC)	*DICTRA*, Dispersed phase model	EPMA
Larsson & Engström, 2006, [141]	High Cr-Ni steels	Diffusion bonding	1100 – 1200 $°C$ (Mixed FCC & BCC)	*DICTRA*, Homogenisation model	EPMA
Alexandrov et al., 2012 [75]	Alloy 625 Low alloy steel	Fusion welding	677 $°C$ (FCC – BCC)	*DICTRA*, Homogenisation model	WDX
Anand et al., 2013 [97]	9Cr-1Mo 2.25Cr-1Mo steel	Fusion welding	550 – 750 $°C$ (BCC – BCC)	*DICTRA* Dispersed phase model	EPMA
Anand et al., 2013 [97]	Alloy 625 2.25Cr-1Mo & 9Cr-1Mo	Fusion welding	550 – 750 $°C$ (FCC – BCC)	*DICTRA* Cell model	EPMA

2.3 Summary

There is a reasonable body of work documenting the evolution of interfaces and welds between dissimilar metals. However, is it not exhaustive, and there are gaps in the literature, such as:

- Much of the published work focusses on welds involving 2.25Cr-1Mo steels, while there is relatively little surrounding the evolution of welds involving 9Cr-1Mo steels, such as P91 and P92.
- The finer details of welding-induced microstructural features and their impacts on ageing behaviour, particularly concerning the interfacial martensite band, are not well known and warrant further investigation.
- The precise mechanisms of failure modes are not known with certainty, making failures an on-going issue in service.
- Research involving thermodynamic software is still in its infancy, leaving significant room for advancement. While there are disparate works on individual systems, there is no wide-ranging generic model. There is also very little work regarding ferritic-austenitic weld systems.

The present work will focus on the investigation of dissimilar interfaces by a combination of experimental and computational means. This will be primarily on a P92 – Alloy 625 welded interface, with some data drawn from other systems to support conclusions. Experimental investigation involving microstructural characterisation and microhardness testing will be carried out on samples in a range of aged cases. These results will then be compared with results from the computational models. If confidence can be gained in them, then they may be used to predict the long-term behaviour of dissimilar welds in service conditions.

Chapter 3

Modelling Methods

Mathematical modelling of thermodynamic systems has always been desirable, since it allows predictions to be made about their behaviour on the basis of limited experimental data. However, the calculations are inevitably very complicated in multicomponent systems, and so have traditionally been limited to evaluations of low order systems where analytical methods can be applied.

The processing power of modern computers opens up new avenues. Using appropriate software, complex multicomponent systems can be numerically analysed in ways that would otherwise have been insurmountable. Since the 1980s, several commercial software packages have been developed for the purpose of performing thermodynamic calculations. These belong to the CALPHAD (CALculation of PHAse Diagrams) family. One of the more widely used programs is *Thermo-Calc*, developed at the Royal Institute of Technology in Stockholm, Sweden. It can be used to calculate equilibrium phase behaviour and a wide range of thermodynamic properties for multicomponent alloy systems using experimentally assessed data

from lower-order systems. It has proven itself to be a very useful tool, allowing researchers to accurately predict the phases that may be present in alloys as functions of temperature and composition, streamlining experimental work and alloy development.

As useful as *Thermo-Calc* and other similar tools are, they provide only equilibrium data. The evolution of a system due to diffusion processes cannot be analysed. This gap has been partially filled by the *DICTRA* (DIffusion-Controlled TRAnsformations) software, developed by the same group who were responsible for *Thermo-Calc*. This is a one-dimensional finite difference simulation method which combines data from *Thermo-Calc* with its own kinetic data in order to perform diffusion calculations. It allows the evolution of the elemental distribution in a system to be modelled.

3.1 Calculation of Phase Equilibria

A phase within a material, be it liquid, gas or a crystalline solid, will exist in equilibrium if it has the lowest Gibbs free energy with respect to other possible phases. For a given set of state variables, this condition will determine which phase, or combination of phases, is present. It is this principle of determining the equilibrium balance of phases that underpins CALPHAD methods [146].

The Gibbs free energy, G, of a phase can be defined by the following expression:

$$G = U + PV - TS \tag{3.1}$$

where U is the internal energy of the system, P is pressure, V is volume, T is thermodynamic temperature and S is entropy. In a system consisting of two elements, there may be a number of possible phases, each with an associated Gibbs free energy (the sum of which, weighted by their relative proportions, is the total energy of the system).

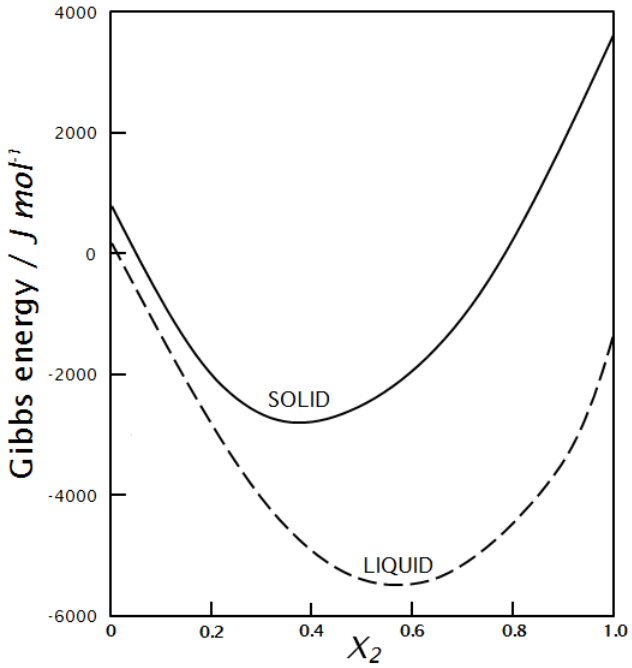

Figure 3.1: Diagram showing the free energies of two phases in a binary system at temperature T_1. The liquid phase has a lower free energy at all compositions.

Gibbs energies may best be realised when plotted graphically as functions of composition. Consider the free energies of an arbitrary binary system, shown in figure 3.1, with a composition defined by the mole fractions of the two components, x_1 and x_2. This system is evaluated at a temperature T_1. At this temperature, let us assume there exists a solid phase and a liquid phase. In this case, the free energy of the liquid phase is less than that of the solid phase over all possible compositions, and is hence the equilibrium phase.

However, at a different temperature, T_2, the liquid and solid phase curves overlap, as shown in figure 3.2. There will be three possible phase balances in this case. When $x_2 < x_S$, the solid phase will be in equilibrium. When $x_2 > x_L$, the liquid phase will be in equilibrium. However, when x lies between x_S and x_L, both phases will coexist.

The gradients of free energies (i.e. the partial derivatives of the free energies) are important quantities. These are known as the chemical potentials, μ_i, which can be formally defined as: [147]

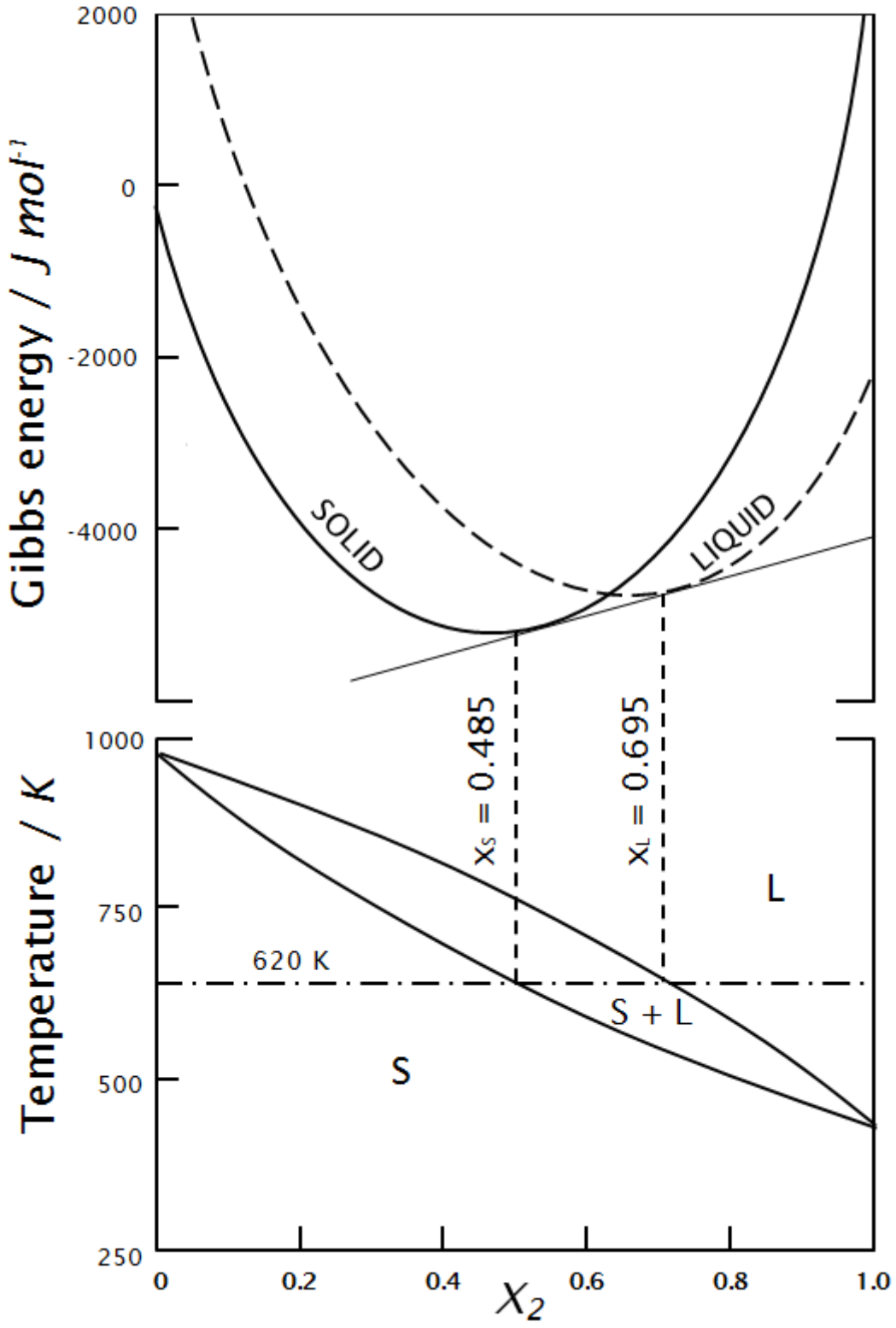

Figure 3.2: Diagram showing the free energies of two phases in a binary system. Also illustrated in the lower section is the means by which free energy calculations are used to construct phase diagrams by the common tangent method, where **S** and **L** denote areas of solid and liquid phase respectively.

$$\mu_1 = \left(\frac{\partial G}{\partial N_1}\right)_{T,P,N_2,N_3...} \tag{3.2}$$

where N_1 is the number of moles of species 1. Equivalent expressions exist for μ_2, μ_3, etc. The chemical potential of a component is therefore the gradient of free energy with respect to the number of moles of that component, whilst all other conditions are held constant. A system will be in equilibrium when the weighted sum of all its chemical potentials is zero, i.e. when:

$$\sum_{i=1}^{n} \mu_i dN_i = 0 \tag{3.3}$$

where n is the number of components in the system. At the most basic level, the CALPHAD approach aims to calculate G for each phase in a given system at a certain composition. It will then alter the composition of the system, and calculate the resulting change in G for each phase. This process is repeated iteratively until the free energies for all phases are minimised, i.e. when the condition in equation 3.3. At this point the equilibrium phase balance has been calculated. This method then extends to systems of more than two phases and/or components, at the cost of increasing the complexity of the calculations.

This iterative process gives the phase equilibrium for a given set of system state parameters (temperature, pressure, composition). The process can be extended to calculate equilibria as one of these conditions is varied. This process is called stepping, and it allows phase information to be determined as a function of the dependent variable. Mapping is a further extension of the iterative process, in which two conditions are varied. Varying over composition and temperature produces data that can then be plotted as a traditional binary phase diagram. An illustration of how mapping is used to produce a phase diagram can seen in figure 3.2.

Since this iterative method calculates the Gibbs energy of phases at a given

state condition, other thermodynamic variables (chemical potential, entropy, enthalpy, etc.) are determined as a matter of course. These can be mapped and plotted, adding to the versatility of the CALPHAD approach.

Calculations such as these are subject to the caveat that they must obey Gibbs' phase rule. This rule is defined as:

$$F = \chi - \phi + 2 \tag{3.4}$$

where F is the number of degrees of freedom in a system, χ is the number of components and ϕ is the number of phases in equilibrium. The value of F defines the number of intensive (i.e. volume-independent) variables that can be altered without impacting one another. Thus, in order to calculate a binary phase diagram as described above, F must be 2 or greater. This rule must always be considered when attempting thermodynamic calculations.

In a condensed system (i.e. a solid, which covers all cases of relevance to this thesis), pressure is considered to have a negligible impact on the thermodynamic properties. It can hence be neglected, and equation 3.4 is modified to become:

$$F' = \chi - \phi + 1 \tag{3.5}$$

where F' is the number of degrees of freedom when pressure is excluded.

3.2 Diffusion Calculations

The CALPHAD method deals with the thermodynamics of equilibrium systems. However, it is important to understand the rates at which systems out of equilibrium change. This is the field of kinetics, and this study of phase transformations and diffusion in non-equilibrium systems is an important topic in materials science. The mechanism of phase transformations and the progression to

equilibrium generally involves diffusion.

3.2.1 Fick's Laws of Diffusion

The phenomenological laws of diffusion were first derived by Adolf Fick in 1855, after the observation was made that substances would tend to diffuse from areas of high concentration to those of low concentration. This is just as true in solids as it is in liquids or gases, although harder to observe. Fick's first law describes steady-state one-dimensional diffusion flux in simple binary cases as follows:

$$J_k^V = -D_k \frac{\partial C_k}{\partial z} \tag{3.6}$$

In this equation, J_k^V is the atomic flux of species k in the z axis and the volume-fixed reference frame, D_k is a diffusivity (in units of $m^2 s^{-1}$) and C_k is the concentration of the diffusing element (the amount of substance per unit volume). This extends to three spatial dimensions by replacing the partial derivative with a gradient operator.

In order to calculate the change in concentration as a function of time, t, a second equation is needed. This is obtained by combining equation 3.6 with the mass continuity equation, as described by:

$$\frac{\partial C_k}{\partial t} = -\frac{\partial J_k^V}{\partial z} \tag{3.7}$$

The result of this combination is Fick's second law:

$$\frac{\partial C_k}{\partial t} = \frac{\partial}{\partial z}\left(D_k \frac{\partial C_k}{\partial z}\right) \tag{3.8}$$

In the case that D_k is constant, it can be brought out of the derivative, though in general it is not. By application of Fick's laws, analytical solutions to diffusion problems in certain simple cases can be derived.

3.2.2 Mechanisms of Diffusion in Solids

The relative sizes of the atoms in a system determine the way in which diffusion occurs; a large atom moving through a matrix of smaller atoms will require a high activation energy for each step, and vice versa. The possible range of relative sizes leads to two distinct diffusion mechanisms - interstitial diffusion and substitutional (or vacancy) diffusion. In general, the diffusivity is predicted by an Arrhenius-type equation:

$$D = D_0 \exp \frac{-Q_{I,S}}{RT} \tag{3.9}$$

Here, D_0 is the diffusivity at infinite temperature (a material constant), $Q_{I,S}$ is the activation energy necessary for diffusion to occur. Equations 3.6 and 3.9 show that the most significant variables dominating diffusion flux are concentration gradient and temperature.

When the diffusing species is sufficiently small relative to the matrix species to occupy interstitial lattice sites, atoms are able to move between between sites in a random jump process, as illustrated in figure 3.3. The activation energy (in this case, Q_I) can here be expressed simply as the enthalpy required for a single jump i.e. $Q_I = \Delta H_M$ [148]. The energies required for this process are low, resulting in fast mobility when compared to other mechanisms. An example of an element that diffuses in this way is carbon in steels and similar alloys.

When the two atomic species are of comparable size, or the diffusing species is larger, diffusion generally occurs by the movement of atoms into adjacent vacancies in the lattice. As such, a flow of atoms in one direction can be seen as a flow of vacancies in the opposite direction. This process is illustrated in figure 3.4. The activation energy is modified to account for the enthalpy associated with vacancies, becoming $Q_S = \Delta H_M + \Delta H_V$. This mechanism is typically slower than interstitial diffusion since activation energies are higher (often by multiple orders

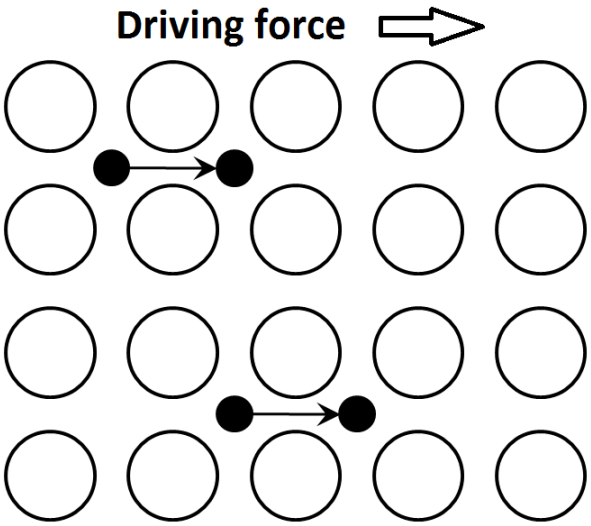

Figure 3.3: Schematic overview of the interstitial diffusion process. Atoms of the diffusing species are represented as small solid black circles, while those of the lattice species are larger hollow circles.

of magnitude) and since the rate depends on local vacancy density, itself a function of temperature.

3.2.3 Frames of Reference

It is necessary when formulating fluxes and diffusivities to also define frames of reference [149]. The fluxes in equations 3.6 and 3.7 were given in the volume-fixed reference frame, defined such that:

$$\sum_{k=1}^{n} V_m J_k^V = 0 \tag{3.10}$$

In this frame of reference, the molar volume V_m (defined as $V_m = \sum_{k=1}^{n} C_k V_k$, where V_k is the partial molar volume of k) remains constant either side of inert markers. In other words, there is no net flow of volume, although crystal lattice planes may move. This is closely related to the number-fixed reference frame, in which there is no net flow of atoms across an inert marker; the volume-fixed is equivalent to the number-fixed frame restricted to elements that contribute to volume (i.e. substitutional elements). These frames of reference are the most

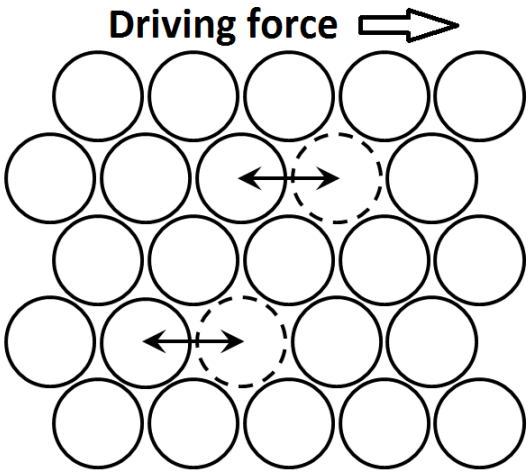

Figure 3.4: Schematic overview of the substitutional diffusion process. Atoms (solid-bounded circles) move in the direction of the driving force, while vacancies (dotted circles) move in the opposite direction.

convenient for simple diffusion calculations based on Fick's laws.

For other approaches, a lattice-fixed reference frame may be applied, in which the crystal lattice remains fixed while volume may flow; in other words, the co-ordinate system is fixed to the lattice planes. The velocity of this frame can be defined such that:

$$\sum_{k=1}^{n} J_k^L = -J_{Va} \tag{3.11}$$

where J_{Va} is the vacancy flux. The transformation between volume and lattice-fixed reference frames can be achieved by considering diffusive flow and physical movement past a stationary observer, and is performed as follows:

$$J_k^L = J_k^V - C_k \nu_L \tag{3.12}$$

where ν_L is the velocity of the lattice-fixed frame relative to the volume-fixed frame.

3.2.4 Extension to Multicomponent Systems

It is unusual for a real alloy system to have only two atomic species, so practical calculations must be extended to multicomponent interactions. An equation for one-dimensional diffusion fluxes in systems of n components was proposed by Onsager, as a modification of Fick's first law: [150]

$$J_k^V = -\sum_{i=1}^{n} D_{ki} \frac{\partial C_i}{\partial z} \tag{3.13}$$

Where D_{ki} is the diffusivity of component i with respect to component k. The following multicomponent equivalent of Fick's second law can hence be written as follows:

$$\frac{\partial C_k}{\partial t} = \sum_{i=1}^{n} \frac{\partial}{\partial z} \left(D_{ki} \frac{\partial C_i}{\partial z} \right) \tag{3.14}$$

Equations 3.13 and 3.14 are sometimes referred to as the Fick-Onsager laws. An important characteristic of multicomponent diffusion that is apparent from these equations is that the diffusion flux of a component is a function not only of its own concentration gradient, but also on those of other components in the system. This was first observed experimentally by Darken in the form of carbon diffusing against its own concentration gradient at the interface between two different steels [86].

3.2.5 Phenomenological Approach to Diffusion

It is not always convenient to use the Fick-Onsager approach to diffusion, since it predicts that diffusion occurs only due to concentration gradients. An alternative approach is to consider that diffusion always acts to decrease local free energy, and hence chemical potential. Equilibrium for a component is reached if the chemical potential associated with that component is homogeneous throughout

the system in question. Furthermore, diffusion is assumed to occur in the lattice-fixed frame of reference. This is known as the phenomenological approach because it comes from empirical observations. It has been described in detail in a set of related publications, the essences of which will be recounted here [151] [152] [153].

If it is assumed that diffusion occurs down chemical potential gradients (or, alternatively, activity gradients) rather than concentration gradients, then the following expression for multicomponent, lattice-fixed diffusion flux can be formulated:

$$J_k^L = -\sum_{i=1}^{n} L_{ki} \frac{\partial \mu_i}{\partial z} \tag{3.15}$$

where L_{ki} is a term describing atomic kinetics. Additionally, based on the assumption of diffusion by vacancy exchange, the lattice-fixed flux can be defined as:

$$J_k^L = -C_k y_{Va} F_{kVa} \frac{\partial \mu_k}{\partial z} \tag{3.16}$$

where y_{Va} is the fraction of vacancies on the crystal lattice and F_{kVa} is a kinetic factor which describes the rate of exchange between an atom and an adjacent vacancy. Equation 3.16 may be simplified further by introducing a new mobility variable M_k, defined as:

$$M_k = y_{Va} F_{kVa} \tag{3.17}$$

This formulation is useful, but it is still more practical to consider diffusion in the volume-fixed reference frame, and with composition gradients as the driving forces. Equation 3.15 must therefore be modified. It is first converted to the volume-fixed frame, by modifying the kinetic term:

$$J_k^V = -\sum_{i=1}^{n} L'_{ki} \frac{\partial \mu_i}{\partial z} \tag{3.18}$$

where volume-frame kinetic term L'_{ki} is related to the lattice-fixed kinetic term as:

$$L'_{ki} = \sum_{j=1}^{n} \left(\delta_{kj} - C_k V_j\right) L_{ji} \tag{3.19}$$

Here, δ_{ik} is the Kronecker delta. To then introduce concentrations into Equation 3.18, it is expanded by application of the chain rule of derivation, as follows:

$$J_k^V = -\sum_{i=1}^{n} L'_{ki} \sum_{j=1}^{n} \frac{\partial \mu_i}{\partial C_j} \frac{\partial C_j}{\partial z} \tag{3.20}$$

By comparison with equation 3.13, the phenomenological diffusivity can be identified:

$$D_{kj} = \sum_{i=1}^{n} L'_{ki} \frac{\partial \mu_i}{\partial C_j} \tag{3.21}$$

Substituting equation 3.21 back into equation 3.20 results in the following:

$$J_k^V = -\sum_{j=1}^{n} D_{kj} \frac{\partial C_j}{\partial z} \tag{3.22}$$

i.e., the same result as equation 3.13, the first Fick-Onsager equation. From this expression, it is clear that the fluxes and concentration gradients are n-component vectors, while the diffusivities form an $n \times n$ rank 2 tensor.

3.2.6 Diffusion Equations in *DICTRA*

DICTRA applies the mathematical methods described in the previous sections to simulate multicomponent diffusion in one dimension. The basic schematic process used by *DICTRA* is shown in figure 3.5. *Thermo-Calc* is called as a subroutine

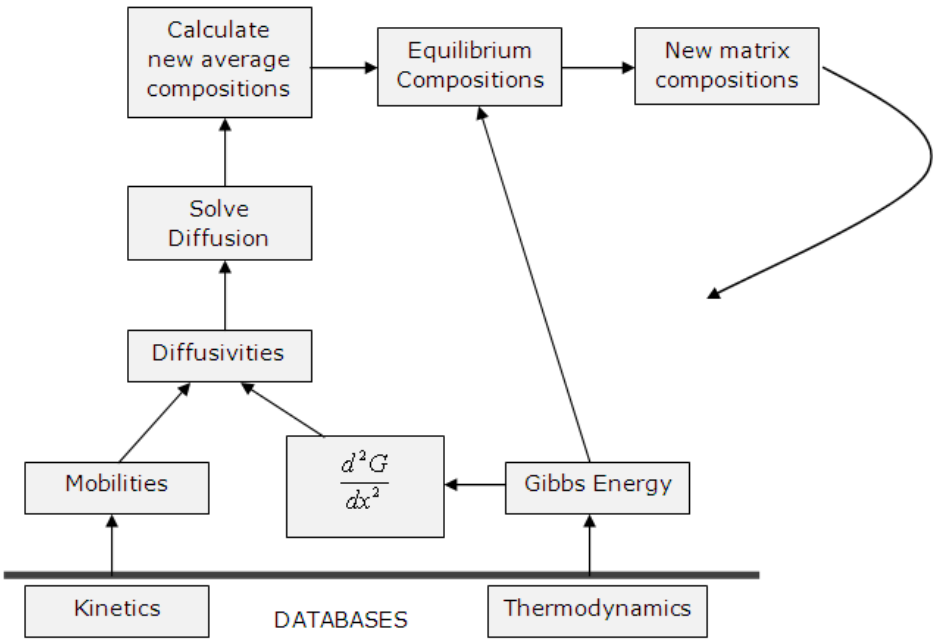

Figure 3.5: Schematic of the calculation process employed by *DICTRA*. The variable x is the mole fraction of a given component. Adapted from Engstrom [154].

to calculate thermodynamic equilibrium, while mobility data are called from separate databases.

The *DICTRA* program makes use of assumptions to simplify the diffusion calculations and reduce the amount of empirical data that must be stored. Firstly, it is assumed that all substitutional species have the same molar volume, and that interstitial species have zero contribution to volume. One component is then removed from the diffusivity matrix as follows:

$$D^n_{kj} = D_{jk} - D_{kn} \tag{3.23}$$

$$D^n_{kj} = D_{jk} \tag{3.24}$$

Equation 3.23 applies to substitutional elements, while 3.24 applies to interstitials. D^n are known as the reduced diffusivities. The eliminated component is, conventionally, the solvent component (for example, iron in an alloy steel). When these are applied, the multicomponent flux equation can be written as:

$$J_k^V = -\sum_{j=1}^{n-1} D_{jk}^n \frac{\partial C_j}{\partial z} \tag{3.25}$$

The inclusion of reduced diffusivities means that only $n-1$ independent flux balance equations are required. This is justified on the basis that the local concentration changes and fluxes of the eliminated component can be trivially found once the equations have been solved.

3.2.7 Mobilities and Kinetics

The form of D_{kj} in equations 3.21 and 3.22 can be derived from kinetic arguments to be:

$$D_{kj} = -\sum_{i=1}^{n} \left(\delta_{ik} - C_k V_k\right) C_i M_i \frac{\partial \mu_i}{\partial C_j} V_m \tag{3.26}$$

By comparison with equation 3.21, the volume-frame kinetic term L'_{ki} can be identified:

$$L'_{ki} = \sum_{i=1}^{n} \left(\delta_{ik} - C_k V_i\right) C_i y_{Va} M_i \tag{3.27}$$

The major unknown term in equation 3.27 is the mobility term, M_i. For the purposes of the *DICTRA* approach, it is defined by an Arrhenius-type relation:

$$M_i = M_i^0 \exp \frac{-Q_i}{RT} \tag{3.28}$$

where there exists an approximately linear relationship between M_i^0 and Q_i. These values are determined experimentally and stored in databases for use by *DICTRA*.

It can be seen in equation 3.26 that the two key terms used in the determination of D_{kj} are the mobility, M_i, a purely kinetic term, and the term $\frac{\partial \mu_i}{\partial C_j}$, which corresponds to the thermodynamic factor first identified by Darken. This

thermodynamic factor can be calculated from thermodynamic databases using *Thermo-Calc* for a given system.

The rationale behind this approach hence becomes apparent; the kinetic and thermodynamic contributions to the diffusivities are calculated separately, using separate databases. Additionally, the amount of empirical data required is smaller than if diffisivities were stored, since an n-component system requires n mobilities, but $(n^2 - 1)$ reduced diffusivity tensor components.

3.2.8 Numerical Integration Schemes

The equations described in section 3.2.4 are too complicated to solve analytically for most practical systems. For this reason, approximate solutions to the equations are found by finite difference numerical integration. The functions, C_k in this case, are evaluated over discrete steps in x and t rather than being continuous. D_k is assumed to be constant. These methods are described in detail elsewhere [155]; the parts of relevance will be summarised here.

The first stage in numerically solving differential equations is to form approximations for the derivatives of the function. This is done by Taylor expansion, with the assumption that second order and higher terms are negligible. Let u and v represent co-ordinates in the x and t axes respectively, separated by finite increments Δx and Δt (this is illustrated graphically in figure 3.6). The resultant approximations for derivatives of a generic function f between steps in x are as follows:

$$\frac{\partial f(z,t)}{\partial z} \approx \frac{f(z_{u+1},t_v) - f(z_u,t_v)}{\Delta z} \tag{3.29}$$

$$\frac{\partial f(z,t)}{\partial z} \approx \frac{f(z_{u+1},t_v) - f(z_{u-1},t_v)}{2\Delta z} \tag{3.30}$$

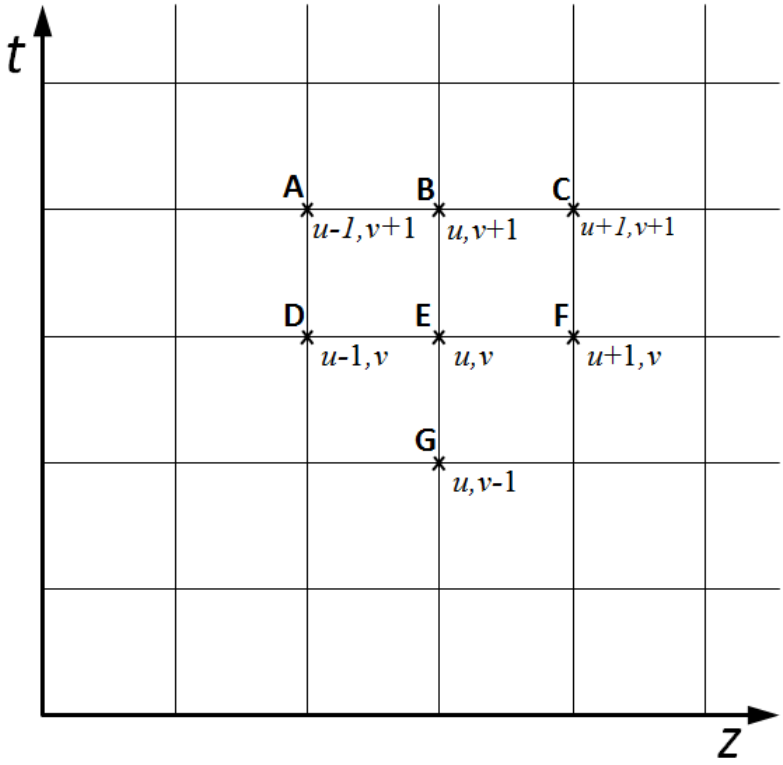

Figure 3.6: Graphical view of the $z-t$ plane in the finite difference scheme. The plane is split into discrete segments with spacings of Δz and Δt.

$$\frac{\partial f(z,t)}{\partial z} \approx \frac{f(z_u,t_v)-f(z_{u-1},t_v)}{\Delta z} \tag{3.31}$$

Equations 3.29, 3.30 and 3.31 are known as the forward, central and backward differences respectively. An approximation for the central difference of the second derivative of f can also be found:

$$\frac{\partial^2 f(z,t)}{\partial z^2} \approx \frac{f(z_{u+1},t_v)-2f(z_u,t_v)+f(z_{u-1},t_v)}{\Delta z^2} \tag{3.32}$$

Equivalent forms of these four equations also exist for the case differentiated with respect to t. These equations form the basis of the various possible numerical integrations schemes.

The simplest integration scheme is the explicit scheme. This solution is reached using the forward difference in time and the second order central difference in space (equations 3.29 and 3.32). By applying these approximations to equation

3.8 (Fick's second law), the following solution is reached:

$$C_k\left(z_u, t_{v+1}\right) \approx D_k r\left(C_k(z_{u+1}, t_v) + C_k(z_{u-1}, t_v)\right) - (1 - 2D_k r)C_k(z_u, t_v) \quad (3.33)$$

The variable r is defined as $\left(\frac{\Delta t}{\Delta x^2}\right)$. This approach is called the explicit method because the unknown value of C_k at step t_{v+1} is calculated solely from known values at step t_v - on figure 3.6, it can be seen that point **B** is calculated based on points **D**, **E** and **F**. This makes calculations relatively simple, but the method has limitations; for instance, it can be shown that the method is only valid for $r \leq 0.5$. Solutions based on this method also tend to be less accurate than those of more sophisticated methods.

By using the backward difference in time, one can arrive at the implicit solution:

$$C_k(z_u, t_v) \approx -D_k r C_k(z_{u+1}, t_{v+1}) - D_k r C_k(z_{u-1}, t_{v+1}) + (2D_k r + 1)C(z_u, t_{v+1}) \quad (3.34)$$

In this case, the value of C_k at the step in time t_{v+1} is calculated using values at the current time step as well as the previous step (i.e. point **B** is calculated using **A**, **C** and **E**).

Calculations under the fully implicit scheme are generally more complicated than those of the explicit scheme, since the dependence of values on those at adjacent points in space (i.e. **B** depends upon **A** and **C**) means a set of simultaneous equations must be solved at each time step. However, implicit methods provide more accurate results in most cases, and are unconditionally stable over all values of r. As such, the implicit scheme will be used for calculations in this work.

3.2.9 Homogenisation Model

The specific computational scheme within *DICTRA* that is used in this research is called the "Homogenisation Model". It is based on a phenomenological consideration of transport phenomena (not specific to atomic diffusion), and an alternative consideration of phases and mobilities to conventional methods [141] [156]. This approach effectively calculates diffusion through a single phase, with the one phase having the local average kinetic and thermodynamic properties of all the phases that would exist in equilibrium at the given point.

In this case the diffusion flux J_k of species k in the lattice-fixed reference frame between two planes/points a and b, derived from absolute reaction rate theory, is as follows:

$$J_k^L = -\frac{M_k^{eff} RT}{V_m \Delta \tilde{z}} \sqrt{x_k^a x_k^b} 2 \sinh \frac{\Delta \mu_k}{2RT} \tag{3.35}$$

In this equation, M_k^{eff} represents the effective mobility of species k (i.e. the averaged mobility across all local phases), while x_k^a and x_k^b are the mole fractions of species k at a and b. V_m is the molar volume of the system in question, while $\Delta \mu_k$ is the local change in chemical potential. The variable $\tilde{z}$ is related to the standard spatial co-ordinate in a way that connects the lattice-fixed and volume-fixed reference frames; to define this relation, consider the velocity of an inert marker, fixed to the lattice, relative to the volume-fixed frame:

$$\nu_z = -V_m \sum_{k=1}^{n} J_k \tag{3.36}$$

If ν_z is the velocity of $\tilde{z}$, with the initial condition at $t = 0$ that $\tilde{z} = z$, then the fluxes are calculated in the lattice-fixed frame, while the resulting changes in concentration can be calculated in the volume-fixed frame.

This approach is well-suited to simulations of dissimilar welds in multicompo-

nent alloys due to the averaging of kinetic properties. A single matrix phase is not required, eliminating the need for the distinct interface (for example, between a ferritic alloy and an austenitic alloy). Phase balances are instead calculated based on local compositions. Secondary phases such as carbides and intermetallics can also be included without issue.

Of critical importance to this approach is the way in which M_k^{eff} is calculated. It must be a combination of all the individual mobilities in question that provides a suitable approximation to the real multi-phase system. The simplest, and most applicable, combinations are the Wiener bounds, which are upper and lower limits of mobility based on the local volume fractions of phases, f^i. The lower bound is defined as:

$$M_k^{eff} = \frac{1}{\sum \frac{f^i}{M_k^i}} \tag{3.37}$$

And the upper bound is defined as:

$$M_k^{eff} = \sum f^i M_k^i \tag{3.38}$$

Geometrically, these bounds correspond to alternating layers of all present phases aligned perpendicular to (lower bound) and parallel to (upper bound) the z direction. From this, it is apparent that the upper bound is the more suitable; if secondary phases were aligned perpendicular to the diffusion direction, they would act as complete barriers to diffusion. A graphical representation of the effective mobilities calculated by the Weiner bounds in a binary system is shown in figure 3.7. Other bounds exist in the program, but they are not relevant to the present case and so will not be discussed.

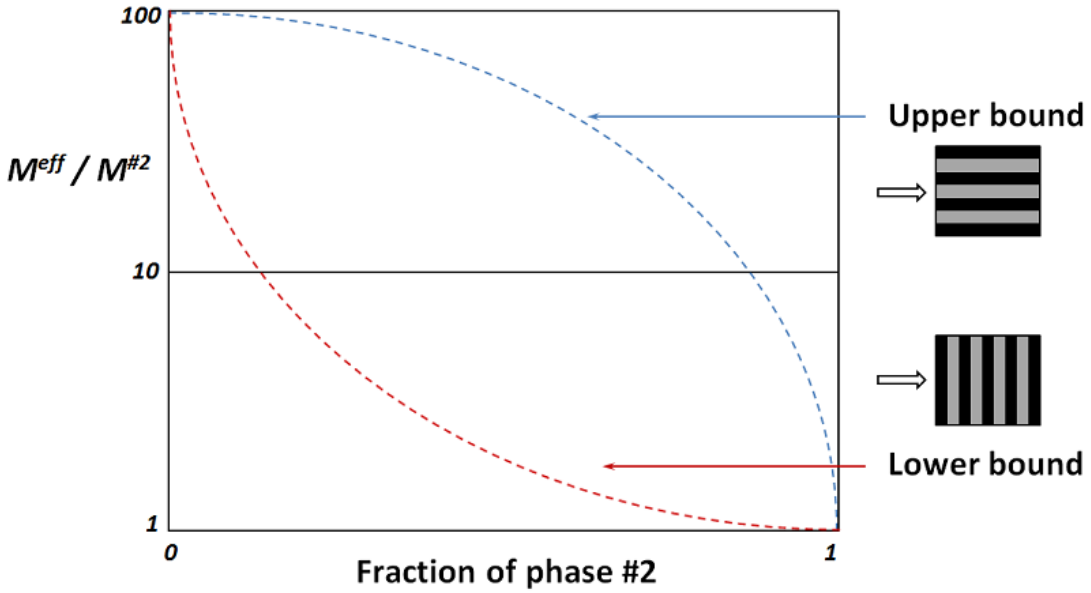

Figure 3.7: Graphical illustration of the values of the Weiner bounds in a binary system, in the specific case that the mobility of phase # 1 is 100 times greater than that in phase # 2.

3.3 Summary

The two software packages described here will be used at various points throughout the thesis, with the aim of making predictions about the evolution of alloys and welds. Data from *Thermo-Calc* will be presented in chapter 6, and at various points throughout the discussion sections. Data from *DICTRA* will be presented primarily in chapters 6 and 9 and appendix A.

Chapter 4

Experimental Methods

The experimental procedures and tools that have been used to attain the information presented in this thesis will be described in this chapter. The manufacturing processes and heat treatments used to prepare each of the samples will be outlined, followed by the methods of preparation for experimental investigation. Finally, the various experimental characterisation techniques, including assessments of their uses and limitations, will be described.

4.1 Materials and Fabrication Processes

4.1.1 Bead on Plate Weld

The main focus of experimental work was on a custom-made bead on plate weld, which had been originally created for a prior research project. The manufacturing was carried out at Doosan Babcock's welding facilities, at the request of E.On.

Starting from a Tenaris P92 steel pipe, of wall thickness 30 mm and outer

diameter c. 500 *mm*, a section of thickness 14 *mm* was removed from the end of the pipe (i.e. with the cutting direction perpendicular to the cylindrical z-axis). An arc was cut from the resultant circular piece, and welding was performed onto one of the 30 *mm* wide faces. The welding consisted of two runs - one single pass, one triple pass - of Nimrod Alloy 625, using no pre-heating. All samples examined in this thesis were cut from the triple pass section. The finished piece was received in the as-welded condition, with no post-weld heat treatment applied. A picture of the piece is presented in figure 4.1.

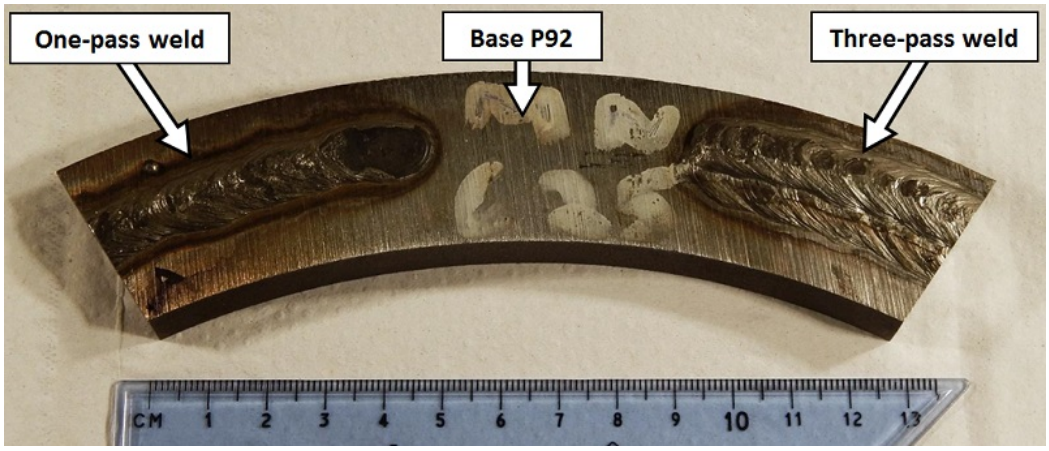

Figure 4.1: An overview of the P92 steel – Alloy 625 bead on plate weld, showing the single-pass and three-pass areas. Samples examined in this thesis were taken from the three-pass area.

An overview of the macrostructures in the triple pass case is shown in figure 4.2. This shows the base steel and the three weld beads applied to it, as well as the HAZ resulting from the welding process (which is distinguished from the rest of the steel by appearing lighter in contrast). The weld beads labelled as 1a and 1b have been applied directly to the steel. Weld bead 2 has been applied over the other two. As such, beads 1a and 1b will hereby be described as making up the first weld pass, and weld bead 2 as making up the second weld pass.

Sections containing weld beads were cut from this piece perpendicular to the welding direction, a minimum of 6 *mm* in thickness, by electrical discharge machining (EDM). These pieces were then cut vertically down the centre of the weld

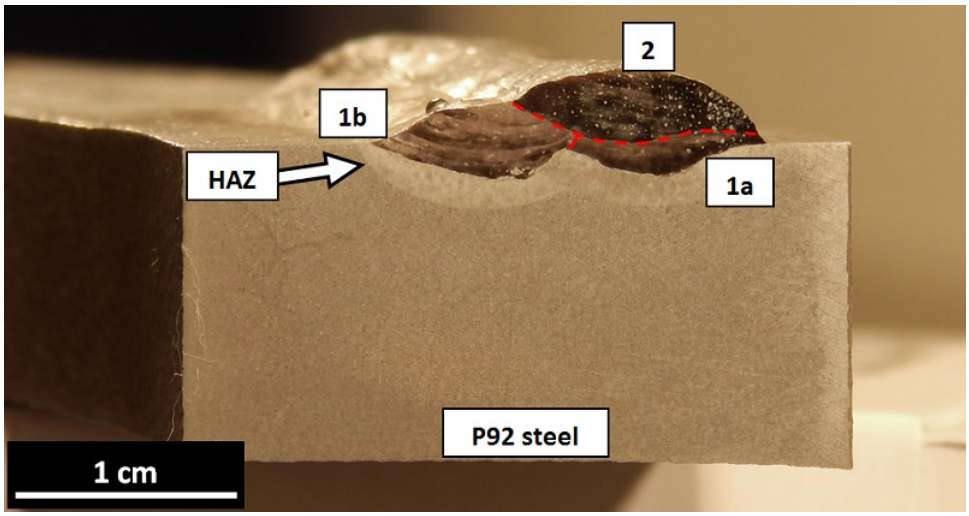

Figure 4.2: Image of the macrostructures in the as-welded system after etching with aqua regia, showing the three-bead weld structure (labelled as 1, 2 and 3, and separated by white lines). The HAZ is also clearly distinguishable from the base P92 steel.

beads, so that different pieces could be heat treated for different lengths of time. After completion of each heat treatment, a 1-2 mm strip was cut from the edge of the sample using a silicon carbide cut-off wheel, so as to expose an unoxidised surface for metallographic examination.

Samples were given heat treatments in laboratory furnaces, so as to simulate the conditions that may occur during fabrication or in service in thermal power plants. Heat treatments were performed at approximately atmospheric pressure in air, and samples were air-cooled after the treatments. The furnaces were heated to the treatment temperature before samples were inserted. Three types of heat treatment were used:

- Normalisation, which was performed at 1050 $°C$ for 2 hours. This heat treatment closely replicates that which is used in the manufacturing of bulk CSEF steels, in which the steel is austenitised and then quench cooled so as to form fresh martensite. This treatment is not normally applied to welds, but has been proposed as a solution to type IV weld failure by removing the HAZ (as the fresh martensite ought to have a uniform prior austenite grain size).

- Tempering, which was performed at 760 $°C$ for 2 hours. This is the second stage of the normal manufacturing process for CSEF steels, and is also performed as standard for welded joints involving such steels. This treatment tempers the martensite, softening it to a degree to which it becomes suitable for service conditions, while also leading to the formation of the characteristic precipitates ($M_{23}C_6$ and MX) that strengthen these steels.

- Pseudo-service conditions, which were performed at 625 $°C$. Treatments of this type were performed as short term (32 days, or 768 hours) and long term (125 days, or 3000 hours) conditions. The temperature used is slightly higher than P92 steel would likely be exposed to in service; the rationalisation for this temperature is that it would accelerate microstructural evolution and diffusion phenomena without introducing new effects. As such, analogues to ex-service samples could be created after relatively short times.

These heat treatments were performed in different combinations as an analogue to conditions that may be experienced in an industrial setting. A full list of heat treatments is given in table 4.1. On sample A-W, microstructural analysis was performed on the cross-section parallel to the welding direction (i.e. the longitudinal section) and the cross-section perpendicular to the welding direction (i.e. the transverse surface). On all heat treated samples, analysis was performed on the longitudinal section only, so as to minimise time spent polishing and sawing away oxidised/decarburised layers. When analysing transverse sections, only two weld beads (i.e. the first or second and the third) can ever be seen due to the nature of the cut; On longitudinal sections, all three weld beads may be visible if the vertical cut was made in a suitable location.

Table 4.1: Heat treatments used in the P92 steel – Alloy 625 bead on plate weld system. The acronyms STA and LTA stand for 'short term ageing' and 'long term ageing' respectively.

	Heat Treatment			
Sample Name	**Normalisation**	**Tempering**	**STA**	**LTA**
A-W	-	-	-	-
N	✓	-	-	-
NT	✓	✓	-	-
T	-	✓	-	-
STA	-	✓	✓	-
LTA	-	✓	-	✓

4.1.2 Ex-service weld samples

A set of sections from ex-service P91 – Alloy 625 welds were provided by Alstom for analysis. These came from two separate pipes, both of which were exposed to the same temperature (c. 565 $°C$) for similar lengths of time (c. 40,000 hours) at an unknown stress level. Both pipes were used to carry high-temperature air. The pipes had an outer diameter of approximately 160 mm, and a thickness of 13.5 mm.

Three samples were taken from each pipe at 120 ° intervals, hence giving six samples in total. The welds were fabricated by arc welding using the 'buttering' technique, with a standard PWHT (760 $°C$ for 2 hours) being applied in the workshop. The final welding was then carried out on site without a subsequent PWHT.

Alstom's in-house analysis [157] revealed that one of the pipes (a section from which is shown in figure 4.3) had experienced low-ductility creep failure at the fusion line. This took the form of a crack covering a maximum of 40% of the pipe thickness in a 120 ° arc, extending inwards from the outer edge. The cause of the cracking could not be conclusively identified by Alstom's engineers.

Three samples were subjected to in-depth experimental investigation. The first, labelled 'FP-C', was cut from the centre of the crack in the failed pipe. Sample 'FP-U' was cut from an un-cracked area of the failed pipe. The third

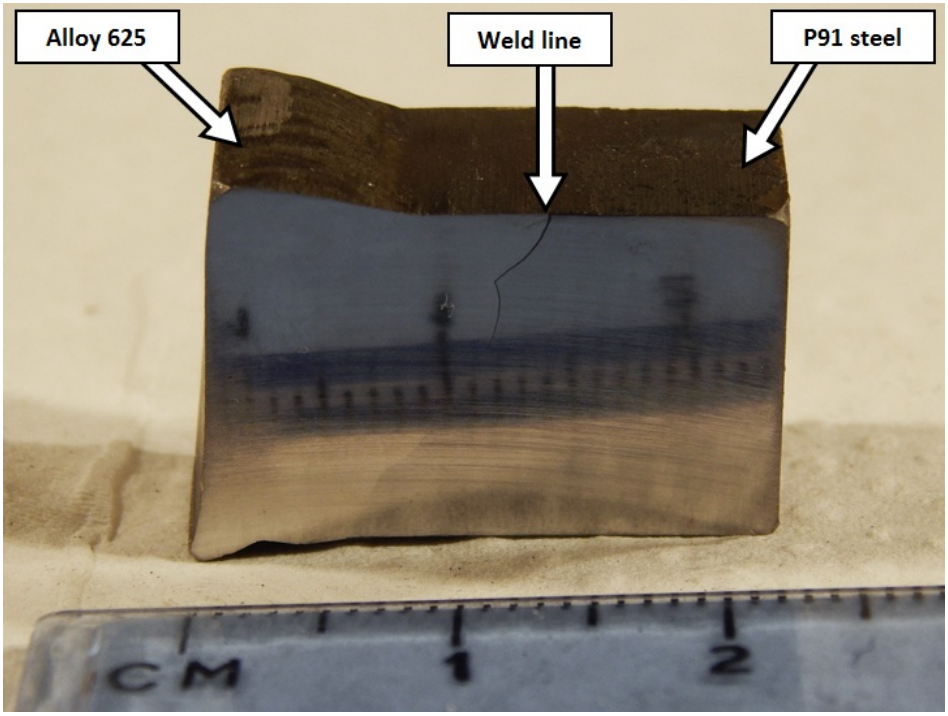

Figure 4.3: A section of one of the P91 – Alloy 625 ex-service weld samples (specifically sample 'FP-C'). The cracking at the weld line can be seen in the top half of the sample as a dark line.

sample, 'PS', was taken from the other pipe, which had showed no apparent signs of failure.

4.1.3 P87 Weld Sample

The final sample to be investigated was a section from a bespoke groove weld between P91 and P92 steels, with the recently-developed P87 weld metal used as filler. This sample was provided by EPRI. Mulit-pass welding was performed by TIG/GTAW, with a 150 $°C$ preheat and a PWHT of 746 $°C$ for 1 hour. The sample was subsequently heat treated at 649 $°C$ for 3149 hours (131 days and 5 hours). A picture of this sample is presented in figure 4.4.

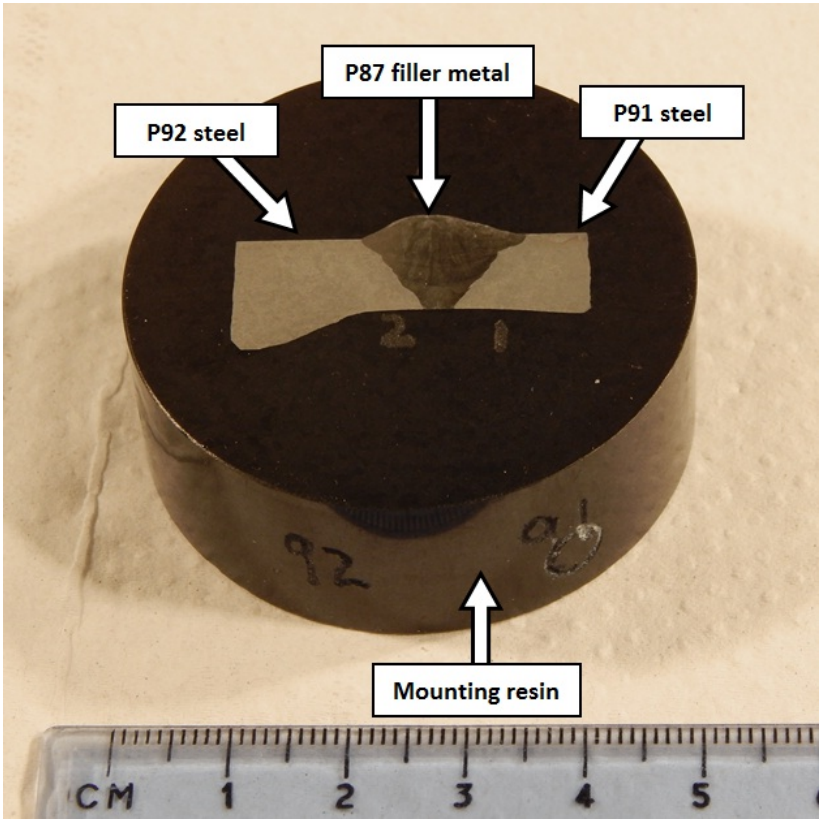

Figure 4.4: An overview of the P91 – P87 – P92 weld sample.

4.2 Metallurgical Sample Preparation

Samples to be investigated were first mounted in a conductive resin, to aid with the subsequent preparation. The surface was then ground back using sequentially finer silicon carbide grit papers. The surfaces were then polished using 6 and 1 μm diamond wheels, such that a mirror shine was obtained from the metal surface. A final polish using 0.025 μm colloidal silica was employed when preparing for electron microscopy.

Chemical etchants were used when appropriate to highlight the microstructures of the various alloys. These act by selectively dissolving certain parts of a sample, such as grain boundaries; the resultant changes in surface topography can be observed under a microscope. An unfortunate consequence of the different composition across a DMW interface is that the two sides have different corrosion resistances (with nickel-based alloys being generally more resistant than steels),

and hence require different etchants. As such, the process must be done in stages. A number of etchants and conditions were tested, until two suitable candidates were found:

- The grade 91 and 92 steels were found to be best etched using Vilella's reagent, a mixture of 1 g of picric acid, 5 mL of hydrochloric acid and 100 mL of ethanol. This etchant required between 15 and 30 seconds at room temperature to produce good results.

- The nickel-based alloys 625 and P87 were etched using aqua regia, a mixture of hydrochloric and nitric acid in a 3:1 ratio, heated up to around 50 $^{\circ}C$ before use. This proved to be a very fast-acting solution, requiring exposure times of around 10 seconds. This etching condition eroded a large amount of material from the steel, rendering its microstructure unsuitable for examination. The samples hence needed to be thoroughly re-ground and polished before re-examining the steel.

4.3 Microstructural Characterisation

4.3.1 Microhardness Testing

The microhardness testing method is used to measure local variations in hardness of a material. This is done by applying a load to a polished sample using a diamond-tipped indenter. The size of the resulting indent is then measured; using this information and the force with which the indent was applied, the local hardness of the material can be calculated.

Two different machines were used for microhardness testing. Manual testing was performed using a Buehler MMT-7 Digital Microhardness Tester. A Vickers indenter was used, with a 50 g load a 5 second dwell time. Automatic microhardness mapping was performed using a Zwick Roell ZHμ automated hardness

indenter. A Vickers indenter and 5 second dwell time were again used, but with a 100 g load, meaning that there may be discrepancies between readings that ought to be equivalent from the two machines. Readings from the former machine will be given in units labelled 'VHN_{50}', while those from the latter will be labelled 'VHN_{100}'.

4.3.2 Optical Microscopy

Etched samples were examined using a Nikon Eclipse LV100ND optical microscope operating in bright-field mode. This microscope was equipped with five objective lenses, with magnifications of 5×, 10×, 20×, 50× and 100×, allowing samples to be examined on a range of scales. The microscope was linked to a computer, allowing digital images to be recorded.

4.3.3 Scanning Electron Microscopy

The bulk of scanning electron microscopy (SEM) analysis was performed on a Phillips-FEI XL-30 ESEM, operating in high vacuum mode. A small amount of work was carried out on an FEI Nova 600 Nanolab dual beam microscope. Both of these systems use field emission gun-type electron sources.

An SEM operates by accelerating an electron beam at a sample in a vacuum chamber [158]. The electron beam comes from either a conventional thermionic tungsten filament or a more modern field emission gun (FEG), and is accelerated through voltages of 1 - 30 kV. The beam is converged down a small probe at the sample surface using magnetic condenser lenses, and rastered across the sample. As the beam hits the sample, it will penetrate the surface and travel a short distance into the material, ballooning outwards in the process. The penetration depth, and thus interaction volume, can be reduced by lowering the accelerating voltage. Different parts of the volume provide different types of emission; the

three of relevance here are inelastically scattered electrons, elastically scattered electrons and characteristic X-rays, which will be discussed in detail later. These emissions are picked up by three different detectors, which feed the information back to the computer control software. Each of them can be used to garner different information about the sample.

Spatial resolution in an SEM is significantly better than in an optical microscope since electrons that are used have a much lower wavelength than the photons that comprise visible light. This lowers the minimum object size that can be resolved. Potential magnifying power is also much greater, since it is not controlled by the objective lens; it is instead determined by the rastering conditions.

4.3.3.1 Secondary Electrons

The basic imaging mode in an SEM is secondary electron (SE) mode. The secondary electron detector primarily picks up inelastically scattered electrons, meaning those which interact with the surface of the sample. This mode is the most similar to a conventional optical microscope, in that contrast comes mainly from surface topography; a flat surface appears almost completely featureless. This mode has been used primarily to examine chemically etched sample surfaces with a working distance of 10 mm and an accelerating voltage of 20 kV (i.e. standard operating conditions).

4.3.3.2 Backscattered Electrons

In backscattered electron (BSE) mode, electrons that have interacted elastically with the sample will be detected. Most of the elastic interactions come from the sub-surface region of the sample. This, combined with the balloon-shaped interaction volume, give BSE images a lower resolution than SE images under otherwise similar conditions. The contrast of BSE images is a combination of factors, chiefly surface topography, local average atomic mass and diffraction. By

controlling the condition of the sample and the beam, individual factors can be isolated.

This mode has been used on polished samples to analyse grain structure and distribution of high-atomic number secondary phases. The working distance and voltage were both lowered (to 7 mm and 15 kV respectively) in order to maximise contrast.

4.3.3.3 X-ray Emission

When electrons strike atoms, there is a chance of them ejecting electrons from orbital shells. When this happens to a low-energy shell, an electron from a higher energy shell will subsequently fill the gap. This transition results in the emission of an x-ray, the energy of which corresponds to the energy difference between the orbital shells in question. Since energy differences between these shells are discrete, and characteristic of the atomic species, the resultant x-rays can be used to identify the atom from which they came. These emissions will be analysed in the present work by the technique known as energy-dispersive x-ray analysis (EDX); it may elsewhere be known by the acronyms EDS or EDAX. At high voltages, the resolution of EDX will be limited by the large interaction volume.

The SEM-EDX work presented in this thesis has been done by two distinct methods. The concentration of relatively high atomic number elements (i.e. 12 or higher) was measured using the Phillips-FEI XL-30 ESEM, using an Oxford Instruments X-max silicon drift detector and an accelerating voltage of 20 kV. Testing for carbon content, on the other hand, needed to be done by a different method due to issues with carbon contamination in the vacuum chamber on the aforementioned microscope. It was instead done on the FEI Nova 600 Nanolab dual beam microscope, using an Octane 60 silicon drift electron energy dispersive spectroscopy detector at a voltage of 5 kV. To minimise the effect of contamination, the samples for carbon analysis were cleaned for 1 hour immediately before

analysis in a Hitachi ZONE desktop sample cleaner. These methods may be referred to as 'traditional' and 'low-voltage' EDX methods respectively in this thesis.

4.3.3.4 Limitations of SEM and SEM-EDX Methods

The SEM is a powerful tool, but, like the OM, is ultimately limited by resolution. Features that are 50 nm or smaller may not be resolved well in an SEM (and, even if they are, they will not be observed clearly). Resolution is a particular issue for EDX analysis, due to the ballooning nature of the interaction volume (i.e. x-rays may come from a larger area than observed in electron imaging mode). Additionally, SEMs are limited to only analysing the surface layers of a sample.

4.3.4 Transmission Electron Microscopy

Transmission electron microscopy is a technique that, at a glance, appears similar to SEM. Many of the same principles and mechanisms are used in both cases. However, the two methods are capable of providing vastly different results, with different strengths and limitations [159] [160].

The principal difference between TEM and SEM is in the way electrons interact with the sample. While an SEM detects electrons that are reflected or backscattered by a material, TEM relies upon electrons being transmitted through it. This means that a high accelerating voltage is required (200 kV being used in the present work). This higher voltage than that used in an SEM means that the electrons have higher energy, and hence shorter wavelength, which increases the permissible resolution by lowering the Bragg diffraction limit. Since electrons must be transmitted, extremely thin samples are required; TEM samples generally need to be less than 200 nm thick, and as such require special preparation methods.

The TEM work presented in this thesis was performed on two separate machines. Conventional TEM images and diffraction patterns were gathered on a

JEOL 2000fx microscope, while STEM (scanning TEM, which will be described in section 4.3.4.8) images and EDX data were gathered on a Phillips/FEI TECNAI F20 TEM.

4.3.4.1 FIB Sample Extraction

TEM foils have traditionally been prepared by electropolishing, but this technique cannot reliably provide site-specific samples. In recent years, focussed ion beam (FIB) methods have been developed to the point that TEM specimens from areas of interest can be created with high precision - in the present work, specimens have been extracted from across weld lines. The extraction of FIB specimens was carried out at the University of Loughborough on the FEI Nova 600 Nanolab dual beam microscope (the same machine used for low-voltage EDX analysis).

The method used in the present work consists of several stages. First, a strip of platinum is deposited on top of the area of interest, so as to mark out the area and to protect it during the rest of the process. This strip is roughly 15 $\times$ 2 $\times$ 2 μm in length, width and depth respectively. A gallium ion beam is then used to cut "trenches" either side of the strip, as shown in figure 4.5(a). These trenches usually cover an area of 30 $\times$ 20 μm, with the long axis parallel to the length of the strip. The depth of the trench varies, but may be as much as 10 μm. The dividing wall between the trenches, which is to become the TEM specimen, is then cut out (again using the gallium ion beam) and welded to a probe (by platinum deposition). The probe is then used to bring to a small copper grid, suitable for insertion into a TEM, to which it is attached (as shown in figure 4.5(b)). Final thinning of them specimen is performed by using the gallium ion beam at slightly off-vertical angles to remove material from either side. The final electron-transparent area of each specimen was around 10 $\times$ 5 μm.

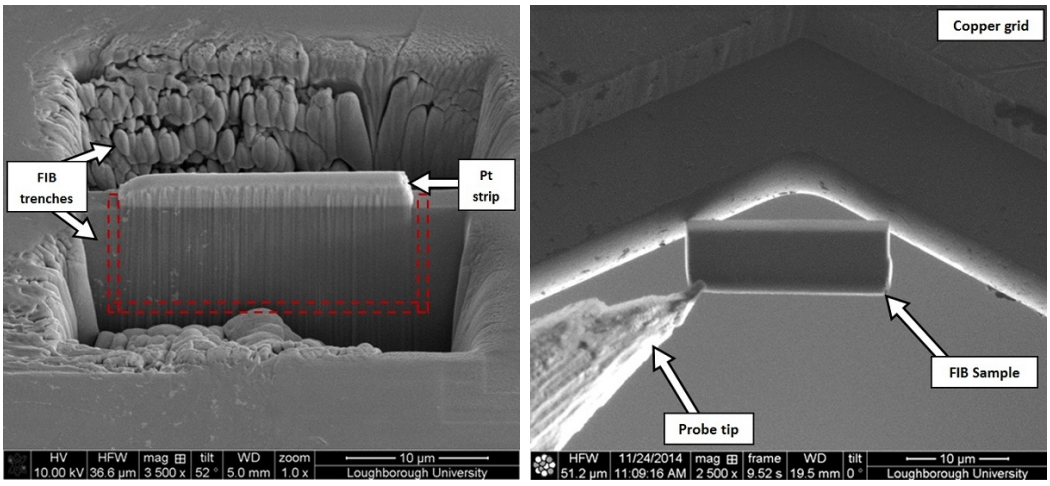

(a) **(b)**

Figure 4.5: Images of stages of the FIB extraction process for preparing TEM specimens. Image (a) shows trenches either side of a feature of interest (viewed at an angle of 52° to the sample surface). The dividing wall is cut out along the red dotted lines. Image (b) shows a FIB specimen about to be attached to a copper grid, suitable for insertion into a TEM, before the final thinning stage.

4.3.4.2 TEM Electron Optics

The first TEM was built in the early 1930s, and the fundamental design has changed little since then. A standard TEM takes the form of a columnar high-vacuum chamber, with the electron gun at the top. The electron beam travels down the column, passing though a series of apertures and magnetic lenses which control the state of the beam; they can be thought of as performing roles analogous to glass lenses in an optical microscope. A highly simplified schematic of a TEM column is shown in figure 4.6.

The first set of lenses are the condenser lenses, which control the condition of the beam before it interacts with the sample. These lenses are similar to the condenser lenses in an SEM. Most TEMs have two condenser lenses, with the beam crossing over between them. Each lens is encircled by an aperture which arrests electrons travelling at large angles relative to the optical axis. The aperture on the second lens can be set to one of a number of diameters, with smaller diameters resulting in decreased beam intensity.

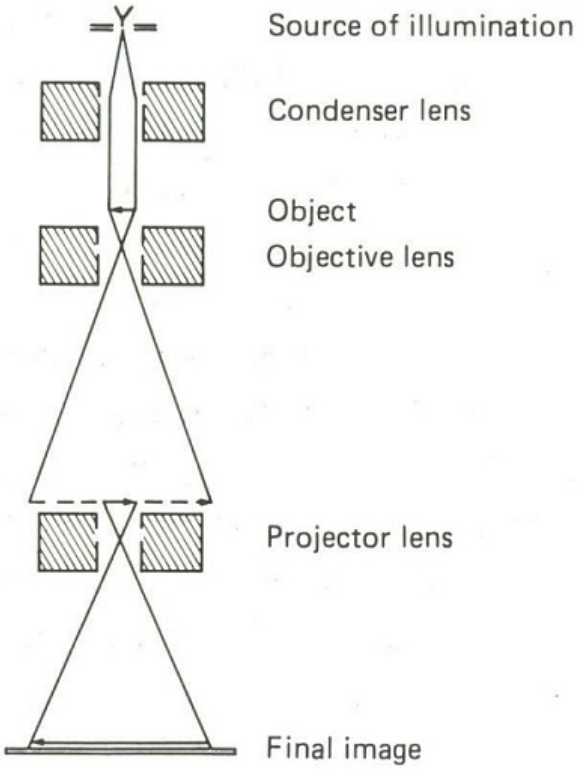

Figure 4.6: A highly simplified schematic of the lenses in a TEM column.

The beam then passes through the specimen, and is immediately affected by the objective lens (the sample stage is usually inside the magnetic field of the objective lens, making it an 'immersion lens'). This lens forms the first intermediate image. In some TEM designs the objective stage may be a pair of lenses, one above and one below the sample. Associated with this objective stage are two apertures: the objective aperture and the selected area diffraction (SAD) aperture. The former is in the back focal plane of the objective lens, limiting the angle of electrons than can pass and hence providing diffraction contrast. The latter is in the image plane of the objective lens, and is used to isolate small areas for diffraction analysis.

The beam then passes through the intermediate lenses, which act as magnifiers, before finally being projected onto a phosphorescent screen, which lights up when struck by electrons. Images and diffraction patterns can be observed on this screen. The projection is recorded by having the screen swing out of the beam path, hence exposing a camera underneath. This may be a conventional film camera, or a more

modern CCD linked to a computer.

4.3.4.3 Bright Field Imaging

The convention operation mode for imaging a TEM is to illuminate the entire area of observation simultaneously using a parallel electron beam (in contrast to an SEM, in which the beam is rastered across an area). The image can hence be thought of as a projection of sample onto the screen. When this is done with the objective aperture centred on the transmitted beam, a bright field image is formed. Image contrast in this mode is determined primarily by a combination of diffraction and absorption. The latter effect is readily apparent – if a part of the sample is thick or is composed of high atomic number elements, then proportionately more electrons will be absorbed, making the area appear dark. Strong diffraction will occur if the electron beam is incident upon a low-index crystal plane. This will send parts of the beam in many directions and hence reduce the number of electrons that are transmitted down the column. TEM stage holders allow the sample to be tilted, changing the relative angle between the incident beam and crystal planes and hence varying diffraction contrast [161].

4.3.4.4 Selected Area Electron Diffraction

As was mentioned above, electrons may be diffracted through the crystal lattice. This occurs because the lattice acts as a series of slits, while the electrons behave as waves (with wavelength comparable to typical lattice spacings). Diffraction patterns are formed in the back focal plane of the objective lens (as opposed to images, which are formed in the image plane). Patterns can therefore be projected by adjusting the imaging lenses so that the back focal plane of the objective lens becomes their object plane [162].

In this way, all diffraction events from the illuminated area are projected. This is unsuitable in most cases, since the features from which one may wish to

obtain diffraction (grains, particles, etc.) are often rather small. It is hence more convenient to isolate certain parts of the image using a selected area aperture. This takes the form of an electron-opaque sheet, perpendicular to the electron beam, with one or more circular holes in it, usually of a range of sizes. The sheet is in the image plane of the objective lens, and can be inserted or removed from the beam path at will. By placing the aperture over a feature of interest, the diffraction pattern from that area alone is obtained. This is known as a selected area diffraction pattern (SADP).

By tilting the sample relative to the electron beam, diffraction patterns from different crystal planes may be obtained. TEM stage holders designed for diffraction studies have two tilt axes, allowing a large range of angles to be investigated. This is essential, since the most clear diffraction patterns are formed from low order zone axes (i.e. orientations at which crystal planes such as [001], [011], etc. are parallel to the beam).

4.3.4.5 Dark Field Imaging

In conventional bright field imaging mode, the majority of the image is formed by electrons that travel straight through the sample without interacting; areas that appear dark do so because of strong absorption or diffraction, limiting the electron transmission. In some circumstances, it may be desirable to block the transmitted beam, and limit the admitted electrons to those which have interacted with the sample. The result is a dark field image, so called because the background is dark.

Dark field imaging is most commonly used in conjunction with selected area diffraction. By shifting the objective aperture away from the transmitted beam and onto one or more spots in the diffraction pattern, the resultant image will contain only electrons that have diffracted from the feature that caused the pattern (assuming there is no overlap with diffraction events from other features). The image hence highlights the diffracting feature, making dark field imaging of this

manner useful for confirming the source of diffraction events.

4.3.4.6 Convergent Beam Mode

While it is desirable to have low-index diffraction patterns, they may not be easy to find. The best one can do using only the methods described above is to tilt the sample randomly until the area of interest appears dark, implying strong diffraction contrast, and then acquiring a diffraction pattern. This may result in a clear pattern, but the method is unreliable and involves much trial and error. Additionally, it can be difficult to apply to some secondary phase particles, which may appear dark for other reasons (such as strong electron absorption).

This is overcome by operating in convergent beam mode. The beam is brought to a point at the sample surface, thus removing the well-ordered diffraction patterns produced by a parallel beam and instead introducing strong inelastic scattering. These scattered electrons can then undergo diffraction events; the resultant diffraction pattern takes the form of a series of lines, which exist in pairs known as Kikuchi bands. Each band corresponds to diffraction from a lattice plane. The points of intersection between bands correspond to zone axes, with lower order zone axes having more intersecting bands. Tilting the sample causes the bands to move, so one may tilt the sample so as to follow a band to the desired zone axis. Once at a suitable angle, a SADP may be acquired by setting the beam back to parallel. This technique allows good diffraction patterns to be found quickly and consistently; as such, the Kikuchi bands are considered to be a 'map' in reciprocal space.

4.3.4.7 TEM-EDX

Energy dispersive x-ray analysis on a TEM operates in much the same way as it does on an SEM. The electron beam is focussed on an area of the sample, and the resultant x-ray emission is collected and analysed. The key difference is

in resolution; due to the extremely thin nature of TEM samples, the interaction volume of electrons in the sample is much smaller than in an SEM, hence allowing EDX data to be collected from far smaller volumes.

4.3.4.8 Scanning Transmission Electron Microscopy

While the basics of TEM have not changed significantly since its inception, one notable addition has come in the form of a different operating mode: Scanning transmission electron microscopy (STEM) [163]. This can be thought of as a cross between SEM and TEM, in that the beam is focussed to a point (as if being operated in convergent beam mode) and rastered across the sample to form an image. The resultant images are often presented as a pair: a bright field image, similar to a conventional TEM bright field image in that it is formed primarily from electrons scattered through low angles, and a dark field image, formed of electrons scattered through particularly high angles. The latter may be referred to as a high-angle annular dark field (HAADF) image.

This mode offers several advantages over conventional TEM, most pertinently the ability to form compositional maps using EDX (conventional TEM-EDX allows only for the analysis of points). The efficiency of x-ray detection is also improved due to the larger solid angle subtended by the detector.

4.3.4.9 Limitations of TEM/STEM

While TEM and STEM are extremely powerful tools, they are not without limitations. One of the major shortcomings is the small size of the samples. A typical sample may only offer an examinable cross section of 50 μm^2, which is small compared to many common microstructural features. This means that features contained within the sample may well not be wholly representative of the material from which they came. The small size of samples limits the amount of material that can be examined; by one estimation, less than 1 mm^3 of material has ever

been examined by TEM.

Another issue is coincidence (or occlusion) of features. Since TEM samples are necessarily transparent to electrons, transmission may occur through two or more features, resulting in them all being observed simultaneously. The problem is exacerbated if one of the samples is a particularly strong electron absorber, as it may completely obstruct the view of other features. This also poses an issue for EDX analysis, since if two occluded features have different compositions then neither can be measured reliably. For this reason, care must be taken when interpreting images and data (though some clarification may be gained by manipulating the tilt angle of the sample).

There is also the issue that TEMs, and the dual-beam SEMs used to extract FIB samples, are expensive to purchase and maintain. They also require skilled technicians to operate. These factors impose a budgetary constraint which limits how much work can be done. This is compounded by the time-consuming nature of sample preparation and the analysis of TEM data.

4.4 Summary

The experimental methods described here will be applied to all of the weld systems, with the results presented in chapters 5, 8 and 9, as well as appendices A and B. The microscopy methods (optical and electron) will allow for a thorough characterisation of the microstructural and chemical evolution of the various weld systems over a wide range of distance scales, with each of the methods complimenting one another. Additionally, microhardness testing will shed some light on the variations in mechanical properties across welds.

Chapter 5

Characterisation of the P92 – Alloy 625 Weld System

Experimental results from the P92 steel – Alloy 625 bead on plate weld system in various aged conditions will be presented in this chapter. The heat treatments, as outlined in chapter 4, have been designed to emulate the conditions that may be experienced by a real weldment at various stages of its service life. Data will be presented from the following cases:

- The as-welded state ('sample A-W') i.e. with no post-weld heat treatment (PWHT) applied. Characterisation of this case is of great importance, since the properties of the as-welded state will determine evolution during subsequent heat treatments.
- The tempered state ('sample T'), heat treated at 760 $^{\circ}C$ for 2 hours, mimicking the regulation PWHT.
- The short term aged state ('sample STA'), which has been given the standard

tempering treatment and subsequently aged at 625 $°C$ for 32 days (768 hours).

- The long term aged state ('sample LTA'), which has also been given the tempering treatment, but subsequently aged at 625 $°C$ for 125 days (3000 hours). These heat treatments at 625 $°C$ are slightly higher than typical service conditions, with the intention of accelerating evolution.

5.1 Microhardness Profiles

Microhardness mapping was performed on samples A-W, T, STA and LTA, in a grid of 70-80 $\times$ 10-12 indents, with 100 μm spacings between indent centres, in accordance with the procedure described in section 4.3.1. The long axis of this grid was perpendicular to the weld line, and the grid was centred close to it, as shown in an optical micrograph in figure 5.1. Averages were then taken of the columns of indents, so as to construct a single linear hardness trace across the weld line in each sample. In the event that the weld line was not parallel to the indent grid, as was the case in figure 5.1, then this was accounted for by manually offsetting rows to bring the weld line into alignment and avoid influencing the averaging calculations. The hardness results from all four samples are presented in figure 5.2.

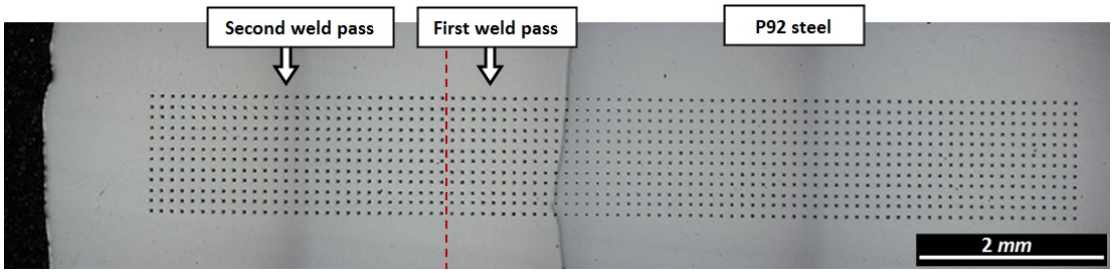

Figure 5.1: Optical micrograph of the hardness indents in sample A-W.

The unaffected steel (i.e. that from around -4.0 to -3.4 mm) in sample A-W has an average hardness of 252 $\pm$ 6 VHN_{100}, which is reasonable for as-manufactured

P92. From this point toward the weld line, mechanical changes begin. Firstly, there is a gradual softening from -3.2 to -1.7 *mm*, the minimum of which is approximately 230 VHN_{100}. This corresponds to the over-tempered region at the edge of the HAZ. From there, hardness begins to increase, initially up to a plateau at approximately 300 VHN_{100}, and then on to a peak value of 483 VHN_{100} immediately adjacent to the weld interface. This area of increased hardness, 1.6 *mm* in width, corresponds to the HAZ. This includes all three sub-zones: the CGHAZ, the FGHAZ and the ICHAZ, as were described in section 2.2.2.2.

The base steel in sample T has been softened by the tempering process, now having a hardness of 233 ± 6 VHN_{100}. The HAZ too has softened, though much more drastically; its peak hardness is now around 280 VHN_{100}, down from 483. The HAZ appears to be smaller in this case, as the softest point (221 VHN_{100}), which loosely marks the edge of the HAZ, is only 1.2 *mm* away from the interface. This difference may simply be a consequence of local variations in the welding parameters, or may may be due to the sample being taken from a slightly different location in the weld macrostructure.

The steel away from the HAZ in sample STA is found to have an average hardness of 242 ± 5 VHN_{100}, which is softer than sample A-W, though harder than sample T. The HAZ extends for a total of approximately 1.8 *mm* into the steel. The outer part of the HAZ, between 0.9 *mm* from the weld and the bulk steel, is associated with softening, reaching a minimum of 228 VHN_{100} at 1.1 *mm* from the weld line. The rest of the HAZ is observed to harden, reaching a maximum of 271 VHN_{100} adjacent to the weld line.

The steel in sample LTA away from the HAZ is is found to have an average hardness of 240 ± 4 VHN_{100}. The hardness across the HAZ is relatively uniform and similar to that of the bulk, making it difficult to ascertain a distinct start point, though there is a noticeable trough around 1.6 *mm* from the weld line in which the hardness drops to a minimum of 226 VHN_{100}. This indicates that the

FGHAZ and/or ICHAZ are still present.

The weld metal of sample A-W appears at first to be reasonably uniform, but there are in fact two distinct areas. The first, extending from 0 to 0.9 mm, has an average hardness of 214 ± 11 VHN_{100}. The second, extending from 1.0 mm to the edge of the recorded area, has an average hardness of 222 ± 13 VHN_{100}. This is the distinction between the first and second weld passes.

The weld metal of sample T displays the same two-pass structure as sample A-W, with some differences. The first weld pass is larger, in this case around 1.8 mm, and the second smaller. This may be for the same reasons as the variations in HAZ size. The other difference is that both weld passes are harder in this case than in the as-welded case; the first pass now has a hardness of 224 ± 5 VHN_{100}, while the second is now 233 ± 6 VHN_{100}.

The hardness of the weld metal in sample STA is, on average, 234 ± 11 VHN_{100}. This is with the exception of the area within 0.7 mm of the weld line, which is harder than the rest of the weld metal (peaking at approximately 300 VHN_{100} adjacent to the weld line). There is no immediately apparent distinction between the first and second weld passes in this case, which may indicate that the difference in hardness is too small to detect. Alternatively, it could mean that the scanned area was too small to include the second weld pass in this case.

Conversely, the weld metal in sample LTA has hardened significantly during the heat treatment. As in previous cases, the first weld pass is the softer of the two; the average hardness of the first bead is 272 ± 14 VHN_{100}, while that of the second pass is 289 ± 15 VHN_{100}. These findings indicate that microstructural changes must have occurred in the weld metal.

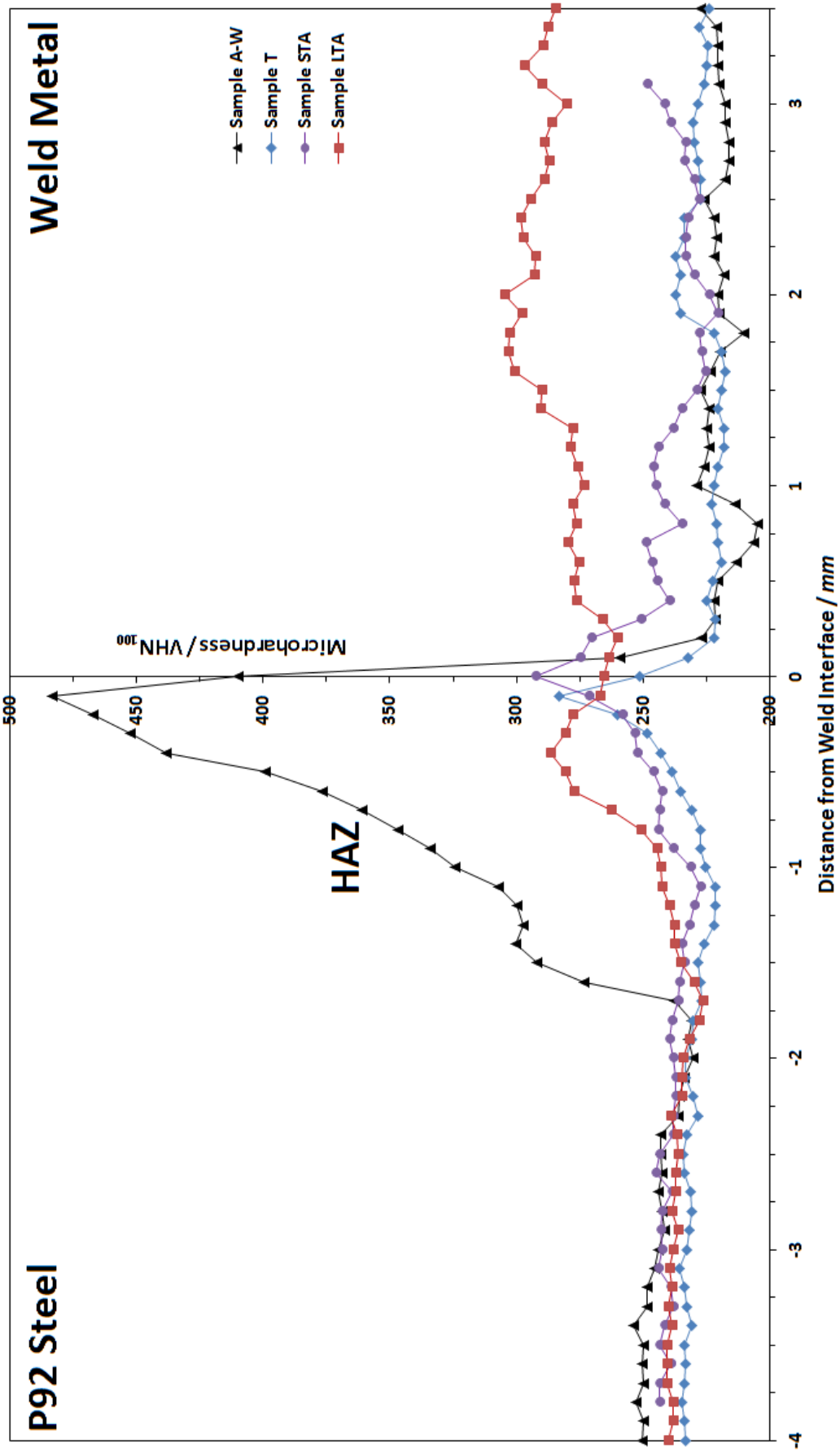

Figure 5.2: Microhardness plots across the P92 steel – Alloy 625 weld interface in samples A-W, T, STA and LTA, using data averaged from 12 passes across the welds.

5.2 Evolution of the Bulk P92 Steel

The bulk of the P92 (away from the HAZ) in sample A-W is still in the as-manufactured condition, having not received any significant high temperature exposure from the welding process. Accordingly, its microstructure, as shown in figures 5.3(a) and 5.3(b), consists of tempered martensite, typical of bulk, wrought P92. It has a prior austenite grain size of between 10 and 20 μm, with precipitates forming at the PAGBs. These are likely $M_{23}C_6$ carbides, based on the known behaviour of P92 in this state. Within the grains there is a well-developed lath structure, with $M_{23}C_6$ carbides forming along the lath boundaries. The average size of the $M_{23}C_6$ particles is between 100 and 200 nm. There are also smaller particles present that may correspond to MX carbonitrides, but they are too small to be identified with certainty. No Laves phase particles can be identified, as is expected. This microstructure is virtually unchanged by the tempering treatment (as shown in figures 5.3(c) and 5.3(d)).

The microstructure of the bulk steel (i.e. away from the weld and the HAZ) in sample STA is shown in figures 5.4(a) and 5.4(b). Evolution has taken place during the 32-day heat treatment, in that additional secondary phase particles have precipitated, chiefly along PAGBs. These new particles are distinctly bright when viewed in BSE mode; based on this and the known metallurgy of P92 steel, they are almost certainly tungsten-rich Laves phase. These particles are between 200 and 500 nm in size (with an average of around 300 nm), and are blocky in shape. They also appear throughout the HAZ, with the same distribution and size as in the bulk. The distribution and size of other particle types does not appear to have changed significantly.

The bulk of the steel away from the HAZ in sample LTA, as seen in figures 5.4(c) and 5.4(d), is almost indistinguishable from that of sample STA. Both have the same tempered martensitic lath structure, and the same three precipitates

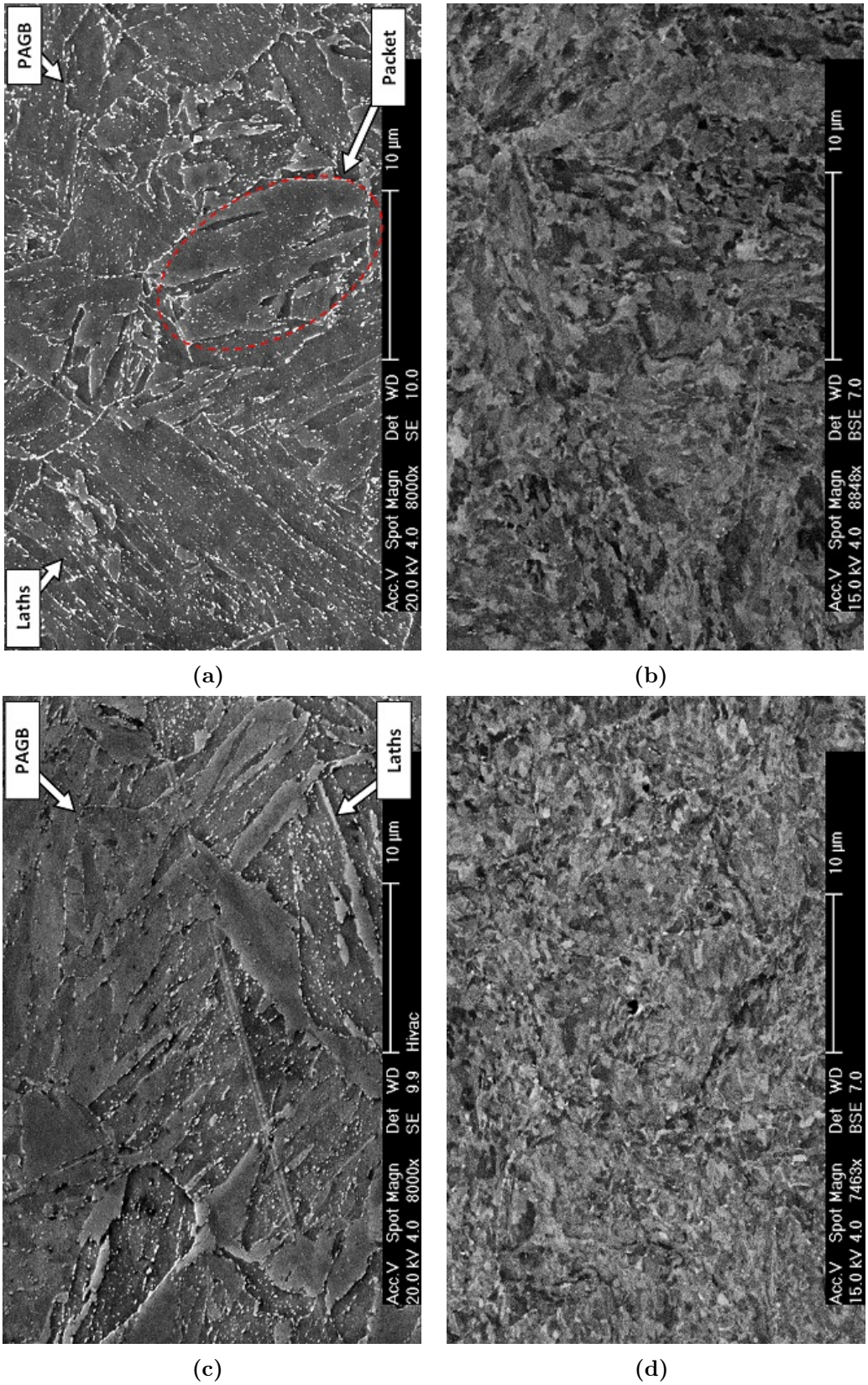

Figure 5.3: SEM images of the bulk steel (away from the weld line) in samples A-W (**(a)** and **(b)**) and T (**(c)** and **(d)**). Images **(a)** and **(c)** are SE images after etching with Vilella's reagent, while **(b)** and **(d)** are BSE images of the polished states.

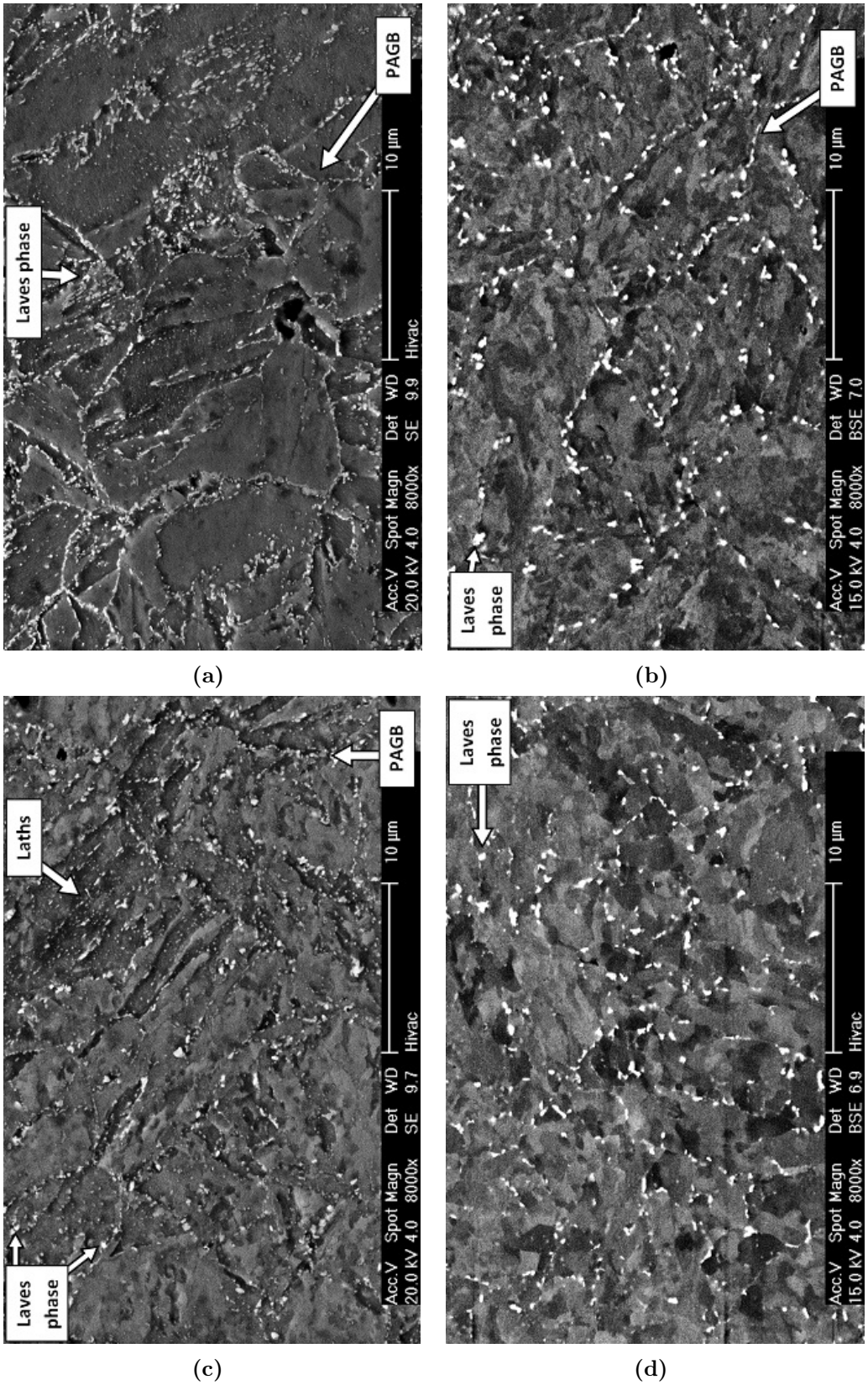

Figure 5.4: SEM images of the bulk steel (away from the weld line) in samples STA (**(a)** and **(b)**) and LTA (**(c)** and **(d)**). Images **(a)** and **(c)** are SE images after etching with Vilella's reagent, while **(b)** and **(d)** are BSE images of the polished states.

present. The MX and $M_{23}C_6$ carbide phases do not appear to have coarsened significatly, but the Laves phase particles (observed as distinctly bright in the BSE image) have; their average size is now around 400 nm.

5.3 Evolution of the P92 Heat-affected Zone

The HAZ is clearly visible in the as-welded state, and all of its constituent parts (the CGHAZ, the FGHAZ, the ICHAZ and the over-tempered soft zone) are identifiable. These are shown and labelled in figure 5.5. The total width of the HAZ (c. 1.5 mm) matches well with that found by the microhardness map.

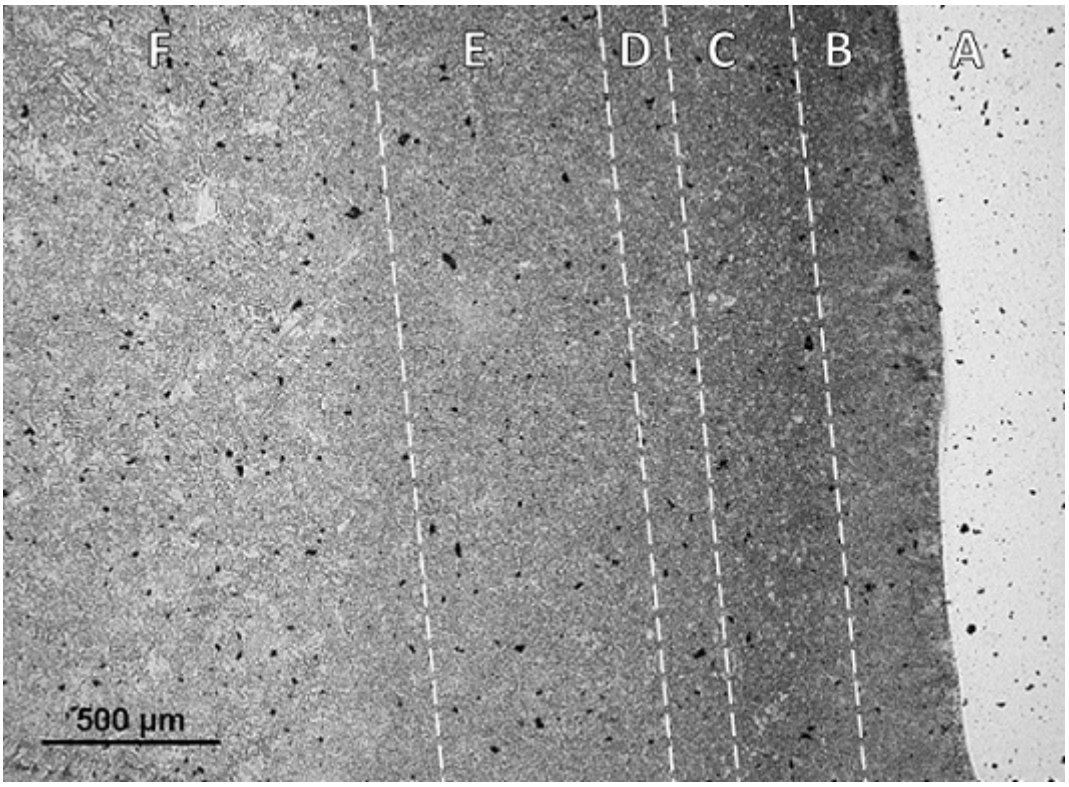

Figure 5.5: Optical micrograph of the HAZ in sample A-W after etching with Vilella's reagent. The labelled regions are: A) the weld metal; B) the CGHAZ; C) the FGHAZ; D) the ICHAZ; E) the overtempered region; F) the unaffected base steel. The black marks correspond to dirt on the surface, and are not microstructural features.

The CGHAZ extends for 200 - 400 μm into the steel, depending on location, and is characterised by the eponymous coarse grains. SEM SE images of this area are displayed in figure 5.6(a). The precipitates that delineate PAGBs in

the unaffected base metal have dissolved during the welding process, making the grain size difficult to estimate. Within the PAGBs there are highly distinctive untempered martensite laths and no visible precipitates. The laths are grouped within a sub-grain packet structure, with typical packets being 10 - 15 μm in size.

The FGHAZ, a section of which is shown in figure 5.6(b), extends from the CGHAZ for 300 - 400 μm. It contains extremely fine prior austenite grains, most being no larger than 10 μm. Within these grains there is untempered martensite, but of a different form to that observed in the CGHAZ. The martensite structure in this area is poorly developed, with the laths being far shorter (due to the smaller prior austenite grains), and there is a higher density of block-like structures. There does not appear to be a sub-grain packet structure, again due to the small prior austenite grains. There are some visible precipitates in this case, on both PAGBs and laths, typically around 300 - 400 nm in size. The number density of precipitates increases with distance from the interface, though they are generally few in number compared to the unaffected bulk.

Extending outward from the FGHAZ is the ICHAZ, shown in figure 5.6(c). Its size is difficult to determine due to its similarity to the adjacent zones, but it may be as much as 200 μm in width. In terms of prior austenite grain size, it may be thought of as being intermediate between that of the unaffected bulk and the FGHAZ. It contains block-like structures similar to those seen in the FGHAZ, and the lath structure is also poorly developed. However, the precipitates present here are generally smaller and more abundant than those of the FGHAZ, being similar to those of the unaffected bulk.

The various sub-zones of the HAZ in sample T have been examined in detail by SEM. Figure 5.7 shows the CGHAZ, 100 μm away from the weld line. It can be seen that the tempering process has resulted in the precipitation of secondary phase particles along lath boundaries and PAGBs. These are up to 200 nm in size, and are assumed to be MX and $M_{23}C_6$ phases, as these phases are known to

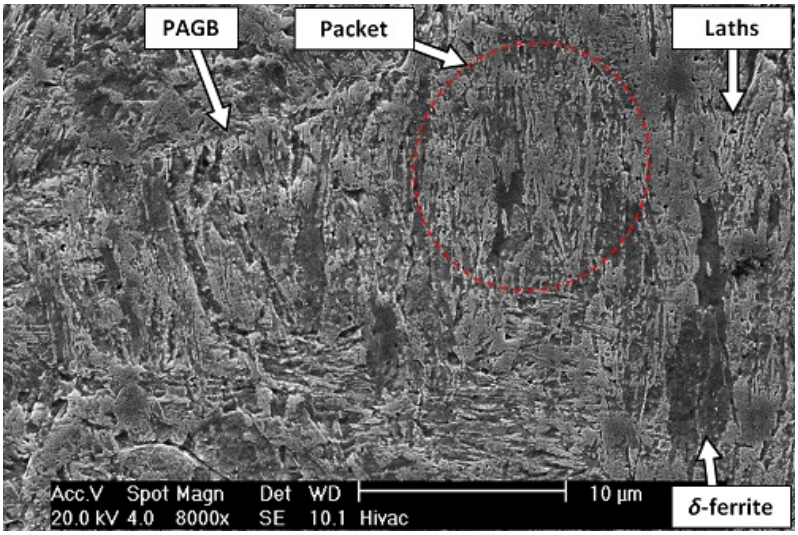

(a)

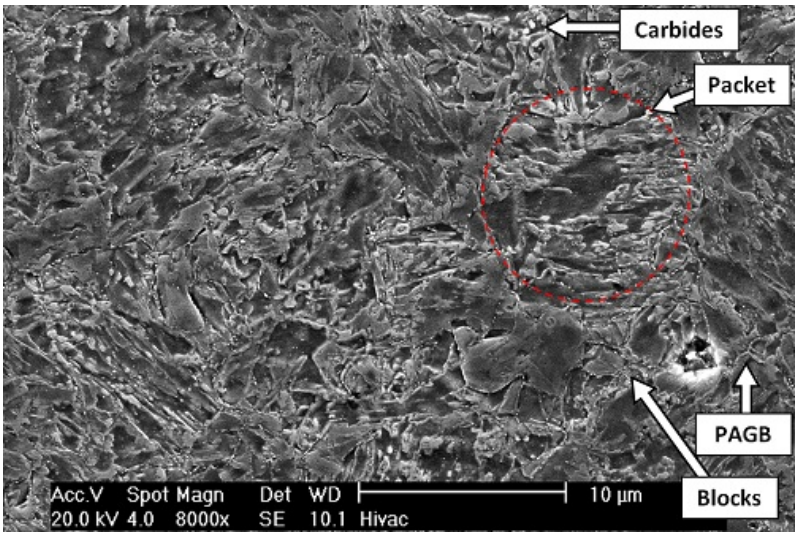

(b)

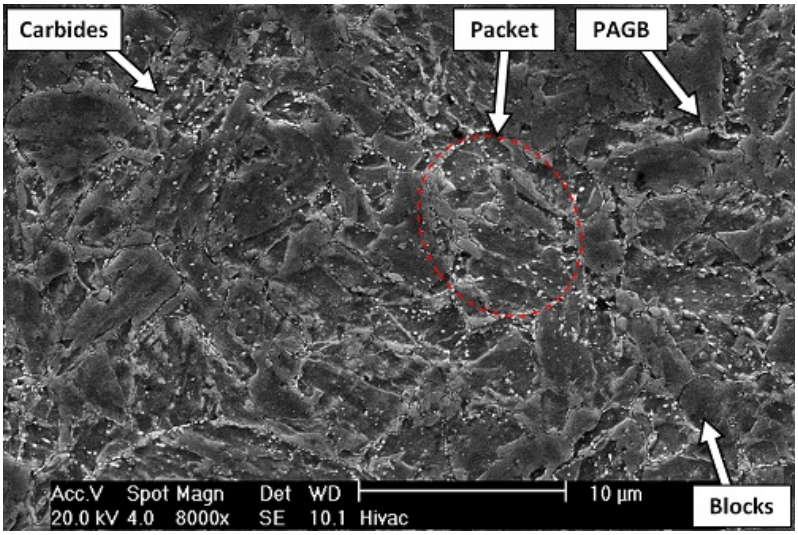

(c)

Figure 5.6: SE micrographs of the HAZ in sample A-W after etching with Vilella's reagent, showing **(a)** the CGHAZ, **(b)** the FGHAZ, **(c)** the ICHAZ.

precipitate on tempering [42]; BSE imaging reveals no evidence for the presence of Laves phase. There does not appear to have been any significant grain growth during the tempering process.

SEM images of the FGHAZ and ICHAZ in sample T are shown in figures 5.7(b) and 5.7(c). The microstructures of both regions have been successfully tempered; the 'blocky' features have disappeared, and the precipitate distributions are now similar to that of ideal P92. The process has affected both regions in much the same way, to the point that they are almost indistinguishable from one another. The key difference appears to be in the extent of carbide coarsening, as the average particle size in the ICHAZ (c. 300 nm) is larger than that in the FGHAZ (c. 200 nm).

The HAZs of the cases aged at 625 $°C$ have not evolved significantly in terms of grain size and distribution from those of the tempered case (though Laves phase particles have formed on grain boundaries), so for brevity they are not included.

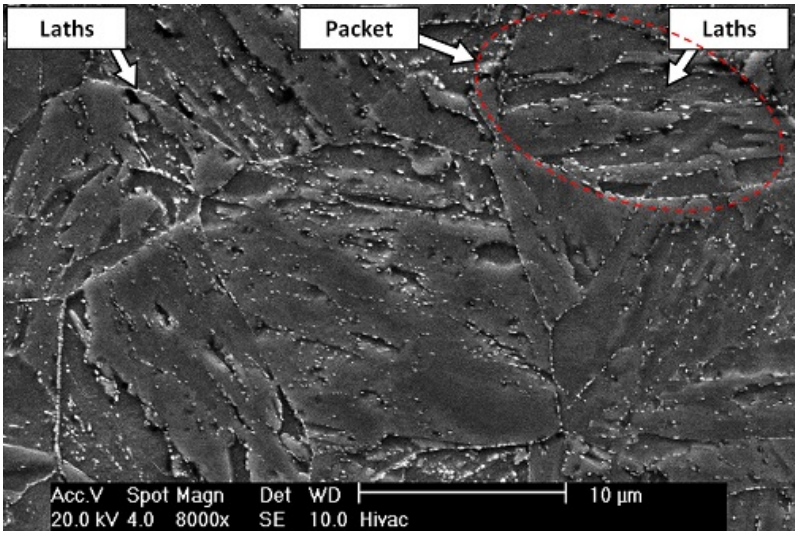

(a)

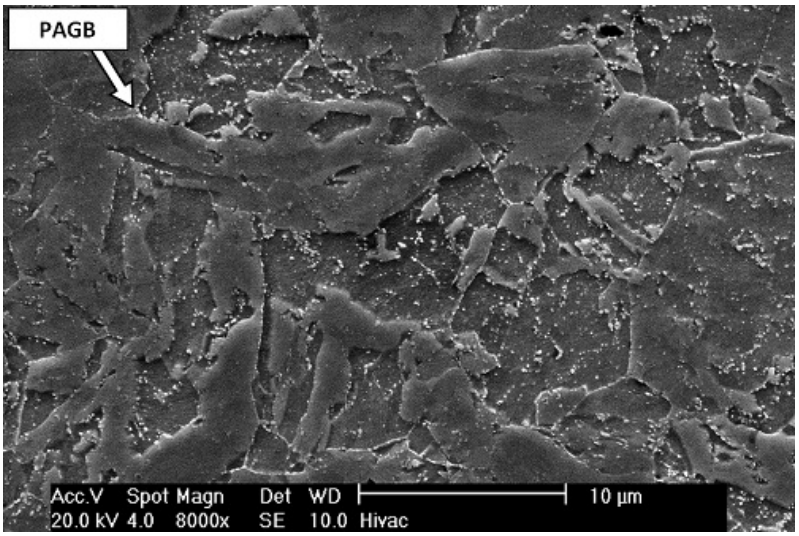

(b)

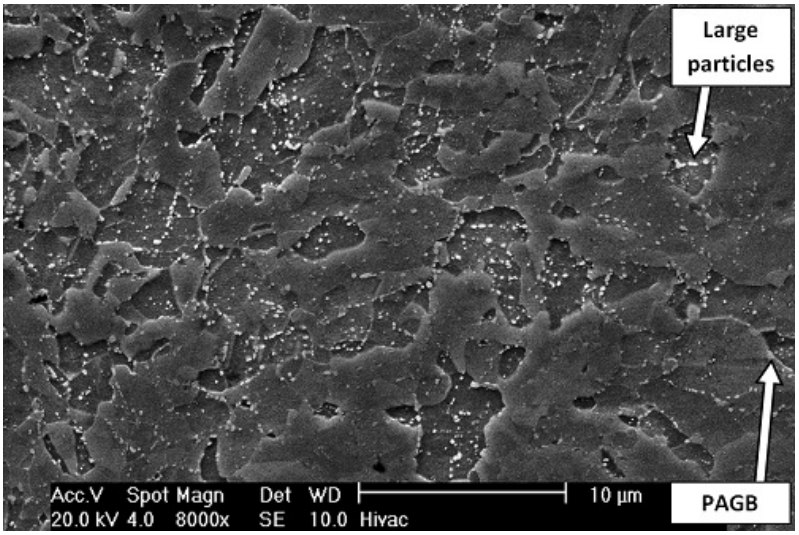

(c)

Figure 5.7: SEM SE micrographs of the HAZ in sample T after etching with Vilella's reagent, showing, **(a)** the CGHAZ, **(b)** the FGHAZ, and **(c)** the ICHAZ.

5.4 Evolution of the Alloy 625 Weld Metal

5.4.1 As-Welded and Tempered States

The weld metal contains three visible beads, collectively making up two layers. In the area analysed, the first weld pass is between 0.8 and 1.2 *mm* in width and the second is up to 3 *mm* in width. An OM overview of a transverse section of the two weld passes in sample A-W is shown in figure 5.8. This shows that both areas have dendritic microstructures, with dendrites oriented near-perpendicular to the weld line.

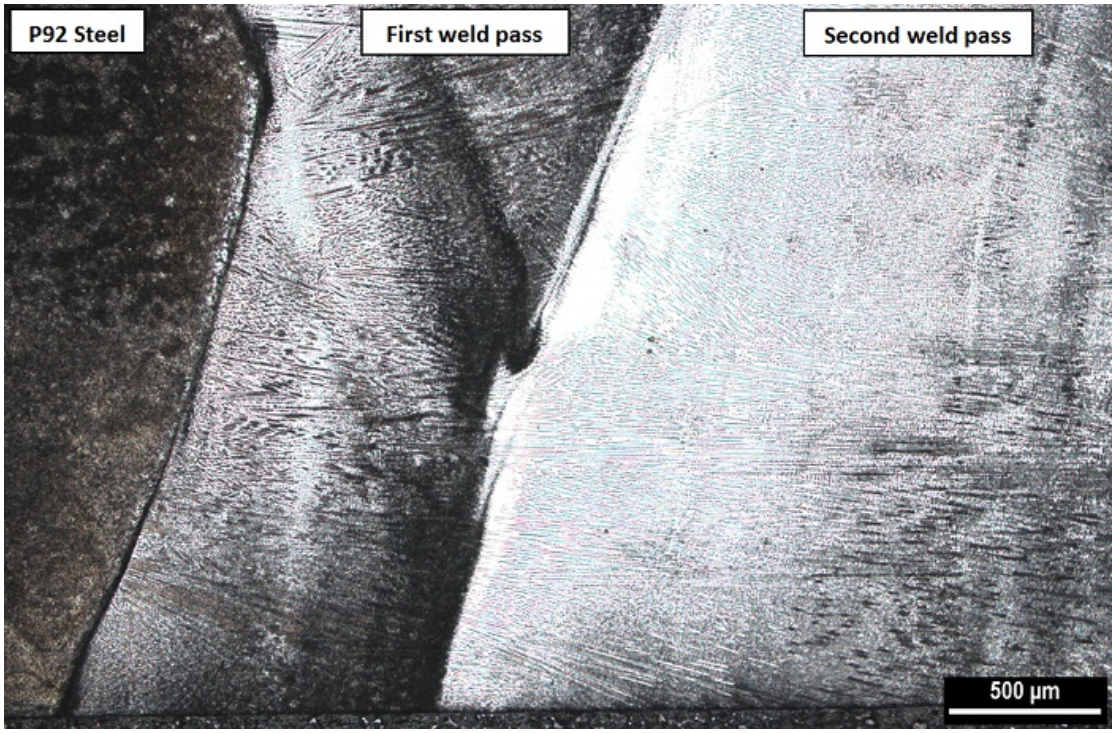

Figure 5.8: Optical micrograph of the transverse section of the first and second weld passes in sample A-W, showing the columnar-dendritic microstructures. The darker shade of the first weld bead indicates that it has been more heavily etched.

Despite sharing a similar grain structure, the first weld pass displays rather different etching properties to the second, as seen in figure 5.8. The first pass responded well to the aqua regia etch, which revealed a dendritic substructure aligned parallel to the long axis of the grains (and hence nearly perpendicular to

the weld line). A closer view of this dendritic structure is provided in figure 5.9. The second pass, on the other hand, proved to be much more resistant to the etchant, implying that it is of different composition (though the areas that were successfully etched appear to have a similar dendritic structure to that of the first bead). The boundary between weld beads corresponds to the location of the small measured change in hardness seen in figure 5.2. This dendritic structure appears to be almost identical in samples A-W and T, indicating that it is not affected significantly by the tempering process.

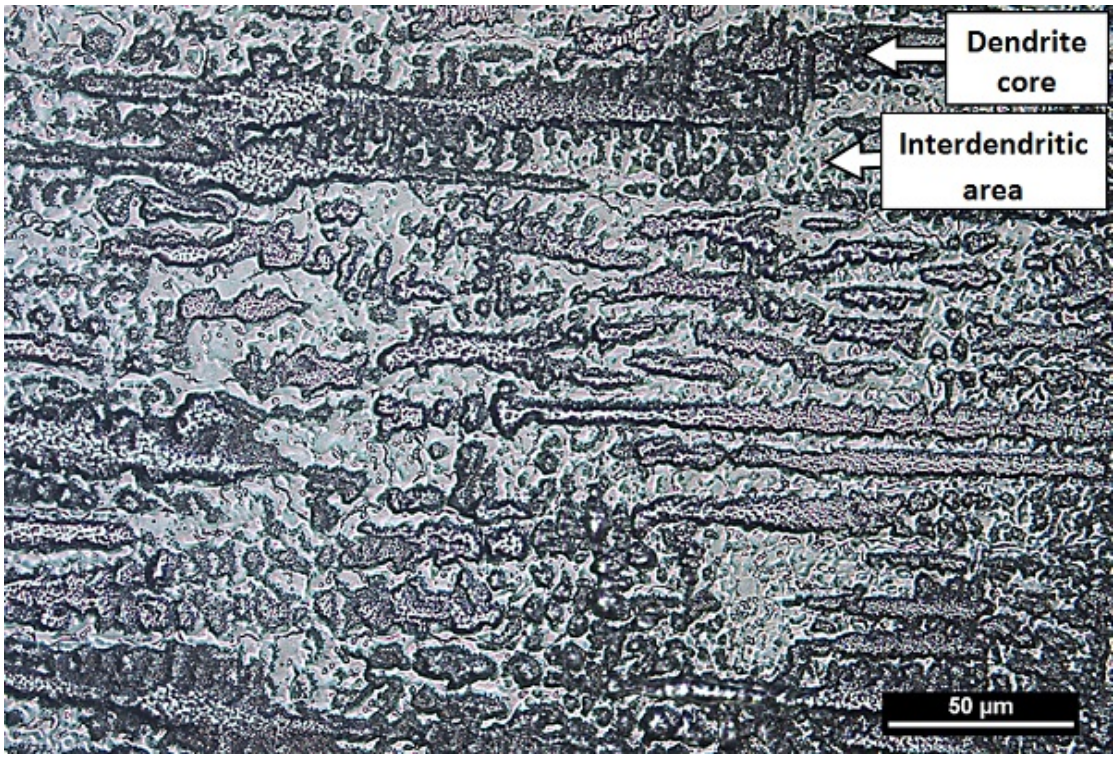

Figure 5.9: Optical micrograph of the dendritic structure of the first weld bead in sample A-W after etching with aqua regia. The darker areas are the dendrite cores.

The dendrites exist as a sub-structure within columnar grains, with the two being near-parallel in orientation. These are seen most clearly in BSE images, such as that in figure 5.10. There is significant variation in the apparent size of grains, with some being up to 100 μm wide and several hundred μm long. This is likely due to the fact that many of the grains are not parallel to the plane of the polished surface. It is also possible that some of the features that appear to be

particularly large grains are in fact multiple closely-aligned grains.

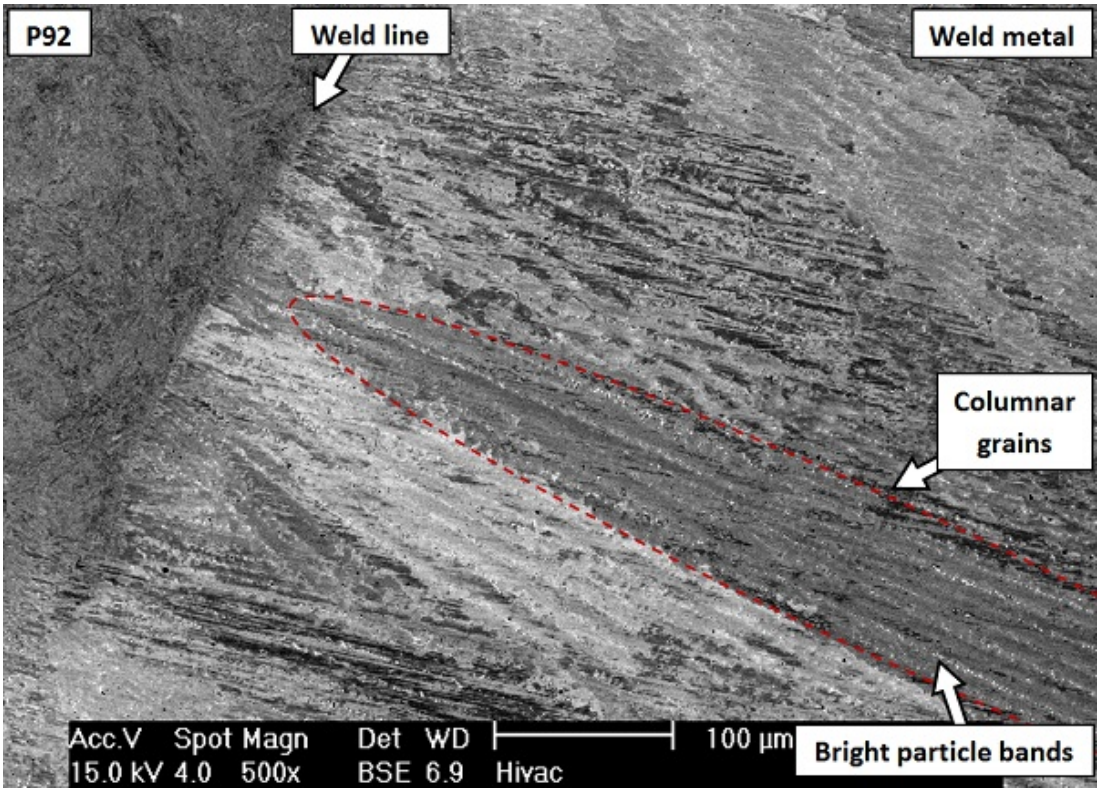

Figure 5.10: An SEM BSE micrograph of the transverse section of the weld metal (first weld bead) in the polished state showing the columnar grain structure (delineated by contrast variations) and parallel lines of bright secondary phases.

There are visible secondary phase particles in the weld metal, which appear distinctly bright in BSE images (such as 5.10). Many of these particles exist in parallel lines, running along grain boundaries. In the larger grains, the particles run along the length of the grains in distinct bands. Based on the known solidification metallurgy of Alloy 625 and the light appearance of the particles, these could be Nb and/or Mo-rich Laves phase, or niobium carbide (NbC) [58]; the bands within grains would hence correspond to the interdendritic areas of the microstructure.

The second phase particles in the weld metal are confirmed by EDX to be enriched in molybdenum and niobium. They are also found to be enriched in silicon, supporting the conclusion that these particles are Laves phase (as it was noted in section 2.1.5.1 that Laves phase in Alloy 625 may contain Si). This is shown in figure 5.11(a).

EDX measurements taken away from the weld interface, in the first weld pass, indicate iron concentration of around 30 wt%, as a result of dilution during the welding process. The second pass, however, contains only around 14 wt% iron. These differences in iron level explain the difference in etching properties between the first and third weld beads. These iron levels are far above the nominal level in Alloy 625 (c. 4 wt%). Using equation 2.4, the dilution in the first weld pass can be calculated to be $d = 31.2$ %. This will have an effect on the properties of the alloy, including its thermodynamic properties, mechanical strength and corrosion resistance. The measured average compositions of the two weld beads are given in table 5.1.

Table 5.1: Average compositions of the first and second weld beads, as measured by EDX scans over c. 2500 μm^2 areas.

	Element (wt %)						
	Cr	Fe	Mn	Mo	Nb	Ni	Si
Weld bead 1	17.7	30.2	0.7	6.6	2.7	41.8	0.5
Weld bead 2	19.6	14.2	0.7	9.0	3.3	52.7	0.6
Uncertainty (±)	0.3	0.4	0.2	0.4	0.4	0.4	0.1

By means of EDX, the chemical variations around the weld line area and in the weld metal have been analysed semi-quantitatively, as presented in figure 5.11(c). The elemental concentrations are shown to be near-constant in steel adjacent to the weld line, but then vary smoothly from that of the steel to that of the diluted first weld bead over a range of 50 – 60 μm. This is most apparent in the levels of Cr, Fe and Ni. Beyond 60 μm from the weld line, the composition of the first weld bead remains approximately constant. The compositional change in the weld metal corresponds to the PMZ, as described in section 2.2.2.1. Also measured across this region are the concentrations of molybdenum and niobium. They show a general increasing trend across the PMZ, but with significant local variations due to the electron probe crossing dendrites. These composition profiles across the weld line do not appear to evolve as a function of time.

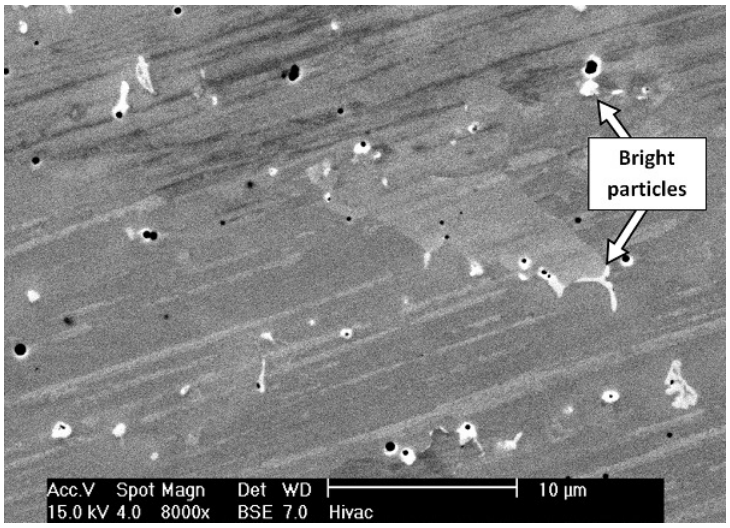

(a)

	Element (wt %)						
	Cr	Fe	Mn	Mo	Nb	Ni	Si
Particle	13.5	19.9	0.7	17.8	16.8	28.9	2.0
Uncertainty (±)	0.2	0.25	0.1	0.4	0.4	0.3	0.1
Matrix	17.2	32.6	0.7	5.5	1.1	42.3	< 0.5
Uncertainty (±)	0.2	0.3	0.1	0.3	0.25	0.3	0.1

(b)

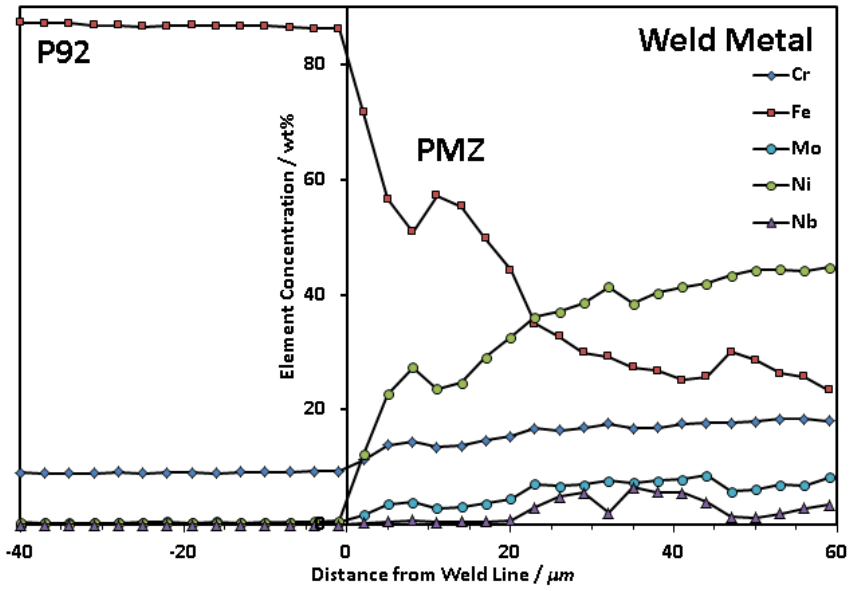

(c)

Figure 5.11: EDX analysis of the weld metal in sample A-W in the polished state, showing **(a)** second phase particles in BSE mode, **(b)** a table of measured compositions of a bright particle and of the metal matrix, and **(c)** EDX measurements across the weld line, showing the PMZ. The results in **(b)** are not fully quantitative, due to the large interaction volume relative to the size of features, but they do indicate that the particles are enriched in Nb and Mo relative to the matrix.

5.4.2 Short and Long Term Ageing

The weld metal evolves in certain distinct ways during ageing at 625 $°C$. The columnar-dendritic structure is still present, and appears at a large scale to be unchanged. However, closer analysis of the interdendritic areas, as shown in figure 5.12 reveals changes in the form and distribution of precipitates. Looking first at sample STA, there are at least two families of precipitates present. The first type are blocky phases, up to 1 μm in diameter. They are generally disconnected from one another, though some areas (likely grain boundaries) contain vein-like features which may correspond to bands of these particles. The particles cannot be identified on this evidence, though possible candidates are Laves phase or NbC.

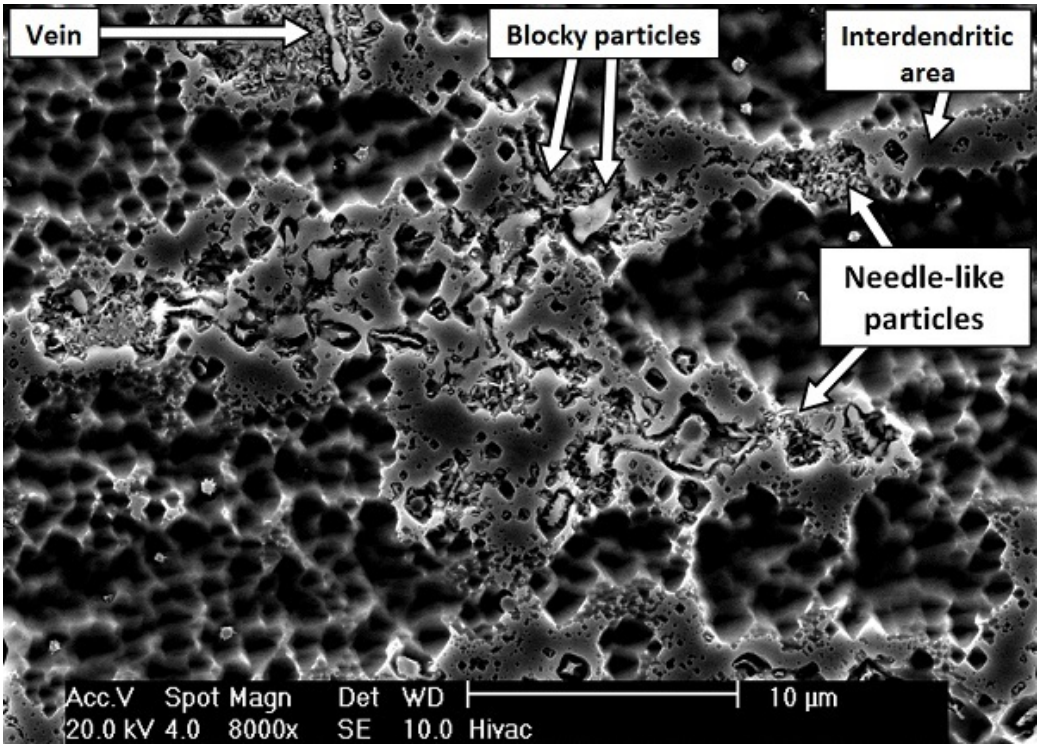

Figure 5.12: SEM SE image of the bulk weld metal in samples STA, after deep etching with aqua regia, showing the two distinct types of precipitate phase.

The second particle type takes the form of a series of extremely fine needle-shaped objects. These particles are between 100 and 200 nm in width, and up to 500 nm in length, oriented in seemingly random directions. They seem to form primarily in the vicinity of the aforementioned blocky particles and veins, placing

them largely in the interdendritic areas and around grain boundaries. Based on their distinctive morphology, and the known properties of aged Alloy 625, these particles are highly likely to be γ'' (tetragonal Ni_3Nb), δ-phase (orthorhombic Ni_3Nb), or some combination of the two.

The weld metal of sample LTA appears in many ways similar to that seen in sample STA. The differences in this sample, illustrated in figure 5.13, are in form of the features associated with extended ageing, most notable the needle-like particles in interdendritic areas, which are now much more pronounced. They still occur in the interdendritic areas and around grain boundaries, but the number and density of them has increased dramatically when compared to sample STA. Individual particles are now larger, now being up to 1.3 μm in length (though still generally no wider than 100 nm). These particles still exist alongside larger, blocky particles, the distribution of which does not appear to have changed significantly.

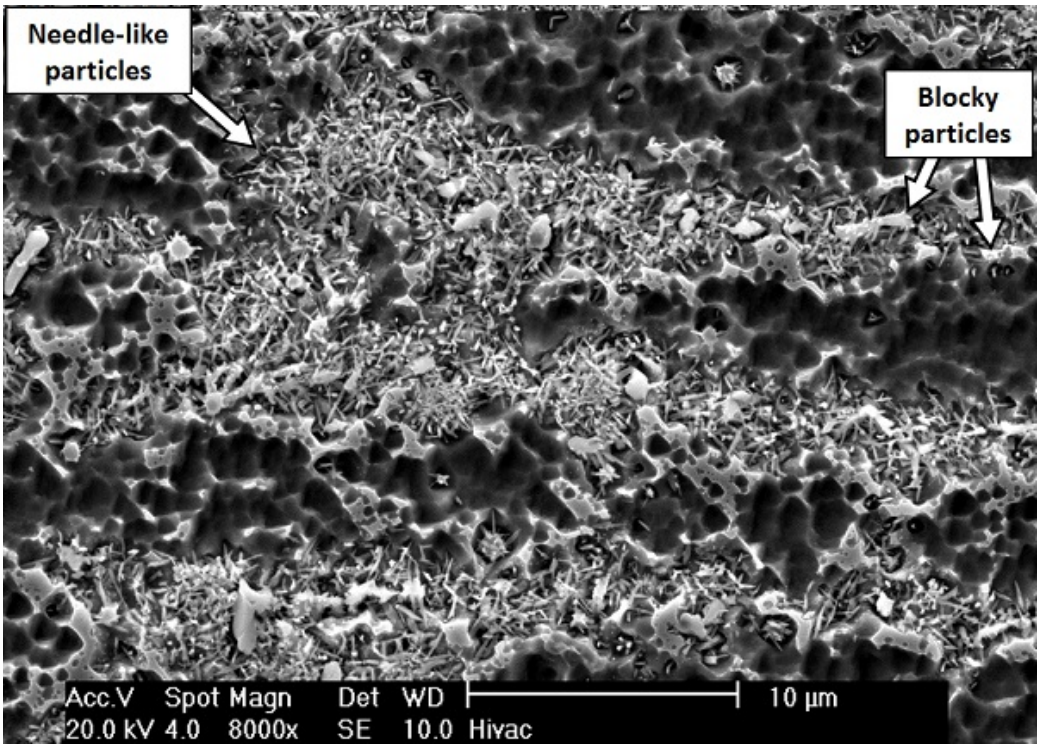

Figure 5.13: SEM SE image of the bulk weld metal in sample LTA, after deep etching with aqua regia. The needle-like secondary phases are clearly larger and more numerous than in sample STA.

5.5 Evolution at the Weld Interface

5.5.1 P92 Steel Side

The steel immediately adjacent to the weld line in sample A-W, shown in figure 5.14(a), is very similar from that of the CGHAZ away from the weld line. However, a key difference is in the form of patches of δ-ferrite. These are almost exclusively within 50 μm of the weld line. They have irregular shapes, with most being no larger than 10 μm in any dimension.

However, the area immediately adjacent to the weld line in sample T, shown in figure 5.14(b), demonstrates a distinctly lower fraction of secondary phases than the rest of the CGHAZ of this sample. Many of the laths and PAGBs are hence precipitate-free. The relative lack of carbides may be a result of carbon diffusion into the weld metal during the tempering treatment, which would make this area the carbon denuded zone (CDZ). This zone is estimated to be $20 - 40$ μm in width.

SEM images of the area around the weld interface in sample STA are shown in figure 5.15. There is some evidence of slight decarburisation/de-nitriding in this area, in the form of a reduced density of precipitates, as well as a slight reduction in average precipitate size. This effect is only apparent in the $10 - 20$ μm adjacent to the weld line. The extent of decarburisation appears to be less pronounced than in sample T.

The distribution of the bright Laves phase particles is different in this small CDZ area than in the rest of the steel. They do not appear to follow the PAGBs in this area, instead existing mainly as large, widely spaced particles. The particles in this band have grown up to 800 nm in size, which is much larger than other areas of the steel.

Additionally, there is an observable build-up of particles in the 1 μm adjacent to the weld interface. These particles are mostly around 200 nm in size. These

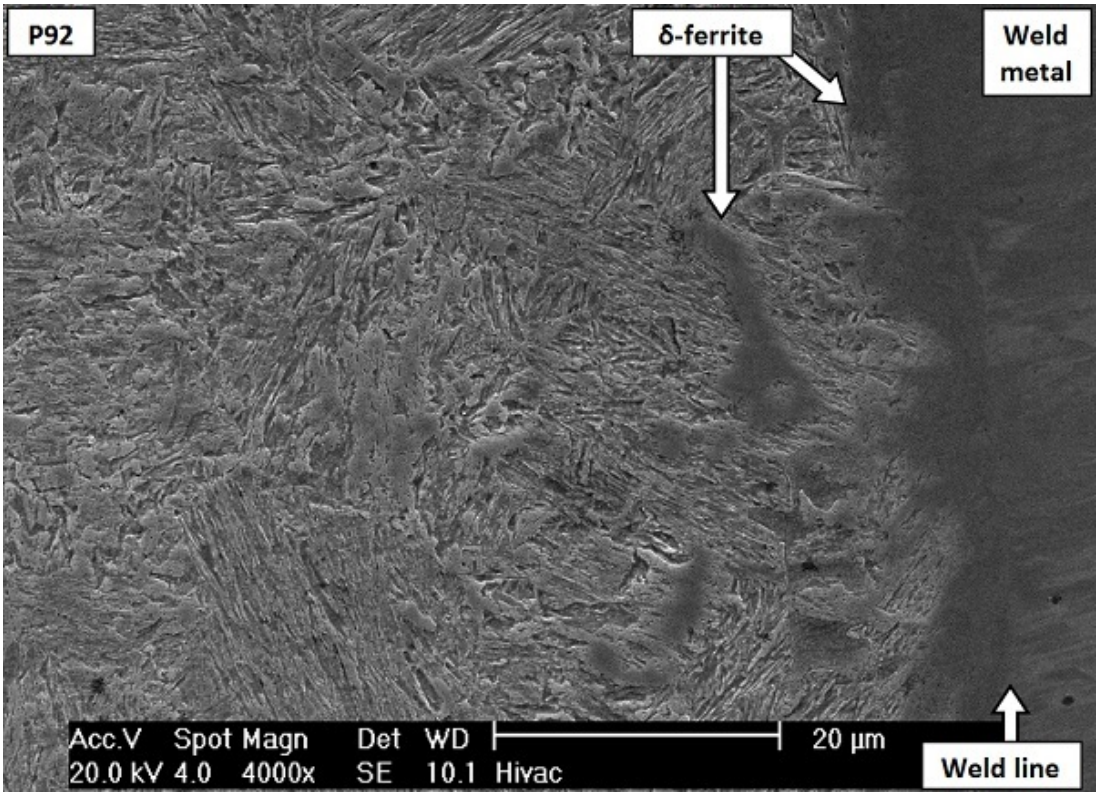

(a)

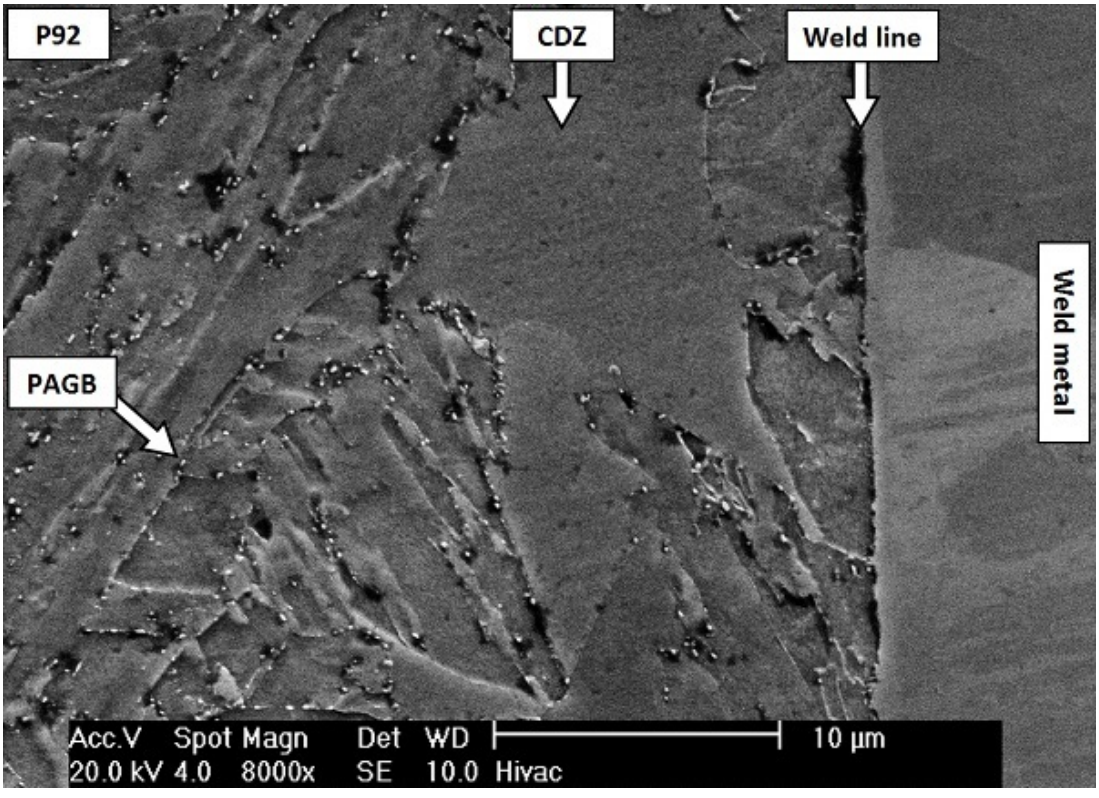

(b)

Figure 5.14: SEM images of the weld line area in **(a)** sample A-W, and **(b)** sample T, after etching with Vilella's reagent. Note that **(a)** is at a lower magnification since the features of interest are larger.

particles may correspond to the type I carbides previously observed in other systems. Additionally, BSE imaging reveals that there may be some Laves phase particles close to the weld line, but they are almost all 100 nm or smaller.

The steel close to the weld interface in sample LTA, as shown in figures 5.16, also shows evidence of decarburisation/de-nitriding. The PAGBs and laths have fewer particles on them than in the bulk, and many of those that remain are smaller (though at no point is the steel completely denuded of secondary phases). The extent of decarburisation appears to be greater than in sample STA, with up to 50 μm of the steel being affected, and fewer particles remaining. The same phenomenon of large Laves phase particles precipitating within the CDZ that was observed in sample STA is also observed here. Within 10 μm of the weld line, there are Laves phase particles up to 800 nm in size. The effect is less apparent here than in sample STA, since the Laves phase particles away from the CDZ have coarsened, while the already-large ones near the weld line have not coarsened as extensively.

Along the weld line there is a disconnected band of precipitates. These particles are mostly less than 500 nm in size, and appear to consist of both carbides and Laves phase, based on a comparison of SE and BSE images. These may correspond to type I particles, which have coarsened during the longer heat treatment. These particles are forming along the edge of the interface which, in the area shown, has areas of smooth and sawtooth morphologies. Around these particles are a network of smaller particles, too small to identify.

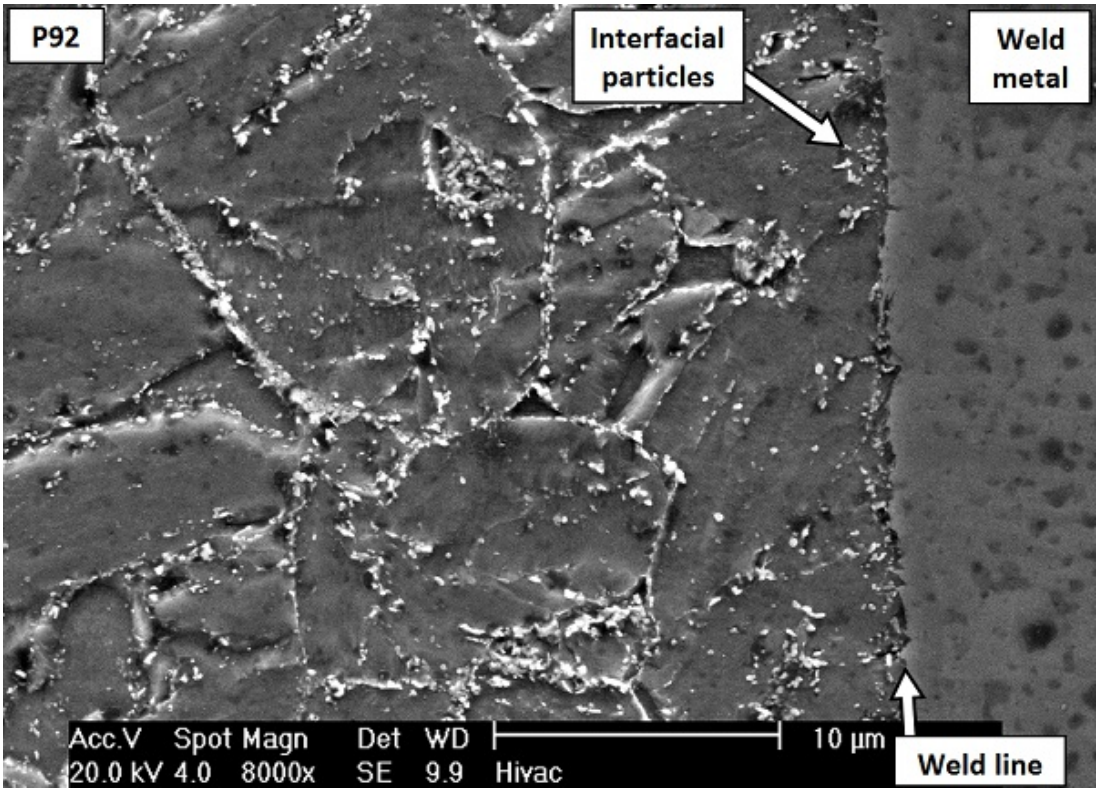

(a)

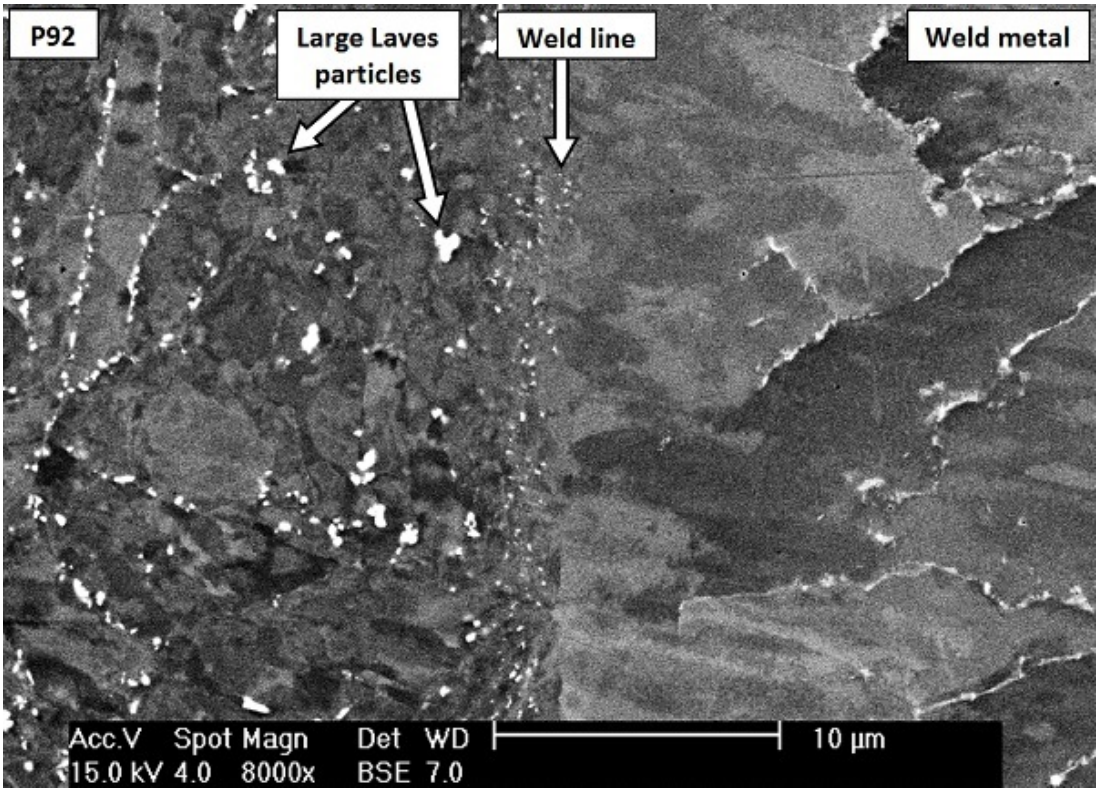

(b)

Figure 5.15: SEM images of the weld line area in sample STA. Image **(a)** is an SE image of the surface after etching with Vilella's reagent, and **(b)** is of the polished state in BSE mode.

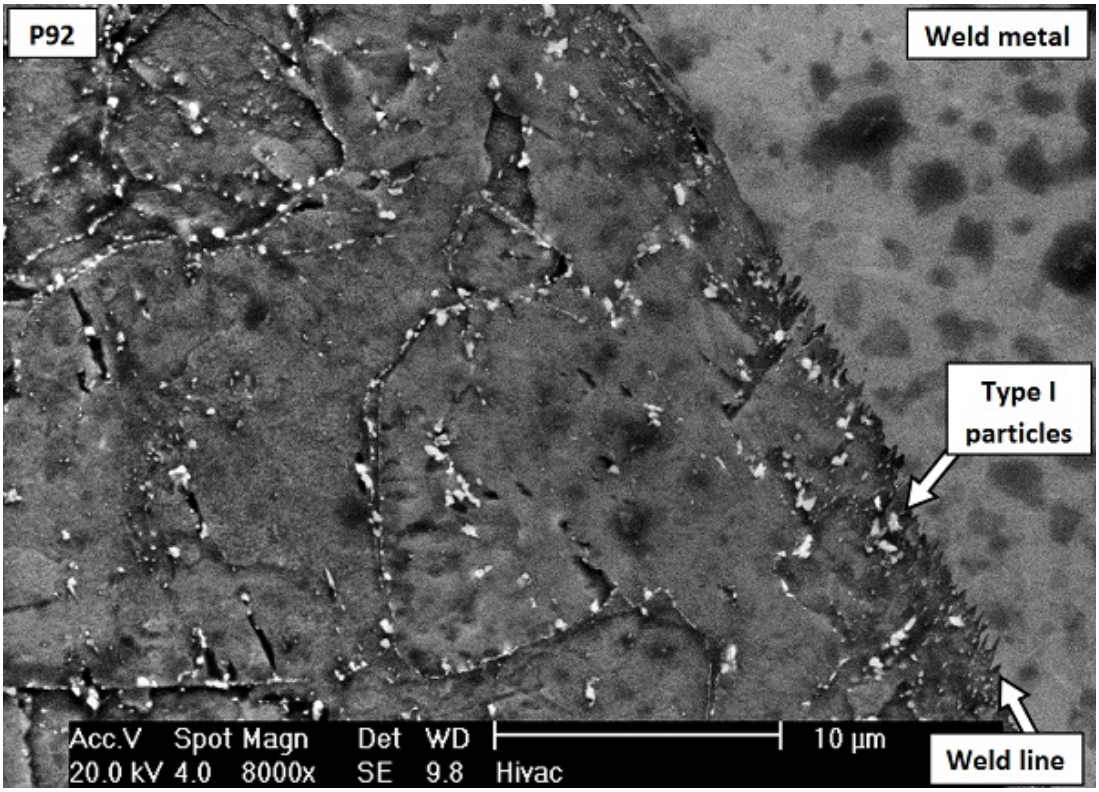

(a)

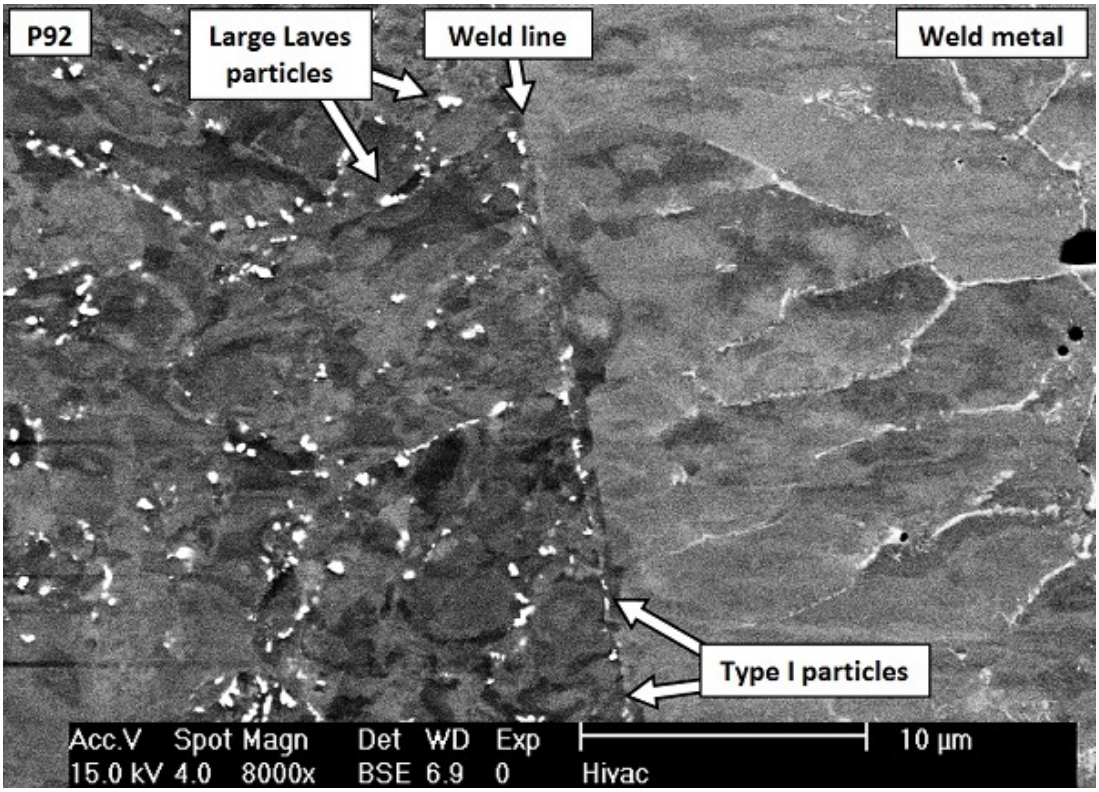

(b)

Figure 5.16: SEM images of the steel near the weld line in sample LTA. Image **(a)** is an SE image after etching with Vilella's reagent, **(b)** is a BSE image of the polished state.

5.5.2 Weld Metal Side

The area immediately adjacent to the weld line in sample A-W deviates from the typical dendritic structure. There is a band here, between 20 and 30 μm in width, that displays markedly different etching properties. This area is likely to be the partially mixed zone (PMZ), as was measured chemically in figure 5.11(c). It is shown in SE mode in figure 5.17(a), where it can be seen to have its own distinctive appearance. Associated with this area are features that may correspond to cellular growth, and a lower visible fraction of the bright secondary phase particles.

The microstructure of the weld metal after the tempering treatment has changed only in rather subtle ways. The columnar grain structure and dendritic substructure are still present, as is the PMZ. The principal change has come in the appearance of vein-like features, forming along what appear to be grain boundaries in the PMZ. Many of these vein-like features start at the weld line, extending for some distance (typically no more than 30 μm) through the PMZ. These are similar to the veins observed in the bulk, though they are generally wider and more consistent near the weld line. These features may be carbide and/or carbonitride precipitation on grain boundaries, a known phenomenon in aged Alloy 625; this would explain their greater abundance and width near the weld interface, due to diffusion from the steel.

The weld metal of sample STA near the weld line, as shown in figure 5.18(a), shows many similar features to previous cases; the columnar-dendritic microstructure, bright grain boundary particles (examples of which can be seen on the right side of figure 5.15(b)) and the PMZ from sample A-W are still present, as is the network of vein-like features from sample T. The needle-like particles that are present throughout much of the weld metal are not observed in the PMZ. It is possible that the bright particles seen in BSE images and the veins seen in SE images may be the same features observed in different ways.

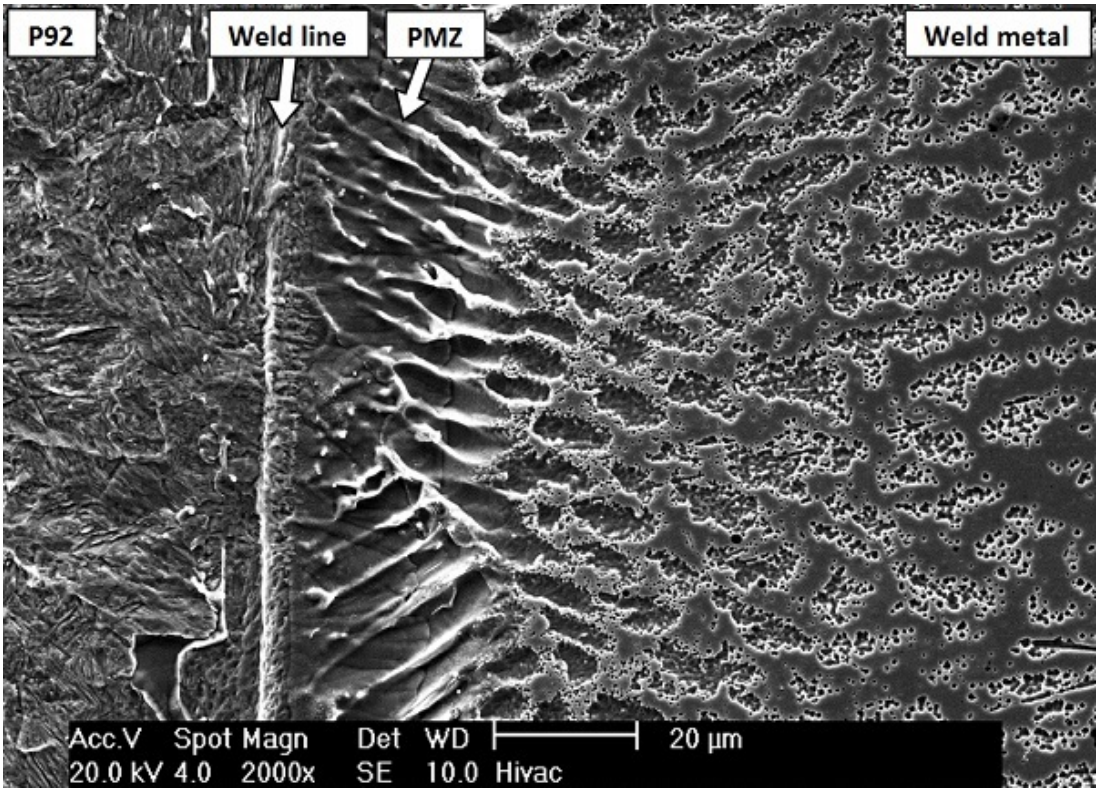

(a)

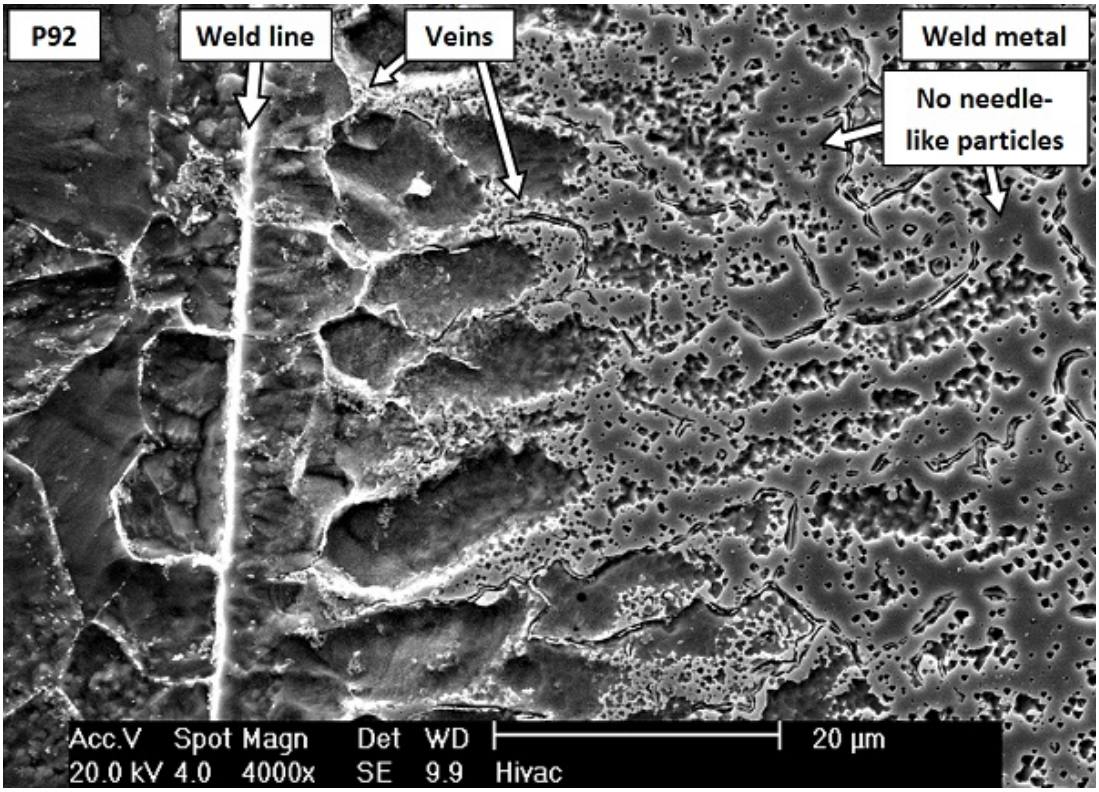

(b)

Figure 5.17: SEM SE images of the weld metal adjacent to the weld line in samples **(a)** A-W and **(b)** T after deep etching with aqua regia. Note that **(a)** is of lower magnification since the features of interest are larger.

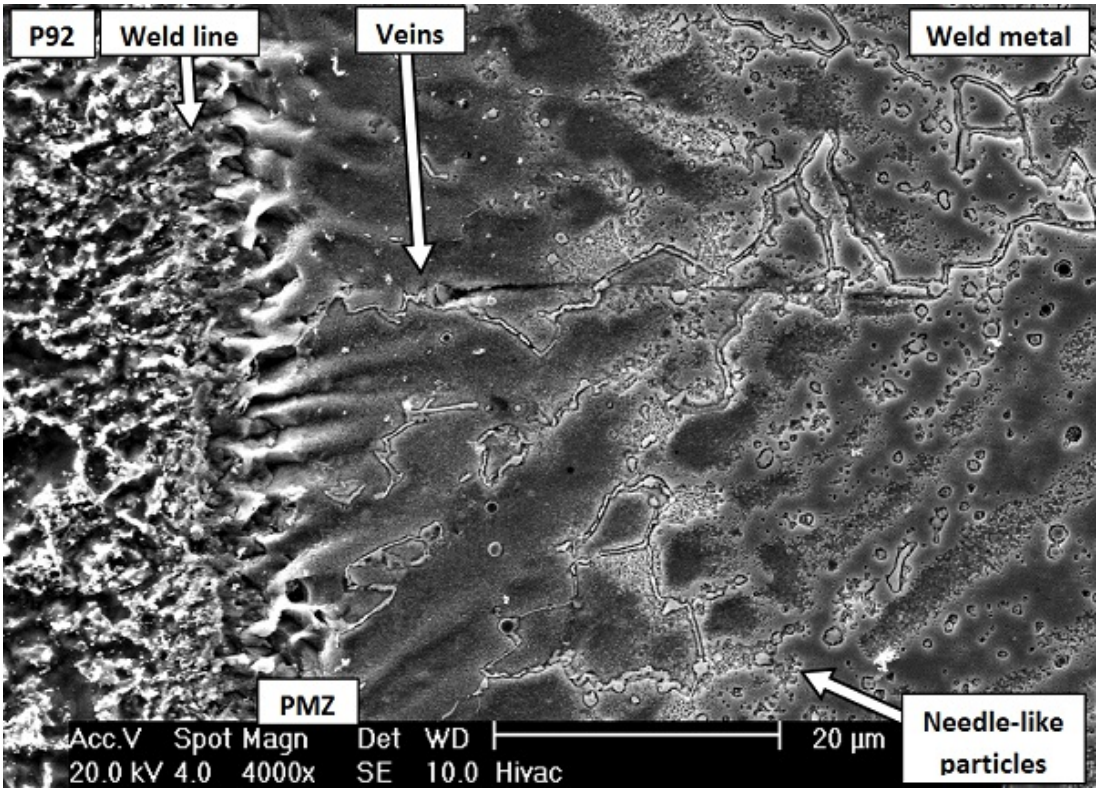

(a)

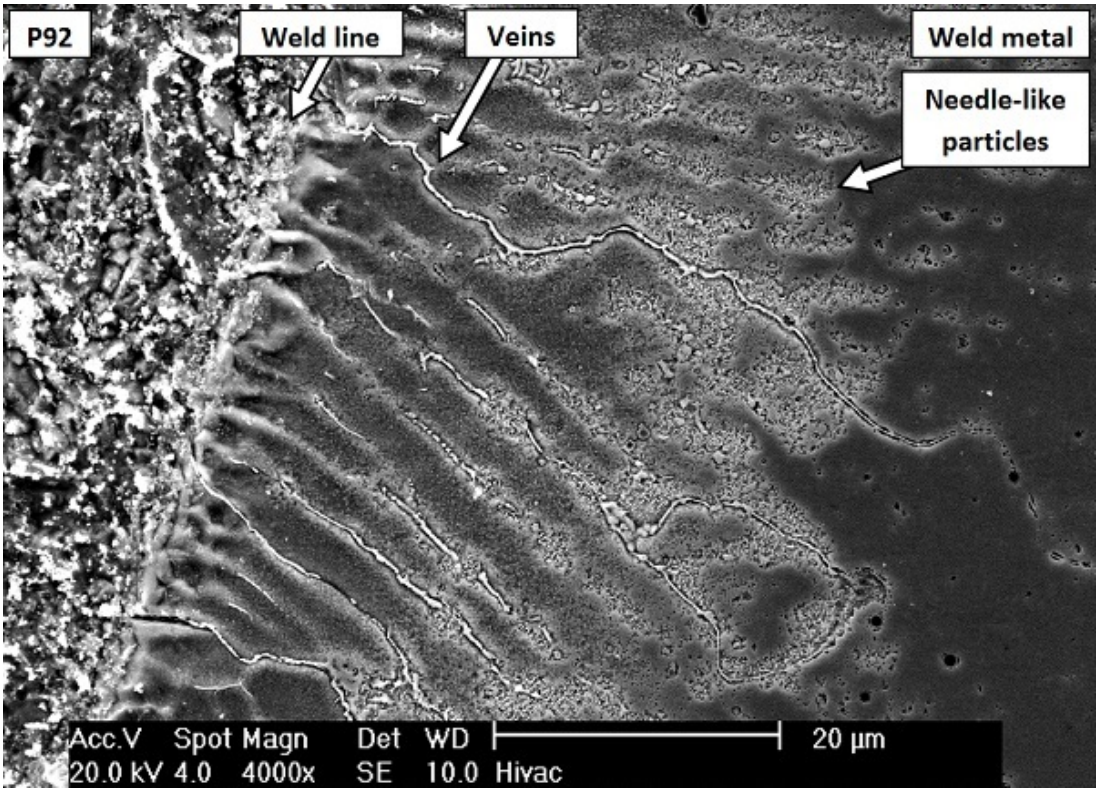

(b)

Figure 5.18: SEM SE images of the weld metal adjacent to the weld line in samples **(a)** STA and **(b)** LTA after etching with aqua regia.

The weld metal in sample LTA appears in many ways similar to that seen in sample STA. The differences in this sample, illustrated in figure 5.18(b), are in form of the features associated with extended ageing. The most apparent of these features are the veins, which are now more frequent, with more of them running from the weld line through the PMZ. The widths of these veins now distinctly decrease as a function of distance from the weld. These facts are consistent with the idea that the veins are pathways for the diffusion solute elements, including carbon and/or nitrogen.

A higher-magnification image of the veins in sample STA is shown in figure 5.19. This reveals the veins to be near-continuous. This appearance is consistent with a joined-up band of blocky particles, such as carbides. The equivalent veins in sample LTA are very similar in structure. Figure 5.19 also confirms that the needle-like particles (previously identified in the bulk weld metal of samples STA and LTA) are all but absent within 10 – 20 μm of the weld interface (i.e. the PMZ, or the most iron-enriched part of it).

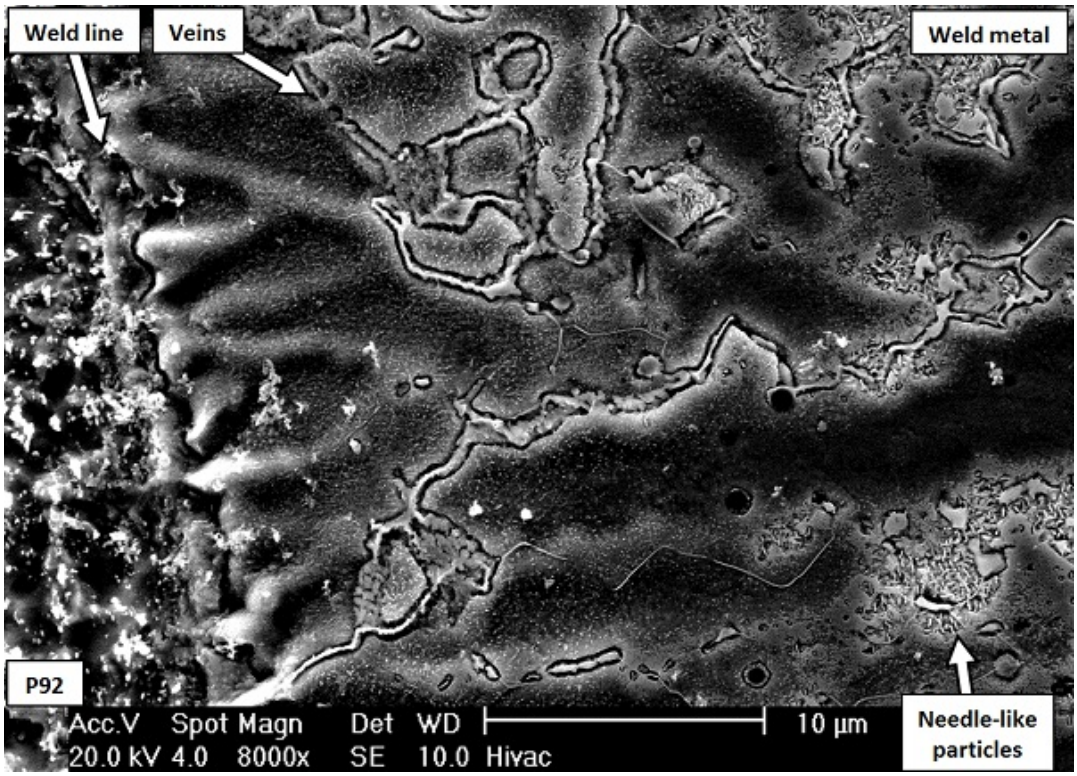

Figure 5.19: An SEM SE image veins in the weld metal adjacent to the weld line in sample STA after etching with aqua regia.

5.6 Oxidation Behaviour

The oxidation of the alloys in the various thermal conditions has been investigated. In sample A-W there is no discernible oxide on the surface of either alloy, indicating that it does not form during the welding process.

In sample T, an oxide scale has formed over the P92 steel and the PMZ of the weld metal. This is shown in figure 5.20. It is between 15 and 20 μm thick on the steel, and diminishes in width over the PMZ. No oxide notching at the weld line is observed, and no significant oxidation can be observed on the weld metal away from the PMZ.

Following the high temperature exposure, an oxide scale has formed on the surface of the steel in sample STA, as shown in figure 5.21. This scale is between 10 and 20 μm in thickness, and extends across the entirety of the steel. The oxide scale also exists on the weld metal, within 30 μm of the weld line (i.e. above the

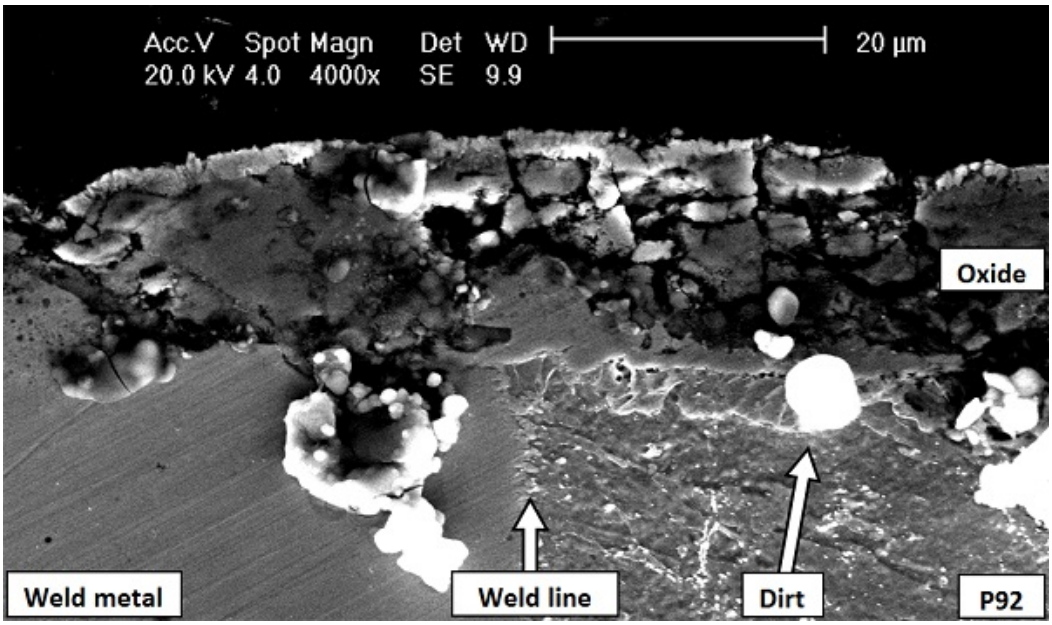

Figure 5.20: An SEM image of the oxidation on sample T. The bright white particles correspond to contamination, and are not microstructural features.

PMZ). This oxide scale appears to be growing inwards at the weld line, acting to separate the two alloys. This has penetrated to a depth of around 15 μm, relative to the surrounding oxide. This is likely to represent the early stages of oxide notching. In addition, there is a crack extending from the outer surface of the oxide to the notch, which may or may not be significant in the notching process.

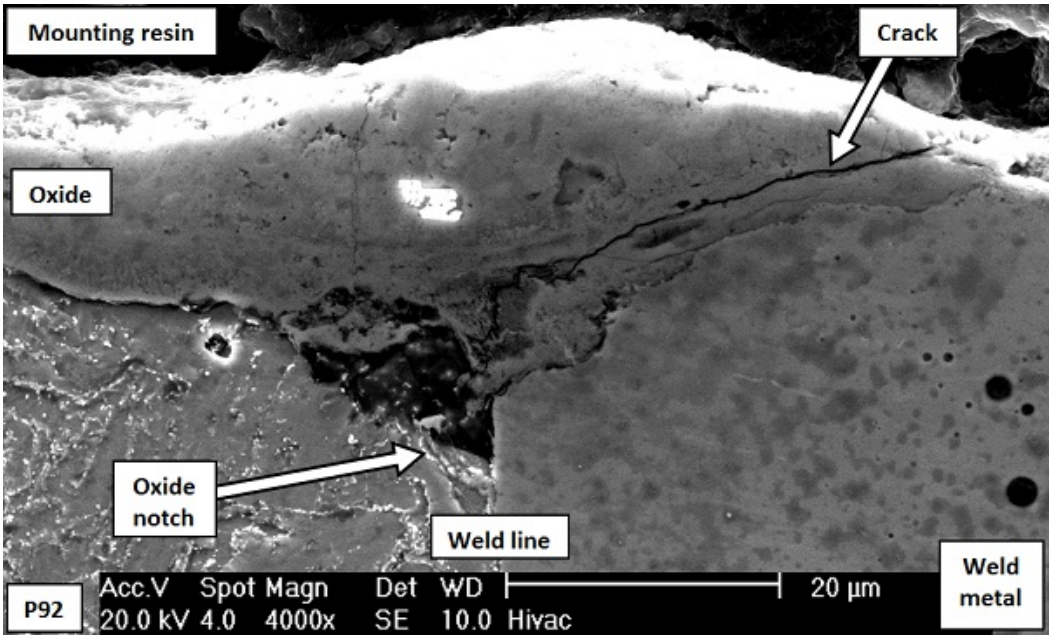

Figure 5.21: An SEM image of the early stages of oxide notching in sample STA.

The oxidation behaviour of sample LTA, as shown in figure 5.22, appears to be very similar to that of sample STA; the scale thickness is again between 15 and 20 μm, and it extends over all of the steel and the PMZ. Like the previous cases, the bulk of the weld metal does not appear to have oxidised to any degree. The lack of relative growth in oxide between the samples indicates either that the oxide is stable during long term ageing, or that material has been lost. Once more, oxide notching is observed at the weld line, with oxide penetrating to a depth of around 10 μm.

A two-layer oxide structure can be discerned in this case; an inner layer, contains small bright patches and numerous voids, and an outer layer, which is slightly darker in shade and relatively featureless. EDX analysis shows that the inner layer contains chromium, iron and oxygen, while the outer layer contains only iron and oxygen. This two-layer growth is in line with previous observations of oxidation of P92 steel [48].

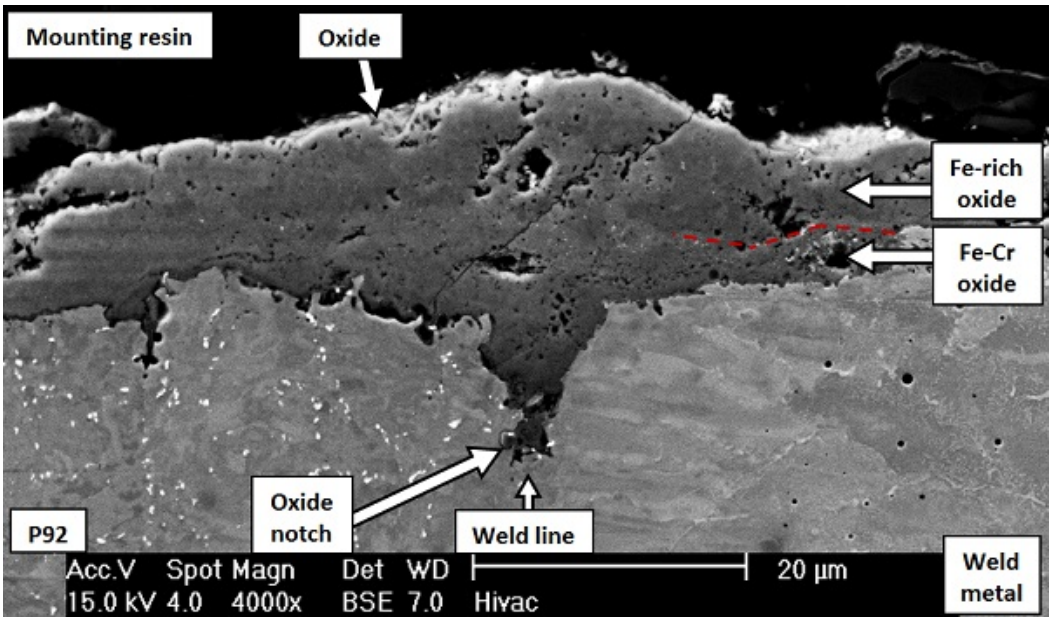

Figure 5.22: An SEM image of the oxide scale in sample LTA in the polished state, showing the ingress of oxide at the weld interface.

5.7 Measurement of Carbon Migration

By applying the low-voltage EDX method, as described in section 4.3.3.3, the variation of carbon level across the welds in samples A-W, T and LTA has been determined in terms of local count rates. These results are shown in figure 5.23. While not quantitative, this method ought to be able to demonstrate the effects of carbon diffusion.

In sample A-W no measurable carbon enrichment or depletion around the weld line has been detected. The count rates in the two alloys are, within margins of error, equivalent to the base level count rates at all ranges. While not fully quantitative, this indicates that carbon diffusion has probably not taken place to any significant degree during the welding process, as the levels in both alloys close to the weld line are within margins of error of the base levels.

The results of the investigation of sample T by this method reveal slight variations from the base level concentrations either side of the weld line. The steel displays a small CDZ, with carbon concentration being lower than the bulk level over a range of around 30 μm. Conversely, the weld metal displays a similarly-sized CEZ. These features appear to match up with the microstructural features observed in figures 5.14(b) and 5.17(b) (i.e the reduced amount of carbide in the steel and the vein-like features in the weld metal).

This EDX method has also been applied to sample LTA. These data show some limited carbon enrichment in the weld metal, over a range of approximately 40 μm, as well as depletion in the steel over a range of approximately 70 μm, which again appears to match up with microstructural features. The differences between peak/trough and base level count rates are greater than in sample T, indicating that more carbon has diffused in this case.

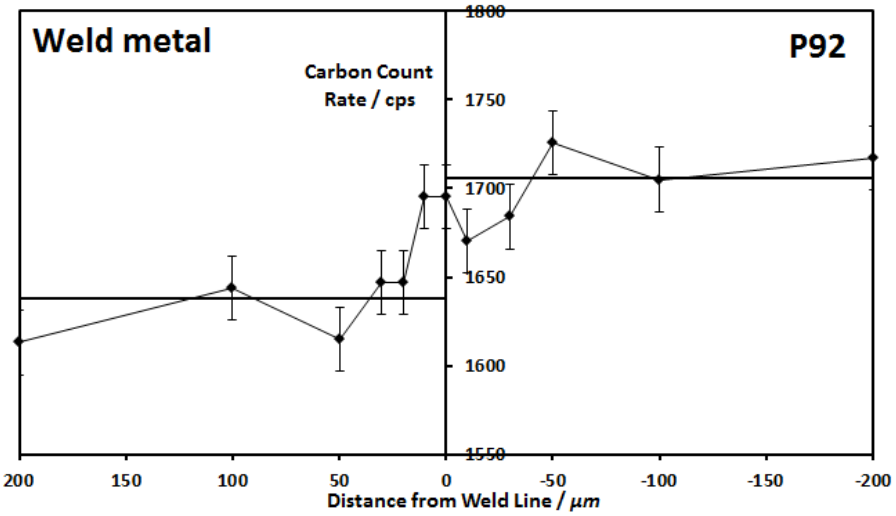

(a)

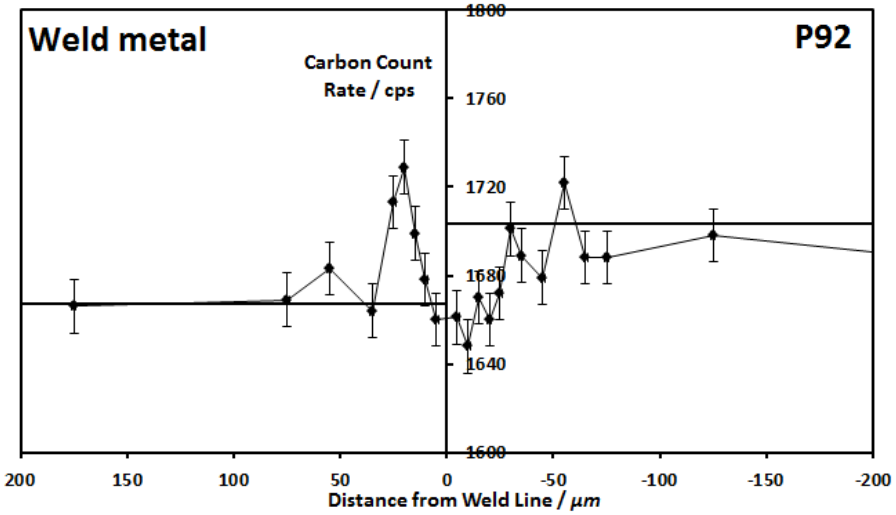

(b)

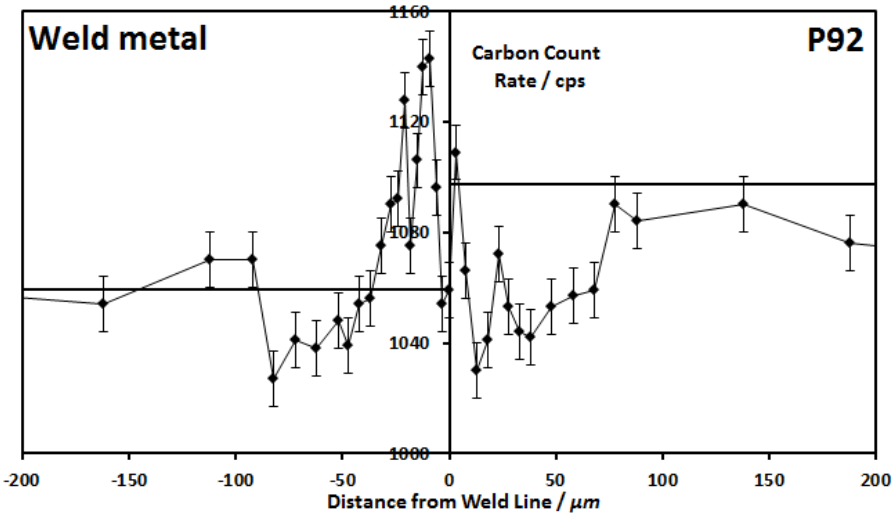

(c)

Figure 5.23: EDX measurements of carbon count rate variation across the weld interfaces in samples **(a)** A-W, **(b)** T, and **(c)** LTA, in units of 'counts per second' (cps).

5.8 TEM Observation of the Weld Interface

5.8.1 As-Welded State

A FIB specimen was extracted from around the weld in sample A-W, centred approximately on the weld line. A STEM bright field - dark field image pair showing an overview of the specimen are presented in figure 5.24. The P92 steel exhibits a martensitic lath structure. These laths are distinguished (in figure 5.24(a)) by slight variations in contrast, and the boundaries are marked with dark lines. The structure does not appear to contain any precipitates. By comparison, the weld metal has only three visible grains and neither significant sub-grain structure nor secondary phases. There is a band running down the middle of the specimen which appears different in structure and contrast to either alloy. The start and end points of this band are marked on figure 5.24 with dotted lines. This is presumed to be the 'interfacial martensite band' as described in section 2.2.2.3.

The chemical distribution across the specimen is illustrated by way of STEM-EDX maps, which are given in figure 5.25, taken from the same area as the images in figure 5.24. The iron level appears to be reasonably uniform across the specimen, as do the levels of the minor elements; the major features are the step changes in chromium and nickel levels at the edge of the interfacial band. There is no evidence for the existence of any secondary phases in either alloy, supporting the observations made from the bright field/dark field images.

Semi-quantitative measurements of composition by way of STEM-EDX point analysis are shown in figure 5.26. These show that, immediately adjacent to the weld line, the iron concentration in the PMZ of the weld metal peaks at 70.9 wt%, with corresponding chromium and nickel values of 11.6 and 12.2 wt%. This supports the high dilution levels in this area that were measured by SEM-EDX. Other element concentrations were measured, but have been excluded for

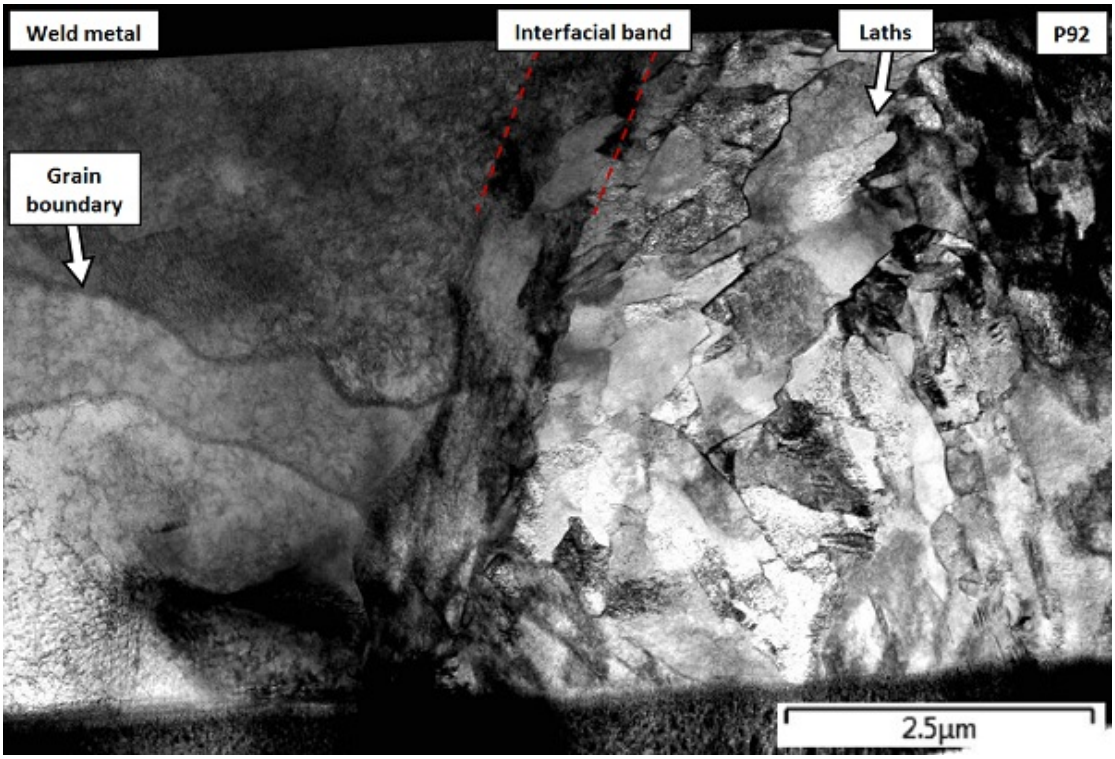

(a)

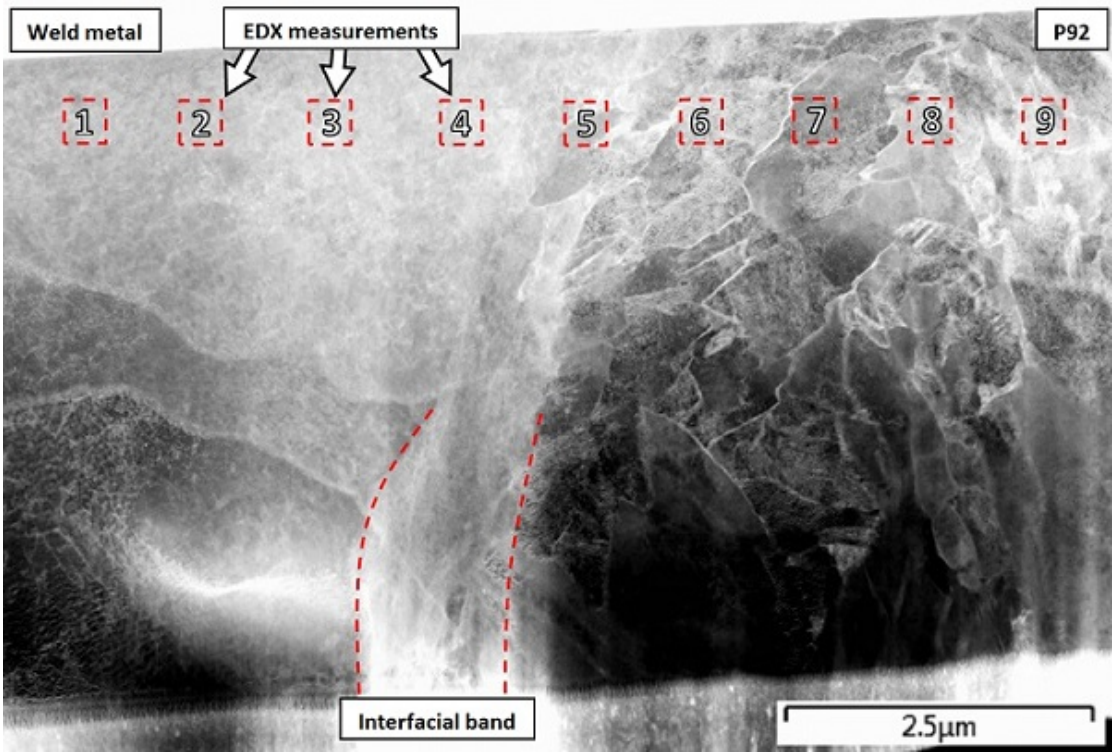

(b)

Figure 5.24: STEM images of the area around the weld line in sample A-W. Figure **(a)** was taken in bright field mode, **(b)** in dark field mode. EDX measurements from the points in figure **(b)** are presented graphically in figure 5.26.

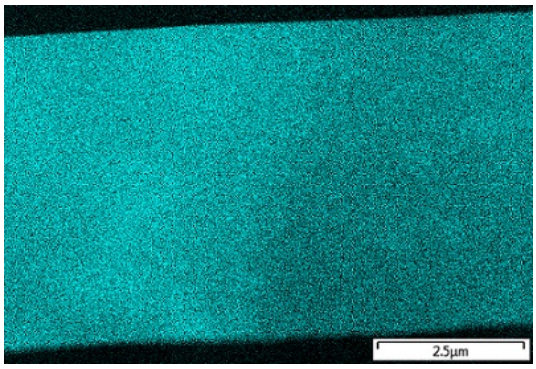

(a) Cr EDX map

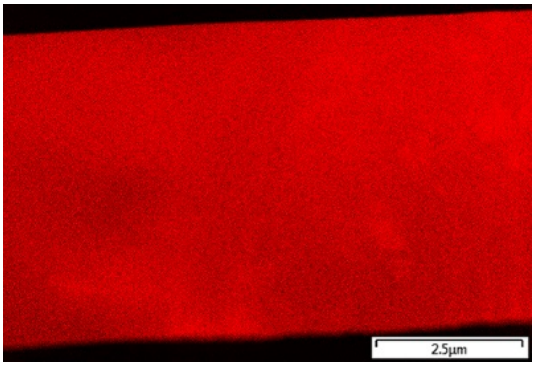

(b) Fe EDX map

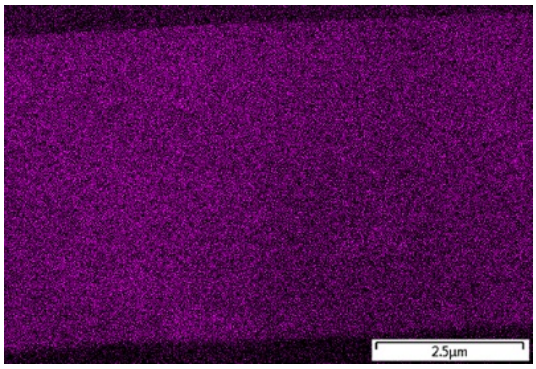

(c) Mn EDX map

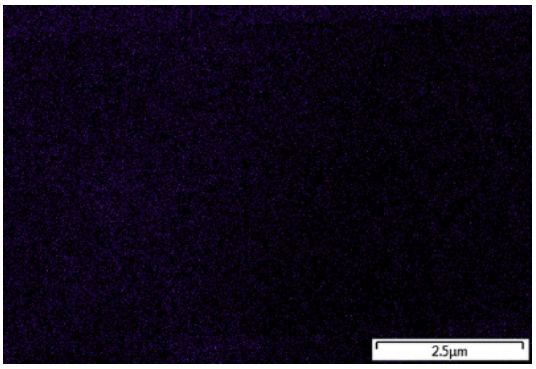

(d) Mo EDX map

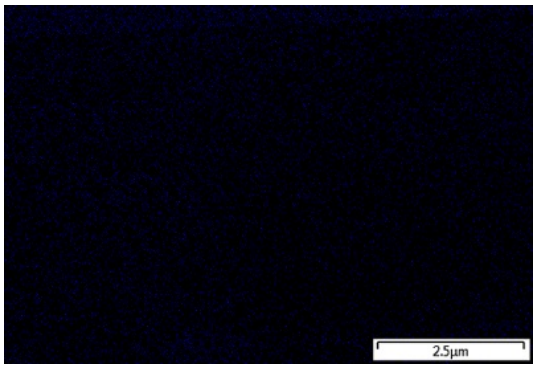

(e) Nb EDX map

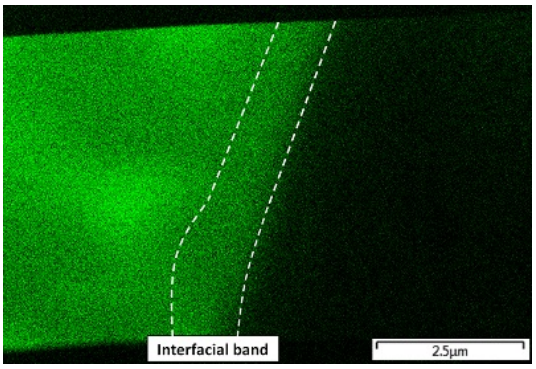

(f) Ni EDX map

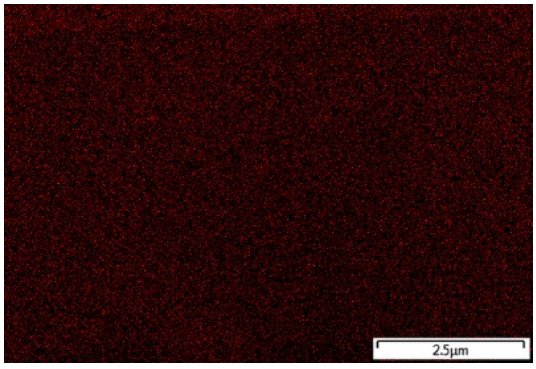

(g) V EDX map

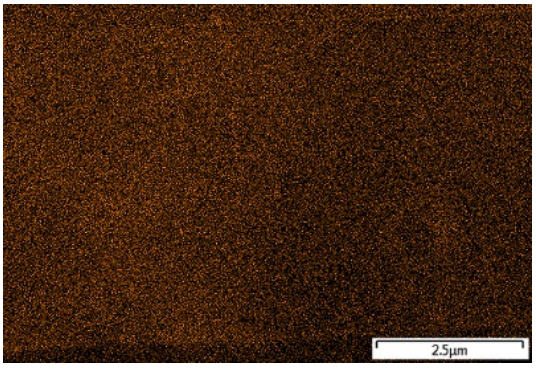

(h) W EDX map

Figure 5.25: STEM-EDX maps of the area around the weld line in sample A-W. The elements shown are **(a)** Cr, **(b)** Fe, **(c)** Mn, **(d)** Mo, **(e)** Nn, **(f)** Ni, **(g)** V, **(h)** W.

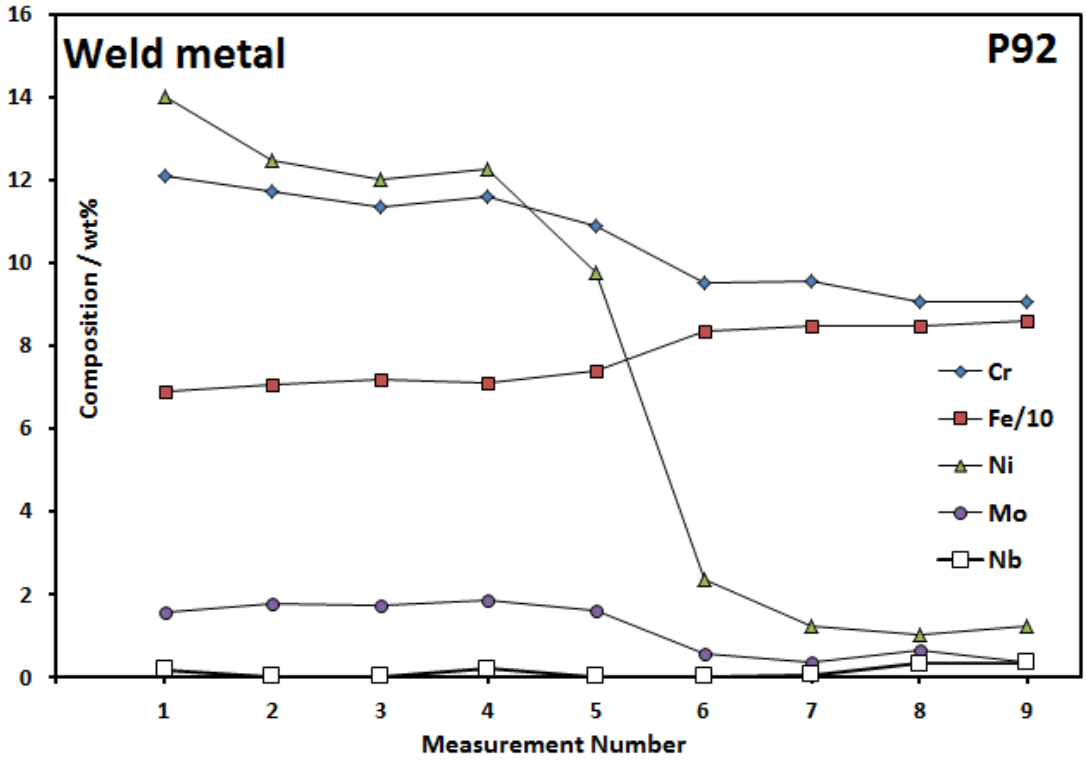

Figure 5.26: Concentration of Cr, Fe, Mo, Nb and Ni across the weld interface in sample A-W as measured by STEM. Measurements were taken at the points marked in figure 5.24(b). Other element concentrations were measured, but have been excluded for simplicity.

simplicity. The molybdenum and niobium levels are uniformly low, supporting the SEM-EDX results in figure 5.11(c).

By conventional TEM methods, images and SADPs from the P92, the weld metal and the interfacial band have been obtained. These are shown in figure 5.27. The patterns from the P92 correspond to BCC, while those from the weld metal correspond to FCC. The measured lattice parameters of these phases are both overestimated with respect to the database values (given in appendix C) by approximately 2.5%, indicating that the method includes a systematic error. The degree of tetragonal distortion in the BCC lattice induced by the martensitic transformation is hence insufficient to manifest itself in the diffraction pattern, as the BCC pattern is no more distorted than that of the FCC weld metal; as such, the crystal structure of the steels from this point onward will be described

as BCC, as opposed to BCT.

By careful tilting of the FIB specimen, an orientation was found at which strong diffraction contrast (i.e. a low-order zone axis diffraction pattern) was obtained from the interfacial band. The SADPs from the band also correspond to BCC, while the images conclusively prove that the band is of a different orientation to the adjoining P92 and weld metal. The part of the band at the top of the TEM specimen which does not contribute to the diffraction pattern is at a different orientation. The iron, chromium and nickel concentrations within the interfacial band are 73.9 wt%, 10.9 wt% and 9.8 wt% respectively (shown as the fifth measurement point on figure 5.26), which is intermediate between those of the steel and the PMZ.

The implication of these images is that the interfacial band results in two boundaries between the steel and the weld metal: one separating the P92 from the band (in this case a BCC-BCC boundary), and one separating the band from the weld metal (in this case a BCC-FCC boundary). As such, ambiguity is introduced in the meaning of the term 'weld line', as it could refer to either of these boundaries. This is not necessarily an issue when dealing with SEM images, since the band is not so readily resolved. The term 'weld line' will hence not be used when describing and discussing TEM images.

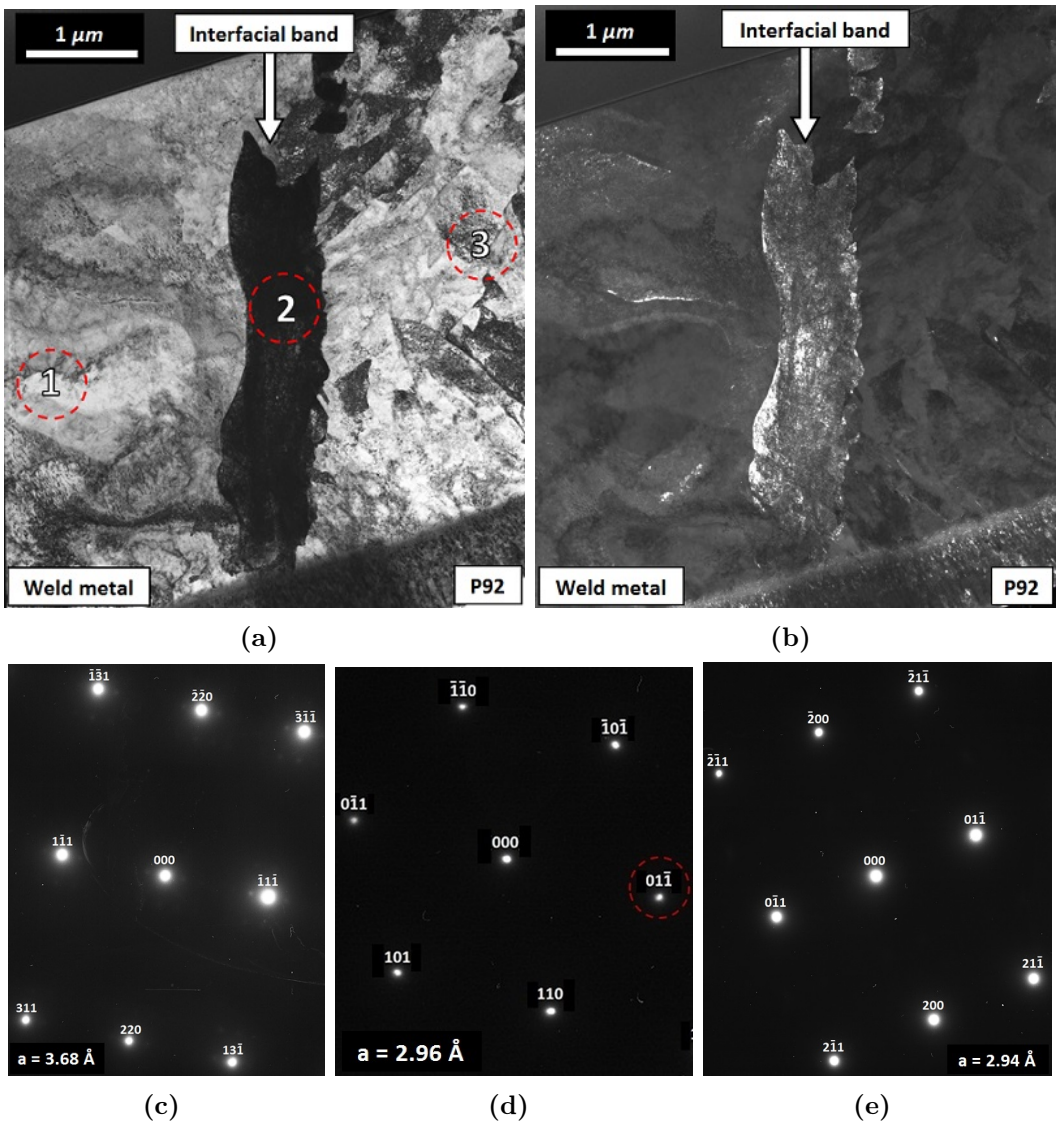

Figure 5.27: TEM images from sample A-W, showing **(a)** a bright field image, and **(b)** a dark field image, both of an orientation which provided diffraction contrast from the interfacial band. Figures **(c)** – **(e)** are SADPs from the areas labelled as 1, 2 and 3 respectively. Figure **(c)** is a SADP of the weld metal (FCC-[11$\bar{2}$] zone axis), **(d)** is a SADP of the interfacial band (BCC-[011] zone axis), and **(e)** is a SADP from the P92 steel (BCC-[111] zone axis). The bright and dark field images were taken with the specimen at the same tilt angle as for the SADP in **(d)**, with the dark field image formed from the circled diffraction spot. The SADPs in **(c)** and **(e)** were taken at different tilt angles.

5.8.2 Tempered State

A FIB specimen for TEM analysis was extracted from the weld line area of sample T, as was done for sample A-W. Bright and dark field STEM images of this FIB specimen are shown in figure 5.28, while corresponding STEM-EDX maps are shown in figure 5.29. These figures show evidence of temperature-induced evolution when compared to sample A-W.

Microstructurally, the steel demonstrates a sawtooth-like morphology of tempered martensite laths oriented near-perpendicular to the weld interface. These laths appear to be adjoined to the interfacial band, which is different in form to that seen in the as-welded case; it is wider here, at around 2.5 μm, and the edge linked to the steel is jagged, not smooth. This is likely an example of the 'wide' interfacial bands that have been found to occasionally occur in DMWs [82]; the width of the band and the jagged morphology hence may not be a result of the tempering process.

The weld metal has retained much the same microstructure as the as-welded case, with four visible grains and a similar sub-grain structure. There has been extensive precipitation of secondary phase particles in both alloys during the tempering process, on laths in the steel and on grain boundaries in the weld metal. Five distinct types of particle, the approximate compositions of which are given in table 5.2, can be identified in the steel:

- Chromium-rich particles, a TEM and SADP of which is shown in figure 5.30, which appear to be precipitating along martensite laths. These particles also appear to contain small amounts of other elements, most notably tungsten and molybdenum. These are by far the most abundant particles in the steel. Their average size is between 200 and 250 nm, with a maximum size of 350 nm, and their shapes are typically elongated parallel to the laths. The measured lattice parameter from electron diffraction patterns is closest to

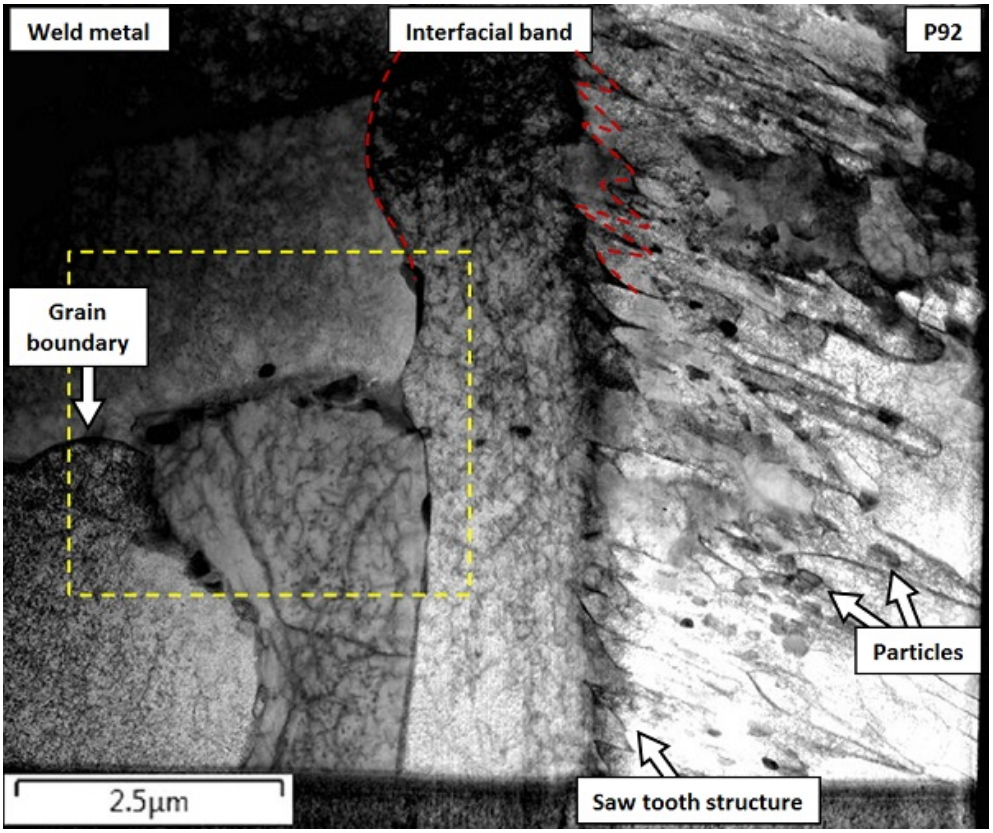

(a)

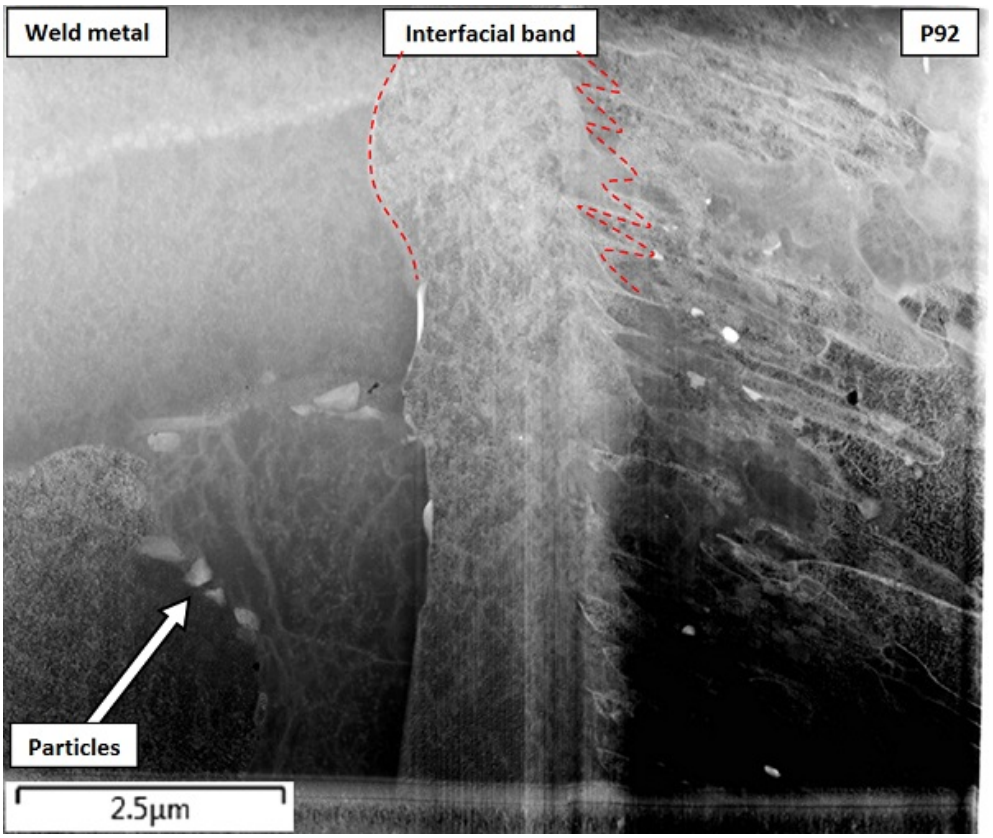

(b)

Figure 5.28: STEM images of the area around the weld line in sample T. Figure **(a)** was taken in bright field mode, **(b)** in HAADF mode.

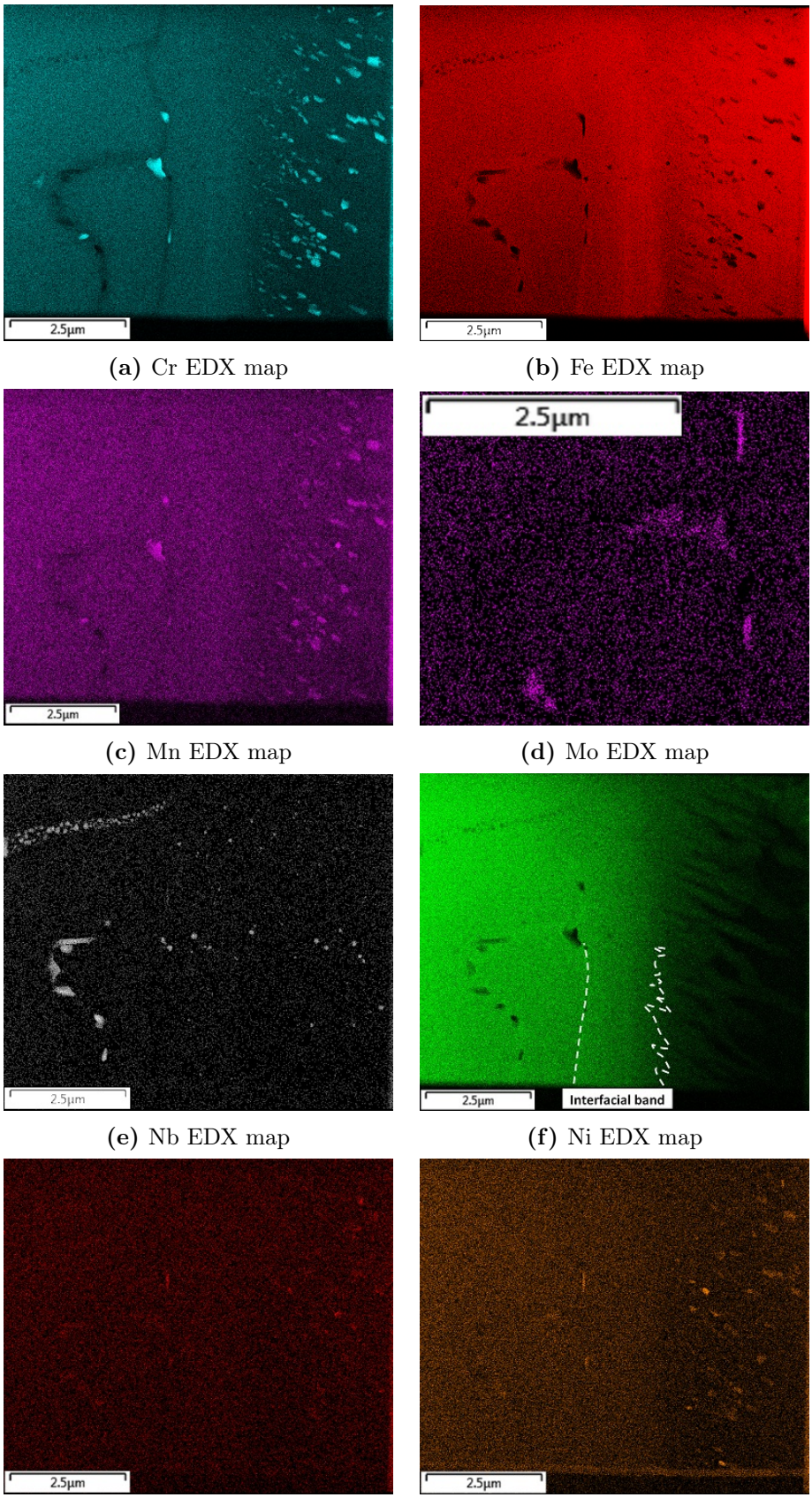

(a) Cr EDX map

(b) Fe EDX map

(c) Mn EDX map

(d) Mo EDX map

(e) Nb EDX map

(f) Ni EDX map

(g) V EDX map

(h) W EDX map

Figure 5.29: STEM-EDX maps of the area around the weld line in sample T. Map **(d)** is zoomed in on the area in the yellow box in figure 5.28(a).

Table 5.2: Approximate compositions of the various types of particles in the P92 in sample T, as measured by STEM-EDX. Note that the iron levels may be overestimated due to overlap (i.e. occlusion) between particles and the metal matrix. No reliable data could be gathered for the V- or Mn-rich particles. The levels of carbon and nitrogen are not quantified, and are instead categorised as strong (**S**) or weak (**W**) signals.

	Element (wt %)								
	C	Cr	Fe	Mo	N	Nb	Ni	V	W
Cr-rich particles	**S**	48.8	29.6	7.2	**W**	< 0.5	< 0.5	0.6	12.7
Uncertainties (±)	-	1.8	2.0	1.1	-	0.4	0.2	0.2	0.8
W-rich particles	**W**	7.5	36.4	20.7	**W**	1.8	0.7	0.9	31.8
Uncertainties (±)	-	0.5	1.4	1.7	-	0.6	0.2	0.2	1.4
Nb-rich particles	**S**	7.3	57.5	< 0.5	**S**	30.0	0.7	1.8	1.9
Uncertainties (±)	-	0.5	2.9	0.0	-	1.9	0.2	0.2	0.5

that of $M_{23}C_6$ carbide, being overestimated by approximately 2.3% (similar to the inaccuracies observed in sample A-W).

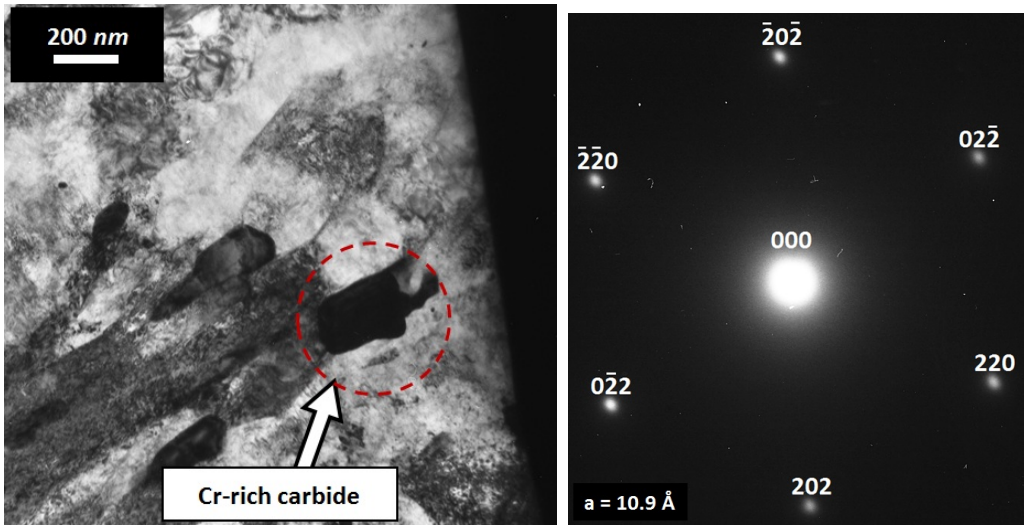

(a) **(b)**

Figure 5.30: TEM analysis of one of the Cr-rich carbides in the steel in sample T, showing **(a)** a bright field image, and **(b)** an indexed SADP from the area circled in red in the image, corresponding to the FCC-$[11\bar{1}]$ zone axis of $M_{23}C_6$.

- Tungsten-rich particles, which are uncommon; only three are present in this specimen. They are only around 150 *nm* in size. They also contain a large amount of molybdenum. Due to their small size, their structure cannot be identified by electron diffraction. Their extremely low levels of carbon and nitrogen make them highly unlikely to be carbides or carbonitrides; it is

hence likely that they are Laves phase.

- Niobium-rich particles, which are dotted throughout the steel, with a few also appearing in the interfacial band. They are small, typically around 100 nm, and circular. They are presumed to be MX-phase carbonitrides, of type Nb(C,N), based on their size and composition, but they are too small to be able to confirm this by electron diffraction.

- Vanadium-rich particles, of which only a few can be identified (all away from the interfacial band). They closely resemble the Nb-rich particles in size and shape, hence making it likely that they are also MX-phase (of type V(C,N)).

- A single manganese-rich particle, which also contains sulphur. It is around 150 nm in size and nearly circular. Based on its composition, it is highly likely to be a manganese sulphide inclusion, present from the steel casting process, and will not be discussed further.

Additionally, the weld metal contains different types of particle, the compositions of which are given in table 5.3. These particles are:

Table 5.3: Approximate compositions of the various types of particles in the Alloy 625 in sample T, as measured by STEM-EDX. Note that the iron and/or nickel levels may be overestimated due to overlap between particles and the metal matrix. The levels of carbon and nitrogen are not quantified, and are instead categorised as strong (**S**) or weak (**W**) signals.

	Element (wt %)									
	C	Cr	Fe	Mo	N	Nb	Ni	Si	V	W
Nb-rich particles	**W**	7.2	33.3	2.0	**S**	41.5	14.5	< 0.5	0.6	0.7
Uncertainties (±)	-	0.35	1.4	1.3	-	1.8	0.7	0.2	0.1	0.3
Cr-rich particles	**S**	56.0	21.0	12.9	**W**	< 0.5	4.0	< 0.5	0.5	4.8
Uncertainties (±)	-	1.5	0.6	0.7	-	0.2	0.2	0.2	0.1	0.4
Mo-rich particles	**W**	11.3	45.9	15.3	**W**	< 0.5	19.5	2.4	< 0.5	4.2
Uncertainties (±)	-	0.4	1.5	0.9	-	0.3	0.7	0.3	0.1	0.5

- Niobium-rich particles, precipitating exclusively along grain boundaries. There are significant variations in size and morphology; the smaller particles are

circular, around 100 to 150 *nm* in size, while the larger particles are elongated along the grain boundaries, and are up to 500 *nm* in length. A TEM bright field image and a corresponding SADP from one of these larger particles are given in figure 5.31. The SADPs are consistent with MX-phase carbonitrides, with EDX analysis confirming them to be of type NbN (as little to no carbon was detected).

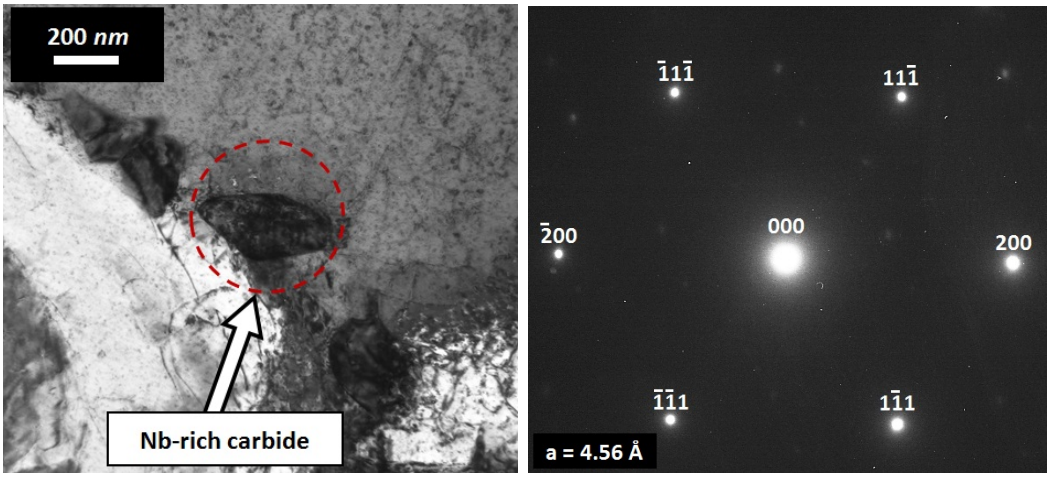

(a) **(b)**

Figure 5.31: TEM data from one of the Nb-rich particles in the weld metal in sample T, showing **(a)** a bright field image, and **(b)** an indexed SADP from the area circled in red in the image, corresponding to the FCC-[011] zone axis of MX phase.

- Chromium-rich particles, precipitating at grain boundaries and on the boundary between the weld metal and the interfacial band. Only five particles of this type can be seen. A TEM bright field image and a corresponding SADP from one of these particles are given in figure 5.32. From this and EDX data they are identified as $M_{23}C_6$ carbide. These particles contain a large amount of molybdenum, as well as a smaller amount of tungsten.

- Molybdenum-rich particles, precipitating at grain boundaries and on the interface between the weld metal and the interfacial band. There is significant overlap between these particles and the matrix, making it difficult to obtain reliable diffraction patterns or EDX data. The best estimate, based on their

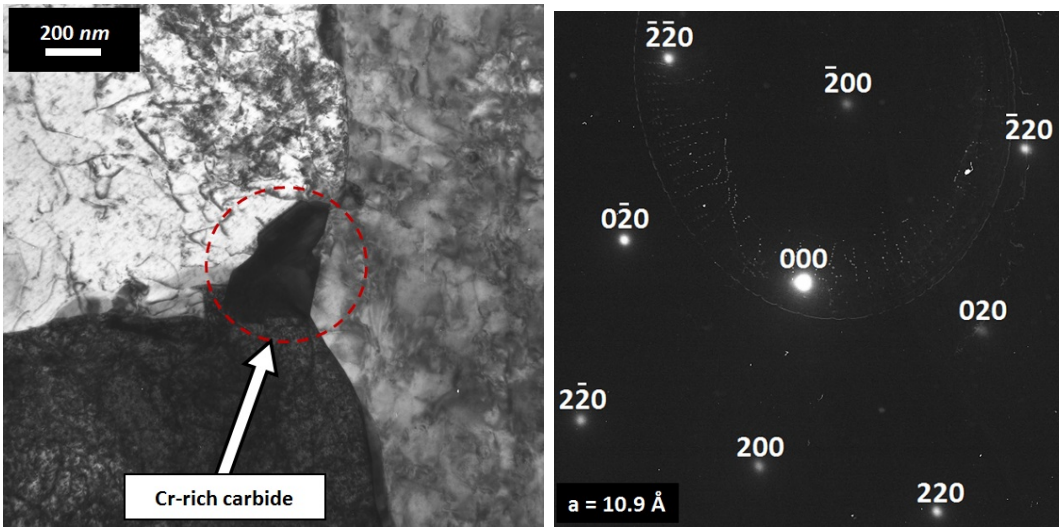

(a) **(b)**

Figure 5.32: TEM data from one of the Cr-rich particles in the weld metal in sample T, showing **(a)** a bright field image, and **(b)** an indexed SADP from the area circled in red in the image, corresponding to the FCC-[001] zone axis of $M_{23}C_6$.

compositions, is that they are Laves phase.

Closer analysis of the interfacial band by bright field and dark field imaging, shown in figure 5.33, reveals that the sawtooth-like features extending into the steel are in fact part of the band, as they share the same crystallographic orientation. Diffraction analysis indicates that the band is FCC in crystal structure (as opposed to the BCC band observed in sample A-W). The approximate composition of the band, as measured by STEM-EDX, is given in table 5.4. The steel away from the band is BCC and the weld metal is FCC, as was found in sample A-W.

Table 5.4: Approximate composition of the interfacial band in sample T, as measured by STEM-EDX.

	Element (wt %)							
	Cr	Fe	Mo	Nb	Ni	Si	V	W
Band	13.0	65.2	3.1	< 0.5	15.0	< 0.5	< 0.5	2.4
Uncertainties (±)	0.2	0.3	0.3	0.0	0.2	0.1	0.05	0.2

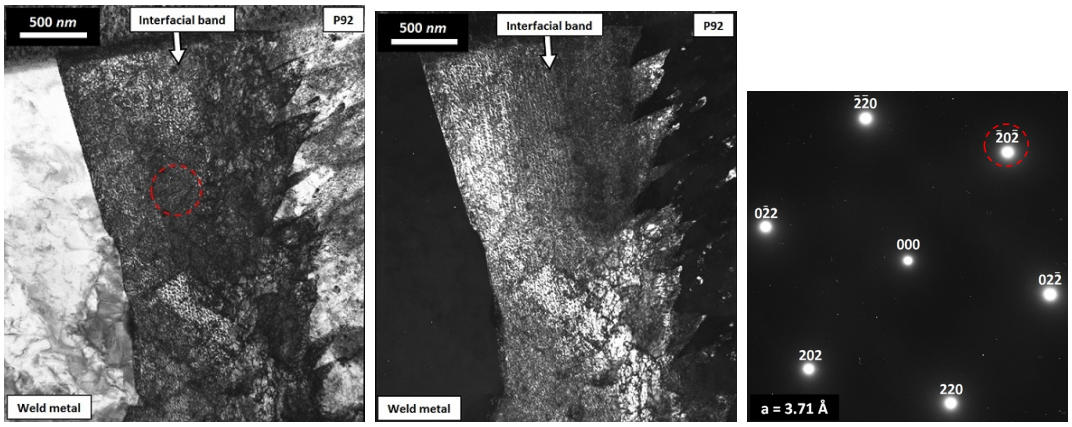

(a) **(b)** **(c)**

Figure 5.33: TEM data from the interfacial band in sample T, showing **(a)** a bright field image, **(b)** a dark field image, and **(c)** an indexed SADP from the interfacial band of the FCC-$[11\bar{1}]$ zone axis. The dark field image was taken with the aperture centred on the diffraction spot circled in red, and the pattern formed from the area circled in the bright field image.

5.8.3 Short Term Aged State

A TEM specimen was extracted from sample STA from the weld line area by FIB methods, as was done for previous samples. Bright and dark field STEM images of this specimen are shown in figure 5.34, while EDX maps are shown in figure 5.35. It should be noted that this specimen is not uniformly thick; the bottom half of the specimen is distinctly thicker than the top half, with a sudden step change in thickness appearing as a horizontal line around half way down the specimen. This increase in thickness affects the contrast of the electron images, and increases the EDX count rates. These changes should not be interpreted as real microstructural or chemical features.

The bright and dark field images reveal the steel to have a mixed microstructure. Much of the specimen contains tempered martensite laths, and a network of secondary phase particles. These features are to be expected from aged P92 steel. However, parts of the steel (notably the bottom left corner of figure 5.34(a)) are featureless in structure, with no laths or precipitates. This could correspond to either reformed α-ferrite or retained δ-ferrite. The weld metal contains a very

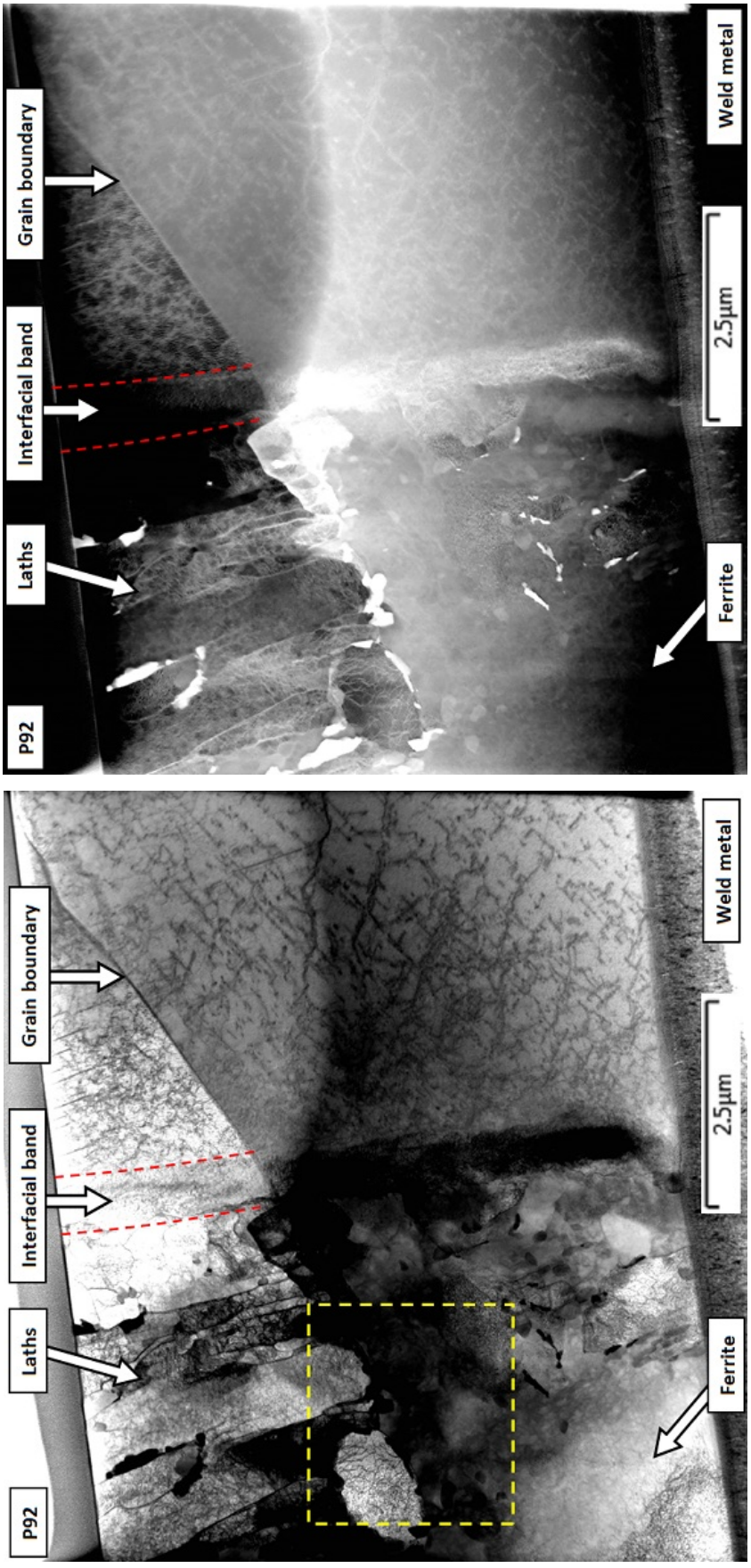

Figure 5.34: STEM images of the area around the weld line in sample STA. Figure **(a)** is in bright field mode, **(b)** in HAADF mode.

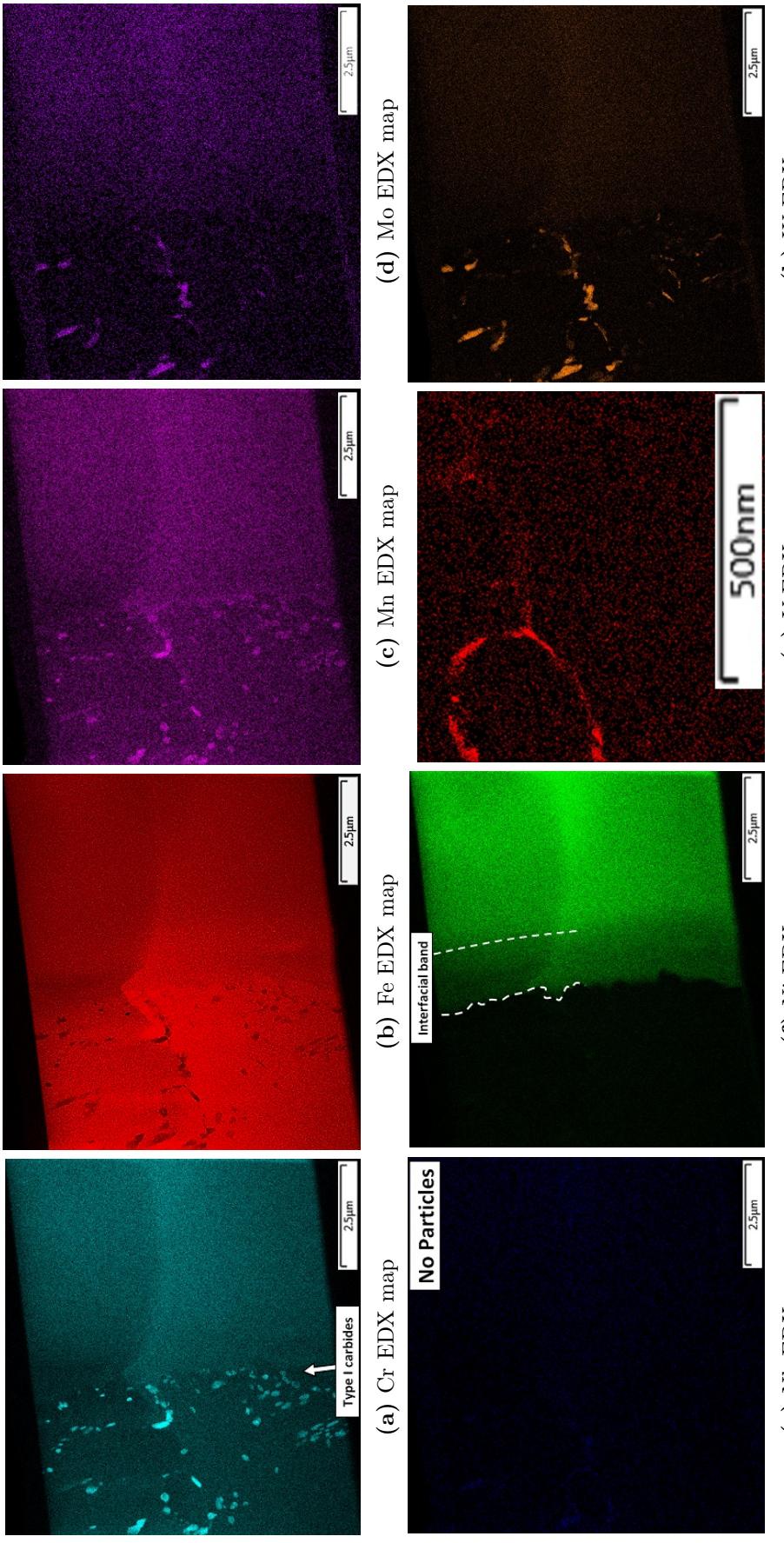

(a) Cr EDX map (b) Fe EDX map (c) Mn EDX map (d) Mo EDX map

(e) Nb EDX map (f) Ni EDX map (g) V EDX map (h) W EDX map

Figure 5.35: STEM-EDX maps of the area around the weld line in sample STA. Map **(g)** is zoomed in on the area in the yellow box in figure 5.34(a).

similar microstructure to those seen in previous cases. Two grains are visible, but there are no secondary phase particles.

The EDX maps reveal the chemical variations around the weld interface, in particular highlighting the distribution of precipitates in the steel. They occur in three distinct families:

- Cr-rich particles, many of which are concentrated in a band close (and parallel) to the weld interface. One such particle is shown in figure 5.36(a). These particles are, on average, 200 *nm* in diameter, and are typically circular (though some, especially the larger ones, are elongated and angular in shape). Diffraction analysis, shown in figure 5.36, confirms these particles to be FCC, with a lattice parameter of 10.6 Å; this is smaller than previous Cr-rich carbides, though still consistent with $M_{23}C_6$, as would be expected in P92 steel. They appear to contain small amounts of other elements, principally tungsten and molybdenum.

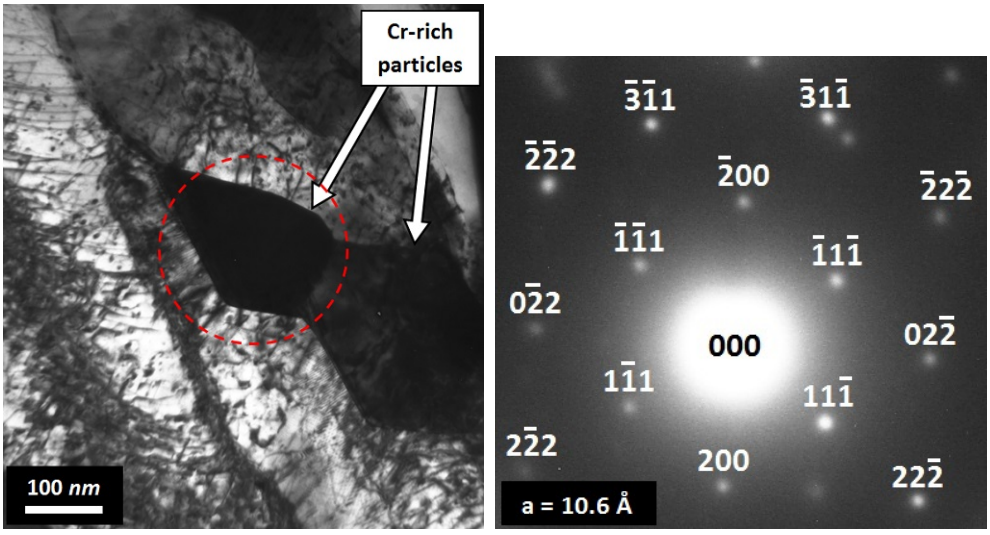

(a) **(b)**

Figure 5.36: TEM data from one of the Cr-rich particles in the weld metal in sample STA, showing **(a)** a bright field image, and **(b)** an indexed SADP from the circled area, corresponding to the FCC-[011] zone axis.

- W-rich particles, which are fewer in number than the Cr-rich particles. An example is shown in figure 5.37(a). These particles are all elongated in

shape, but show significant variation in size; the smallest are around 50 × 300 nm, while the largest are 150 × 600 nm. The direction of elongation generally appears to be along grain or lath boundaries. These particles are also distinctly enriched in Si and, to a lesser extent, Mo. No definitive diffraction data could be obtained from any of these particles (an example pattern, which could not be indexed, is shown in figure 5.37(b)), but based on their composition and the known phase behaviour of P92 they are highly likely to be Laves phase.

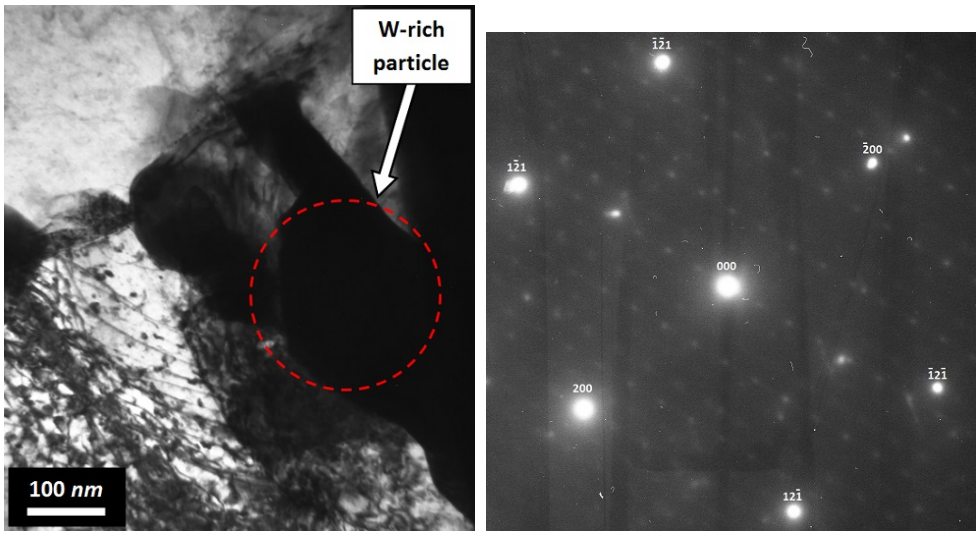

(a) **(b)**

Figure 5.37: TEM data from one of the W-rich particles in the weld metal in sample STA, showing **(a)** a bright field image, and **(b)** a SADP from the circled area, with indexed points corresponding to the metal matrix (zone axis BCC-[012]). The smaller diffraction spots, corresponding to the W-rich particle, cannot be indexed.

- V-rich particles, which are fewer still in number than either the Cr-rich or W-rich particles. The majority of these particles exist in a ring-like formation in the steel, away from the interfacial band; the ring also contains particles of the other two types. Additionally, some isolated particles exist in other areas of the steel. Based on the composition and small size of these particles, they are highly likely to be MX phase.

The compositions of these three precipitate types, as measured by STEM-

Table 5.5: Approximate compositions of the various types of particles and the interfacial band in sample STA, as measured by STEM-EDX. Note that the iron levels in the particles may be exaggerated due to overlap with the metal matrix. The levels of carbon and nitrogen are not quantified, and are instead categorised as strong (**S**) or weak (**W**) signals.

	Element (wt %)								
	C	Cr	Fe	Mo	N	Nb	Ni	V	W
Cr-rich particles	**S**	36.1	49.2	3.0	**W**	< 0.5	0.7	0.8	9.4
Uncertainties (±)	-	1.4	1.9	0.7	-	0.0	0.2	0.2	0.8
W-rich particles	**W**	12.2	46.5	6.5	**W**	< 0.5	< 0.5	< 0.5	33.5
Uncertainties (±)	-	1.0	3.3	1.9	-	0.0	0.0	0.2	2.6
V-rich particles	**S**	10.0	71.1	< 0.5	**S**	2.8	0.6	10.9	4.6
Uncertainties (±)	-	1.1	5.5	0.0	-	1.4	0.4	1.1	1.0
Interfacial band	**W**	11.3	69.3	2.1	**W**	< 0.5	13.6	< 0.5	2.6
Uncertainties (±)	-	0.2	0.4	0.3	-	0.1	0.2	0.05	0.3

EDX, are given in table 5.5. The EDX maps also reveal that the nickel composition undergoes two step changes, from a high level in the weld metal, to an intermediate level, to the low base level in the steel. This intermediate level corresponds to the interfacial band, which is similar here to that seen in sample A-W (i.e. it is smooth, as opposed to the sawtooth morphology observed in sample T).

The band has been investigated by conventional TEM analysis, as shown in figure 5.38, while its composition is given in table 5.5. This shows that the band, as in previous cases, is of distinct orientation to either alloy, while the diffraction pattern demonstrates that it is BCC in crystal structure. The band in this particular case is relatively narrow, at only 500 nm. It is interesting to note that the band is entirely precipitate-free, and the Cr-rich carbides are forming at the edge of it. This would indicate that these carbides are in fact examples of the 'type I' carbides previously observed in other DMW systems (as discussed in detail in section 2.2.3.3).

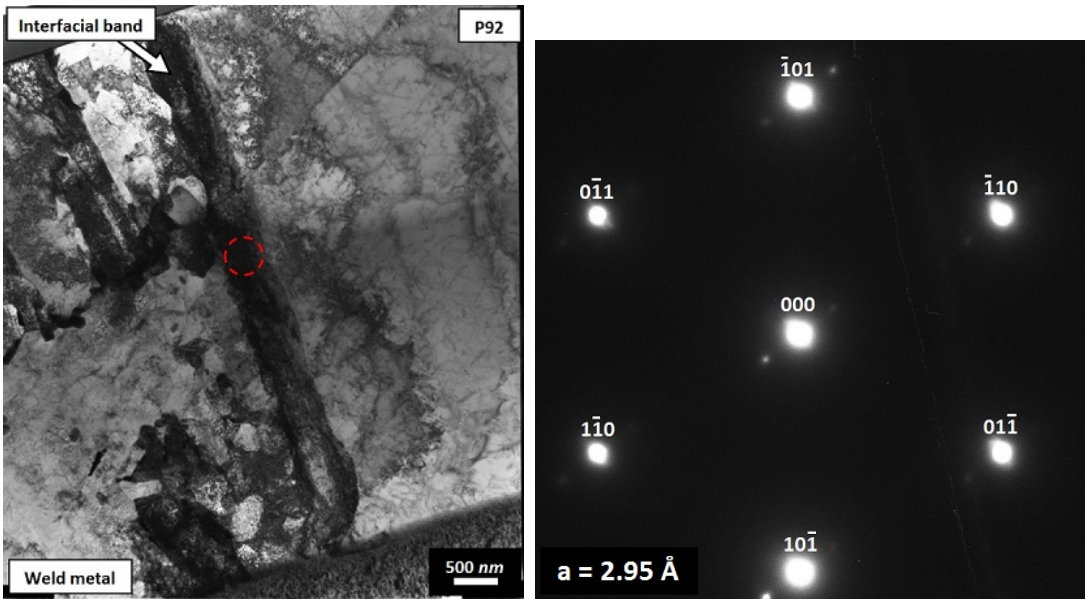

(a) **(b)**

Figure 5.38: TEM data from one of the interfacial band in sample STA, showing **(a)** a bright field image, and **(b)** an indexed SADP, from the circled area, of the BCC-[111] zone axis.

5.8.4 Long Term Aged State

A TEM specimen was extracted from across the weld line in sample LTA, in the now-familiar manner. A STEM bright field/dark field image pair is shown in figure 5.39, while EDX maps of the specimen are shown in figure 5.40. The microstructure of the steel appears to be predominantly tempered martensite, containing a network of secondary phases (including one anomalously large precipitate). There do not appear to be any areas of featureless ferrite, as were seen in sample STA. The weld metal appears to closely resemble those of the previous cases, with three visible grains; a notable difference from previous cases are the clusters of particles close to one of the grain boundaries. Separating the two metals appears to be a largely featureless interfacial band.

The EDX maps reveal the chemical variations around the weld interface, most notably the five visible types of particle: three in the steel, two in the weld metal. The compositions of these particles are given in table 5.6. The three particles in

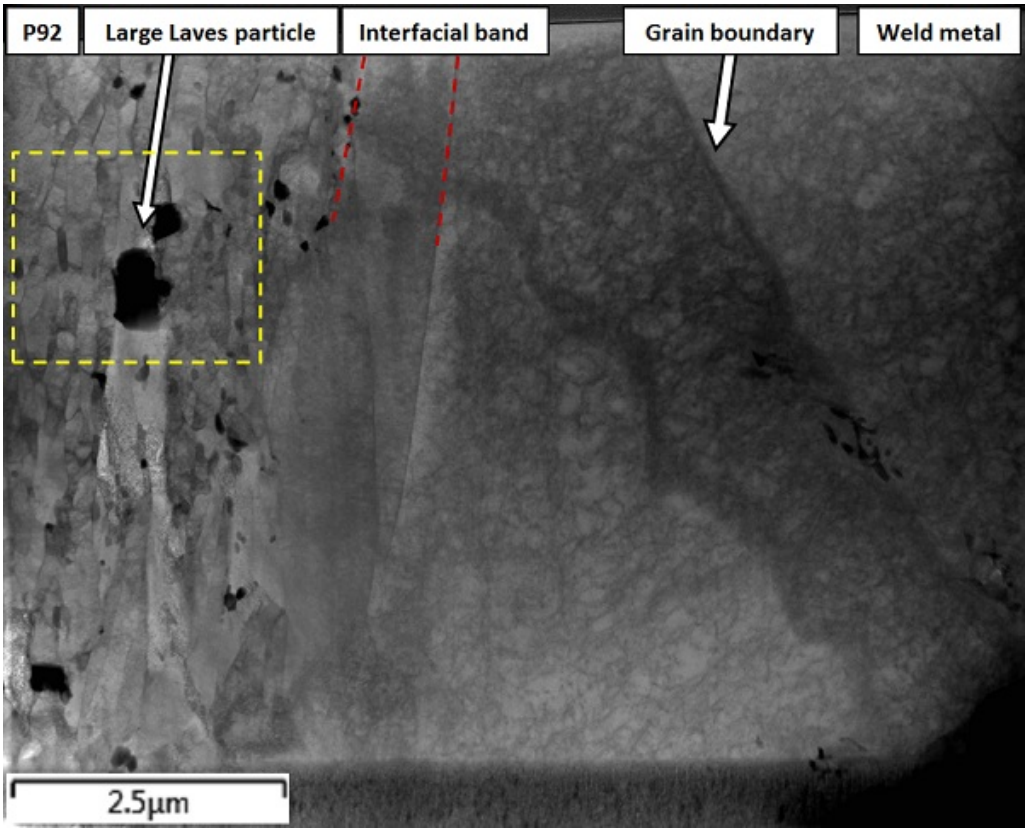

(a)

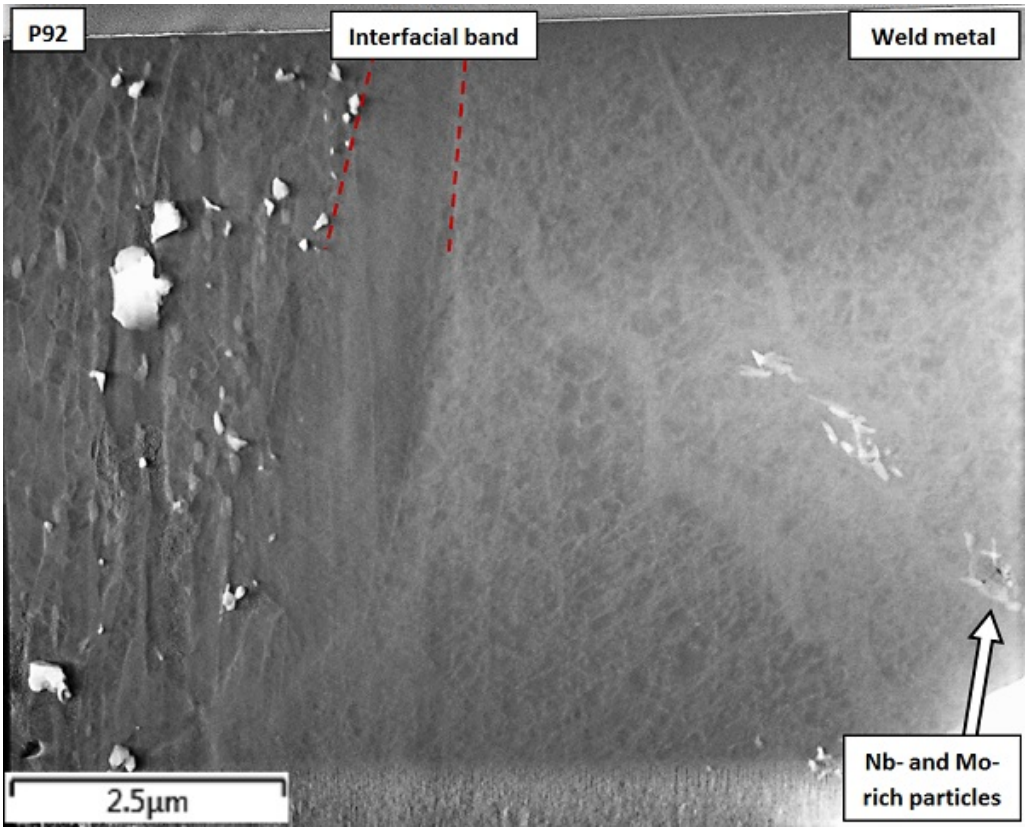

(b)

Figure 5.39: STEM images of the area around the weld line in sample LTA. Figure **(a)** was taken in bright field mode, **(b)** in dark field mode.

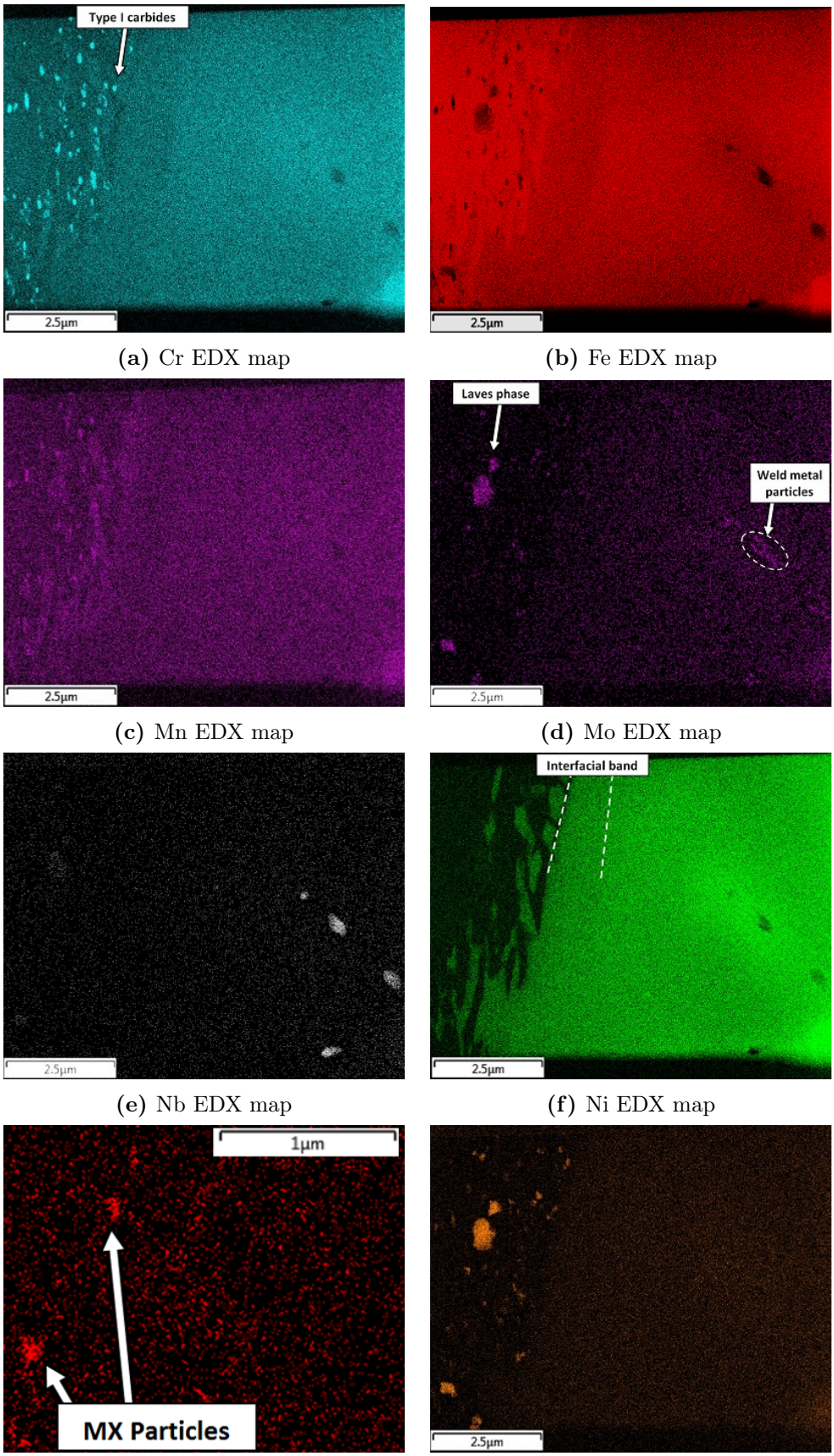

(a) Cr EDX map

(b) Fe EDX map

(c) Mn EDX map

(d) Mo EDX map

(e) Nb EDX map

(f) Ni EDX map

(g) V EDX map

(h) W EDX map

Figure 5.40: STEM-EDX maps of the area around the weld line in sample LTA. Map **(g)** is zoomed in on the area in the yellow box in figure 5.39(b).

Table 5.6: Approximate compositions of the various types of particles and the interfacial band in sample LTA, as measured by STEM-EDX. Note that the iron and/or nickel levels in the particles may be exaggerated due to overlap with the metal matrix. The levels of carbon and nitrogen are not quantified, and are instead categorised as strong (**S**) or weak (**W**) signals.

	Element (wt %)									
	C	Cr	Fe	Mo	N	Nb	Ni	Si	V	W
Cr-rich particles	**S**	31.9	53.1	4.3	**W**	< 0.5	1.5	< 0.5	0.5	8.3
Uncertainties (±)	-	1.7	2.6	1.1	-	0.4	0.3	0.0	0.2	1.0
W-rich particles	**W**	6.1	31.3	15.7	**W**	0.9	0.9	1.9	< 0.5	42.7
Uncertainties (±)	-	0.2	0.8	0.9	-	0.3	0.1	0.3	0.1	1.1
V-rich particles	**S**	9.5	75.1	< 0.5	**S**	2.6	2.2	1.3	5.6	3.6
Uncertainties (±)	-	1.2	5.8	0.0	-	1.3	0.5	0.6	0.8	1.1
Nb-rich particles	**S**	10.5	28.7	8.2	**S**	36.4	10.9	0.5	1.0	3.7
Uncertainties (±)	-	0.3	0.6	0.9	-	0.9	0.3	0.1	0.1	0.3
Mo-rich particles	**W**	13.4	49.5	11.1	**W**	1.6	17.9	1.7	< 0.5	4.8
Uncertainties (±)	-	1.2	2.9	2.7	-	1.4	1.5	0.6	0.0	1.7
Interfacial band	**W**	11.5	70.7	1.6	**W**	< 0.5	12.7	< 0.5	< 0.5	2.5
Uncertainties (±)	-	0.2	0.5	0.4	-	0.2	0.3	0.1	0.1	0.3

the steel, as in case STA, are:

- Cr-rich carbides, of very similar size, distribution and chemistry to those seen in sample STA. Diffraction analysis reveals them to be $M_{23}C_6$, like in sample STA; for brevity, SADPs for this case are not displayed. Again, some of the particles are precipitating along the edge of the interfacial band (i.e. as type I carbides), though not as distinctly as in sample STA.

- W-rich particles, which appear to be Laves phase. It is one of these particles that is the large precipitate seen in the STEM images (c. 800 μm in diameter); this is line line with prior SEM observations of Laves phase coarsening near the weld line. Even from this particularly large particle, no definitive diffraction data could be obtained. These particles also contain molybdenum and chromium, but very little carbon or nitrogen, supporting the conclusion that they are Laves phase.

- V-rich particles, which are again assumed to be MX-phase carbonitrides based on their size and composition. They are fewer in number in this

case than in sample STA, which may be taken as indication that they are dissolving.

In the weld metal, two distinct types of particle can be identified:

- Nb-rich particles, of which four are visible, with a blocky morphology and an average size of around 500 *nm*. TEM images and an SADP from one of these particles are shown in figure 5.41. They are all on, or extremely close to, grain boundaries. By a combination of EDX and SADPs, they are found to be carbonitrides of form Nb(C,N).

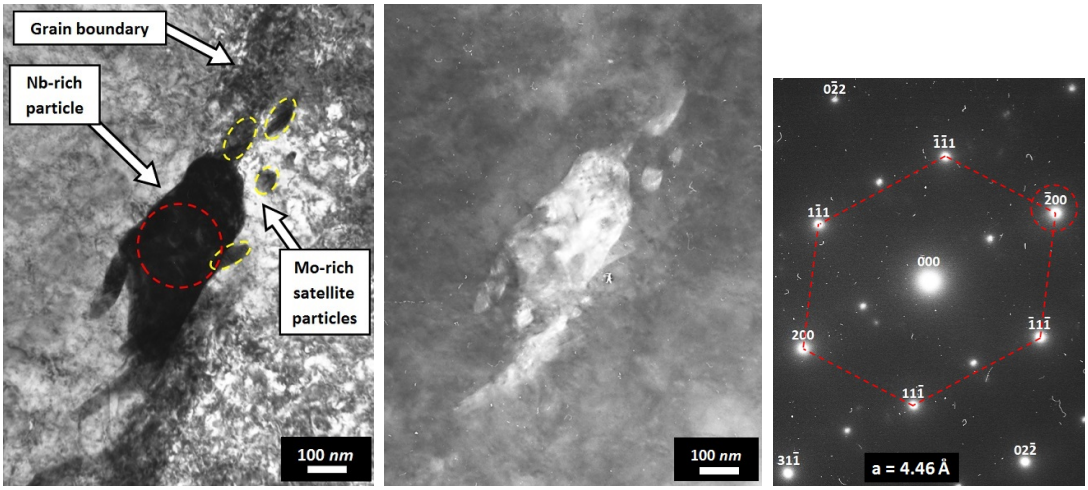

(a) **(b)** **(c)**

Figure 5.41: TEM data from one of the Nb-rich particles in the weld metal in sample LTA, showing **(a)** a bright field image, and **(b)** a dark field image, and **(c)** an indexed SADP, corresponding to the FCC-[011] zone axis of the particle. The spots that contribute to the pattern are labelled and marked with red lines; the smaller unmarked spots cannot be indexed, and are believed to correspond to double diffraction events. The dark field image in **(b)** was constructed from the circled diffraction spot in **(c)**, while the pattern was formed from the area circled in red in **(a)**.

- Mo-rich particles, which appear as satellites around the Nb-rich particles. They are up to 200 *nm* in size, and mostly elongated in seemingly random directions. They are too small to identify via SADPs, and overlap with the metal matrix and the Nb-rich particles has made EDX analysis problematic. The relatively weak signals for carbon and nitrogen in the EDX spectra

from these particles indicates that they may be intermetallics, or a metal-rich carbide such as M_6C.

The interfacial band, as in other cases, has been analysed by STEM-EDX, as well as conventional TEM methods. Its measured composition is given in table 5.4. It is found by electron diffraction to be BCC in crystal structure, and of distinctly different orientation to the base metals, as shown in figure 5.42. It varies in width, but is on average around 2 μm wide. The interface between the band and the steel is not especially smooth in this case; it does not have a sawtooth-like morphology, as was seen in sample T, but rather it has a 'patchy' morphology (which can be seen in the Ni EDX map in figure 5.40(f)). The lack of a single smooth interface may explain the relative lack of type I carbides in this specimen. The few type I carbides that are visible are best seen in figure 5.40(a).

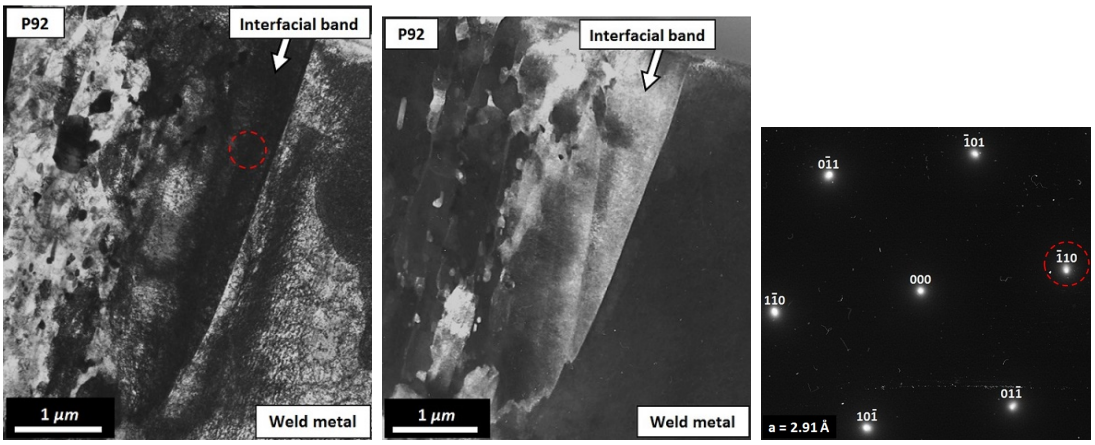

(a) **(b)** **(c)**

Figure 5.42: TEM data from the interfacial band in sample LTA, showing **(a)** a bright field image, and **(b)** a dark field image, and **(c)** an indexed SADP, corresponding to the BCC-[111] zone axis. The diffraction spot circled in red was used to form the dark field image, while the pattern was formed from the area circled in the bright field image.

5.9 Summary

In summary of this chapter, the following key results have been found:

- The P92 steel is found to have a characteristic martensitic structure. A heat-affected zone is observed near the weld, which is tempered but not entirely removed by heat treatments at 760 $°C$ and 625 $°C$. Areas of δ-ferrite have been observed within 50 μm of the weld interface.

- The weld metal is found to have a columnar-dendritic microstructure, and is heavily diluted with iron (up to 30 wt%). Adjacent to the weld interface is a PMZ, through which composition varies smoothly between that of the diluted weld metal and the steel.

- TEM analysis has revealed a band at the weld interface, up to 2 μm in width, of different orientation and composition to either alloy. It is present in the as-welded condition and all aged states.

- The aged P92 is found to contain $M_{23}C_6$ carbides, MX carbonitrides and Laves phase particles, in line with its known properties. No evidence for the existence of modified Z-phase has been found.

- The weld metal is found to have hardened significantly during long-term ageing. This is likely due to the formation of needle-like particles, corresponding to γ'' or δ-phase.

- The steel near the weld line shows a reduced number of carbide and carbonitride particles after ageing treatments. This area is the CDZ, which results from carbon diffusion to the weld metal. Particularly large Laves phase particles are observed in this area.

- The weld metal near the weld line contains a higher density of vein-like features than the bulk after ageing. The veins may be serving as pathways for diffusion. This area is the CEZ.

- Some particles are found to be forming along the weld line after ageing, many of which may be type I carbides.

Chapter 6

Thermo-kinetic Simulations of the P92 – Alloy 625 System

This chapter is dedicated to the results of the computational investigation of the P92 – Alloy 625 weld system, based on the alloy conditions and heat treatments that were reported on experimentally in chapter 5. Thermodynamic simulations were performed using the *Thermo-Calc* Windows software package (version 5.0.4.75), and kinetic simulations using the *DICTRA* software package (version 27.0.1). Some of the theory and mathematics underpinning these computational tools were described in chapter 3. The implications of the data presented here, in the context of the experimental results presented in the previous chapter, will be discussed in chapter 7.

6.1 Phase Equilibria

6.1.1 P92 Steel

Thermodynamic calculations in *Thermo-Calc* have, in the first instance, been performed on the two alloys in question at their nominal compositions. This has been done for the P92 steel, using the TCFE7 database and the composition given in table 6.1. Boron has been excluded from the calculations, since it does not follow the known behaviour (i.e. in actuality it is taken up by the $M_{23}C_6$ carbides, whereas *Thermo-Calc* predicts it to form new phases such as Cr_2B and BN). Additionally, the modified Z-phase has been suspended, since the experimental investigation found no evidence for its formation. This indicates that, while it may be an equilibrium phase, the kinetics of its formation are so sluggish that it cannot form during the present exposure (consistent with the published literature on 9%Cr steels).

Table 6.1: Table of chemical compositions and activities of the various components in nominal P92 steel at 625 $°C$, as calculated by *Thermo-Calc* using the TCFE7 database.

Component	Amount / wt%	Activity
C	0.07	2.72×10^{-4}
Cr	9.0	5.98×10^{-3}
Fe	bal.	7.66×10^{-3}
Mn	0.4	4.46×10^{-5}
Mo	0.5	3.31×10^{-4}
N	0.04	5.59×10^{-10}
Nb	0.05	1.76×10^{-8}
V	0.2	3.20×10^{-7}
W	1.76	1.18×10^{-3}

The P92 system, at 625 $°C$, is found to comprise the following four phases (the constitutions of which are given in table 6.2):

1. BCC matrix, consisting of mostly iron. at a mole fraction of 0.970.

2. $M_{23}C_6$ carbide, rich in chromium, at a mole fraction of 0.0155.

3. MX carbonitride, rich in vanadium, at a mole fraction of 0.00352.

4. Laves phase, rich in tungsten, at a mole fraction of 0.0106.

Table 6.2: Calculated compositions of the four equilibrium phases in P92 steel at 625 $°C$, as calculated by *Thermo-Calc* using the TCFE7 database. Figures are in wt%, with respect to the total weight of the phase in question.

	Element (wt %)								
	C	Cr	Fe	Mn	Mo	N	Nb	V	W
BCC Matrix	0.0	8.34	90.2	0.46	0.20	0.0	0.001	0.048	0.74
$M_{23}C_6$	5.05	61.5	12.9	0.20	14.3	0.0	0.0	0.85	5.24
MX	0.56	0.70	0.026	0.0	0.011	17.3	19.9	61.5	0.0
Laves phase	0.0	5.64	33.7	0.089	5.23	0.0	0.17	0.0	55.2

The software calculates only fractions of the phases (in terms of moles or mass), not the size or distribution of individual particles. The results are qualitatively consistent with the present experimental findings, which are based on volume fraction. As the experimental samples were quench cooled after their heat treatments, the phase balance at 625 $°C$ should have been largely preserved.

The variation of phase fractions as a function of temperature has been calculated, with the results plotted in figure 6.1. This demonstrates aspects of the behaviour of the system, most obviously the start and finish temperatures for austenite formation, A_{e1} = 833 $°C$ and A_{e3} = 921 $°C$. Also calculated are the start and finish temperatures for δ-ferrite formation, being 1138 $°C$ and 1396 $°C$ respectively. Melting occurs over a range of 1460 $°C$ to 1510 $°C$.

The precipitation behaviour as a function of temperature is also predicted in figure 6.1. Firstly, the $M_{23}C_6$ phase level is shown to slowly decrease as temperature increases, dropping to a mole fraction of 0.014 at the A_{e1} temperature. Past this temperature it rapidly dissolves, having disappeared completely at 880 $°C$. The MX carbonitride phase is more stable, maintaining a constant level up to the A_{e1} temperature, then dissolving more slowly beyond this point, finally disappearing at 1177 $°C$. The Laves phase is the least stable of the three, its mole fraction

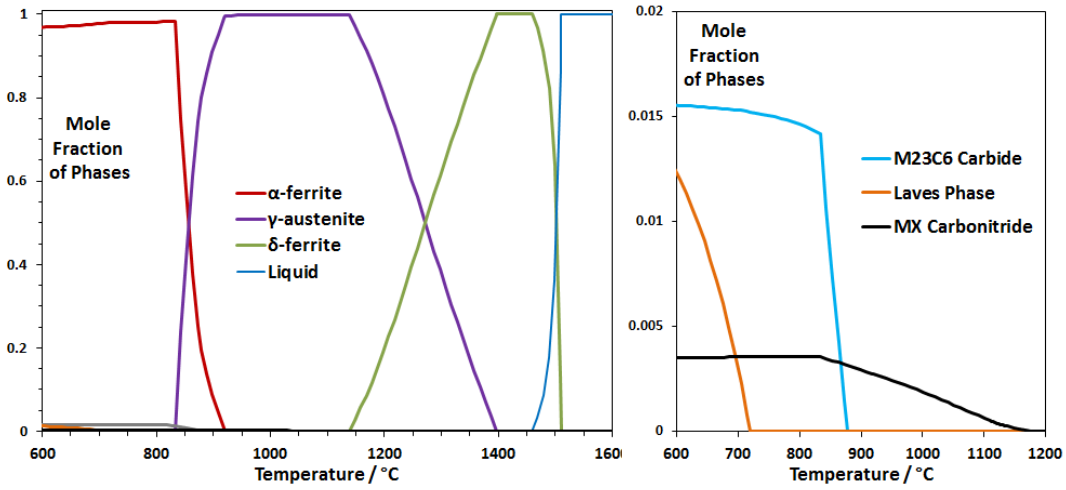

(a) **(b)**

FIGURE 6.1: A plot of phase fraction as a function of temperature for nominal composition P92 steel, as calculated by *Thermo-Calc* using the TCFE7 database, showing **(a)** matrix and liquid phases, and **(b)** secondary phases.

dropping to zero at 720 $°C$ (which explains why it is not observed in the tempered or as-received states).

The thermodynamic activity of each of the components in the nominal P92 system has also been calculated by *Thermo-Calc*, the results of which are presented in table 6.1. Activity is a quantity related to chemical potential by the following relation:

$$A_i = \exp\left(\frac{\mu_i - \mu_i^\star}{RT}\right) \tag{6.1}$$

where $\mu_i^\star$ is the chemical potential of species i under standard reference conditions, i.e. when the mixture is composed entirely of species i. It can hence be seen that a pure substance has an activity of 1. Activity is used as an indicator of the driving force for diffusion (which will happen from areas of high activity to areas of lower activity) in complex systems.

The analysis of nominal P92 steel is useful for reference purposes, though of more importance is the behaviour that takes place as the steel is affected by external factors, most pertinently by diffusion. As has been shown in chapter 5,

the steel immediately adjacent to the weld line will lose some carbon and nitrogen to the adjoining weld metal during the various heat treatments. It is therefore important to determine how the loss of these elements affects the phase balance of the steel.

The most immediate and intuitive consequence of a reduction in carbon and nitrogen levels is that the equilibrium fraction of carbide and carbonitride phases decreases; after reducing the levels of these elements by half, as shown in figure 6.2, the mole fractions of $M_{23}C_6$ and MX have decreased by 46% and 49% respectively (at 625 $°C$). Reducing the levels to zero eliminates these phases entirely.

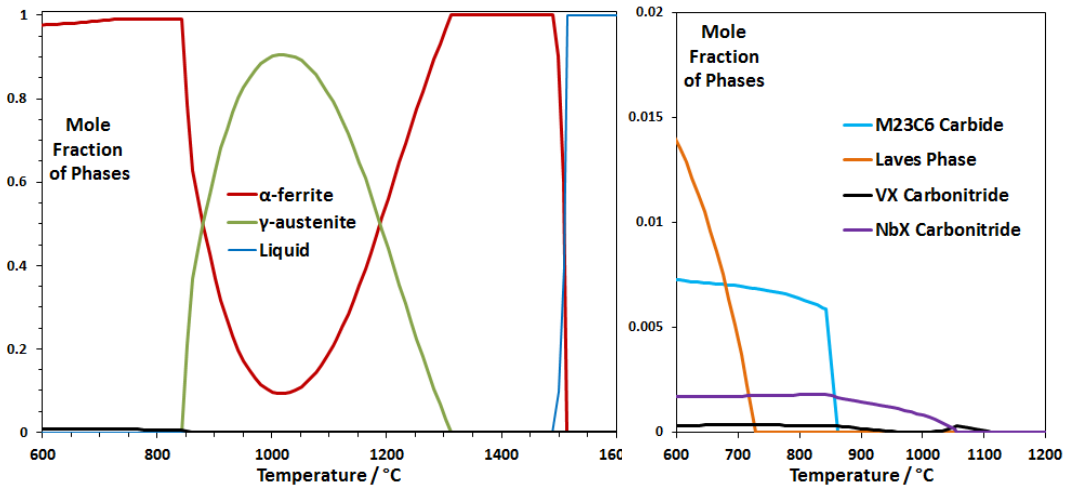

(a) **(b)**

FIGURE 6.2: Simulated phase behaviour as a function of temperature of P92 steel with carbon and nitrogen levels at half of their nominal levels, as calculated by *Thermo-Calc* using the TCFE7 database, showing **(a)** matrix phase fractions, and **(b)** secondary phase fractions.

Reducing the carbon and nitrogen levels acts to stabilise the Laves phase to some extent. With their levels at half, the amount of Laves phase at 625 $°C$ has increased by 14 %, and exists up to 730 $°C$. This may be understood in terms of increased availability of carbide-forming elements. Additionally, the MX carbonitride phase is split into two families in this condition: V(C,N) and Nb(C,N). The latter phase exists at a greater volume fraction at all temperatures below 1055 $°C$, at which point it dissolves while the former phase dissolves at 1120 $°C$.

Another change resulting from reduced carbon and nitrogen levels is that the ferrite phase is stabilised to higher temperatures. Again considering halved carbon and nitrogen content, the A_{e1} temperature has increased to 843 $°C$. The steel never fully transforms to γ-austenite, reaching a peak mole fraction of 0.9 at 1015 $°C$, meaning that there is no A_{e3} temperature and no explicit change between α- and δ-ferrite. The melting range is also reduced, now taking place from 1489 $°C$ to 1515 $°C$.

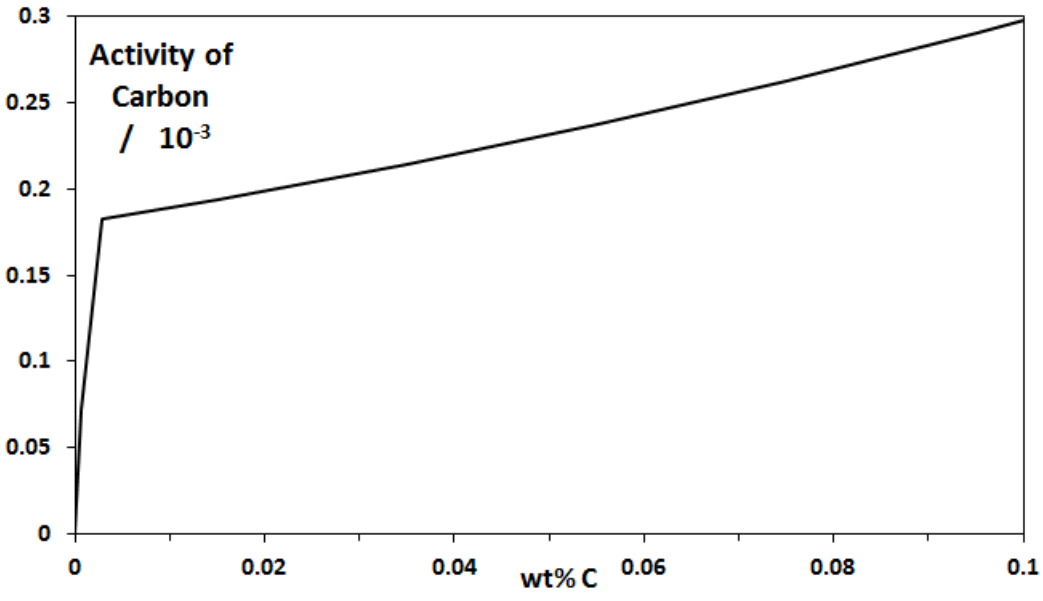

Figure 6.3: A plot of carbon activity as a function of carbon concentration for P92 steel at 625 $°C$, as calculated by *Thermo-Calc* using the TCFE7 database.

Reducing the levels of C and N also causes the activities of these elements to decrease. Taking carbon as an example, as shown in figure 6.3, from its base level of 2.42×10^{-4} at 0.07 wt%, it falls to 2.27×10^{-4} at half this level. It keeps falling at much the same rate down to 0.001 wt%, at which point it drops dramatically (not coincidentally, this point corresponds to the level at which $M_{23}C_6$ dissolves completely). Nitrogen activity behaves in a similar manner. This effect will act to reduce the diffusion driving forces as carbon and nitrogen diffuse away.

6.1.2 Alloy 625

The thermodynamics of a simplified version of Alloy 625 (i.e. with aluminium and titanium levels set to zero) has been calculated at 625 $^{\circ}C$ using the TTNI7 bespoke nickel alloys database with all possible phases enabled. The full chemical composition used for this calculation is given in table 6.3. The equilibrium phases, the compositions of which are given in table 6.4, are found to be as follows:

1. FCC matrix, consisting primarily of nickel and chromium. This phase occupies a mole fraction of 0.78.

2. δ-phase, of the form Ni_3Nb, at a mole fraction of 0.096.

3. $M_{23}C_6$ carbide, rich in chromium, at a mole fraction of 0.0239.

4. μ-phase, which contains molybdenum, chromium, nickel, and occupies a mole fraction of 0.0997. It is known to have sluggish formation kinetics, and hence may not be present in real systems. If this phase is suspended from calculations, it is replaced by σ-phase of similar chemistry.

Table 6.3: Table of chemical compositions and activities of the various components in nominal Alloy 625 at 625 $^{\circ}C$, as calculated by *Thermo-Calc* using the TTNI7 database.

Component	Amount / wt%	Activity
C	0.1	1.42×10^{-5}
Cr	21.0	1.28×10^{-2}
Fe	4.0	4.17×10^{-4}
Mn	0.4	5.06×10^{-7}
Mo	9	2.51×10^{-3}
Nb	4	6.98×10^{-8}
Ni	Bal.	2.23×10^{-3}
Si	0.15	1.45×10^{-11}

Performing this calculation with aluminium and titanium enabled results in an additional phase, Ni_3Ti (i.e. γ'') being formed at a small mole fraction (c. 0.006) at the expense of matrix phase. This phase is not especially stable, dissolving at 680

Table 6.4: Calculated compositions of the four equilibrium phases in nominal Alloy 625 at 625 $°C$, as calculated by *Thermo-Calc* using the TTNI7 database. Figures are in wt%, with respect to the total weight of the phase in question.

	Element (wt %)							
	C	Cr	Fe	Mn	Mo	Nb	Ni	Si
FCC Matrix	0.0	23.0	5.17	0.40	3.92	0.68	66.4	0.40
$M_{23}C_6$	5.13	69.8	0.33	0.0	20.1	0.0	4.59	0.0
δ-phase	0.0	0.14	0.047	0.0	2.31	32.3	65.2	0.0
μ-phase	0.0	24.8	0.72	0.0	47.2	0.014	27.2	0.0

$°C$. These components have hence been omitted from calculations for simplicity. Neither Laves phase nor NbC, two phases that are known to form on dendritic solidification of Alloy 625 [58], are predicted to be present in this equilibrium state at 625 $°C$, confirming that the dendritic structure is a non-equilibrium state.

A plot of phase fraction as a function of temperature for the nominal Alloy 625 is shown in figure 6.4, illustrating the rather complex secondary phase behaviour. Of the phases present at 625 $°C$ (listed above), $M_{23}C_6$ carbide and μ-phase are the first to dissolve, doing so at 820 $°C$. The former is replaced at this point by M_6C carbide. The δ-phase is next to dissolve, at 930 $°C$; it is replaced by Nb-rich MC carbide. M_6C carbide dissolves at 1110 $°C$, followed by MC carbide at 1265 $°C$. Melting begins at 1250 $°C$ and ends at 1335 $°C$. No allotropic phase transformation of the matrix is predicted in this alloy; it is FCC over the entire temperature range.

As was done for the P92 system, the activities of the various components in the nominal Alloy 625 system have been calculated, with the results presented in table 6.3. The differences in activity between these and those of P92 will give rise to diffusion driving forces. As there is nominally no nitrogen in Alloy 625, the activity of it is likely to be extremely low.

The equilibrium calculations of Alloy 625 are in many ways less useful than those presented for P92, since the Alloy 625 is far more significantly affected by the welding process. It is diluted with iron, to an extent which varies with position; iron levels are greater in the first weld bead than in subsequent beads, and

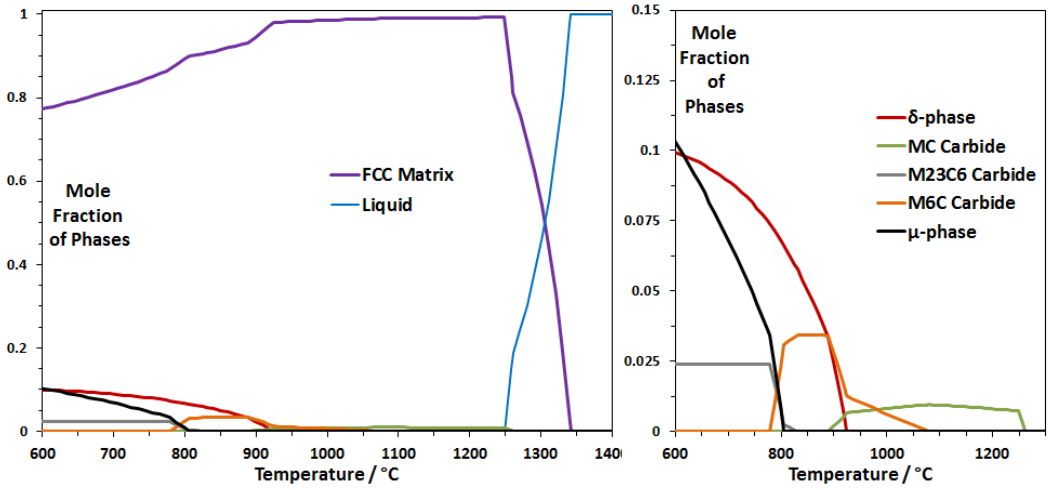

(a) **(b)**

FIGURE 6.4: A plot of phase fraction as a function of temperature for nominal composition Alloy 625, as calculated by *Thermo-Calc* using the TTNI7 database, showing **(a)** matrix and liquid phases, and **(b)** secondary phases.

greater still in the PMZ. Calculations of heavily iron-enriched Alloy 625 must be interpreted with care, as they may be outside the validated range of the TTNI7 database; as such, the same calculations have also been performed using the general alloys database (SSOL5), with any major discrepancies noted.

The effect of increasing the iron level up to 70 wt% at 625 $°C$ is shown in figure 6.5(a). The ratios of other elements in the system were held constant, so that their levels all decreased proportionately as the iron level increased, in the manner described by the following equations:

$$W_{Ni} = 2.8W_{Cr} \tag{6.2}$$

$$W_{Ni} = 6.67W_{Mo} \tag{6.3}$$

$$W_{Ni} = 15W_{Nb} \tag{6.4}$$

where W_i are the masses of the various components. The results of these calculations indicate that the equilibrium phase balance is broadly unchanged up to 17 wt% of iron, at which point μ-phase is replaced by Laves phase of similar

chemistry. The level of δ-phase steadily decreases as iron level is increased, while $M_{23}C_6$ carbide is replaced by MC carbide at around 28 wt% of iron.

Shown in figure 6.5(b) is a phase fraction plot of the system as a function of temperature at a fixed iron level of 50 wt%, as may be found in the PMZ of a weld. This figure, in contrast with the nominal phase behaviour displayed in figure 6.4, indicates that Nb-rich MC carbide is the only stable carbide. The Ni_3Nb δ-phase still exists, but only up to 655 $°C$. Laves phase is also predicted to exist, slowly reducing in quantity up to 1045 $°C$. Finally, the melting range is higher in this case, beginning at 1265 $°C$ and ending at 1380 $°C$.

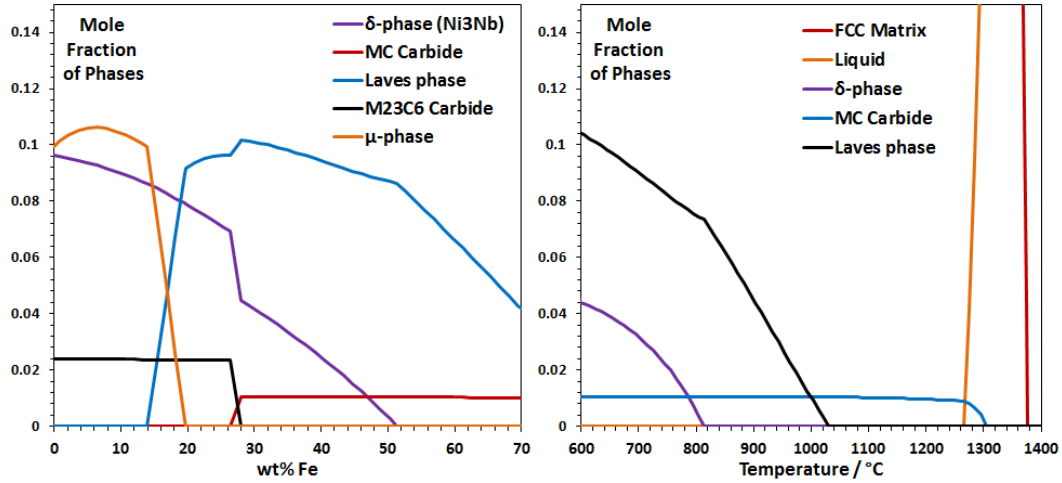

(a) **(b)**

FIGURE 6.5: Simulated thermodynamic behaviour of iron-diluted Alloy 625, with the nominal ratios of other elements held constant, as calculated by *Thermo-Calc* using the TTNI7 database. The graphs are **(a)** phase fractions as a function of iron content at 625 $°C$, and **(b)** phase fractions as a function of temperature at a fixed iron level of 50 wt%.

The activity of carbon as a function of iron level has also been predicted, and is shown in figure 6.6(a). This shows that activity increases steadily from a nominal level of 1.42×10^{-5} to a peak of 3.0×10^{-5} at 27 wt% of iron. It is then predicted to decrease as a function of increasing iron level, reaching a minimum of 4.9×10^{-6} at 53 wt% of iron, before slowly increasing again. However, this activity behaviour may not be entirely accurate, as the SSOL5 general alloys database, which has been largely in agreement with TTNI7 thus far with regards to phase

balance, predicts a steady increase in carbon activity over the same composition range, up to a peak of 4.2×10^{-4} at 70 wt% of iron. These data must therefore be interpreted with caution.

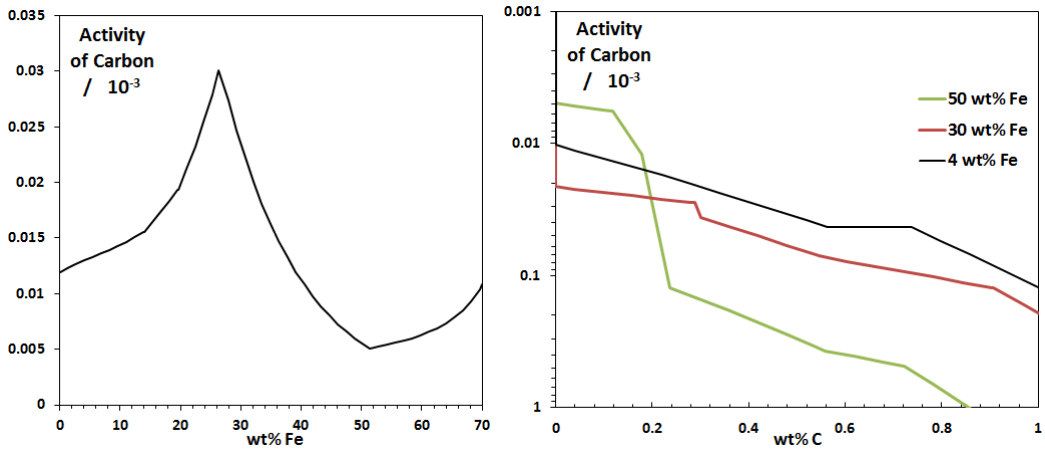

Figure 6.6: Simulated activities in nominal and iron-diluted Alloy 625 at 625 $°C$, with the nominal ratios of other elements held constant, as calculated by *Thermo-Calc* using the TTNI7 database. The graphs are **(a)** carbon activity on a base-10 log as a function of iron level, and **(b)** carbon activities as a function of carbon level in nominal Alloy 625 and Alloy 625 diluted with 30 wt% Fe and 50 wt% Fe.

Also important is the activity of carbon as a function of carbon level, as this will determine the maximum level of enrichment which can occur before an equilibrium is reached. These plots are shown in figure 6.6(b) for three cases: nominal Alloy 625, and Alloy 625 diluted with 30 and 50 wt% iron (as may be found in the diluted weld metal and PMZ respectively). This shows that carbon activity in the diluted case is higher at most points in cases of higher iron level, except below 0.18 wt% of carbon where activity in the 50 wt% diluted case is slightly lower than others. The SSOL5 database predicts a similar trend, only the activities in the diluted cases are higher at all carbon levels.

The fact that carbon activity is generally higher in the iron diluted cases has an important implication for diffusion behaviour, as it means that an equilibrium between the P92 steel and diluted Alloy 625 will be met with less carbon in the latter alloy than in the undiluted case. In other words, the diluted Alloy 625

would be in equilibrium with the P92 at a carbon level of 0.47 wt%, while the nominal case would be in equilibrium at a carbon level of 1.1 wt%. This means that less diffusion will occur across the interface than may have been expected between nominal alloys.

6.2 Diffusion Calculations

In this section the results of diffusion calculations for the various heat treatments, performed using the *DICTRA* software, are presented. Simulations were performed using the homogenisation model, with the upper Weiner rule for calculating effective mobilities and the fully implicit numerical integration scheme.

For these simulations, a grid containing 62 segments was employed. The spacings between them were custom-defined, such that they were spaced close together around the weld line region (a maximum of 1 μm apart), and further apart away from the weld line so as so minimise computational time. The grid represented a total spatial extent of 10 mm. The spacings in the section of the grid around the weld line can be seen in figure 6.7. The maximum size of the time step was limited to a thousandth of the total simulation time so as to optimise the convergence of results.

The initial conditions for the simulations were based on the EDX-measured composition profiles across the weld line, as shown in figure 5.11(c) (the importance of doing this, with regards to carbon activity in the diluted weld metal, having been demonstrated in figure 6.6(b)). Initial composition profiles for major elements (iron, chromium, nickel and molybdenum) are shown in figure 6.7. The initial levels of carbon in the two alloys were taken to be the nominal levels, which, based on the low-voltage EDX results in figure 5.23(a), appears to be a reasonable assumption. As such, the P92 steel was defined to contain 0.07 wt% of carbon, and the weld metal 0.1 wt%.

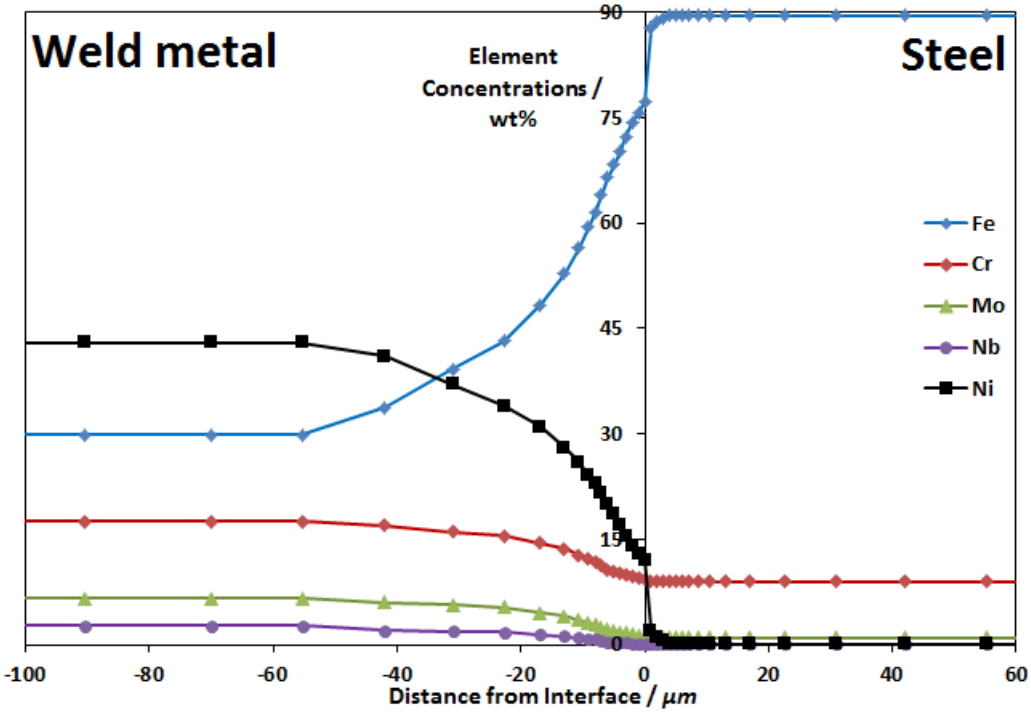

Figure 6.7: A plot of the initial composition variation (excluding carbon, silicon and manganese) used in the *DICTRA* simulation of sample T, based on the EDX-measured compositions from figure 5.11(c). Each plotted symbol on the lines represents a single grid segment.

A slightly simplified version of the P92 – Alloy 625 system was modelled, as was done for the thermodynamic calculations. The elements included were therefore C, Cr, Fe, Mn, Mo, N, Nb, Ni, Si, V and W, and the phases included were the BCC matrix, δ-phase (Ni_3Nb), FCC matrix, Laves phase, MC carbide, $M_{23}C_6$ carbide and M_6C carbide.

Of the phases included, the BCC matrix, $M_{23}C_6$ carbide and Laves phase were described by thermodynamic data called from the TCFE7 database. Thermodynamic data for the remainder of the phases were called from the TTNI7 database. Mobility data for the two matrix phases were called from the MOB2 database.

6.2.1 Tempering

The first simulation to be performed was that of the tempering PWHT (2 hours at 760 $°C$), using the concentration profiles for major elements given in figure 6.7, and step profiles for the concentrations of minor elements. Selected results of this

simulation are shown in figures 6.8 and 6.10.

Figure 6.8 shows that carbon diffusion is predicted to take place from the steel to the weld metal. This leaves a CDZ in the steel, the total width of which is between 100 and 150 μm. Of this zone, the area immediately adjacent to the interface is decarburised to a minimum level of approximately 0.0047 wt%. Conversely, carbon enrichment in the weld metal is predicted. The peak level of enrichment is 0.38 wt% at a distance of 12 μm from the interface, and the total width of the CEZ is approximately 30 μm. Also illustrated is the fact that the computational method is providing self-consistent results by obeying mass balance laws; this is shown by the fact that the integrated areas of the CEZ and CDZ are the same (approximately 3.7 μm.wt% in both cases).

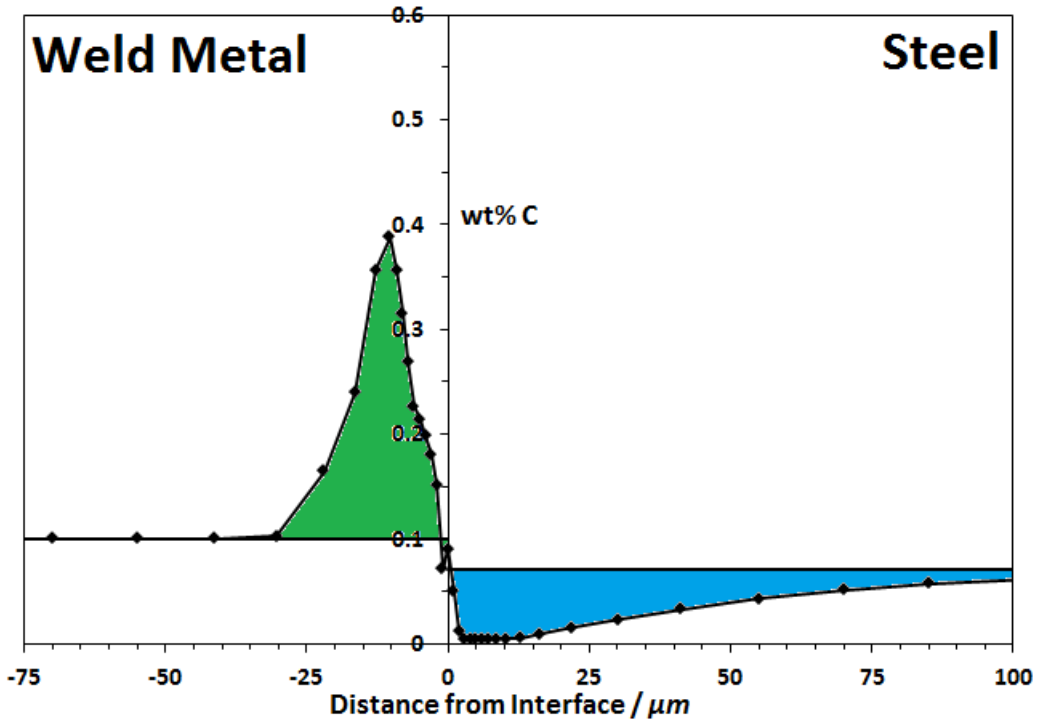

Figure 6.8: Results of kinetic simulations of the evolution experienced during the heat treatment of sample T, as calculated using *DICTRA*, showing the variation in carbon level across the interface. The horizontal black lines represent the initial carbon levels in the two alloys. The integrated areas of the CDZ and CEZ are highlighted in blue and green respectively, and are both approximately 3.7 μm.wt%.

Shown in figure 6.9 are the predictions of nitrogen diffusion during the tempering treatment. Like carbon, nitrogen is predicted to diffuse from the steel to

the weld metal. This leaves a depleted area in the steel, with a minimum level of c. 0.03 wt% adjacent to the weld line, and an enriched area in the weld metal, with a peak level of 0.02 wt% at a distance of 20 μm from the weld line. The amount of nitrogen that has diffused is less than the equivalent amount of carbon, as the integrated areas of the enriched and denuded zones are approximately 0.35 μm.wt% in this case.

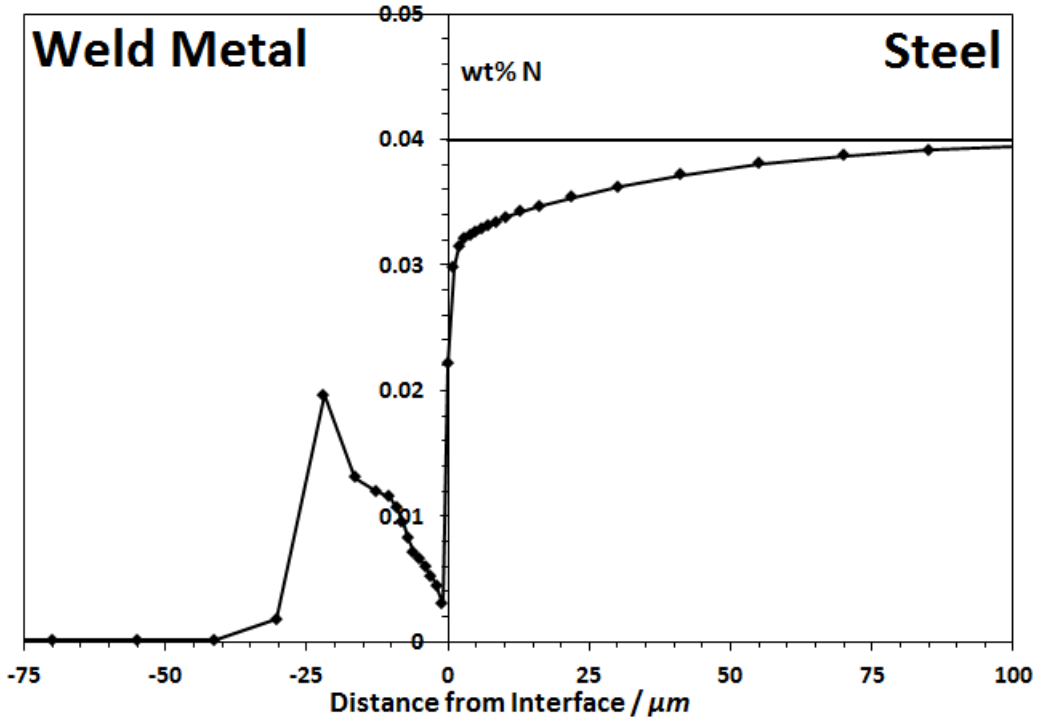

Figure 6.9: Simulated variation in nitrogen level across the weld interface in sample T, as calculated using *DICTRA*. The horizontal black line represents the initial nitrogen level in the steel; there is no corresponding line in the weld metal, as the nominal nitrogen level in that region is zero.

Figure 6.10 shows the phase fraction variation around the weld interface in sample T. The steel is predicted to contain primarily BCC matrix, and the weld metal primarily FCC matrix. The transition between the two phases, near 0 on the horizontal axis, occurs over a range of 3 μm. This small area is duplex in structure, and may correspond in some respects to the interfacial band observed experimentally.

The CNDZ in the steel is shown to be completely denuded of $M_{23}C_6$ carbide within 10 μm of the interface (compared with a base level mole fraction of 0.015),

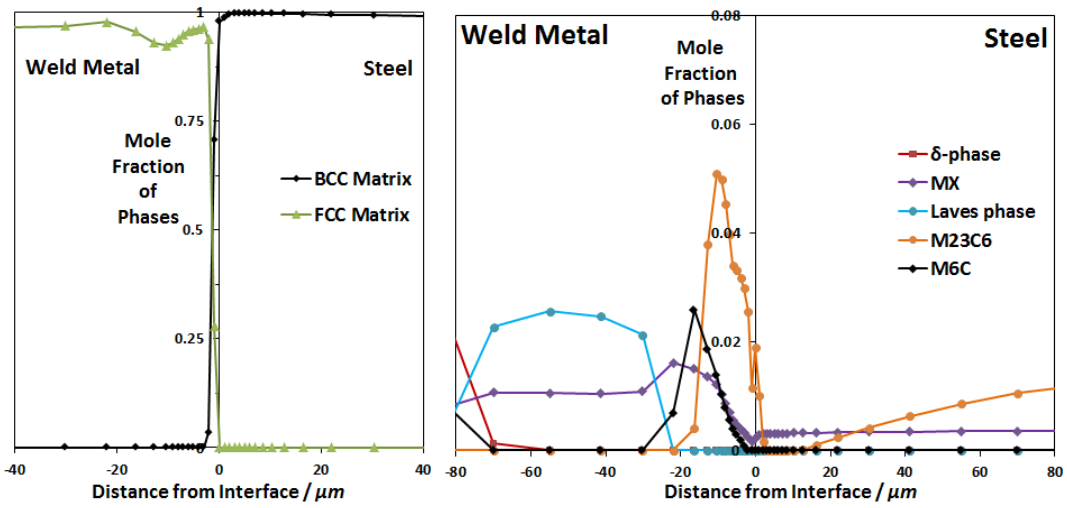

(a) (b)

FIGURE 6.10: Results of kinetic simulations of the evolution experienced during the heat treatment of sample T, as calculated using *DICTRA*, showing the variation in phase balance. Figure **(a)** shows the matrix phases, **(b)** the secondary phases.

indicating that this carbide dissolves in order to supply carbon diffusion. The MX phase is less affected by diffusion, dropping from a base level of 0.0037 to a minimum of c. 0.003 near the interface. No Laves phase is predicted to form in the steel, in accordance with experimental observations and earlier thermodynamic calculations.

The CNEZ in the weld metal is found to contain primarily $M_{23}C_6$ (chromium-rich) carbide, along with smaller amounts of M_6C (molybdenum-rich) and MX (niobium-rich) particles. Nitrogen content is contained primarily within the latter phase. The existence of δ-phase is predicted in the weld metal, though only at distances greater than 60 μm from the weld interface; between 25 and 90 μm from the interface, an iron- and molybdenum-rich Laves phase is predicted to form. M_6C and MX particles are also predicted to be present in the bulk of the weld metal as equilibrium phases (with the latter being of the form of MC in bulk, due to the lack of nitrogen).

6.2.2 Long Term Ageing

The simulation of the long term aged case (2 hours at 760 $°C$, followed by 125 days at 625 $°C$, corresponding to sample experimental LTA) was next simulated, using the compositional data output from the simulation of tempering as a set of initial conditions. The same phases were called as in the previous simulation, and from the same databases. The results from sample STA show largely similar similar trends.

Figure 6.11 shows the simulated carbon profile across the weld interface in samples LTA and STA, indicating that greater carbon diffusion has occurred than in sample T. The peak carbon level of the CEZ in LTA is now 0.56 wt%, and its width is now between 55 μm. The CDZ has now grown too, being around 500 – 600 μm in width (though only 100 μm adjacent to the weld line is plotted). These zones are greater in size than in sample STA, indicating that diffusion is an ongoing process (though there is clearly not a linear relationship between zone width and time). This necessarily means that the volume of steel from which carbon has diffused is greater after longer ageing times; the integrated areas of the CEZ and CDZ are approximately 7.4 μm.wt% and 12.2 μm.wt% in samples STA and LTA respectively, as opposed to approximately 3.7 μm.wt% in sample T.

The CDZ in sample LTA, while wider than in sample T, is also shallower. The minimum carbon level in the CDZ is 0.009 wt% in this case, around 10 μm away from the interface. At the edge of the CDZ (adjacent to the BCC – FCC interface) there is a small peak in carbon concentration, approximately 2 μm in width and with a maximum level of 0.153 wt%.

Figure 6.12 shows the simulated nitrogen profiles across the weld interfaces in samples STA and LTA. These data show that, like carbon, nitrogen has continued to diffuse during the longer term ageing treatments. The width of the nitrogen denuded zone in sample LTA is c. 450 μm, and c. 250 μm in sample STA,

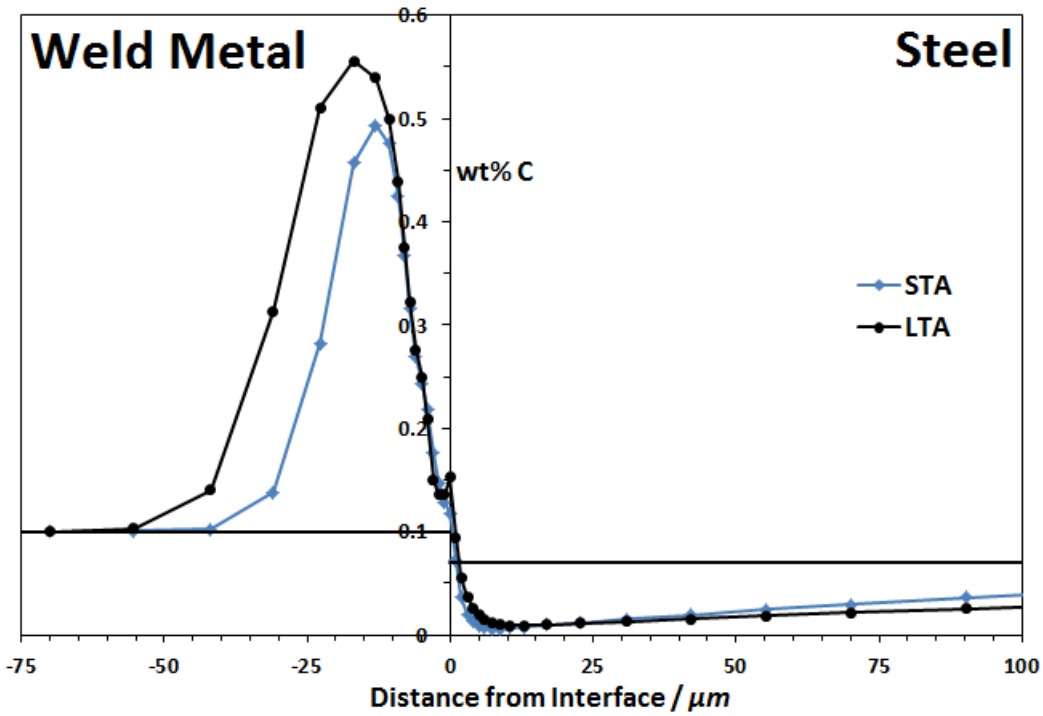

Figure 6.11: Results of kinetic simulations of samples STA (blue) and LTA (black), as calculated using *DICTRA*, showing the variation in carbon level across the interface. The solid black horizontal lines represent the base level concentrations in the two alloys.

indicating that nitrogen diffuses from over a slightly shorter distance than carbon. The minimum nitrogen level in the steel in sample LTA is around 0.03 wt%. The enriched zones are significantly larger than in sample T; that of sample LTA has a peak level of 0.05 wt%, occurring 40 μm from the interface, and its total width up to 100 μm. The enriched zone in sample STA is smaller, though similar in form. As such, the integrated areas of the zones are larger than in sample T, being 0.85 and 1.65 μm.wt% in samples STA and LTA respectively.

The predicted diffusion of substitutional elements in sample LTA is shown in figure 6.13 for the cases of iron, nickel and chromium. This plot indicates that only minimal diffusion of these elements has taken place. The general trend is that these elements are diffusing in such as way as to homogenise concentration gradients; iron is diffusing towards the weld metal, while nickel and chromium are diffusing into the steel. The area of chromium enrichment in the steel adjacent to the weld line, around 4 μm in width and up to 0.75 wt% above the base level,

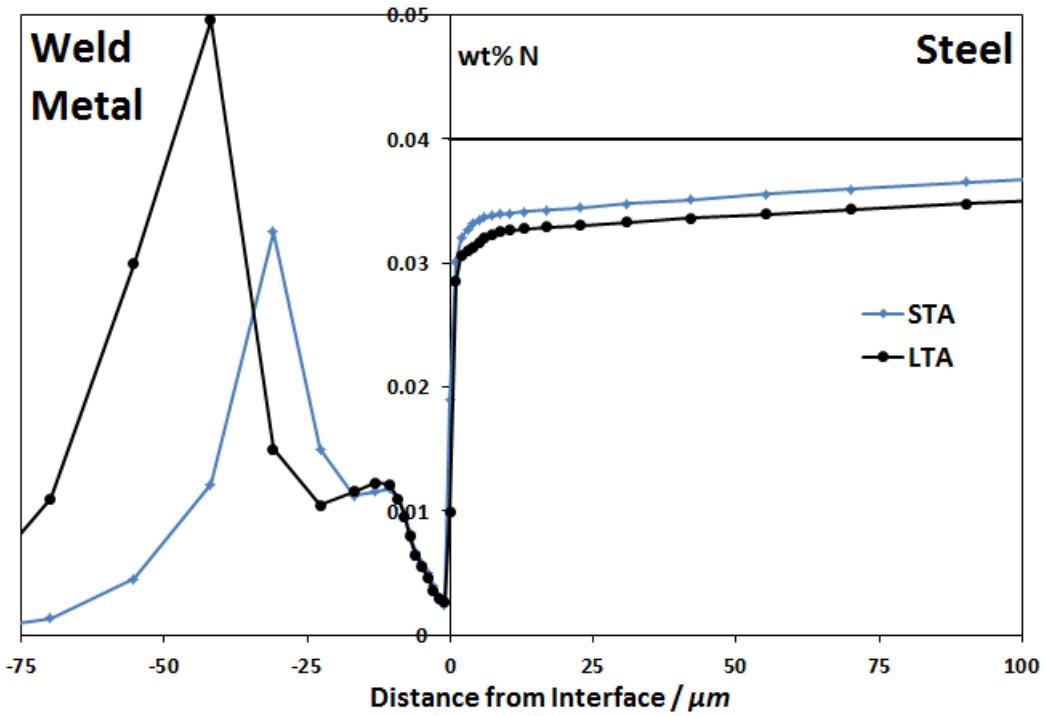

Figure 6.12: Results of kinetic simulations of samples STA (blue) and LTA (black), as calculated using *DICTRA*, showing the variation in nitrogen level across the interface. The solid black horizontal line represents the base level concentration in the steel.

matches up with the small carbon peak observed in figure 6.11.

The phase fraction variation of sample LTA is shown in figure 6.14. This shows that a duplex region (containing both matrix phases) is present around the weld interface, with a width of up to 5 μm. This area has likely been caused by the diffusion of substitutional elements; such diffusion has also caused the position of the interface to shift towards the weld metal by c. 3 – 4 μm, which is important to consider when interpreting data from the previous three figures.

With regards to secondary phases, $M_{23}C_6$, M_6C and MX phases are all predicted to exist in the CEZ (in descending order of peak amount). As in sample T, δ-phase is found only to exist as an equilibrium phase away from the PMZ, while a Fe-Mo Laves phase exists at the edge of the PMZ. The steel, by comparison, contains $M_{23}C_6$ carbide, MX carbonitride and Fe-W Laves phase. As in sample T, much of the carbide phase dissolves to supply diffusion, while the carbonitride phase is less severely affected. The fraction of Laves phase increases slightly in the

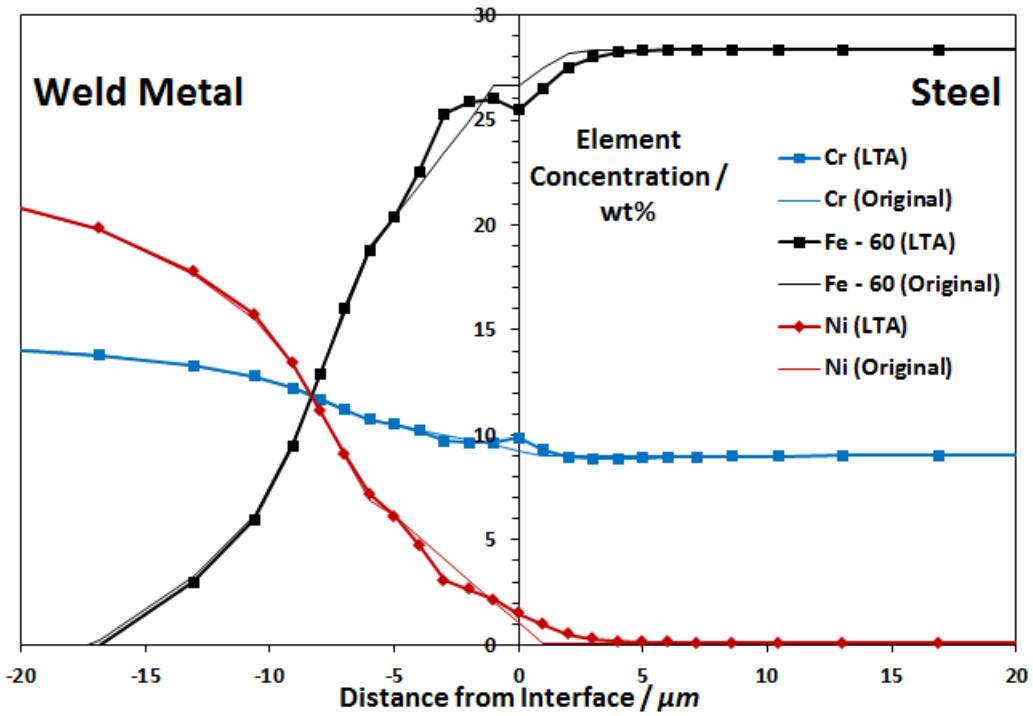

Figure 6.13: Results of kinetic simulations of the evolution experienced during the heat treatment of sample LTA, as calculated using *DICTRA*, showing the variation in levels of Fe, Cr and Ni across the interface, as compared with the original concentration profiles (i.e. the initial conditions). A fixed value of 60 has been subtracted from every Fe measurement, so as to bring the levels on to the same scales as those of Cr and Ni.

CNDZ, from a base mole fraction of 0.011 to a peak of 0.017; this may correspond to the experimentally-observed coarsening of Laves phase particles in this area.

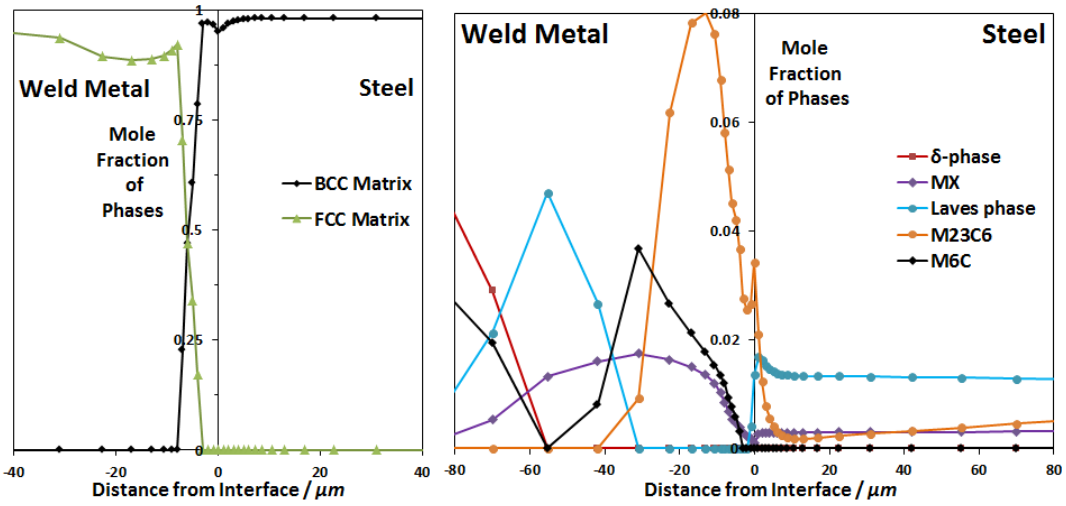

(a) (b)

Figure 6.14: Results of kinetic simulations of the evolution experienced during the heat treatment of sample LTA, as calculated using *DICTRA*, showing the variation in phase balance. Figure **(a)** shows the matrix phases, **(b)** the secondary phases.

6.3 Summary

In this chapter, the software package *Thermo-Calc* has been used to make predictions about the equilibrium phase behaviour of the two alloys, P92 steel and Alloy 625, in their nominal states and various modified states (diluted, decarburised, etc.). The *DICTRA* package has been used to predict interdiffusion across the weld interface after the various heat treatments, and the resultant changes in phase balance.

Chapter 7

Discussion of the P92 – Alloy 625 System

In this chapter the results from the laboratory-aged P92 – Alloy 625 weld system, both experimental and computational, will be discussed. The properties of the base metals and the artefacts of the welding process will be considered, and used as a context for understanding the behaviour at the weld interface (i.e. diffusion and resultant changes in phase balance). The consideration of the effects of microstructural evolution at the interface in regard to consequences for welds in a service environment will be discussed later, in section 8.8.

7.1 The P92 Steel

As shown in section 5.2, the as-received P92 steel (i.e. normalised and tempered) has a typical three-phase structure (consisting of the ferritic steel matrix, $M_{23}C_6$ carbides and smaller MX carbonitrides). Its grain size is between 10 and

20 μm, and it has a distinct martensitic lath structure, with a mean hardness of c. 252 VHN_{100}. These are ideal properties for manufactured P92 steel. The structure does not appear to be affected in any distinct way by the tempering PWHT, neither in terms of grain growth or precipitate coarsening.

It is during the long-term heat treatment at 625 $°C$ that evolution of the bulk material occurs, most evidently in the form of Laves phase formation. This is supported by the thermodynamic prediction (in figure 6.1) that Laves phase is stable below 720 $°C$, which also explains why none is observed in the as-received or tempered conditions. It appears that Laves phase particles grow rapidly, having done most of their coarsening during the 32-day heat treatment, and relatively little additional coarsening after the 125 day heat treatment. The observation of a large number of relatively coarse Laves phase particles is in line with the findings of Rodak et al. [44]. Conversely, the other two precipitate types, where they can be identified, do not appear to have coarsened as significantly during these heat treatments ($M_{23}C_6$ being stabilised by boron [45], and MX being intrinsically resistant to coarsening [36]), and no modified Z-phase particles have been observed.

The impact of this Laves phase formation on the properties of the steel is not likely to be entirely positive. As the particles are relatively coarse, and generally isolated to PAGBs, they will not confer much strength to the alloy by precipitation hardening. Additionally, they will deplete the surrounding metal matrix of tungsten (and, to a lesser extent, chromium and molybdenum) as they coarsen, hence limiting the potential for solid solution strengthening. This depletion may also explain the strongly non-linear growth dynamics of these particles; their initial formation may be rapid as they can take up tungsten and molybdenum from immediately adjacent areas of matrix, but further growth may be limited by the rate of diffusion of these elements from the centres of grains to the particles.

The heat-affected zone of the steel shows the three characteristic sub-zones (CGHAZ, FGHAZ and ICHAZ). They are tempered by the various heat treat-

ments, though not removed entirely, and so may cause problems for real welds in service conditions. Particular issues include the small grains in the FGHAZ and ICHAZ, which may leave these areas vulnerable to creep failure by grain boundary sliding, as identified by Francis et al [135]; this may be exacerbated in the latter region by the presence of particularly coarse carbide particles, which are a product of the tempering process.

Another issue may be the areas of δ-ferrite in the CGHAZ near the weld line, seen most clearly in sample A-W, which may be a particular problem in P92 due to the large temperature range over which δ-ferrite can form. Such areas cannot contain martensite, and may be associated with excessive coarsening of Laves phase particles, and are hence strongly detrimental to mechanical properties [164].

7.2 The Alloy 625-based Weld Metal

The Alloy 625 weld metal in this system is found to be heavily diluted in iron; the first pass contains up to 30 wt% of iron, while the second contains around 15 wt%. This dilution may be expected to cause significant deviation from the known properties of nominal welded Alloy 625, particularly in the first pass. This is certainly true of corrosion resistance, as the second weld pass is more resistant to the aqua regia etchant.

In spite of the extensive dilution, the expected columnar-dendritic microstructure is still present. The grain boundaries and interdendritic areas contain blocky secondary phase particles, which cannot be conclusively identified but are found to be enriched in molybdenum, niobium and silicon relative to their surroundings. It was found by Floreen et al. [58] that the phases in these areas form on solidification and could be NbC and/or Laves phase, depending on the ratio of carbon to niobium in the progenitor liquid. However, their findings were based on nominal Alloy 625; the higher iron content in this case may stabilise additional phases.

The computational approach may not be helpful in this regard, since it is based on equilibrium conditions.

The ageing treatment at 625 $°C$ has resulted in hardening of the weld metal, most significantly in the 125-day aged case (sample LTA). Hardening is more pronounced in the second weld pass than in the first in sample LTA, as is the case in sample T. Sample STA does not appear to display this trend, though its weld metal is harder on average than those of samples A-W or T.

The microstructural analysis reveals the reason for this hardening, in the form of needle-like particles in interdendritic areas. These are only seen in samples STA and LTA, and are larger and far more numerous in the latter. Assuming that these particles are γ'' or δ-phase of form Ni_3Nb, a reasonable conclusion based on their distinctive acicular morphology and EDX evidence, then they can be identified as the cause of mechanical changes by precipitation hardening. The reason for the preferential hardening of the second weld pass in sample LTA is hence apparent, as its lower iron level means that more nickel and niobium are available to form these particles.

7.3 The Interfacial Band

The 'interfacial band' has been observed in all TEM-examined samples. It is the region of material, usually between 1 and 2 μm in width, between the steel and the weld metal. The fact that it is observed in the as-welded samples proves conclusively that it forms during the welding process, supporting the conclusions of [83] and [68]. It is found to be enriched in chromium, nickel and molybdenum relative to the base steel, though generally still BCC in structure (with the exception of sample T, in which it is FCC). It is of different crystallographic orientation to either adjoining alloy in all cases, and is observed to be almost entirely precipitate-free.

The equilibrium thermodynamics of the band have been investigated using *Thermo-Calc*, taking as an example the composition of the band in sample A-W (the compositions of which are shown in figure 5.26, with carbon and nitrogen levels being estimated to be equivalent to the base levels in the steel since they could not be precisely measured). A phase fraction plot as a function of temperature for this composition is shown in figure 7.1, with the secondary phases having been suspended from the calculation since they are not observed experimentally.

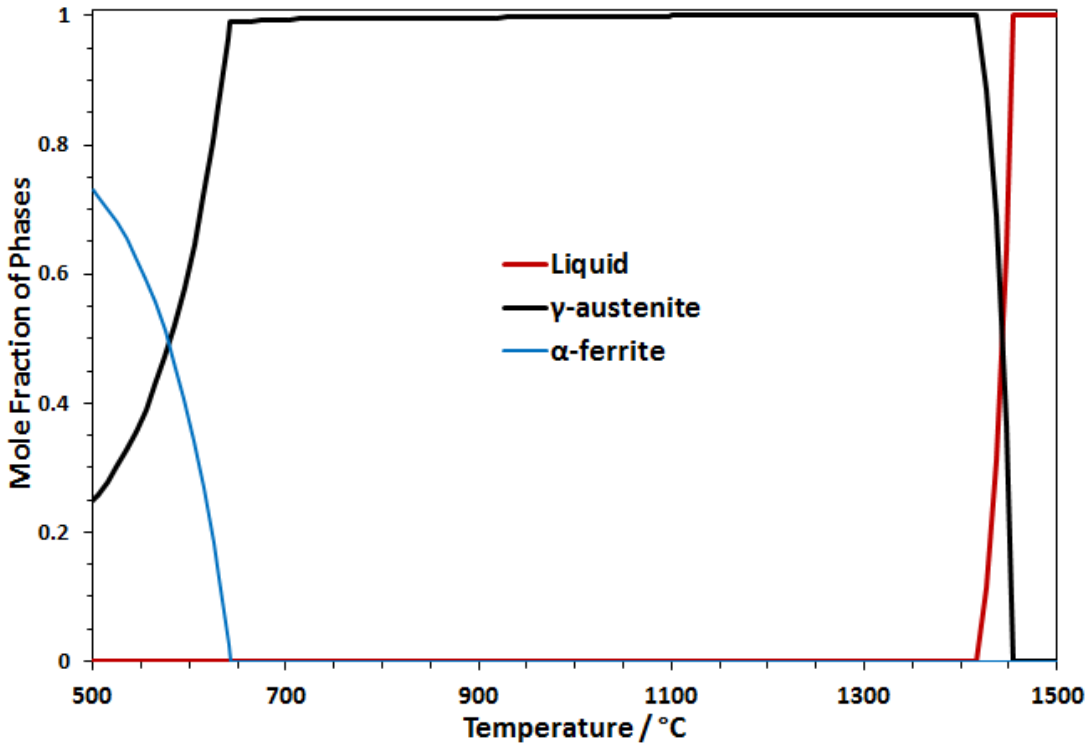

Figure 7.1: A plot of phase fraction as a function of temperature in the interfacial band in sample A-W, as calculated by *Thermo-Calc* using the TCFE7 database with secondary phases suspended.

The calculations indicate that the matrix is duplex at 625 $°C$, containing both FCC-austenite and BCC-ferrite in a ratio of 4.1:1. This duplex nature is reflected by plotting the composition in a Schaeffler diagram, such as that in figure 7.2, as it lies in the austenite + martensite phase field (the exact position depending critically on carbon and nitrogen contents). The BCC phase is not stable at high temperatures, dissolving completely at 640 $°C$. This may explain the presence

of an FCC band in sample T, as this phase may have been stabilised during the tempering treatment and maintained in during quenching, though other factors may be in play here (such as local variations in composition). The matrix in the band is predicted to be solely FCC up to the melting range, which begins at 1420 $°C$ and concludes at 1455 $°C$; there is no transition to δ-ferrite.

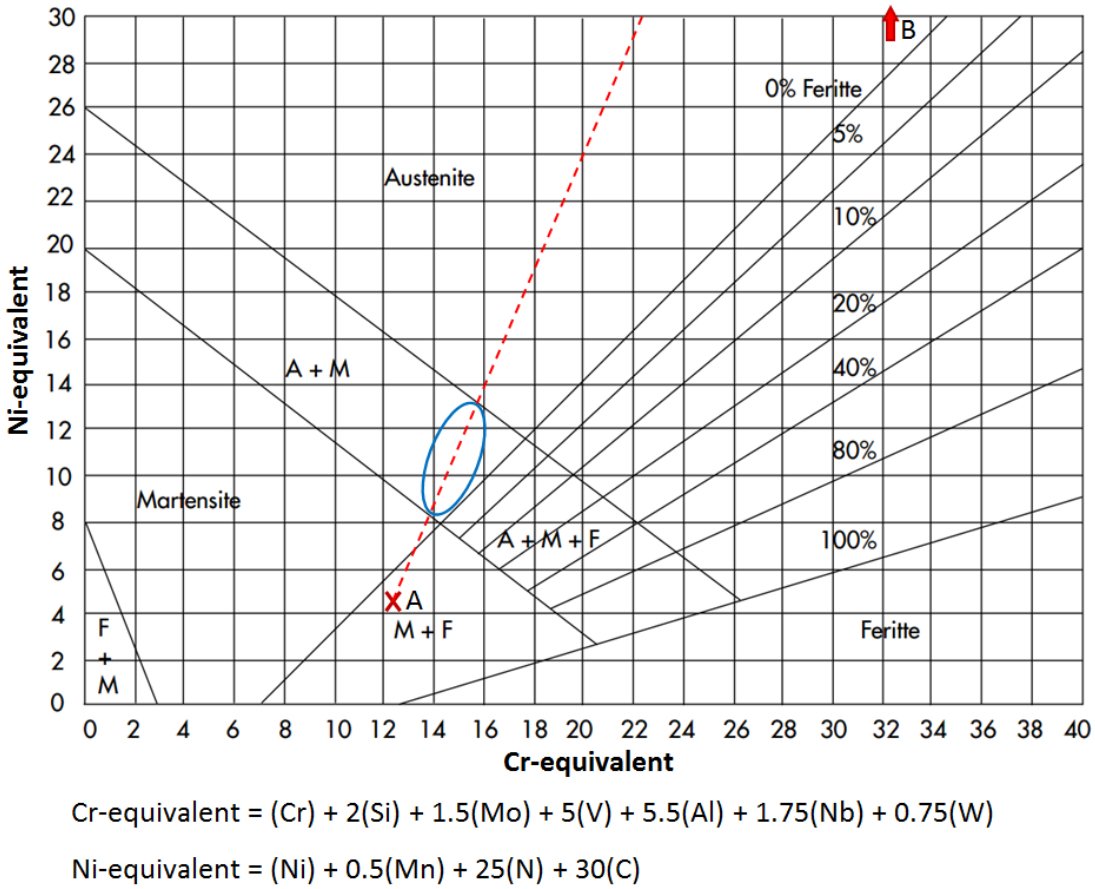

Figure 7.2: A Schaeffler diagram, marked with the positions of P92 steel (marked with a red cross and the letter A) and nominal Alloy 625 (the horizontal position of which is marked with a red arrow and the letter B, with it's vertical position being around 60). The red dotted line joins the two points, and all diluted states of the weld metal ought to lie on this line. The blue circle highlights the austenite + martensite range of dilution, where the interfacial band is thought to lie.

Assuming the predictions regarding melting temperatures and matrix phases to be true, a mechanism for the formation of this band can be proposed. During the welding process, this band is a region of partial melting, sitting in the liquid + δ-ferrite phase field (which, according to the phase fraction plot in figure 6.1, is

between 1460 $°C$ and 1510 $°C$). This allows it to take on some alloying elements from the adjacent molten weld metal by convection. This lowers the melting range according to figure 7.1, causing the affected area to melt completely and allowing the alloying elements to disperse. The adjacent steel remains entirely solid throughout.

Upon cooling, the band will solidify completely at around 1420 $°C$. However, due to its composition, it will solidify as γ-austenite, while the adjoining solid steel is likely to be primarily δ-ferrite. This prohibits solidification by epitaxial growth, forcing new FCC grains to grow at a range of angles in an attempt to minimise the structural mismatch. This explains, or at least allows for, the observed discontinuity in crystallographic orientation between the interfacial band and the base steel. As the weld cools, a martensitic transformation may occur in the band, if the local composition allows for it.

This theory is in some ways consistent with the theory of DMW solidification set out by Nelson et al. [72] [73] and Lippold et al. [74], shown schematically in figure 7.3. They describe the initial welding solidification as being γ on δ, which introduces a structural mismatch. As the weld cools, the base steel becomes γ, and the resultant γ-γ phase boundary migrates into the weld metal. Once the weld has completely cooled, this boundary is locked in place, and is called a type II boundary (distinct from type I boundaries, which are perpendicular to the weld line). If this mechanism applies in this case, then the interface between the weld metal and the interfacial band is hence an example of a type II boundary.

It is possible that the sawtooth-like areas of the band, such as that seen in the TEM observation of sample T (in section 5.8.2) correspond to areas in which the substrate steel was γ-austenite in structure as the band solidified, thus allowing for some degree of epitaxial growth. This would go some way toward explaining the structure of these areas.

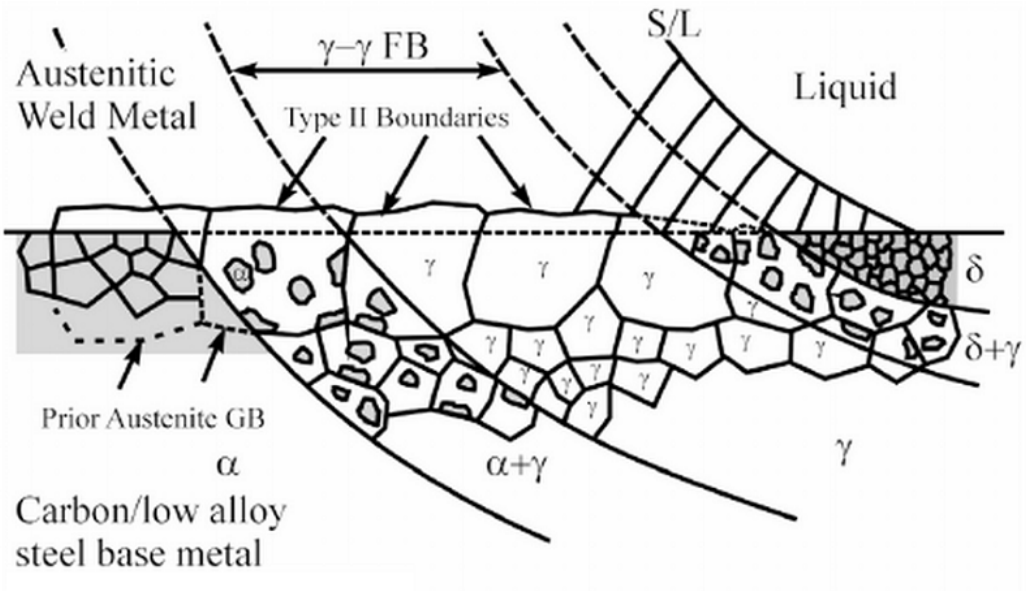

Figure 7.3: A schematic of the microstructures present during dissimilar metal welding. The welding direction is left to right, and the curved lines extending from top left to bottom right are isotherms. This illustrates the formation of 'type II' boundaries at a DMW. From Nelson et. al [73].

7.4 Interdiffusion at the Weld Interface

Evidence has been found for diffusion across the weld interface between P92 steel and Alloy 625, at least to some degree. Both carbon and nitrogen appear to have engaged in diffusion. Though more investigation has been done on the former, both elements are of great importance for the properties of P92 steel in their roles as carbide and carbonitride formers. As such, the diffusion-affected zones either side of the weld line shall hereby be referred to as the CNDZ (carbon & nitrogen denuded zone) and CNEZ (carbon & nitrogen enriched zone).

The diffusion phenomenon appears to be far less pronounced in its effects than in 2.25Cr-1Mo – Alloy 625 weld systems, such as that investigated by Saghafifar [165]. Select novel results from a 2.25Cr-1Mo – Alloy 625 weld that are presented in appendix A illustrate the disparities, in the form of carbon count rates by the low-voltage EDX method, *DICTRA* simulation results, and the form of the CEZ as viewed by TEM. Precedent for this trend has previously been found [92] [104],

though the effects have not before been reported in such detail.

The reasons for this trend may not be immediately apparent, but are a consequence of the variation of the activity of carbon in steel as a function of levels of alloying elements, most significantly chromium. This variation for a simplified system, as predicted in *Thermo-Calc*, is shown in figure 7.4. This shows that, at 625 $°C$ a steel of 2.25 wt% chromium has an activity of carbon of 9.3×10^{-3}. As chromium level increases, carbon activity decreases, reaching a level of 2.3×10^{-4} at 9 wt% chromium. The activity in the latter case is closer to that of nominal Alloy 625 (which was shown in table 6.3 to be 1.67×10^{-5}) meaning that the diffusion driving force will be reduced.

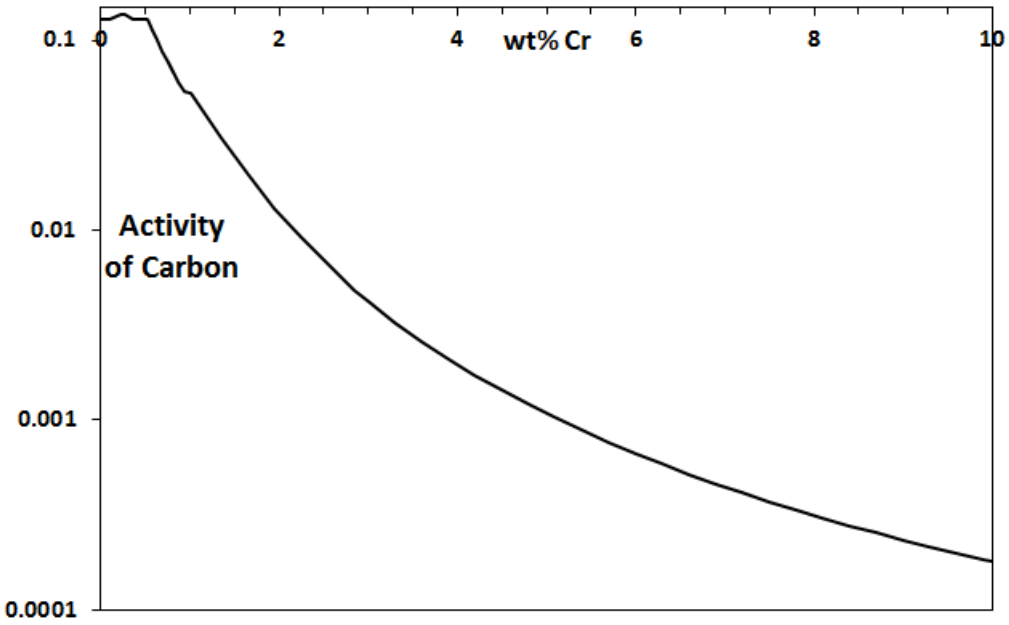

Figure 7.4: A plot of carbon activity as a function of chromium level in a simplified steel (containing 0.4 wt% Si, 0.4 wt% Mn, 1 wt% Mo) at 625 $°C$, as calculated by *Thermo-Calc* using the TCFE7 database.

However, the weld metal is not nominal Alloy 625, in either the laboratory-aged case or the ex-service case. The weld beads are diluted with iron, and the PMZ contains more iron still; this was shown in figure 6.6(a) to increase the activity of carbon, and hence reduce the diffusion driving force further still from that which may be expected based on nominal compositions.

As a result of diffusion across the P92 – Alloy 625 weld interfaces, the phase balances on either side of the interfaces have changed. The carbide and carbonitride phases in the steel have dissolved to varying degrees, and new features have precipitated in the weld metal. There is also the more subtle issue of type I carbide formation to consider.

The initial properties of the as-welded state of the P92 – Alloy 625 system are shown schematically in figure 7.5. In this state there are no precipitates in the steel near the weld line, and no diffusion is thought to have occurred. This is justified on the evidence of microstructures and the low-voltage EDX readings of carbon variation shown in figure 5.23(a). The specific phenomena observed during tempering and long-term ageing will now be discussed in more detail.

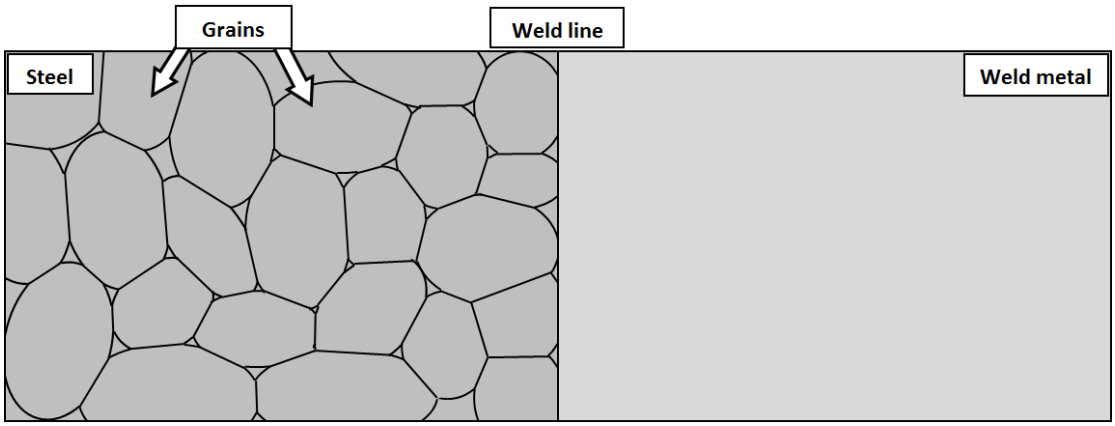

Figure 7.5: A schematic representation of a P92 – Alloy 625 weld system in the as-welded condition. No secondary phases are present in the steel in this condition, and no diffusion has occurred.

7.4.1 Tempering Treatment

Perhaps the best starting point for discussing diffusion behaviour are the results of kinetic calculations in *DICTRA*; for the tempered case, these data were presented in figures 6.8 and 6.10. The key prediction from these results is that carbon is expected to migrate from the steel to the weld metal, in accordance with theoretical expectations. This is supported by evidence from the low-voltage

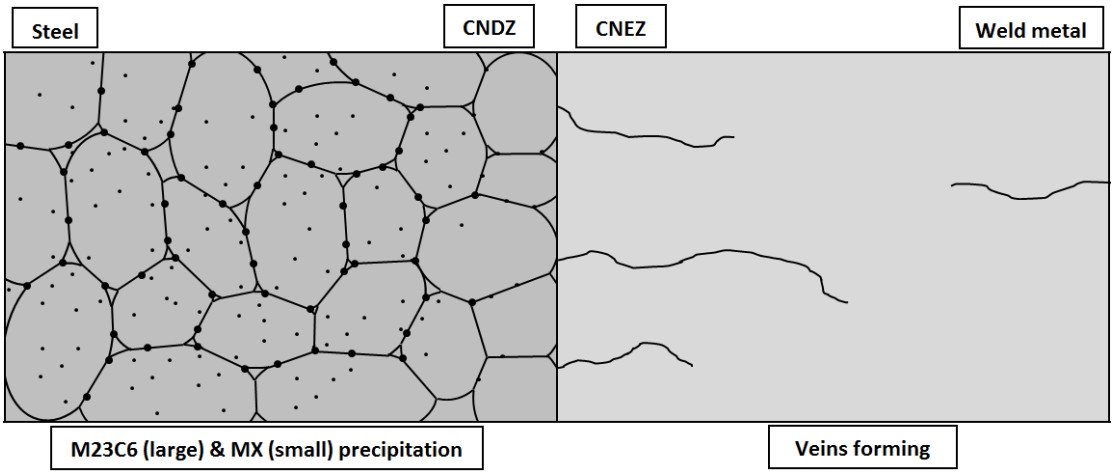

Figure 7.6: A schematic representation of a P92 – Alloy 625 weld system in the tempered condition. $M_{23}C_6$ carbides and MX carbonitrides have precipitated in the steel, with the exception of the CNDZ, where carbon and nitrogen have diffused away into the weld metal. This has resulted in vein-like features at grain boundaries in the weld metal, which serve as energetically favourable pathways for carbon and nitrogen diffusion and the precipitation of carbonitrides.

EDX technique, shown in figure 5.23(b), which shows some carbon building up in the weld metal. This results in a loss of carbides (and carbonitrides, as nitrogen is shown to display similar behaviour to carbon) in the steel, and an increase in carbides and carbonitrides in the weld metal, in forms illustrated schematically in figure 7.6.

Analysis by SEM of the steel near the weld line in sample T has confirmed the loss of carbides in the steel, as there are shown to be distinctly fewer carbide-type precipitates in the CNDZ than in the unaffected bulk steel. Additionally, many of those that remain are smaller than those seen in the bulk. This indicates that diffusion across the weld interface is supplied by the dissolution of precipitates, a finding supported by the model.

Microstructurally, the CNDZ appears to be more apparent in sample T, as seen in figure 5.14(b), than in samples STA or LTA, in that it has the fewest and smallest precipitates. This may seem counter-intuitive, as it has received by far the shortest heat treatment, and the other samples all received the same tempering treatment before their longer exposure. However, it is in line with the results from

DICTRA, which show the CNDZ in sample T to have the lowest carbon level (and hence the lowest carbide fraction). The reasons for this effect are theorised to be two-fold:

1. The tempering treatment (760 $^{\circ}C$ for 2 hours) is much hotter than the long-term ageing condition or service exposure. According to equation 3.9, diffusivities are strongly temperature-dependent, allowing for faster diffusion at high temperatures. Therefore, during the welding process, rapid diffusion of carbon and nitrogen from the small area immediately adjacent to the weld line can take place. The treatment is so short that there is insufficient time for more atoms to diffuse in from the adjacent steel to balance out the deficiency.

2. Laves phase particles are not thermodynamically stable at 760 $^{\circ}C$, as shown in figure 6.1. They are not present in sample T, whilst they are present in the cases aged at 625 $^{\circ}C$. The conclusion that the CNDZ in sample T is the most pronounced may hence be influenced by observational bias, as Laves phase particles are not significantly affected by carbon/nitrogen diffusion (since they are intermetallic) and will make the CNDZ appear more heavily populated if they are present.

Observation by SEM of precipitate distribution in the CNDZ is limited by resolution, and fine details may be overlooked. TEM and STEM have been used to investigate this area in greater detail. The steel in sample T displays the expected families of precipitates: $M_{23}C_6$ carbides and MX carbonitrides. Without an equivalent TEM sample taken from the unaffected bulk material, it is difficult to make judgements on how diffusion has affected the precipitate distribution on this scale.

The microstructure of the CNEZ is somewhat harder to study due to the strong resistance to etching of the Alloy 625 weld metals. However, what is immediately

apparent is that there is no band of dispersed intragranular carbides (as is observed in the 2.25Cr-1Mo – Alloy 625 system presented in appendix A) in any of the P92 – Alloy 625 welds. The impact of diffusion on the microstructure of the weld metal seems to be primarily in the form of vein-like features at grain boundaries that become visible upon etching.

No veins of any sort are observed in sample A-W, indicating that they do not form during the welding process. They begin to appear after the tempering heat treatment, as some are visible in sample T. Many of these veins extend outward from the weld line into the weld metal, though many do not. It can hence be theorised that the veins extending from the weld metal serve as pathways for carbon and nitrogen diffusion, as the grain boundaries serve as energetically favourable locations for this to occur.

The fact that veins are observed in the bulk of these weld metals might be taken as evidence that they are not related to diffusion. However, the opposite may be true, in that the presence of isolated veins in the bulk may confirm that they are carbide-rich. As Alloy 625 is solidified following welding, much of the nominal carbon content is contained in the bulk of grains. As it is heat treated, it is known that carbon will diffuse to grain boundaries to form carbides [58], leading to these vein-like features. According to this interpretation, such features in the CNEZ are hence likely to be carbide/carbonitride-rich.

7.4.2 Long Term Ageing

DICTRA simulations of sample LTA, shown in figures 6.11 – 6.14, reveal evolution from sample T, in ways illustrated schematically in figure 7.7. The carbon enriched and denuded areas are both more pronounced, with the total mass of diffused carbon having increased by a factor of 2.6. This is supported by evidence from the low-voltage EDX technique, as shown in figure 5.23(c), in that carbon count rate in the CNEZ is proportionately higher relative to the weld metal base

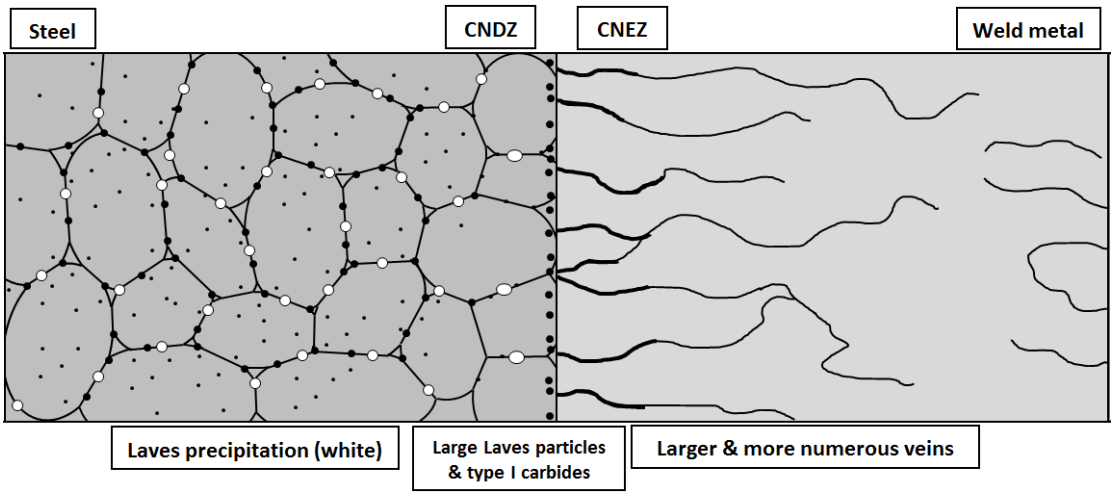

Figure 7.7: A schematic representation of a P92 – Alloy 625 weld system after long term ageing. Laves phase particles have now precipitated in the steel, which are larger in the CNDZ than in the bulk. Type I carbides have formed in the steel immediately adjacent to the weld interface. More extensive diffusion into the weld metal has taken place, leading to more frequent and larger veins, which are wider near the weld line.

rate than in sample T.

The CNDZ in sample LTA is predicted to be wider but shallower than in sample T. The former property is difficult to verify, since the edge of the CNDZ is not apparent in the microstructure, but the latter property is observed; the CNDZ is less pronounced in samples LTA and STA than it is in sample T in terms of the frequency and size of precipitates. This can be understood in terms of carbon diffusing from the bulk of the steel to fill the CNDZ produced by the tempering process. Additionally, there is a small peak in carbon concentration in the steel adjacent to the weld interface, which may correspond to some degree of type I carbide formation.

The CNDZ in samples STA and LTA has been found experimentally to contain Laves phase particles that are larger than those away from the CNDZ, which indicates that these particles are coarsening more rapidly in this area. Additionally, computational results from *DICTRA* predict that the total amount of Laves phase should be higher in this area than in the bulk steel. The cause of this effect is theorised to be due to the local reduction in $M_{23}C_6$ carbide population. As was

shown by STEM-EDX in tables 5.5 and 5.6, these carbides contain chromium, molybdenum, tungsten, and possibly iron. As carbon diffuses away towards the weld metal, the carbides dissolve and these elements are ejected into solid solution. Laves phase in P92 steel is of the form $(Fe,Cr)_2(Mo,W)$, so an increase in the available amounts of these elements will increase the rate at which these particles can coarsen.

TEM and STEM observation of the CNDZ in samples STA and LTA shows the expected precipitate families ($M_{23}C_6$, MX and Laves) to be present. There are some areas, most notably in sample STA, which contain no $M_{23}C_6$ carbides, while neither sample contains many MX carbonitrides. These facts support the SEM observations, that these particles are dissolving to supply diffusion into the weld metal.

The microstructural features of the CNEZ observed in samples STA and LTA are similar in many respects to those of sample T, only they are far more pronounced. Veins are more frequent, longer, and wider near the weld interface, especially in sample LTA. This provides evidence that these features are growing as a function of time, and may be serving as pathways for carbon and/or nitrogen diffusion.

TEM analysis of the CNEZ confirms that the precipitates in the weld metal in sample LTA are isolated to grain boundaries, and that they are primarily carbonitrides of type Nb(C,N). There is also a second particle type that is Mo-rich, but too small to be conclusively identified. These Mo-rich particles are smaller than the Nb-rich particles, and exist as satellites around them. This being the case, it is likely that some degree of cooperative growth is occurring. The fact that these particles in the weld metal contain nitrogen is important, as it makes it likely that they are forming at least partly as a result of diffusion from the steel, since there is nominally little to no nitrogen in Alloy 625.

Though it is difficult to directly compare SEM and TEM data from the CNEZ,

due to the vastly different sample scales and preparation methods, a possible interpretation of the observations is that the grain boundary particles observed by TEM (Cr-rich $M_{23}C_6$ carbides and Nb-rich MX carbonitrides in sample T, and the latter only in sample LTA) may in fact be the same particles that contribute to the veins observed by SEM in all aged Alloy 625 weld metals. The highest magnification SEM image of the veins, shown in figure 5.19 provides some support for this interpretation, as the appearance of the veins is consistent with bands of joined-up particles.

7.4.2.1 Type I/II Carbides

One of the less intuitive aspects of ferritic-austenitic DMWs is the formation of type I/II carbides. These are the particles in the steel, along the edge of the interfacial band (though only rarely inside the band). Such particles are observed in samples STA and LTA, though not in A-W or T. They are most similar in nature to type I carbides, in line with prior findings that they are more common than those of type II in welds between ferritic steels and nickel-based alloys [82] [110]. The particles observed here are far less pronounced than those observed in 2.25Cr-1Mo – Alloy 625 weld interfaces, such as those seen in appendix A, but are significant nonetheless.

These type I carbides appear to be primarily $M_{23}C_6$ in structure, and of the same chemistry as the other particles of this type in the systems. This is in line with the findings of Laha et al. on P91 steel [112]. SEM evidence indicates that some of the particles in the type I position, particularly in sample LTA, may be Laves phase. Some slight particle growth between samples STA and LTA has been observed, and more particles are observed by SEM in the latter system, indicating that the process of formation is ongoing.

No type I particles of type M_6C are observed in this system, while they are observed alongside $M_{23}C_6$ carbides in the 2.25Cr-1Mo – Alloy 625 system (as seen in

appendix A and reported by other authors [82] [110]). The reason for this is likely to be related to the higher ratio of molybdenum to chromium in 2.25Cr-1Mo steel, which acts to stabilise the molybdenum-rich M_6C carbides. Additionally, many of the type I particles observed in the P92 are not much coarser than particles away from the weld interface, and are certainly much less coarse than the equivalent particles in a 2.25Cr-1Mo steel after this thermal exposure. This may be due to the inhibiting effect of boron on carbide coarsening in P92, the slower diffusion rate in this system, or a combination of these factors.

Based on what is now known about diffusion dynamics and the interfacial band, a model for the precipitation of these carbides can be constructed (shown schematically in figures 7.8 and 7.9). In the as-welded state, the band is of a composition intermediate between those of the steel and the weld metal (i.e. it is rich in chromium, nickel and molybdenum relative to the steel). As such, it may be BCC or FCC in structure, depending on the exact level of alloying elements. It presents two boundaries parallel to the weld surface: one between areas of like crystal structure (i.e. a grain boundary), and one between areas of dissimilar crystal structure.

During ageing, carbon and nitrogen are drawn from the steel towards the weld metal. Conversely, chromium, molybdenum and nickel are drawn to the steel, though at a far slower rate. If they meet at the interface between the band and the steel then it will be energetically favourable for carbides and/or carbonitrides to form, as this interface is a grain boundary perpendicular to the diffusion direction. As these carbides coarsen, the band becomes depleted to some degree of alloying elements, hence becoming solely BCC in structure (this effect may be seen more clearly in a more heavily evolved system, such as the 2.25Cr-1Mo – Alloy 625 system in appendix A). The supply of alloying elements from the band may constitute a limiting factor in carbide coarsening.

It is interesting to note that, while type I carbides have been observed on the

interface between the band and the steel, they are almost never observed on the interface between the band and the weld metal. The only recorded instance of this has been in sample T of the P92 – Alloy 625 case, in which the band was FCC in structure. One possible conclusion to be drawn from this is that carbides cannot form on an interface between matrices of dissimilar crystal structure, though no definitive explanation for this can be posited.

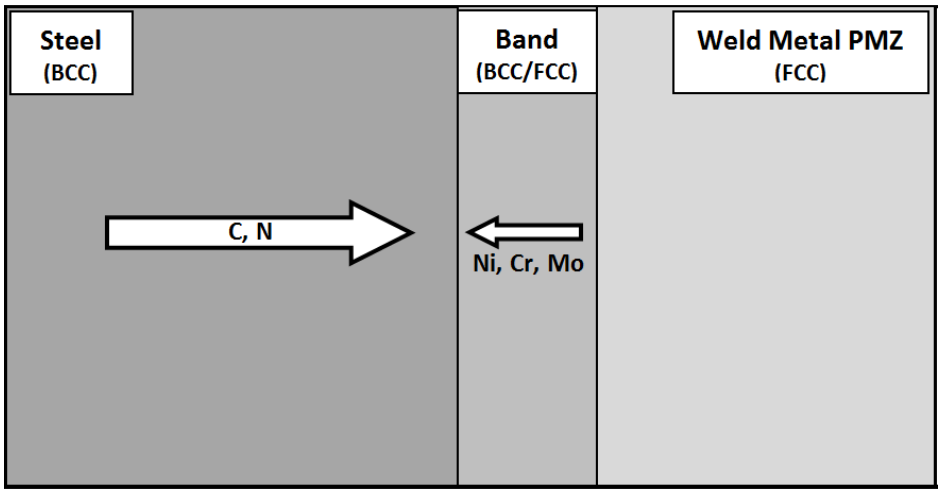

Figure 7.8: A schematic representation of the interfacial band and surrounding areas at a ferritic-austenitic weld interface (e.g. P91/92 – Alloy 625) in the as-welded condition. The interfacial band is of a composition intermediate between those of the base steel and the weld metal PMZ (represented here by being intermediate in shade between the two alloys). It may be BCC or FCC in structure. Carbon and nitrogen from the steel are drawn towards the weld metal, while chromium, nickel and molybdenum (from the band and the weld metal) are drawn towards the steel.

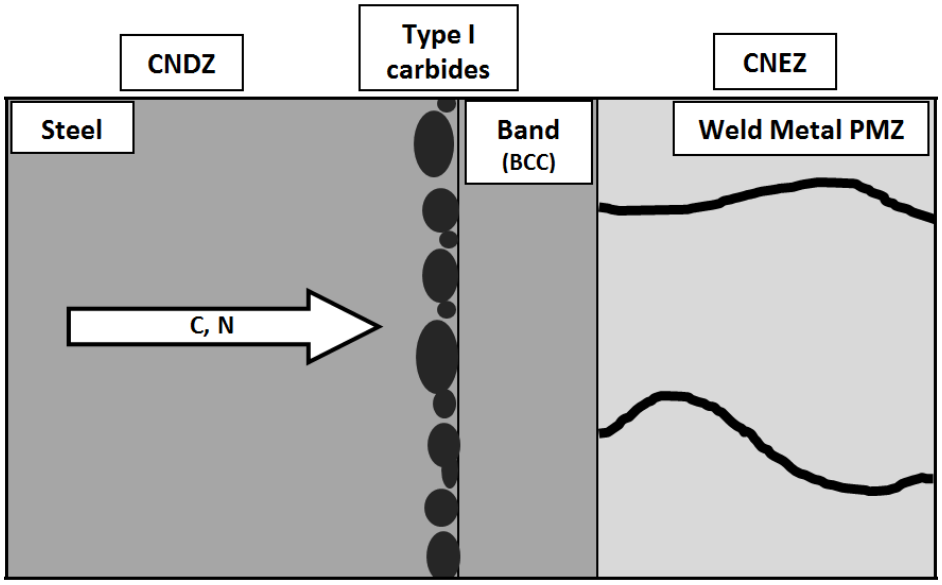

Figure 7.9: A schematic representation of the interfacial band and surrounding areas at a ferritic-austenitic weld interface (e.g. P91/92 – Alloy 625) after long term ageing. The carbon and nitrogen diffusing towards the weld metal have encountered the grain boundary at the edge of the interfacial band, rich in carbide-forming elements, hence causing type I carbides to form. The band loses some of its alloying element content, hence becoming solely BCC in structure. Some amount of carbon and nitrogen is able to move through the band and into the weld metal.

7.5 Shortcomings of Kinetic Simulations

While the kinetic simulations in the *DICTRA* software are useful in illustrating general trends, there are some rather glaring disparities between simulations and experimental data that place limits on the applicability of the tool.

The most apparent of these deficiencies is in the simplified form of the simulations. In order for calculations to be feasible, it has been necessary to suspend vanadium, nitrogen and tungsten, as well as the Laves phase. Not only does this mean that the behaviour of these components is not predicted, but their absence may have impacted the behaviour of the other components in the system (most notably carbon) by altering chemical potentials.

On the topic of chemical potentials, there is also the risk that the TTNI7 thermodynamic database may not be providing correct data for the iron-rich areas of the PMZ, as these compositions are outside the range of validity of this database.

This is apparent in the form of anomalously low carbon activities in iron-rich alloys in the graphs in figure 6.6. The effect that this may have on diffusion behaviour may be impossible to accurately predict, but may result in diffusion distances being overestimated.

On a microstructural level, the form of the predicted CNEZ is an issue. The model takes no account for grain boundary diffusion, hence predicting the CNEZ to consist of carbides and carbonitrides dispersed throughout the metal matrix. As such, the true CNEZ is wider but shallower than the simulated CNEZ. This would need to be overcome at a software development level by fully implementing a model for grain boundary diffusion (as of version 27.0.1 of *DICTRA* such a model does exist, but is incompatible with the homogenisation approach used in this work).

Another feature that suffers from the lack of an explicit consideration of grain boundaries is the type I carbide band. As discussed earlier, these carbides form primarily on the grain boundary between the steel and the interfacial band as carbon migrates across it. With no boundary at this point in the simulations, there is no particular reason for carbides to form here. The small amount of carbide that is predicted to form here does so because of chromium diffusing from the weld metal.

It is clear from this that, while kinetic simulations of the sort performed by *DICTRA* may serve as a useful tool for understanding the general properties of aged DMWs (i.e. the directions in which various components will diffuse, and the subsequent changes in phase balance), the method is far too simplistic and limited in its approach to accurately and precisely simulate DMW evolution; the microstructural phenomena in the alloys and at the interface are too complex for the model to be truly applicable in its present state. The results are of use, but must be interpreted with care, and always understood in the context of the experimental system they represent.

Chapter 8

Industrial Case Study 1: P91 – Alloy 625 Ex-service Weld

The results of the investigation of a set of P91 – Alloy 625 ex-service welds, provided by Alstom Power, will be presented and discussed in this chapter. One of these welds experienced failure in service conditions, by a mechanism believed to be consistent with low-ductility creep failure. This system was investigated internally by Alstom Power employees [157], though no cause of the failure could be conclusively identified.

The samples investigated are described in detail in section 4.1.2. Results presented here have been gathered from the following samples:

- Sample 'FP-C' (failed pipe, cracked), taken from the middle of the cracked area in the failed pipe.
- Sample 'FP-U' (failed pipe, uncracked), taken from an un-cracked area in the failed pipe.

- Sample 'PS' (pipe sample), taken from a pipe which did not experience failure, but was exposed to very similar conditions to that which did.

All of the samples were exposed to approximately the same conditions: a maximum temperature of c. 565 $°C$ for 40,000 hours, and a stress state (a combination of pressure stresses, bending stresses and residual stresses) which cannot be quantified.

8.1 Microhardness Profile

Automated microhardness testing has been performed on sample FP-U, the results of which are shown in figure 8.1. These show the base P91 steel to be softer than the aged P92 samples previously investigated, with an average hardness of 215 $\pm$ 4 VHN_{100}. The HAZ, meanwhile, is harder than the base steel, varying smoothly from the base level up to around 300 VHN_{100} over a range of 2 mm. There is also evidence of a small soft zone, around 2.5 mm from the interface (at the edge of the HAZ), in which the hardness drops as low as 202 VHN_{100}.

The Alloy 625 weld metal has displayed significant hardening. The area adjacent to the weld line has an average hardness of 326 $\pm$ 18 VHN_{100}, and there is a sudden step change up to an average of 352 $\pm$ 15 VHN_{100} at 3.5 mm from the weld line. This change corresponds to the start of the second weld pass.

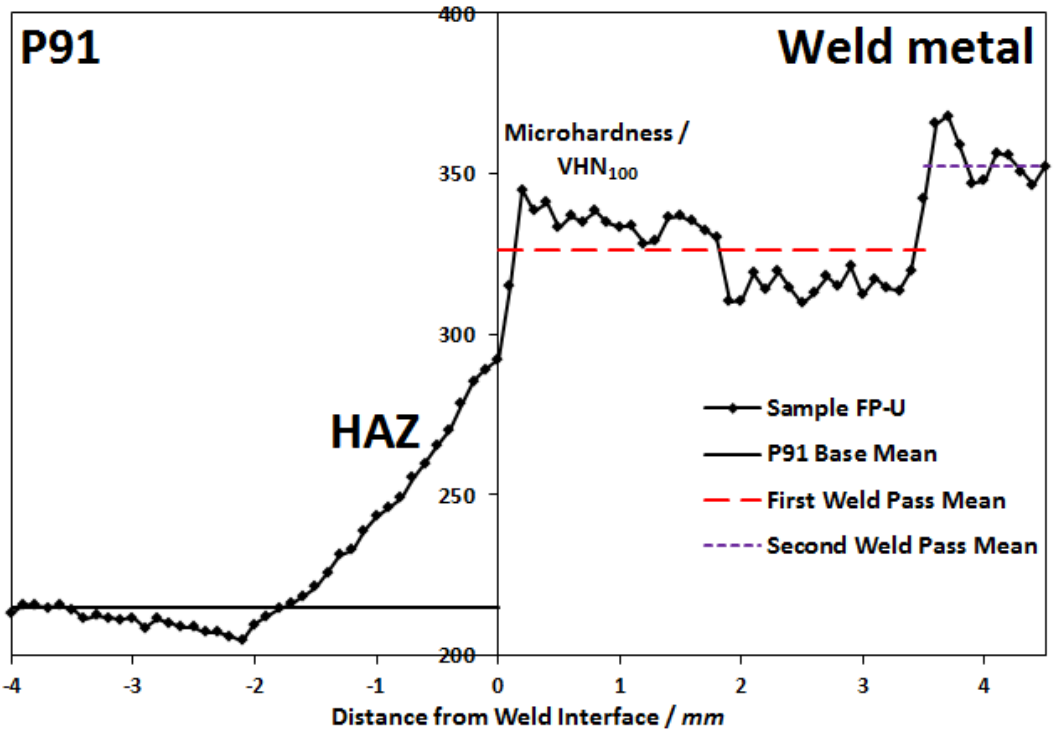

Figure 8.1: Microhardness trace across the weld interface in sample FP-U, constructed from the averages of 10 rows of indents. The horizontal lines represent the mean hardnesses of the various materials.

8.2 Microstructure of the P91 Steel

The microstructure of the base steel in all cases is that of heavily tempered martensite, as shown in figure 8.2. There are precipitate phases on PAGBs, and some on laths. Most of these are between 250 and 300 *nm* in size, though some have coarsened up to 500 *nm* during service. The BSE image in figure 8.2(b) indicates that some Laves phase particles (of form $(Fe,Cr)_2(Mo)$) have formed, appearing bright in contrast with an average size of around 200 *nm*; they appear to be fewer in number than those of the previously-examined P92 steel, though this may be because they are not as distinct in contrast as they lack tungsten. There are fewer of these Laves particles than the total number of particles in the SE image; by a process of elimination, the remaining particles of this size must be $M_{23}C_6$. Very few particles on the scale of 50 – 100 *nm* (i.e. MX carbonitrides) can be seen, which points to one of two conclusions: Either they do not exist (perhaps

having transformed into the modified Z-phase, as described in section 2.1.3.2), or the experimental technique was unsuitable to reveal them.

The samples have comparable HAZ structures (CGHAZ, FGHAZ and ICHAZ) to those seen in the tempered and aged P92 weldments. No type IV creep damage is evident in the HAZ of any of the samples.

The area adjacent to the weld line, as shown in sample PS in figure 8.3(a), shows evidence of a slight carbon denuded zone (CDZ). This is observed in all of the examined ex-service welds. The CDZ is apparent from the lower volume fraction of precipitates than in unaffected areas. The PAGBs have few visible precipitates on them, and there are few precipitates on the martensite lath boundaries. The extent of of this decarburisation is difficult to quantify, as it varies greatly along the weld line, and there is a smooth transition to the unaffected CGHAZ, but it may be estimated that the CDZ is, on average, 20 – 30 μm in width.

The steel immediately adjacent to the weld line shows near-total coverage by a band of type I carbides. This is shown in detail in figure 8.3(b). These particles are up to 700 nm in size, and are present in a continuous band running between 1 and 2 μm away from the visible weld interface. Some particles of similar size and shape also exist in the CDZ.

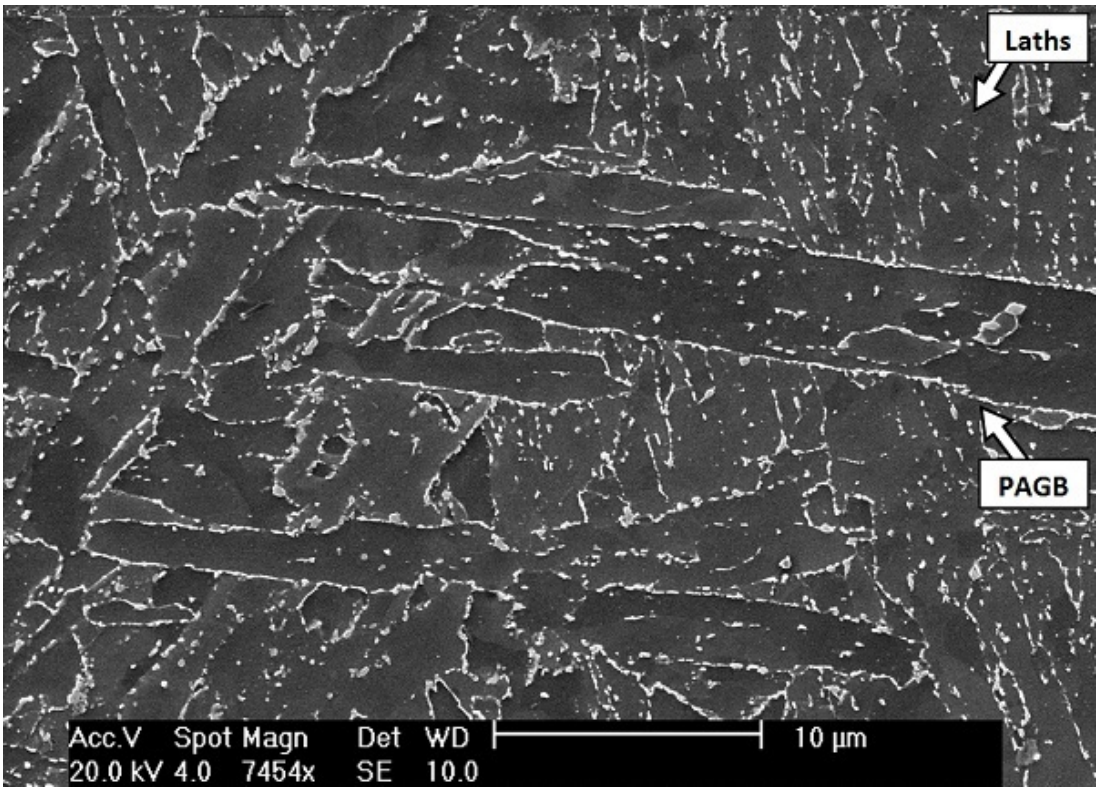

(a)

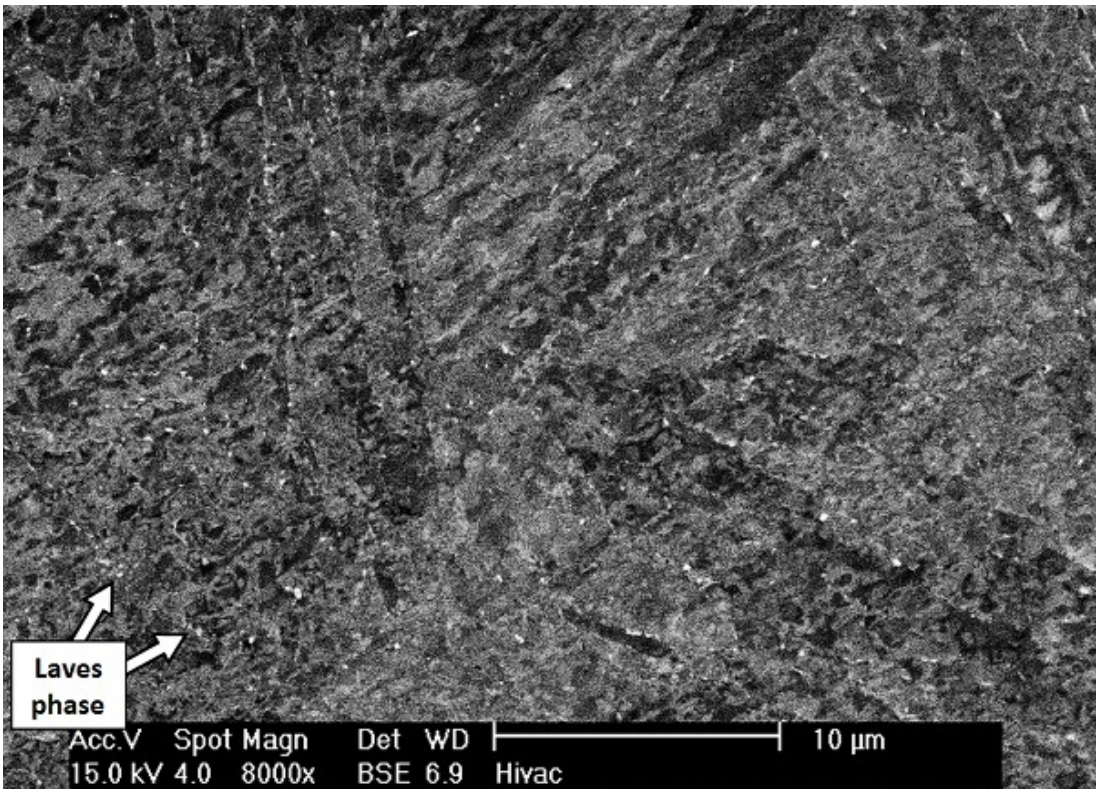

(b)

Figure 8.2: SEM images of the bulk P91 steel in sample FP-C, showing **(a)** an SE image of the sample etched with Vilella's reagent, and **(b)** a BSE image in the polished state. These bulk microstructures are the same in all examined samples.

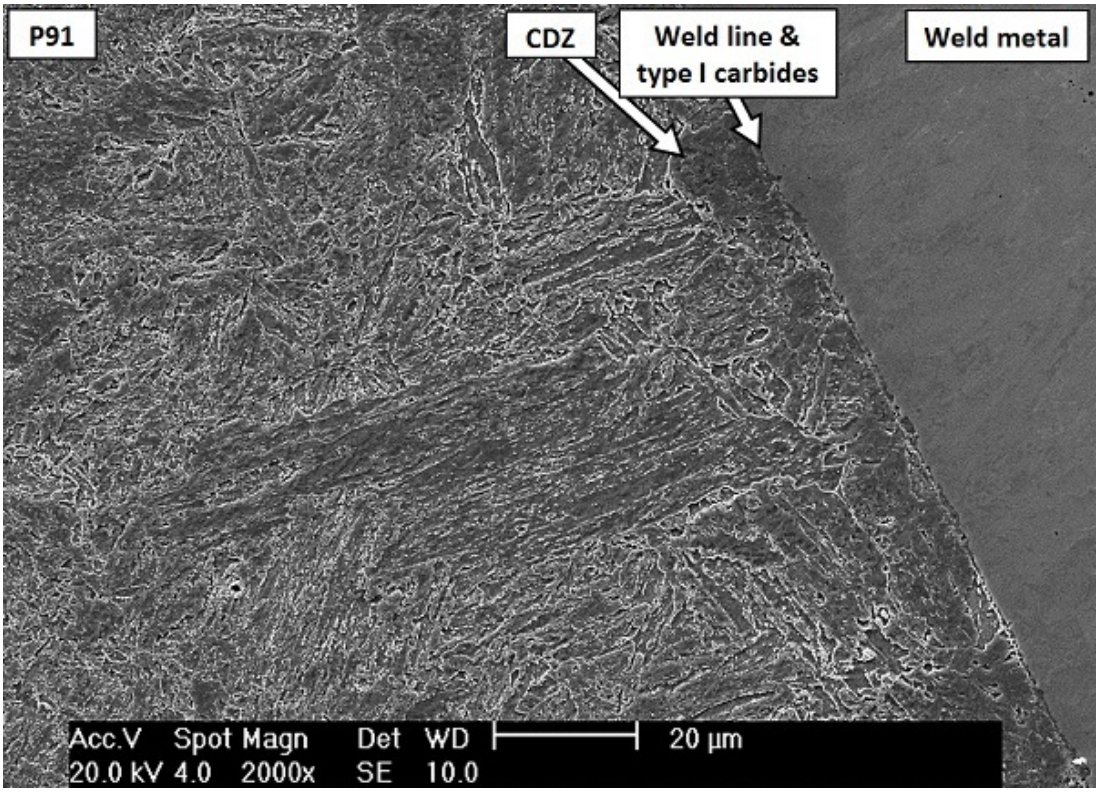

(a)

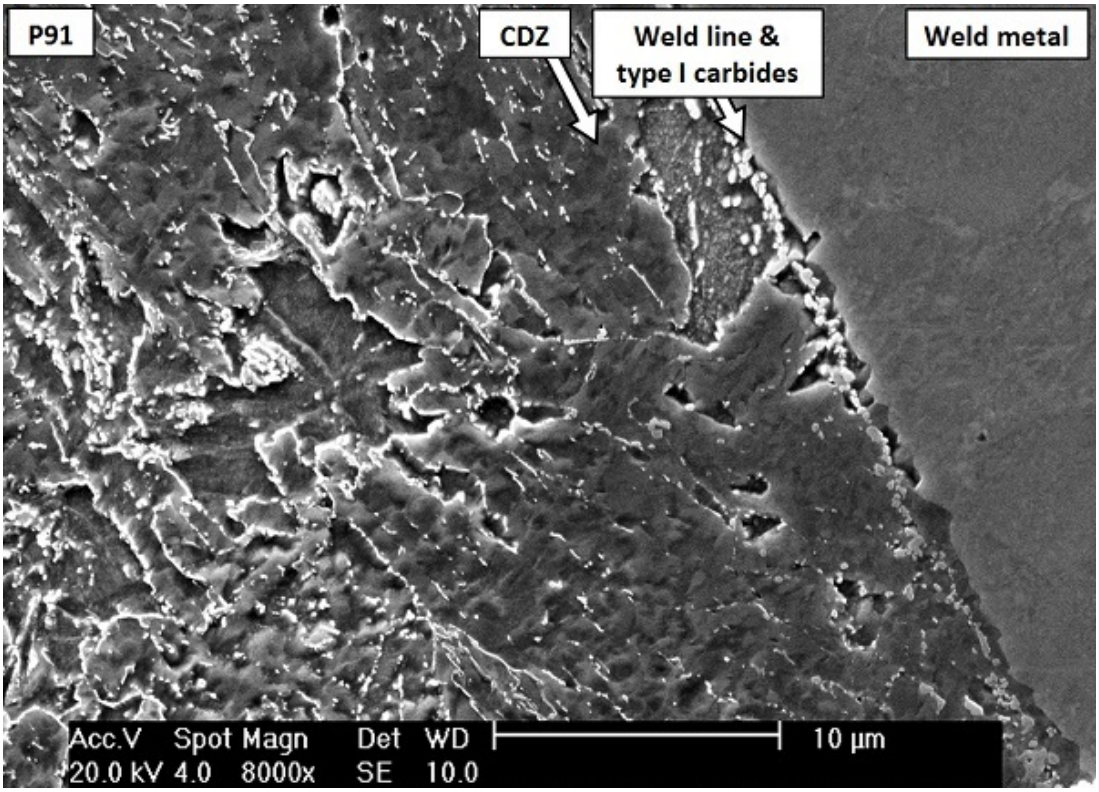

(b)

Figure 8.3: SEM SE images of the P91 steel adjacent to the weld line in sample PS after etching with Vilella's reagent, showing **(a)** a low-magnification image of the area, and **(b)** a closer view of the CDZ and the type I carbide band.

8.3 Microstructure of the Weld Metal

The service-exposed weld metal displays a typical columnar-dendritic structure, characteristic of a welded alloy. The columnar aspect of the structure is shown in figure 8.4, while the dendritic segregation is shown in the inset of this figure in the form of blocky secondary phases, which appear light in BSE images. These precipitates are present in bands aligned with the columnar grains, and often on grain boundaries. These are presumed to be intermetallic phases, rich in niobium and molybdenum, as was previously observed in the P92 – Alloy 625 case.

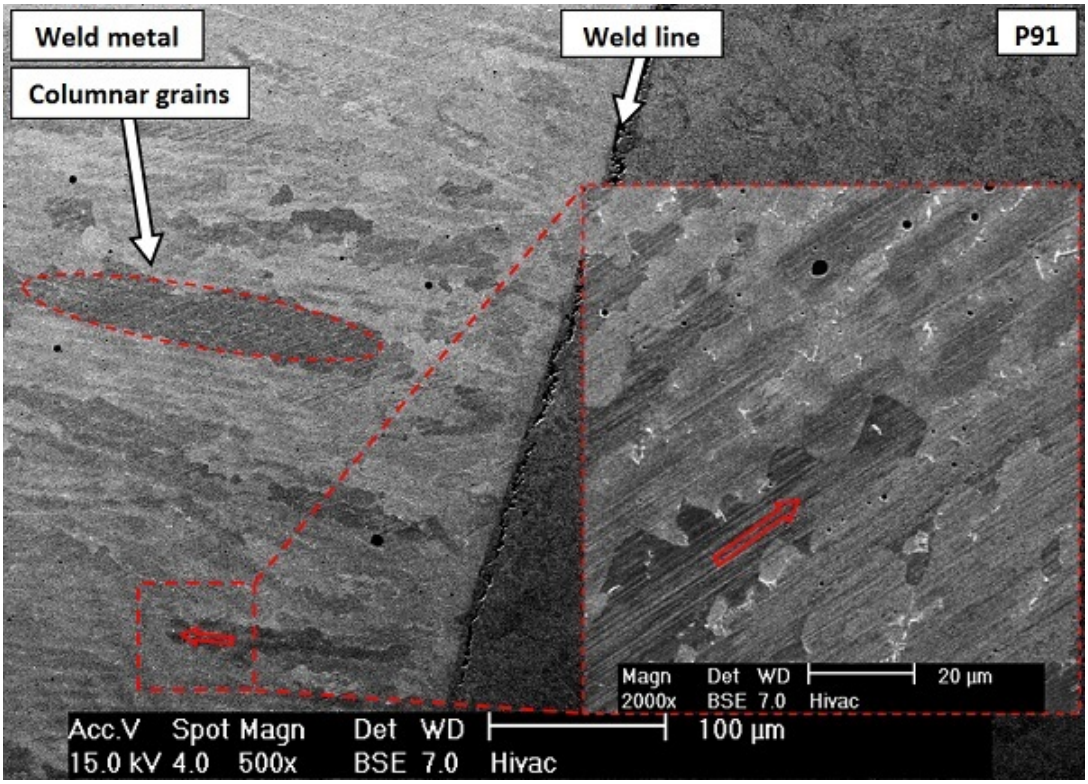

Figure 8.4: SEM BSE image of the weld metal in sample FP-C in the polished condition showing the columnar grain structure, with the inset showing the bands of bright secondary phase particles. The red arrow in the inset indicates the direction of the columnar grains.

Closer examination of the etched condition, as shown in figures 8.5(a) and 8.5(b), reveals the dendritic microstructure, along with arrays of needle-like par-

ticles in the interdendritic areas. These particles may correspond to either γ'' (tetragonal Ni_3Nb) or δ-phase (orthorhombic Ni_3Nb); EDX data shows them to be strongly enriched in niobium, which would support either conclusion. In either case, these particles are likely to be the cause of the extensive hardening of the weld metal. They appear different in form to those seen in the previously-investigated Alloy 625 material, in that they are individually larger but fewer in number, being up to 250 nm in width, and up to 5 μm in length. Additionally, some blocky particles are observed in the interdendritic areas.

The PMZ is also present, with characteristic microstructural features that appear to be 20 – 30 μm in width. Extending outward from the weld line (through the PMZ) are sporadic vein-like features. These veins appear to follow grain boundaries. They are up to 1 μm in width, diminishing with distance from the weld line (though it should be noted that sporadic, disconnected veins are also seen in the bulk material, indicating that they are not solely associated with the interface). These features are shown in figure 8.5(c).

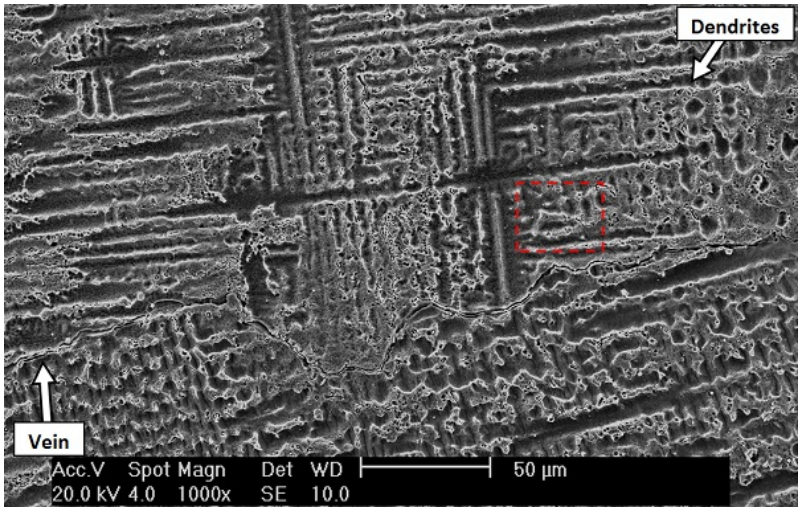

(a)

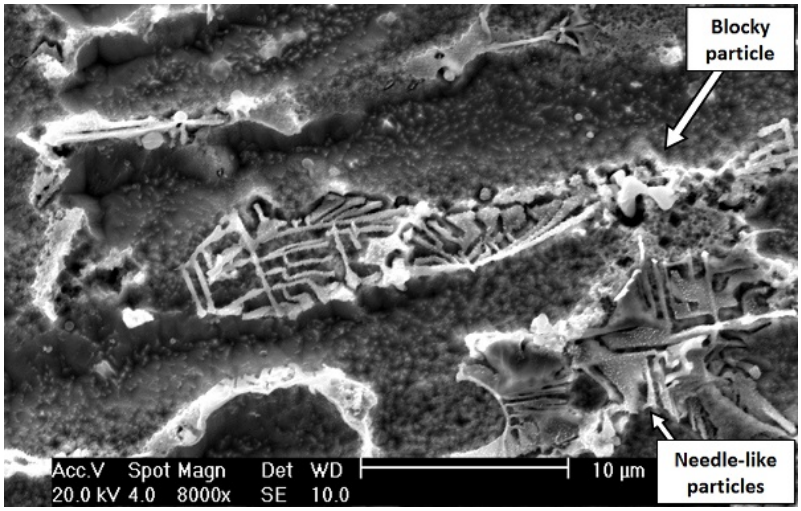

(b)

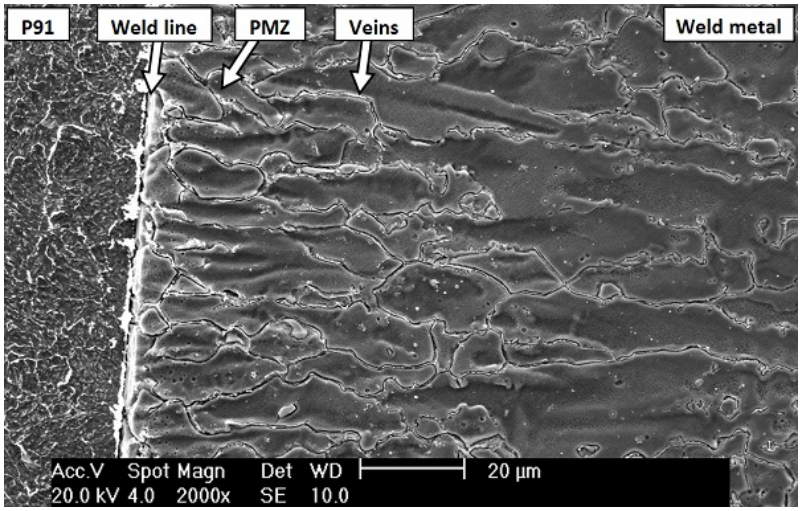

(c)

Figure 8.5: SEM SE images of the weld metal in sample PS after etching with aqua regia, showing **(a)** the dendritic structure in one of the first weld beads, **(b)** a close-up of the area marked with a red box in **(a)** showing the interdendritic particles in more detail, and **(c)** the area adjacent to the weld line, showing the network of vein-like features.

8.4 Chemical Variations Across the Weld Interface

The typical concentration variation of elements around the weld line has been measured semi-quantitatively by EDX point analysis, as shown in figure 8.6 for sample FP-U. These data illustrate the compositional variation across the PMZ, with iron and nickel transitioning smoothly from their levels in the steel to their levels in the weld metal over a range of approximately 50 μm. Molybdenum and niobium levels steadily increase over the width of the PMZ, with peaks and troughs that are likely due to the analysed points coinciding with intermetallic particles. Additionally, there is slight enrichment in chromium and molybdenum at the weld line itself. This indicates that a feature at the weld line, likely the type I carbide band, is rich in these elements.

It is found by EDX point analysis that iron dilution in the first weld pass is around 17 wt%, which compares with the level in the second pass (5-6 wt% Fe) and the nominal level in Alloy 625 ($<$ 5 wt% Fe). Dilution in the first weld pass can be calculated, using equation 2.4, to be d = 15.4 %. These levels of iron dilution explain the observed differences between the first and second weld passes (vis-à-vis hardness levels and etching properties).

The results of carbon level measurement by the low-voltage EDX method are shown in figure 8.7 for sample FP-C. From this, it is clear that there may be slight carbon enrichment at the weld line, which is consistent with the type I carbide band. Away from the weld line, the variation largely falls within the scatter of the results, save for slight depletion in the steel and enrichment in the weld metal. Evidently, the service exposure has not resulted in significant bulk carbon migration to the weld metal; carbon that has diffused may be confined to the vein-like features, such as those observed in figure 8.5(c).

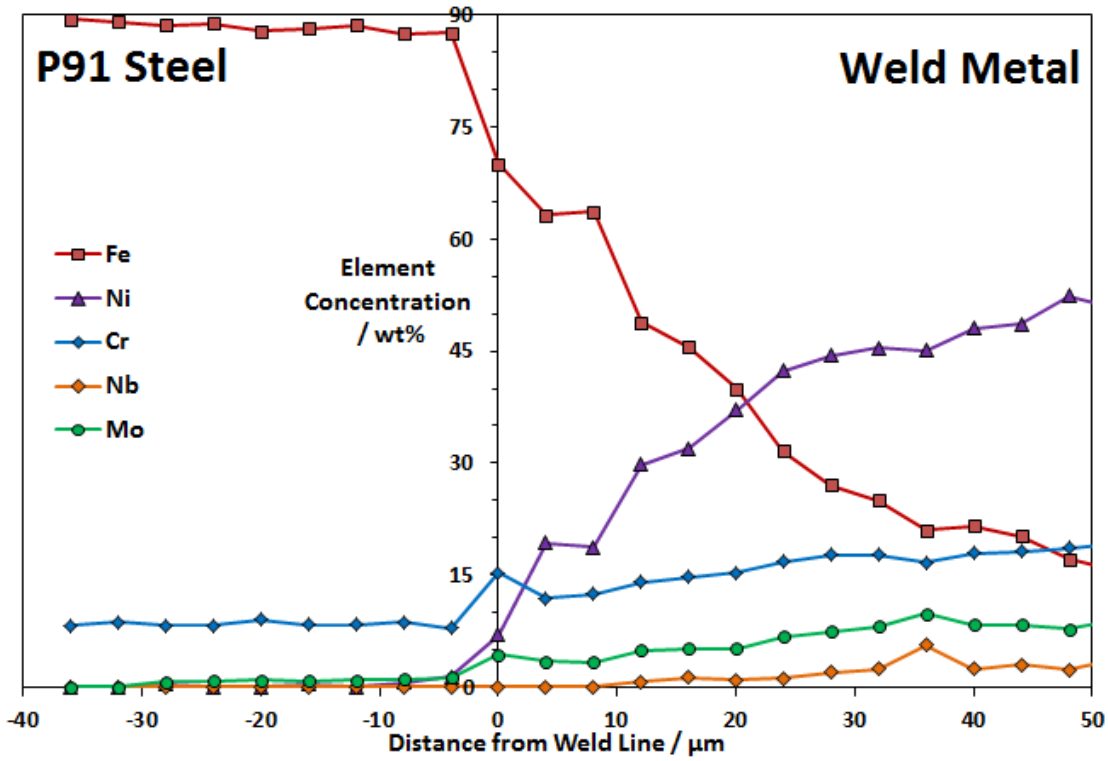

Figure 8.6: EDX measurements of composition across the weld interface in sample FP-U, showing levels of Cr, Fe, Ni, Mo and Nb.

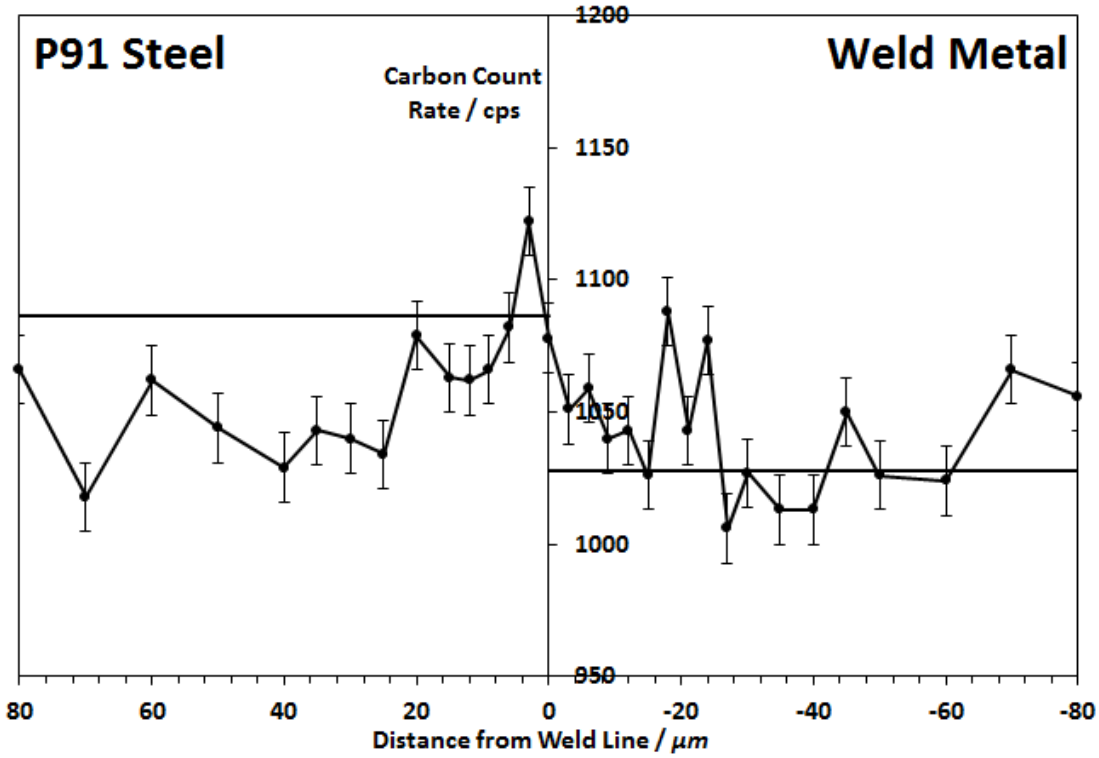

Figure 8.7: EDX measurements of carbon variation across the weld line in sample FP-C (away from the cracked area). The black horizontal lines represent the mean count rates in the two base alloys.

8.5 Oxidation Behaviour

The oxides growing on the surface of the service-exposed P91 steel, as presented in figure 8.8, show a characteristic structure consisting of two main layers; an inner layer of $(Fe,Cr)_3O_4$ (spinel oxide) and an outer layer of Fe_3O_4 (magnetite). There is also a thin layer of Fe_2O_3 (hematite) on top of the magnetite in certain areas. The former two layers are both around 50 μm thick on average, while the latter is approximately 10 μm thick, giving the band a total average thickness of approximately 110 μm. The weld metal, by comparison, has shown only minimal oxidation, confined to the region above the PMZ. This patch of oxide is no more than 20 μm thick, and is of the $(Fe,Cr)_3O_4$ spinel type.

The three-layer structure on the P91 is in line with the known oxidation properties of this material; the presence of all three layers in most areas indicates that the oxide is well preserved (i.e. little has been lost to spallation). The oxide is roughly the same on the inner and outer surfaces of the pipe section, meaning that a total of 220 μm of material has been taken up by oxide. Given that the pipe diameter is 13.5 mm, the reduction in load-bearing area is approximately 1.3%.

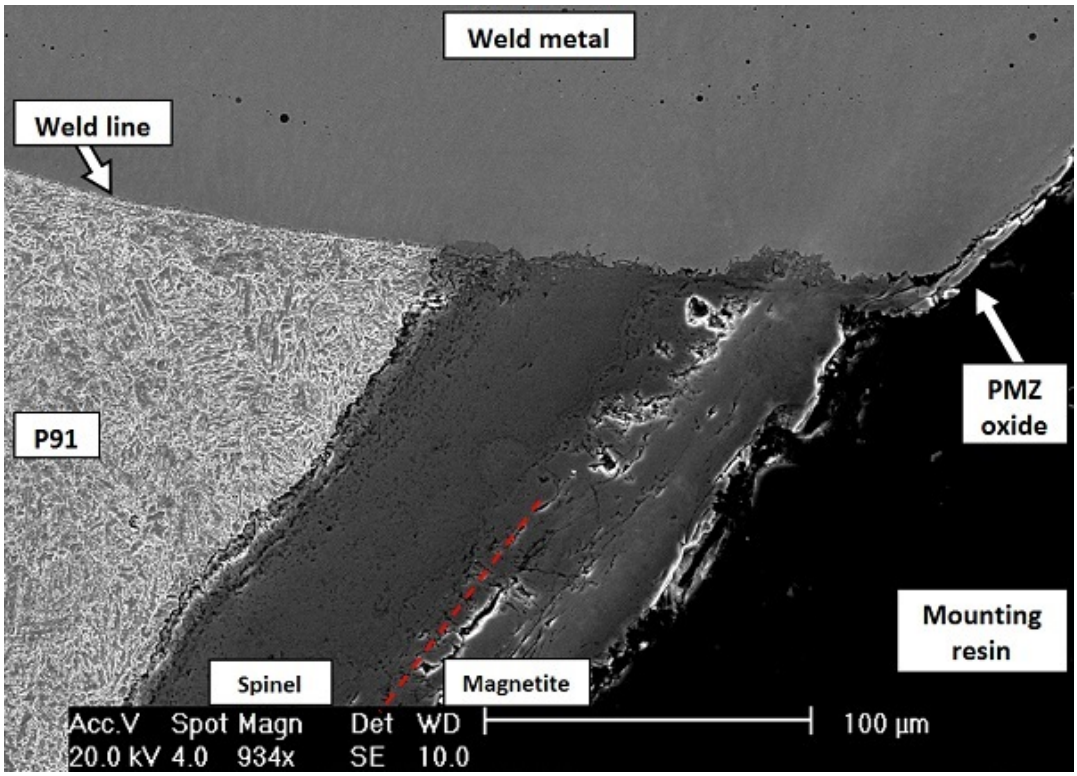

Figure 8.8: SEM SE image of the oxide scale on the surface of sample PS, showing the two-layer spinel-magnetite structure. The outer hematite layer was not present in this particular location.

8.6 Crack Morphology in Sample FP-C

Extending from the outer surface of sample FP-C is a crack, approximately 7.7 *mm* in length, running along the weld line, an overview of which is shown in figure 8.9. Closer inspection reveals that the crack is filled with oxide, which exists as a continuous layer starting from the surface oxide on the steel. The oxide in the crack also contains layers of spinel and magnetite oxides, similar to those seen in figure 8.8. There is a single fissure which can be traced along the entire length of the crack, as well as a number of non-continuous secondary fissures. The width of the oxide layer decreases along the length of the crack, and eventually disappears completely 7.4 *mm* from the surface. The final 0.3 *mm* of the crack consists of oxide-free voids. The extensive oxidation within the crack indicates that it is advancing slowly, though an exact rate cannot be determined.

The advancing crack tip is shown in greater detail in figure 8.10. It consists

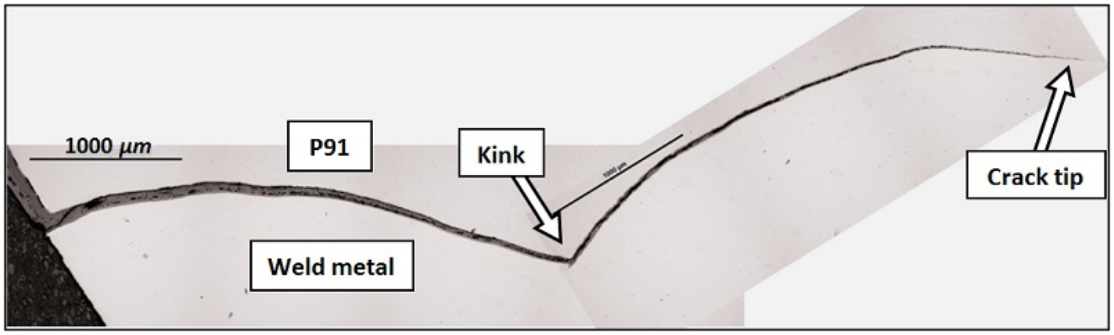

Figure 8.9: A stitch of optical micrographs showing the full extent of the crack in sample FP-C. It follows a path of 7.7 mm along the weld line.

of cavities linked by fissures, presumably caused by creep strain accumulation. Although the oxidised sections of the crack appear to be situated on the weld line, the unoxidised advancing tip is clearly within the steel, between 5 and 10 μm away from the weld line. This places the crack tip in the CDZ. The cracking mode may hence be described as 'type II', according to the definitions set out in section 2.2.4.

The advancing unoxidised tip of the crack is characterised by creep voids, between 3 and 8 μm in diameter, increasing in size with distance from the tip. These are linked by narrow fissures, the width of which also increases with distance from the tip (to the extent that some appear to be voids in their own right). These voids and fissures follow a slightly circuitous path, but are confined to the CDZ area. Around the crack are occasional isolated voids in the CDZ, on the weld line and on type I carbides. These voids are smaller than those constituting the crack, generally being only 1 – 2 μm across. Some voids of this manner also exist in the CDZ ahead of the crack tip, implying that the voids form first and are subsequently joined by fissures. It is not apparent if the voids and fissures form preferentially on any particular microstructural features.

FIB sectioning, by the same method as described in the context of TEM sample extraction in section 4.3.4.1, reveals that these voids exist below the surface of the sample. This is shown in figure 8.11. The sub-surface voids are different in form to those on the surface as they have not been affected by the grinding and polishing

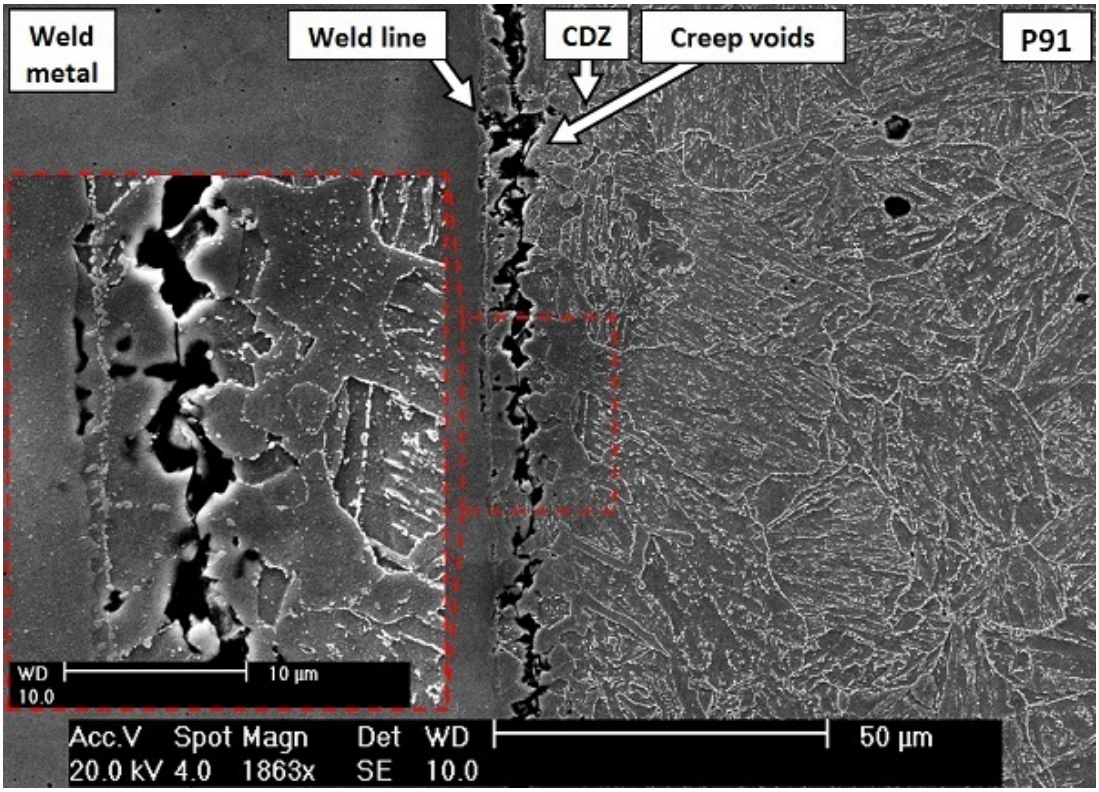

(a)

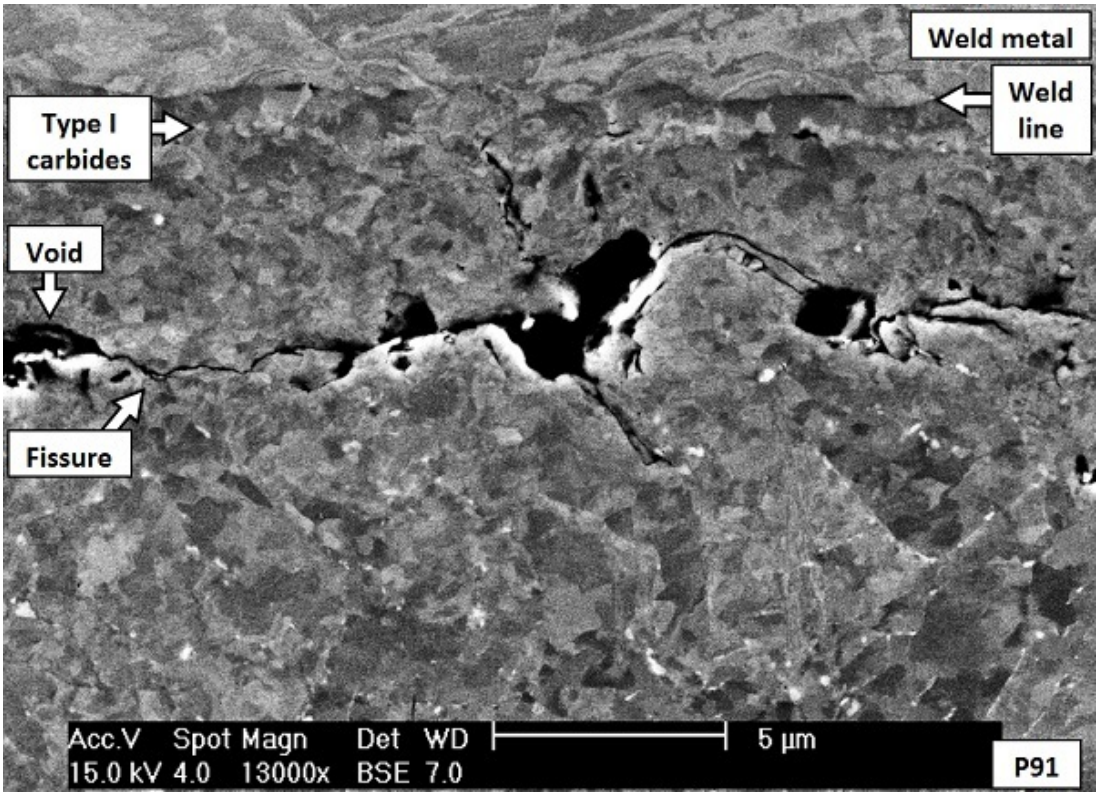

(b)

Figure 8.10: SEM images of the unoxidised crack tip in sample FP-C, showing **(a)** an SEM image of the surface etched with Vilella's reagent, and **(b)** a BSE image of the polished state.

processes.

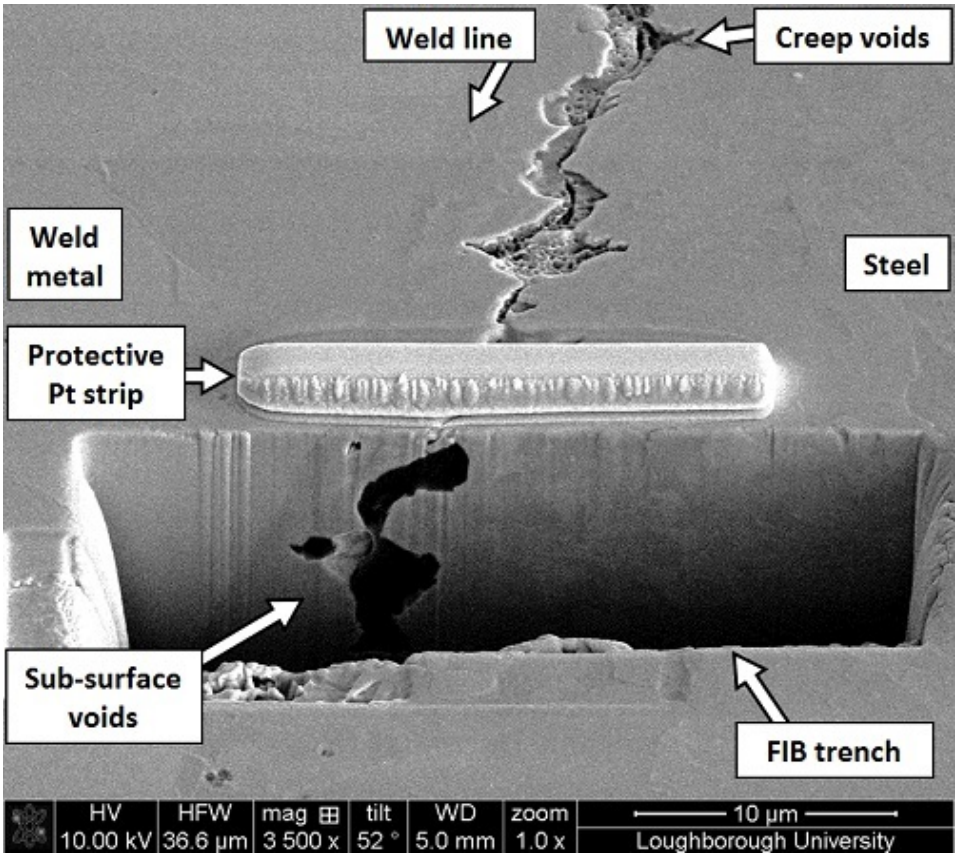

Figure 8.11: An SEM SE image of creep voids near the tip of the crack in sample FP-C, in the polished state, viewed at an angle of 52° to the sample surface. A trench dug across the crack using the FIB, in the same manner as done for TEM sample extraction, reveals creep voids beneath the sample surface.

8.7 TEM Analysis of Sample PS

To aid in the understanding of the microstructural evolution at the weld line, two TEM-FIB specimens were collected. These were both taken from sample PS, to avoid the risk of encountering creep voids that may have been present in samples FP-C or FP-U. One contained mostly steel and the other contained mostly weld metal. This allowed approximately 16 μm of material either side of the weld to be analysed.

The specimen containing primarily P91 steel is shown in the form of a STEM image pair in figure 8.12, with corresponding STEM-EDX maps in figure 8.13. The

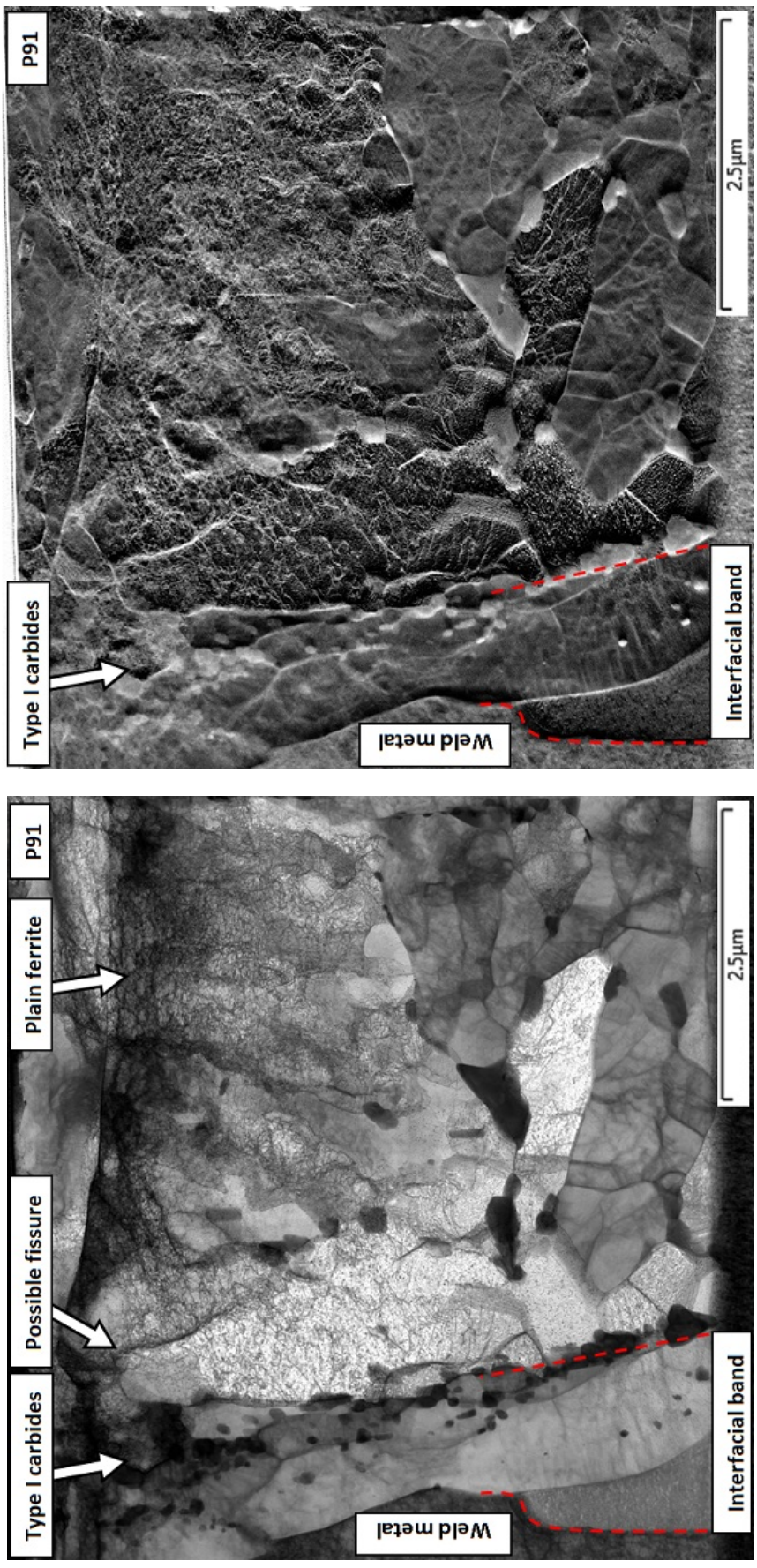

Figure 8.12: STEM images of the steel adjacent to the weld line in sample PS, showing **(a)** a bright field image, and **(b)** a HAADF image.

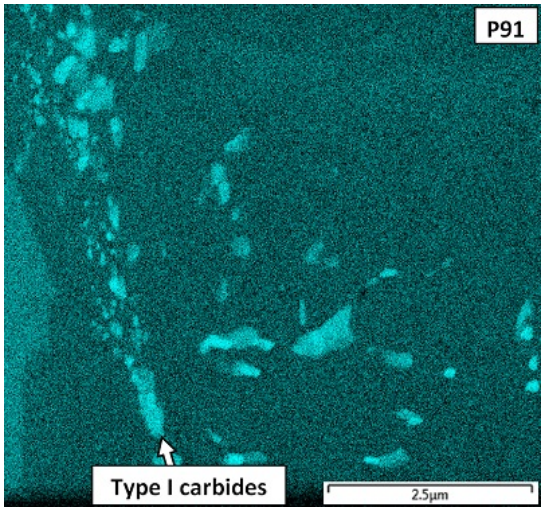

(a) Cr EDX map

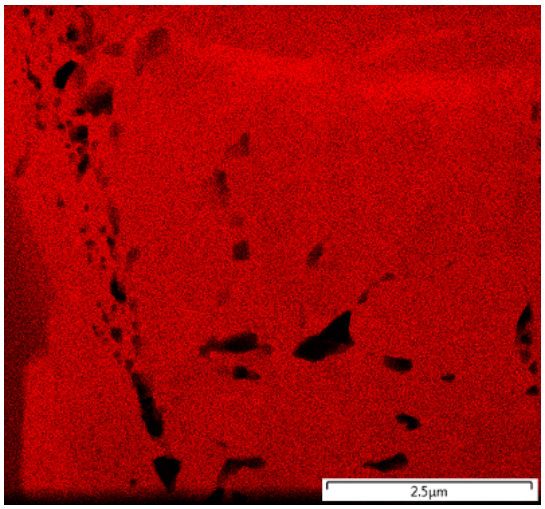

(b) Fe EDX map

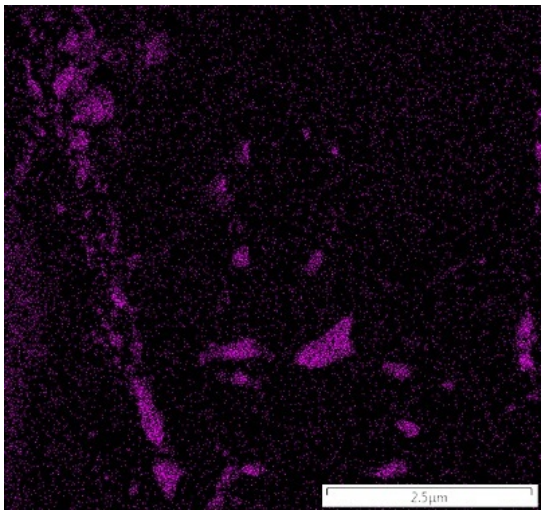

(c) Mo EDX map

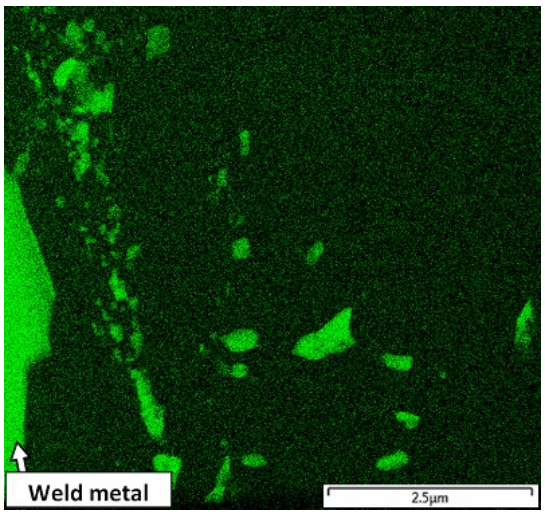

(d) Ni EDX map

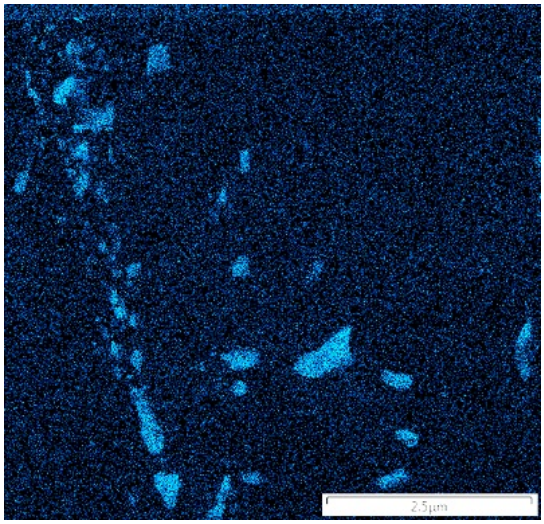

(e) Si EDX map

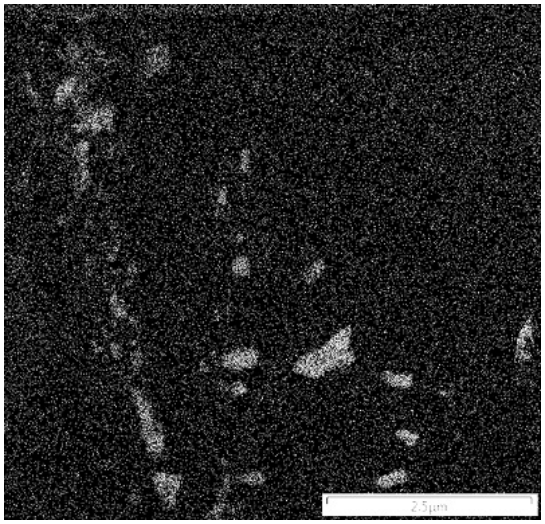

(f) V EDX map

Figure 8.13: STEM-EDX maps of the steel next to the weld in sample PS.

start of the weld metal is seen at the left of the figures, most apparently in figure 8.13(d) in the form of step change in contrast. The type I carbide band is observed as a semi-continuous layer of particles parallel to the edge of the weld metal and around 1 μm away from it, as was seen in SEM micrographs. These particles show significant variation in size; the largest are around 500 nm in diameter, while the smallest are around 100 nm. The smaller particles are generally circular, while the larger ones are typically elongated to some extent in the plane of the weld line. Despite the differences in size and morphology, the particles all appear to have roughly the same stoichiometry, being enriched in Cr, Mn, Mo, Ni, Si and V (though not Nb). STEM-EDX analysis also reveals that both carbon and nitrogen are present in these particles, indicating that they are in fact carbonitrides. The average composition of these particles is given in table 8.1.

Diffraction analysis of the larger particles has been performed, the results of which are presented in figure 8.14. This reveals the particles are FCC in structure, with a lattice parameter of approximately 11.1 Å. Observed simultaneously with diffraction from the type I carbides is diffraction from the surrounding BCC matrix, with a measured lattice parameter of 2.98 Å. This is 4% larger than the database lattice parameter for α-ferrite. This indicates that the lattice parameter of the carbide is also overestimated by the same proportion, which would make the true value approximately 10.6 Å. This corresponds most closely to $C_{23}C_6$, but given the significant chemical differences this is far from certain.

In the area analysed in figure 8.14, the FCC-[011] zone axis of the particle and the BCC-[001] zone axis of the matrix were observed together. This indicates that there is an orientation relationship between these two phases, which can be expressed as:

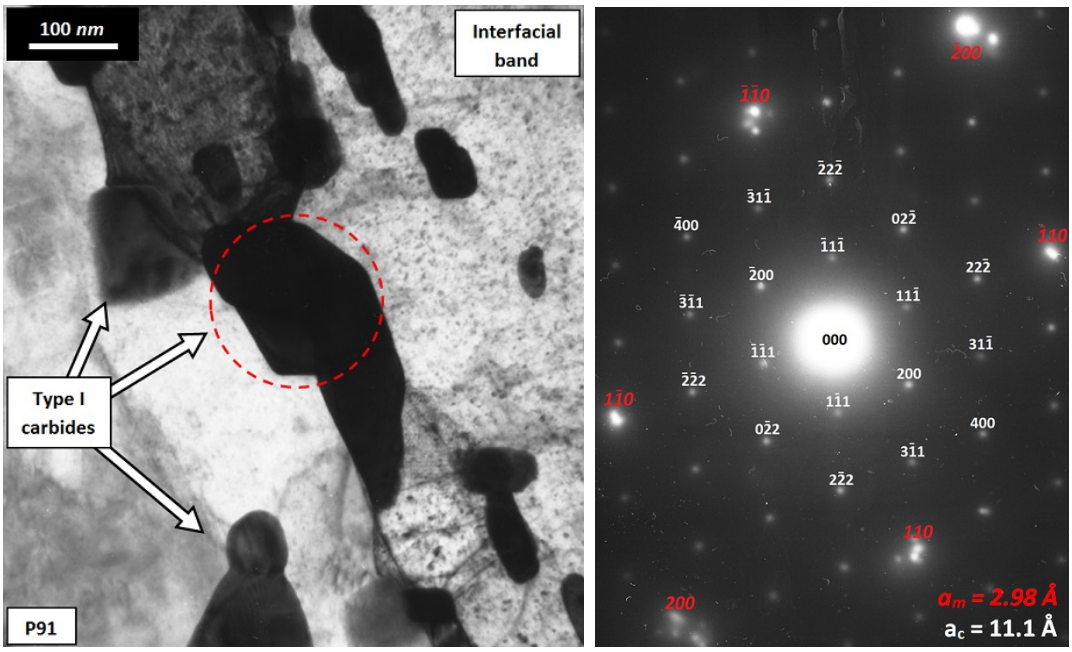

(a) **(b)**

FIGURE 8.14: TEM data from a type I carbide in sample PS, showing **(a)** a bright field image, and **(b)** an indexed SADP taken from the particle in the centre of the image (circled in red). The indices labelled in white text correspond to diffraction from the carbide, and are of the FCC-[110] zone axis, while the indices labelled in red italics correspond to matrix diffraction from the BCC-[001] zone axis. The orientation relationship between these phases is stated in equations 8.1 and 8.2.

$$\{011\}_{Carb} \parallel \{001\}_{BCC} \tag{8.1}$$

$$\langle 0\bar{2}2\rangle_{Carb} \parallel \langle 200\rangle_{BCC} \tag{8.2}$$

The type I carbides have formed on the edge of the now-familiar interfacial band. The band itself is largely free of precipitates, save for occasional small particles (50 – 100 *nm* in size and of approximately the same chemistry as the type I carbides). Its microstructure appears to be that of featureless ferrite, with no visible martensite laths. The bright field-dark field pair of images shown in figure 8.15 confirms that the band is of distinctly different orientation to either the steel or the weld metal, while diffraction analysis reveals the band to be BCC in crystal structure. The composition of the band is given in table 8.1.

Away from the interface, the martensitic structure of the steel appears to be

Table 8.1: Approximate compositions of the various types of particles and the interfacial band in sample PS, as measured by STEM-EDX. Particle compositions will be approximate due to overlap with the metal matrices. The levels of carbon and nitrogen are not quantified, and are instead categorised as strong (**S**) or weak (**W**) signals.

	Element (wt %)								
	C	Cr	Fe	Mo	N	Nb	Ni	Si	V
Type I particles	**S**	33.9	6.6	22.1	**S**	0.7	27.2	5.8	3.5
Uncertainties (±)	-	0.8	0.3	1.5	-	0.3	0.7	0.3	0.2
Interfacial band	**W**	8.1	89.0	< 0.5	**W**	< 0.5	1.8	< 0.5	< 0.5
Uncertainties (±)	-	0.2	0.5	0.3	-	0.2	0.2	0.1	0.1
Nb-rich particles	**S**	6.1	8.6	11.2	**S**	66.7	6.2	0.8	< 0.5
Uncertainties (±)	-	0.3	0.4	1.7	-	1.9	0.3	0.2	0.1
Mo-rich particles	**W**	16.1	31.0	24.3	**W**	3.9	23.5	1.2	< 0.5
Uncertainties (±)	-	0.8	1.3	2.0	-	1.2	1.1	0.3	0.2

in the advanced stages of tempering, with large areas of ferrite present (up to 9 μm^2). This is not uniform across the specimen, as some areas (most clearly the bottom-right) have retained some laths. There is also evidence of creep damage, in the form of a high dislocation density (manifested in the form of curved lines within grains) and nano-scale fissuring.

There are some precipitates away from the type I carbide band, though not nearly as many as one would expect to see in P91 steel, and not of the expected chemistries. Those that remain have coarsened, with the largest being nearly 1 μm in length. This is in line with the SEM observations that this area of the steel is partially decarburised. These precipitates away from the interface have approximately the same compositions as those that comprise the type I carbide band. Critically, there are no vanadium-rich MX-type precipitates in the steel. The absence of these particles goes some way toward explaining the ferrite reformation and creep damage, since these particles are crucial to the stability, integrity and creep resistance of P91.

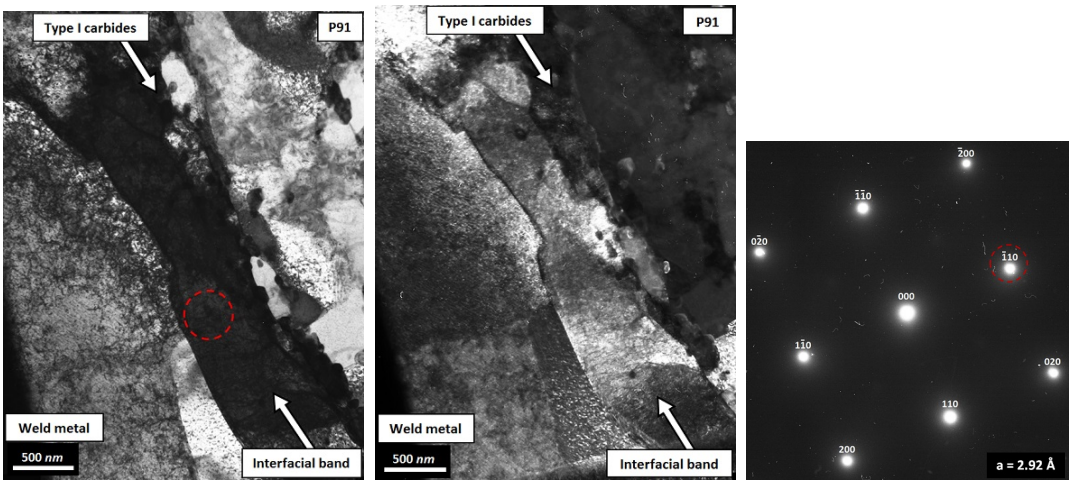

(a) **(b)** **(c)**

FIGURE 8.15: TEM data from the interfacial band in sample PS, showing **(a)** a bright field image, **(b)** a dark field image, and **(c)** an indexed SADP from the interfacial band of the BCC-[001] zone axis. The dark field image in **(b)** was gathered from the circled diffraction spot in **(c)**, while the SADP was formed from the circled area in **(a)**.

The FIB specimen taken from the weld metal reveals two large, relatively featureless grains, with clusters of Nb and Mo-rich particles at various points along the grain boundaries. Iron dilution is high, as is to be expected, peaking at 57 wt% Fe adjacent to the weld line. Diffraction analysis indicates that the metal matrix here is FCC. There is some evidence of dislocations in the weld metal grains, in the form of the same intragranular curved line features as were seen in the steel specimen, indicating that creep strain may also have accumulated here.

Closer inspection of the grain boundary particles, shown in figure 8.17, reveals that they are actually two separate families, consisting of large Nb-rich particles with smaller Mo-rich particles precipitating around them as satellites (much like the particles seen in the weld metal of sample LTA, seen in figure 5.41). The former particles are elongated in the direction of the grain boundaries, being up to 500 *nm* in length, while the latter are more circular and no more than 100 *nm* in diameter. Measured average compositions of these particles are given in table 8.1. From these compositions, and SADPs, the larger Nb-rich particles are found to be MX-type particles, FCC in crystal structure, of type Nb(C,N).

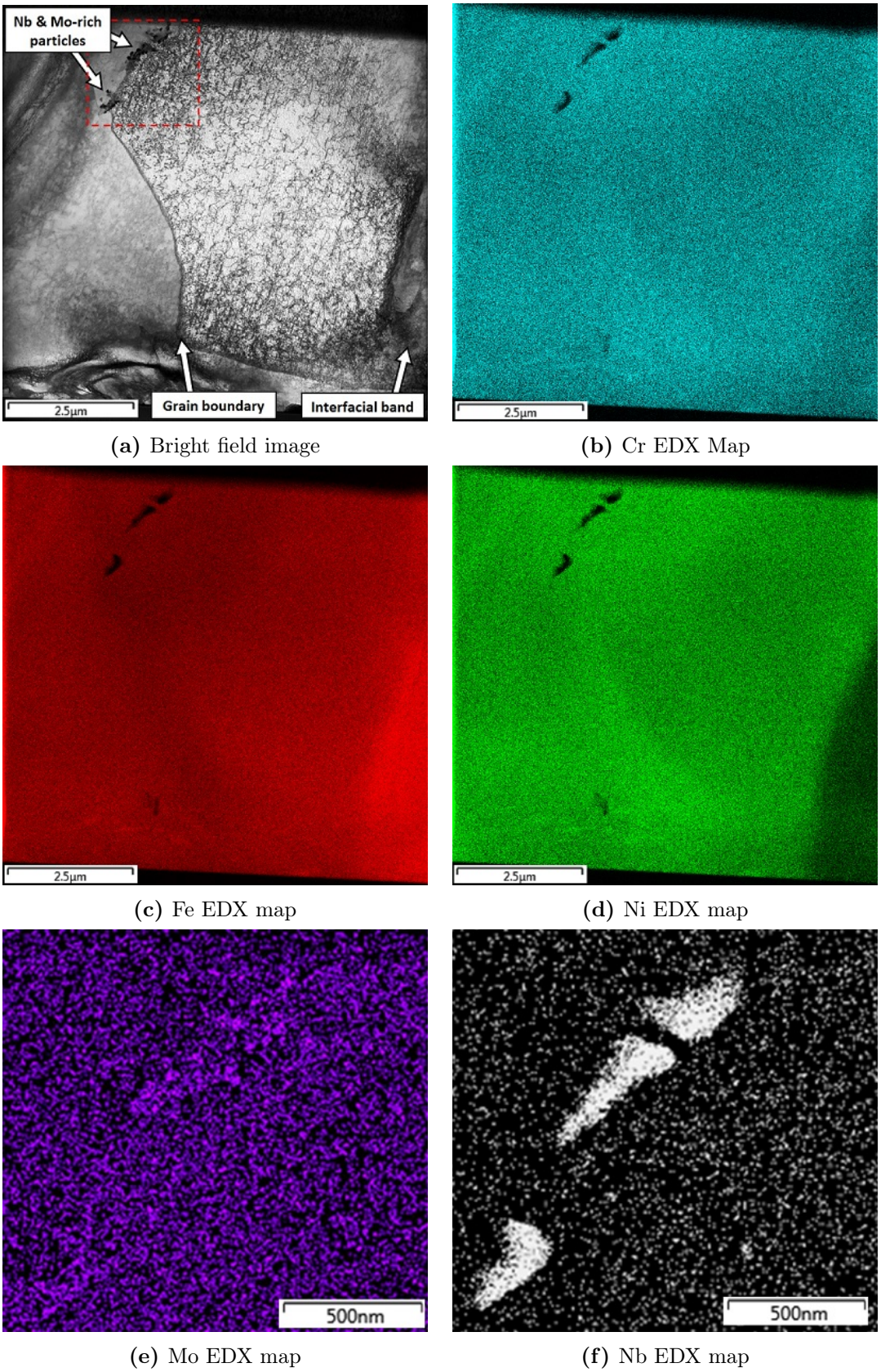

(a) Bright field image

(b) Cr EDX Map

(c) Fe EDX map

(d) Ni EDX map

(e) Mo EDX map

(f) Nb EDX map

Figure 8.16: STEM data of the weld metal adjacent to the weld line in sample PS. Maps **(e)** and **(f)** are zoomed in on the area in the red box in image **(a)**

The smaller particles are too small to identify by diffraction, but based on their composition (most significantly their lack of carbon or nitrogen) they are likely to be intermetallic particles.

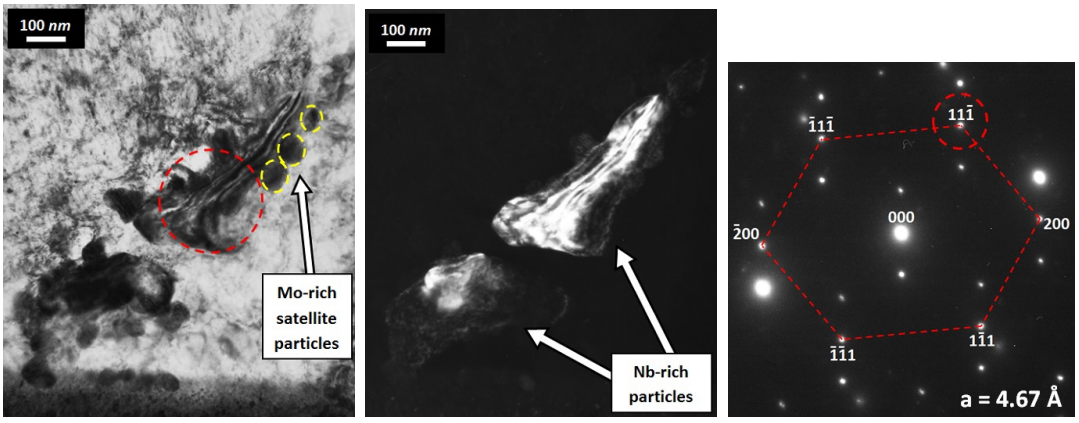

(a) **(b)** **(c)**

Figure 8.17: TEM data from the weld metal particles in sample PS showing the large Nb-rich core particles and the smaller Mo-rich satellite particles. Figure **(a)** is a bright field image, **(b)** is a dark field image, and **(c)** an indexed SADP, from the area circled in **(a)**, of the FCC-[011] zone axis of the Nb-rich particle, consistent with MX phase. Strong double diffraction was observed here, so the main pattern has been marked with red dotted lines. The dark field image was constructed from the circled diffraction spot.

8.8 Discussion

In this section the results of these two cases, particularly with regards to performance in service environments, will be discussed, with reference to previously-discussed cases where appropriate. This will tie in with a consideration of possible weld failure modes and mechanisms, and how these may be mitigated based on the present findings.

8.8.1 The Alloy 625 Weld Metal

The weld metal of the ex-service weld, an iron-diluted form of Alloy 625, has shown more extensive hardening than sample LTA from the P92 – Alloy 625 system. This may be attributable to its lower iron levels, its longer thermal exposure,

the lower temperature of the service exposure, or a combination of the these factors. Microstructural analysis of this ex-service Alloy 625 reveals the acicular interdendritic particles in this material to be of different form to those of samples STA or LTA, being far fewer in number but individually coarser (by a factor of as much as 5).

The reason for this difference in the form of the particles is not immediately apparent. It may be that the two sets of particles are of the same type, but are merely coarser in the ex-service condition. Alternatively, they may be different types of particle entirely. This would make the smaller particles in samples STA and LTA γ''-phase, and the larger particles in the ex-service samples δ-phase, since the latter is known to evolve from the former during ageing [50].

8.8.2 Interdiffusion at the Ex-Service Weld

There is evidence to indicate that some diffusion of carbon and nitrogen has taken place across the P91 – Alloy 625 weld interface during service exposure. This has been revealed by EDX measurements of carbon count rate across the weld interface, and is reflected in microstructural changes (precipitate dissolution in the CNDZ, veins in the CNEZ). The extent of diffusion appears to be comparable to that seen in sample LTA of the P92 – Alloy 625 system.

TEM analysis of the precipitate distribution in the CNDZ of the ex-service sample has revealed it to be entirely different to that of any of the other samples, and certainly different to the ideal distribution of P91 steel. Only a few particles remain, and are of a single type: either $M_{23}X_6$ or M_6X carbonitride. A conclusive distinction between these phases cannot be made due to the similarities in crystal structure, while no precedent exists for particles of either type having the measured chemistry. Many of these particles are coarser than the $M_{23}C_6$ carbides present in other samples. There are no MX carbonitrides at all, and large areas that are precipitate-free, indicating that much precipitate dissolution has taken place.

TEM analysis of the weld metal adjacent to the weld interface has revealed the presence of relatively coarse niobium carbonitrides, of the form Nb(C,N). As was the case in the P92 – Alloy 625 system, the fact that these particles contain nitrogen makes it highly likely that their formation and/or coarsening is supplied by diffusion from the steel, since Alloy 625 contains nominally little to no nitrogen.

The niobium-rich particles are found to be surrounded by small molybdenum-rich satellite particles, which are believed to be intermetallic in nature but cannot be conclusively identified. Almost identical precipitation behaviour was observed in the weld metal of sample LTA, indicating that it may be a standard phenomenon in such systems. The reason why these molybdenum-rich particles precipitate in this manner is not known.

In this system, the type I carbides are far more numerous and more pronounced than in the P92 – Alloy 625 system. They are present in a near-continuous strip along the edge of the interfacial band. Many of these particles are far coarser than any such particles observed in P92 cases, which may be due to the lack of boron (though the different nature of the ageing cannot be discounted). These particles are all of an unusual mixed chemistry, being either $M_{23}X_6$ or M_6X in structure (the same as the occasional particles in the CDZ). There is found to be an orientation relationship between these type I carbides and their host matrix, as described by equation 8.2, though this has not been observed in other samples and hence may not represent a general trend.

8.8.3 Mechanical Properties and Failure Modes

The microstructural evolution of DMWs, as described and discussed thus far, will have an impact on mechanical properties. This in turn may lead to creep failure under the various stresses (pressure stress, bending stress, residual stress from welding or thermal expansion, etc.), and has already done so in the case of ex-service sample FP-C. These effects will be discussed in this section, along with

potential strategies for mitigating failure.

8.8.3.1 Bulk Hardness Variations

The microhardness data gathered from Alloy 625 samples shows a distinct trend of hardness increasing during high-temperature exposure. This is now shown to be a result of precipitation of γ'' and/or δ-phase particles. The effect is most pronounced in the ex-service case, likely due to a combination of longer exposure time and lower iron content. Measurements indicate that as-welded Alloy 625 (in sample A-W) has a hardness of 210 – 220 VHN_{100}, while the aged weld metal has a hardness up to 352 VHN_{100}.

This precipitation hardening is a known ageing response of Alloy 625, and is useful in many situations, but it is not necessarily beneficial to the properties of a DMW in service conditions. While it will strengthen the weld metal, it will have the effect of reducing the amount of creep strain that it can accommodate. This in turn will concentrate creep strain in the steel, which may already be vulnerable due to the precipitate-poor CNDZ. As such, a softer weld metal may be conducive to better creep performance in DMWs.

8.8.3.2 Phase Changes around the Weld Interface

Analysis by TEM has shown that the ideal precipitate structure in the P91/92 steels, consisting of dispersed $M_{23}C_6$ carbides and MX carbonitrides, breaks down near the weld interface with Alloy 625 (i.e. in the CNDZ). This is most apparent in the ex-service P91 – Alloy 625 sample, in which no MX particles at all are observed in the CNDZ, and the carbides are few in number, coarse and of unusual chemistry. As was described in section 2.1.3.2, dispersed precipitates are critical to the creep resistance of P91/92 steels, as they pin features such as dislocations and lath boundaries. Without these precipitates, these features may disappear, leading to the reformation of ferrite crystals (as has been observed by TEM) and

hence disproportionately rapid accumulation of creep strain in this area, potentially leading to failure. This is observed in the failed ex-service P91 – Alloy 625 weld, as the advancing creep crack is located in the CNDZ.

The coarse type I carbides adjacent to the CNDZ may play a role in initiating creep failure, as their brittle nature may cause them to serve as sites for void formation. This is observed to a limited extent in the failed ex-service weld, in the form of some small isolated voids on or around the type I carbide band. However, the majority of the voids contributing to failure are in the CNDZ, 5 – 10 μm away from the band. This would indicate that type I carbides are not directly complicit in this particular failure mechanism. However, coarse particles in the CNEZ may lead to void formation; this could include the isolated coarse carbides in the CNEZ of the P91 steel, or the coarse Laves phase particles in the CNEZ of the P92 steel (assuming this failure mechanism can act in P92).

Another possible point of weakness resulting from phase changes are the grain boundaries in the weld metal CNEZ, many of which are believed to contain carbides/carbonitrides (the 'vein-like' features). Such a large number of particles on the grain boundaries may cause them to be susceptible to brittle failure. However, no evidence of such failure has been observed, indicating that it is not the point of greatest weakness.

8.8.3.3 The Role of Oxide Notching

The form of the crack in the failed ex-service sample ('FP-C') shows that the width of the oxide steadily decreases as a function of distance from the outer surface of the pipe. This makes it likely that the crack initiated at the outer surface and has progressed inwards (at a slow pace, judging by the oxide growth inside the crack). Oxide notching must therefore be considered as a cause of initiation; as described in section 2.2.4, it is a known factor in DMW failure as it reduces the load-bearing area at the weld line, hence concentrating stress on the

remaining material.

Since the cracked surface at the weld line in this sample has been so badly damaged, it is impossible to accurately say if oxide notching was the initiating factor. However, the propensity for oxide notching can be investigated at un-failed surfaces. It is, for instance, observed at the inner surface of the failed pipe. It is also observed in the P92 – Alloy 625 system, in both samples STA and LTA. This points to a number of important trends:

1. Oxide notching can occur in systems that are not subject to pressure or loading stresses (though the effect of stresses due to thermal expansion mismatch cannot be discounted).

2. Oxide notching can affect welds involving both P91 and P92 steel; according to the findings of Mathiazhagan et al. [48], that oxide growth is more rapid on P92, then it is possible that notching will pose more of a threat in such systems.

3. While oxide notching may be common, it does not necessarily result in failure; this is in agreement with the findings of Roberts and Ryder [126] on ferrite-austenite DMWs involving 2.25Cr-1Mo steel.

8.8.4 Mitigation of DMW Failure

Based on the results and discussion presented here, it may appear that the most important step towards improving the performance of DMWs involving P91/92 steels would be to mitigate the CNDZ. By inhibiting the diffusion of carbon and nitrogen, an ideal phase balance could be maintained in the steel. To that end, P87 may be a more suitable weld metal than Alloy 625. The properties of aged P91 – P87 – P92 weld, particularly with regards to diffusion and phase behaviour, will be described and discussed in the following chapter.

One important step in inhibiting DMW failure may be to restrict growth of oxide at the weld interface, as notch formation appears to be a possible initiating factor in weld failure. While protecting the weld from oxidation (for instance, by capping or coating it) would not affect the underlying cause of DMW weakness, it would reduce the likelihood of creep cracks being able to initiate and propagate, potentially increasing the service life of vulnerable components.

8.9 Summary

The findings from this weld system can be summarised by the following key points:

- Failure has been observed at an ex-service weld interface between P91 steel and nickel Alloy 625, after c. 40,000 hours of operation at 565 $°C$.
- The form of the failure has been found to be low-ductility creep, advancing slowly (based on the extensive oxidation) along the weld line.
- The crack initiated at the outer surface of the pipe, and is likely to have been assisted by oxide notching.
- The advancing tip of the crack is located in the precipitate-poor CNDZ of the steel, 5 – 10 μm from the weld line. This may have been exacerbated by extensive hardening of the weld metal, acting to concentrate strain in the CNDZ.
- A band of coarse type I carbides has formed in the steel adjacent to the weld line, covering it nearly completely. They are up to 700 nm in size, either $M_{23}X_6$ or M_6X in structure and of highly unusual chemistry.
- TEM analysis indicates that the CNDZ contains only a few coarse particles, of the same form as the type I particles, and no MX carbonitrides.

Chapter 9

Industrial Case Study 2: P87 Filler Metal

With the preceding chapters having examined the evolution that occurs at welds involving Alloy 625, and the mechanical issues that may result, this chapter will focus on the evolution of a laboratory-aged weld between P91 and P92 steels, with EPRI P87 as the filler metal. As described in section 2.1.5.2, P87 has been developed with the purpose of mitigating DMW failures involving P91/92 steels. The potential effectiveness of P87 in this role will be evaluated and discussed.

The sample in question, as described in section 4.1.3, was given a PWHT of 746 $^{\circ}C$ for 1 hour after being welded, followed by a longer treatment at 649 $^{\circ}C$ (1200 $^{\circ}F$) for 3149 hours. Due to the weld layout, there are two separate interfaces here: P91 – P87 and P92 – P87.

9.1 Microhardness Profiles

Microhardness examination of the P91 – P87 and P92 – P87 interfaces was carried out, using a Buehler MMT-7 manual hardness indenter to perform single line scans across the weld lines. A load of 50 g was used. Indents around the interface were spaced by 25 μm in the direction perpendicular to the weld line (arranged diagonally at an angle of around 30° to the weld line so as to avoid indents affecting one another). Further away from the weld, indent spacings were increased to 100 or 250 μm, depending on location. The results of these scans are presented in figure 9.1.

The results of the P91 – P87 scan show the P91 bulk to have an average hardness of 248 ± 4 VHN_{50}. The P91 steadily hardens over the course of the HAZ, reaching a peak of 275 VHN_{50} near the weld line (with variations of ± 15 VHN_{50}). The HAZ appears to be approximately 2.2 mm in width.

The results of the scan across the P92 – P87 interface show the P92 bulk to have an average hardness of 260 ± 9 VHN_{50}. The HAZ again extends for approximately 2.2 mm into the steel, and in this case is associated with hardening up to around 310 VHN_{50}. There is a soft zone at the edge of the P92 HAZ, in which hardness drops to a minimum of 245 VHN_{50}, which was not apparent in the P91.

The P87 weld metal, away from the weld line, has an average hardness of 201 ± 3 VHN_{50}. Within 300 μm of the weld interfaces, hardness increases up to a maximum of approximately 220 VHN_{50}. The reason for this increase is not immediately apparent. This same behaviour is displayed at both weld interfaces.

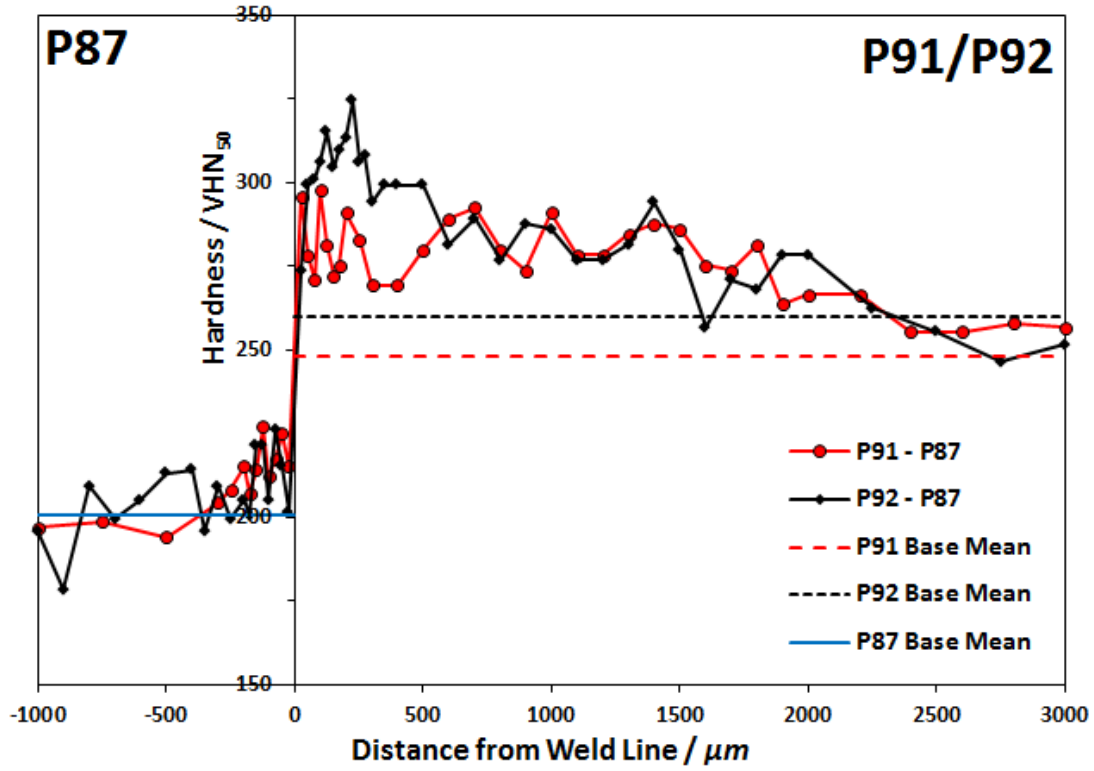

Figure 9.1: Microhardness profiles across the P91 – P87 interface (red) and the P92 – P87 interface (black). The horizontal lines represent the mean base levels away from the weld interfaces in the three alloys, which are 248 ± 4 (P91), 260 ± 9 (P92), and 201 ± 2.8 (P87).

9.2 Microstructures of the P91 and P92 Steels

The microstructures of the P91 and P92 steels away from the heat affected zones are broadly similar to those observed in previous systems, as are the HAZ structures (grain size, precipitate distribution, etc.). These features will hence not be reiterated here. The key differences come in the characteristics of the steels adjacent to the weld interfaces.

The P91 – P87 steel interface is presented in figures 9.2(a) and 9.2(b). It is immediately apparent that little to no decarburisation has taken place in the steel, as a near-uniform tempered martensite structure is maintained right up to the weld line, with little to no apparent precipitate dissolution having taken place.

The principal deviation from ideal precipitate distribution in the P91 is immediately adjacent to the weld line, where a disconnected band of type I carbides

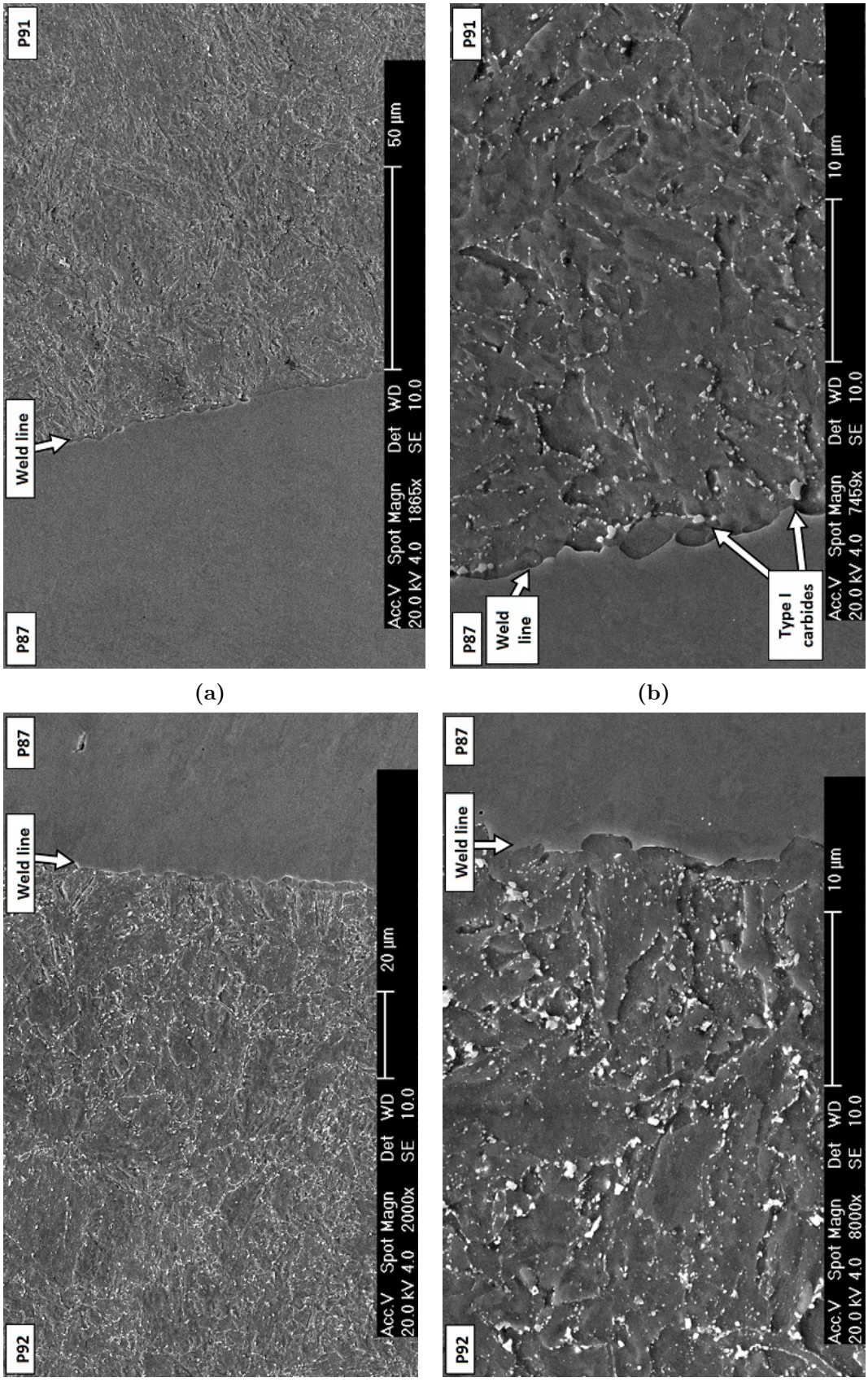

Figure 9.2: SEM SE images of the P91 – P87 (**(a)** and **(b)**) and P92 – P87 (**(c)** and **(d)**) interfaces after etching with Vilella's reagent

has formed. These have an average size of approximately 800 nm and appear, on average, at 5 μm intervals (hence appearing to cover less than a quarter of the observable weld interface). Like the previous cases, these particles form c. 1 – 2 μm away from the visible weld interface. When viewed in BSE mode, as shown in figure 9.3, they appear distinctly bright compared to their surroundings, indicating that they are rich in elements of high atomic number; by a process of elimination, this must be molybdenum and/or niobium.

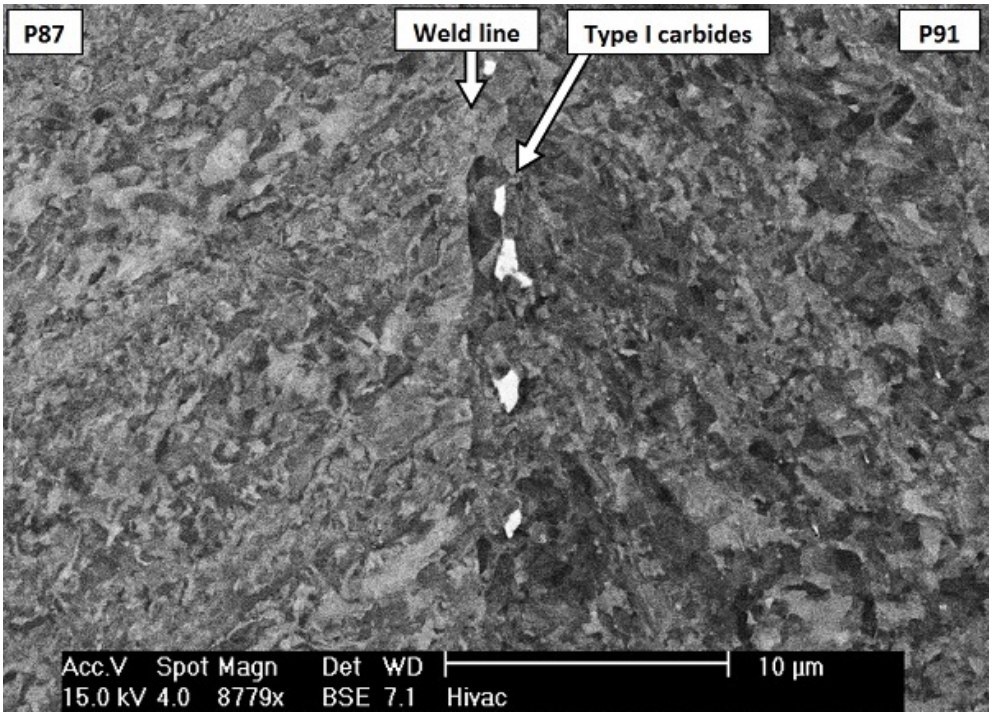

Figure 9.3: An SEM BSE image of the P91 – P87 weld interface in the polished state, showing the type I carbides.

The P92 – P87 interface, as shown in figures 9.2(c) and 9.2(d), is seen to be even more stable than that of P91. The same tempered martensite structure up the weld line is observed, but the type I particles are different. They are far fewer in number (occurring, on average, once every 20 μm), and individually smaller (at around 400 nm on average). Like those in the P91 system, they appear distinctly bright in BSE images, and as such may be carbides (of the type observed at the P91 – P87 interface) or Laves phase. There are no abnormally coarse Laves phase

particles in the area near the weld line, as were observed in the P92 – Alloy 625 weld (samples STA and LTA, section 5.5.1).

9.3 Microstructure of the P87 Weld Metal

The microstructure of the bulk P87 weld metal is shown in figure 9.4. It has a primarily columnar-dendritic structure, but of different form to those shown by the previously-examined weld metals based on Alloy 625. The grains appear up to 100 μm in width, and each contains numerous primary dendrite arms. The grains are oriented roughly perpendicular to the weld line.

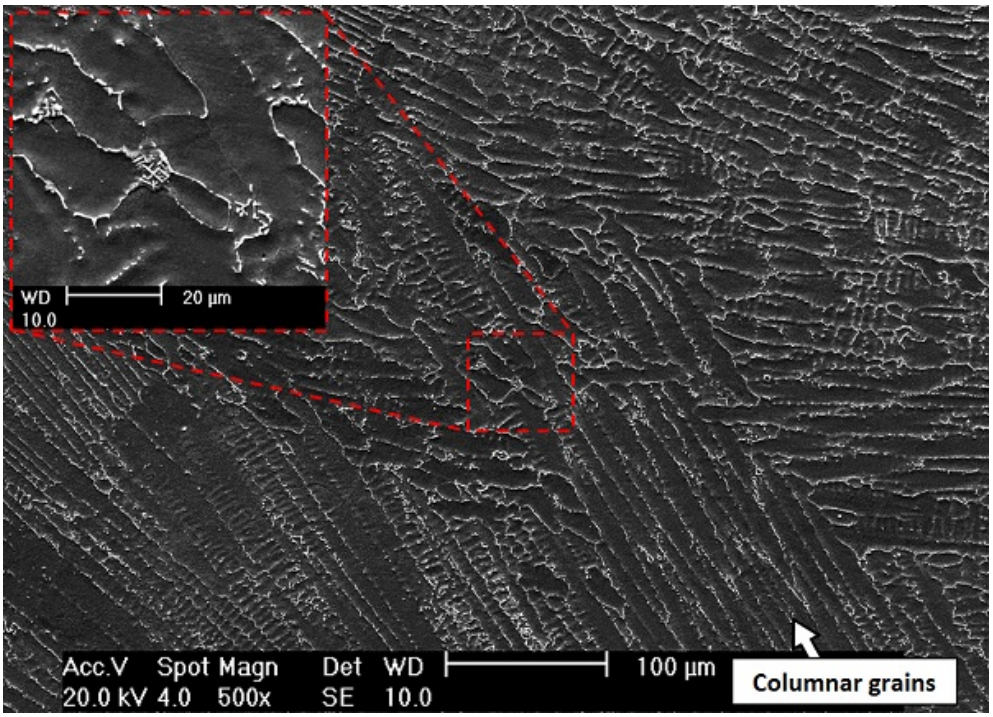

Figure 9.4: An SEM SE image of the bulk P87 weld metal after etching with aqua regia, showing the columnar-dendritic microstructure. The inset shows a close-up of one of the interdendritic particle clusters.

The interdendritic areas in the P87 are clearly delineated by bands of particles. Many of these particles are elongated in the direction of the grains, though some appear as isolated blocky particles. They are generally 1 – 2 μm in size. In certain areas there are clusters of needle-like particles, arranged in criss-cross formations.

The individual particles in these clusters are long and thin, being between 1 and 5 μm in length and up to 1 μm wide. Whilst being fewer in number, these particles closely resemble the interdendritic particles observed in the ex-service Alloy 625, making it possible that they are the same phase (Ni_3Nb, of type γ'' or δ). The smaller blocky particles may be a different phase.

The area of the weld interface adjacent to the weld interface with the P91 steel is shown in figure 9.5 (the interface with the P92 steel appears almost identical). The PMZ is far less apparent in this case than in previous Alloy 625-based welds, presumably due the closer chemical similarity between the two alloys at these welds. None of the vein-like features extending from the weld line that were observed in aged Alloy 625 welds have been observed here.

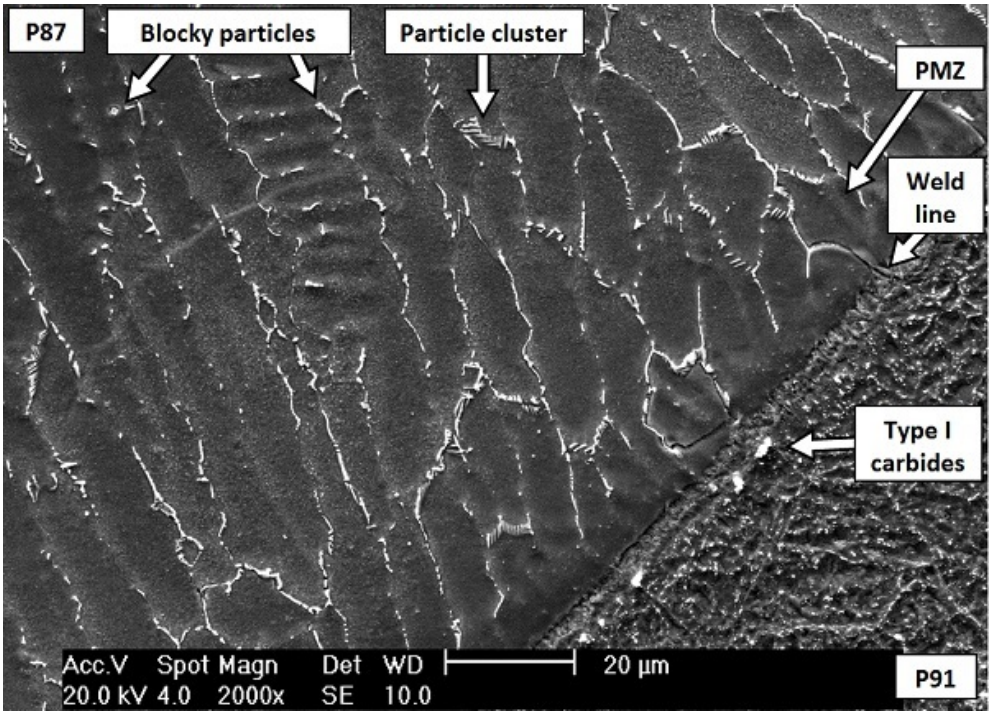

Figure 9.5: An SEM SE image of the P87 weld metal adjacent to the weld line after etching with aqua regia.

9.4 Chemical Analysis

Semi-quantitative SEM-EDX point measurements have been performed to measure the elemental concentration profiles across the weld line of the P91 – P87 weld interface. The results of this are shown in figure 9.6. It is shown that a PMZ exists, between 15 and 20 μm in width. Over this range, the iron and nickel levels vary monotonically between the base level of the P91 and the level in the first weld pass of the P87. The chromium level does not vary to any significant degree across the weld interface, which is to be expected since the nominal levels in the two base alloys are the same. The first weld pass is found to contain an average level of c. 49 wt% iron, as compared to the nominal level in P87 of c. 40 wt%; the level of nickel is reduced to compensate. The P92 – P87 shows very similar chemical behaviour.

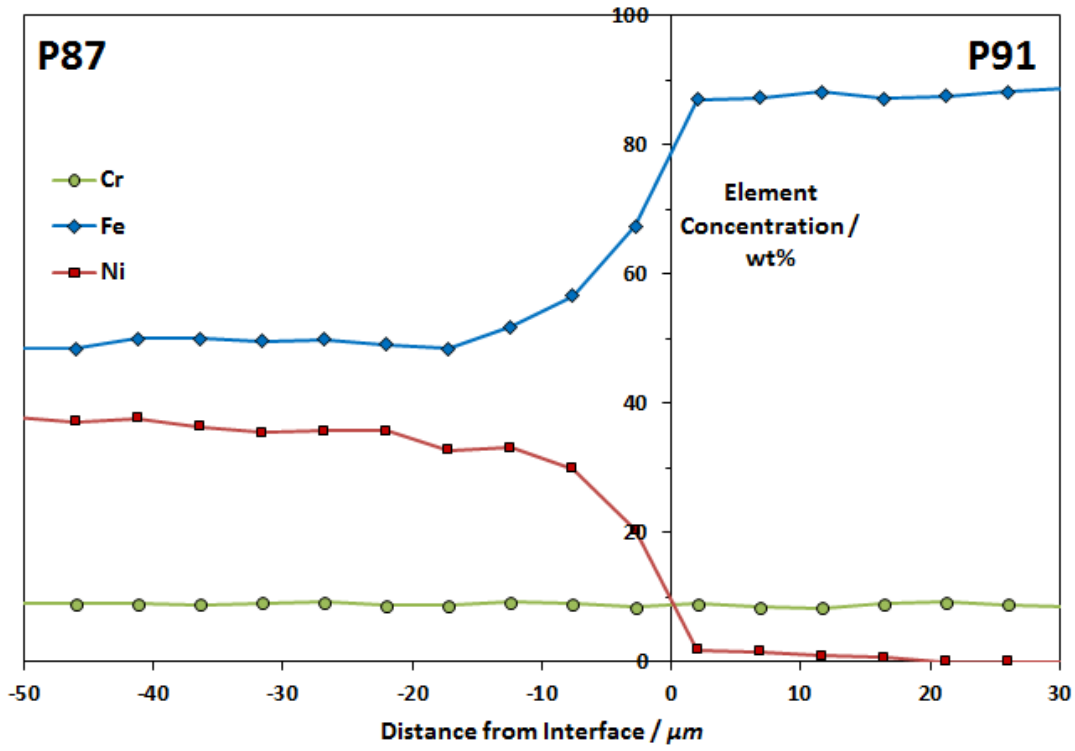

Figure 9.6: SEM-EDX point measurements of levels of Cr, Fe and Ni across the P91 – P87 weld interface.

Point composition analysis by SEM-EDX has been performed on the various

secondary phases identified in the three alloys, results of which are shown in figure 9.7. Starting on the P91, the type I carbides are shown to be distinctly enriched in molybdenum, as well as showing slight enrichment in other elements (notably nickel and silicon). Only minor enrichment in chromium over the surrounding level is shown. These results are consistent with either M_6C carbide or Laves phase ($(Fe,Cr)_2(Mo,Ni)$).

The particles in the type I position in the P92 show compositions that are strongly enriched in tungsten, and less so in molybdenum. This composition is more consistent with Laves phase than any known carbide type. These particles also have the same BSE contrast as particles on nearby PAGBs, which are known in P92 to be Laves phase [42]. The conclusion is hence that they are probably not carbides, but rather Laves phase particles forming in the type I position; this was previously observed in the P92 – Alloy 625 system (see figure 5.16).

The particles of the grain boundary clusters in the weld metal appear to be enriched primarily in niobium, also showing some enrichment in titanium. While not conclusive, this is consistent with γ'' or δ-phase; their acicular morphology also supports this conclusion.

The low-voltage EDX method has been applied to these weld interfaces so as to measure variations in carbon level. The results of this test on the P91 – P87 interface are shown in figure 9.8 (the results of the equivalent investigation on the P92 – P87 interface were near-identical, so for brevity have been omitted). These data show only minimal variations in carbon level around the weld interface, mostly within margins of error from the base levels, indicating that minimal carbon diffusion has occurred. The results appear similar to the as-welded state of the P92 – Alloy 625 system, shown in figure 5.23(a), despite the fact that the present sample had been aged.

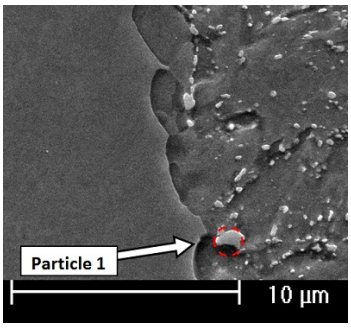

(a)

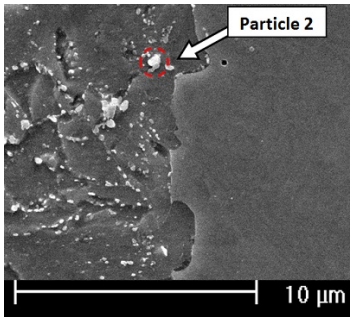

(b)

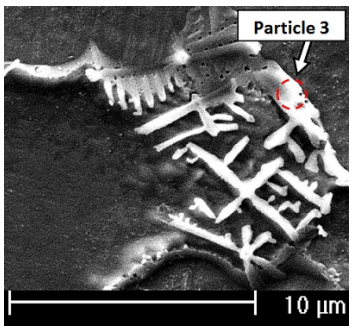

(c)

	Element (wt %)								
	Cr	Fe	Mo	Nb	Ni	Si	Ti	V	W
Particle 1 (P91)	10.5	36.2	34.5	1.6	8.9	5.1	-	2.9	-
Uncertainty (±)	0.2	0.3	0.4	0.3	0.2	0.1	-	0.1	-
Particle 2 (P92)	8.1	41.8	9.3	-	0.8	-	-	-	38.9
Uncertainty (±)	0.1	0.3	0.3	-	0.2	-	-	-	0.3
Particle 3 (P87)	7.1	30.7	2.9	31.2	23.6	< 0.5	3.3	-	-
Uncertainty (±)	0.3	0.7	0.9	0.9	0.7	0.1	0.2	-	-

(d)

Figure 9.7: SEM-EDX results of point analyses on three particle families: **(a)** the type I particles in the P91; **(b)** the type I particles in the P92; **(c)** particles from a grain boundary cluster in the P87; **(d)** tabulated compositions of the measured points.

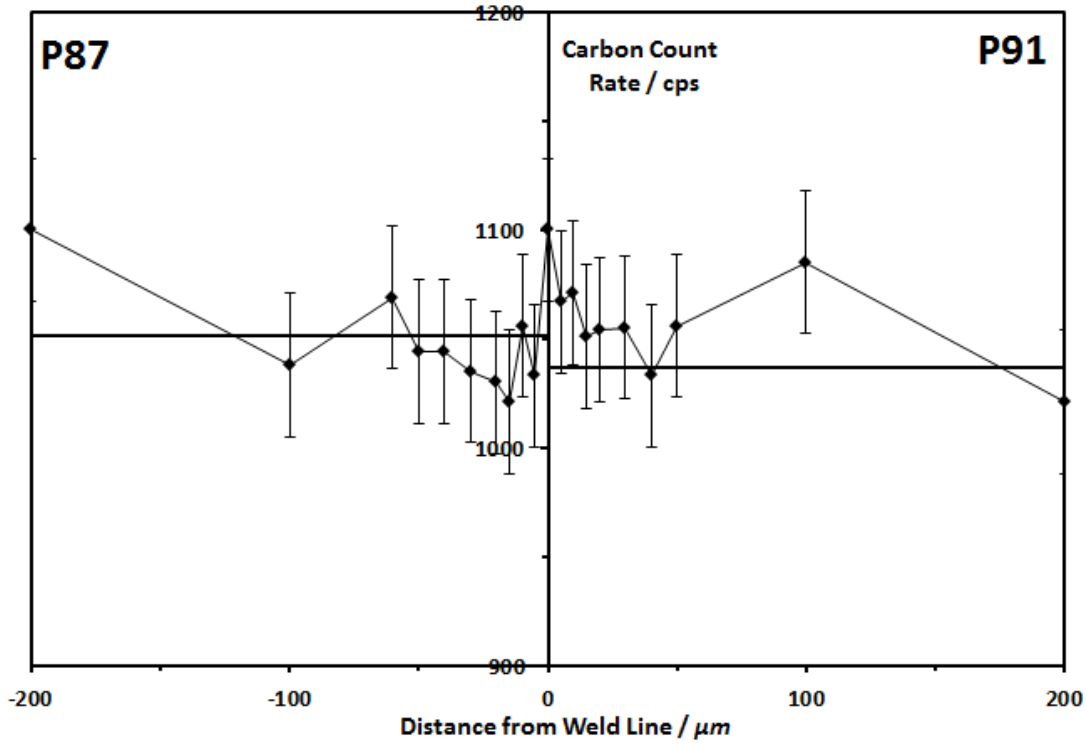

Figure 9.8: EDX measurements of carbon variation across the P91 – P87 weld interface after ageing for 3149 hours at 649 $°C$, using the low-voltage method. The solid lines represent the mean count rates in the two bulk alloys.

9.5 TEM Analysis of the P91 – P87 Weld

A single FIB specimen was extracted from across the P91 – P87 weld line, and analysed by STEM and STEM-EDX. Results of this are shown in figures 9.9 and 9.10 respectively. The bright and dark field images reveal that the P91 steel has a strongly tempered martensitic microstructure. Some areas have maintained their martensite laths, though there are two grains adjacent to the interface, around 2 μm in size, that appear relatively featureless. These are plain ferrite, either reformed α or retained δ. The majority steel microstructure appears to contain dispersed particles, most of which occur on grain or lath boundaries.

The P87 weld metal, by contrast, appears relatively featureless, with only one visible grain, and a similar sub-grain structure to that seen in previous FIB specimens taken from Alloy 625-based weld metals. There are no precipitate phases in the extracted region of P87. The two alloys appear to be separated by an interfacial band, though it is not seen especially clearly in the STEM images.

The STEM-EDX maps reveal the chemical variations around the weld interface, in particular the nature of the precipitate families. There are seen to be dispersed Cr-rich and V-rich precipitates which, based on the known microstructure of P91, likely correspond to $M_{23}C_6$ carbide and MX carbonitride respectively; their average sizes, c. 160 nm and 60 nm respectively, support this conclusion, as do their compositions, which are given in table 9.1. The identity of the former type has been confirmed by SADPs (in much the same manner as in the P92 – Alloy 625 system, in figures 5.30 and 5.36), though the latter are too small to be identified in this manner. These particles are uniformly distributed, with the exception of the two previously identified featureless grains, which do not contain any visible precipitates. The MX particles are far more numerous in this specimen than in those previously examined; at least 30 individual particles of this type can be identified in the steel, whilst none of the P92 specimens contained more than 10,

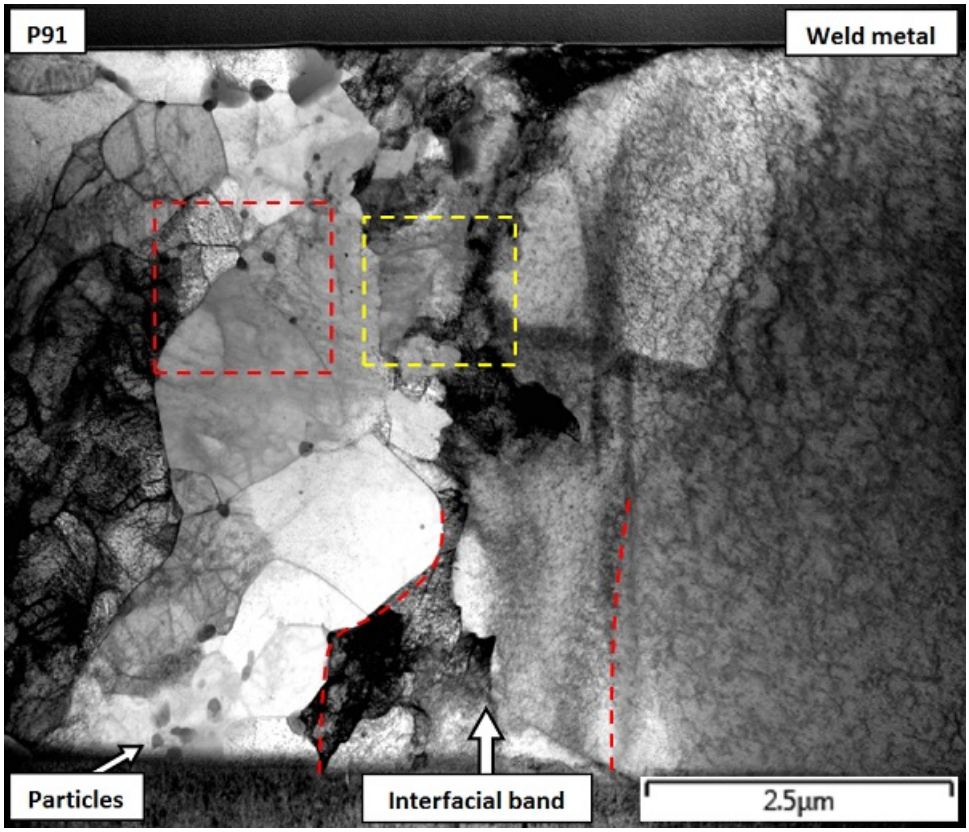

(a)

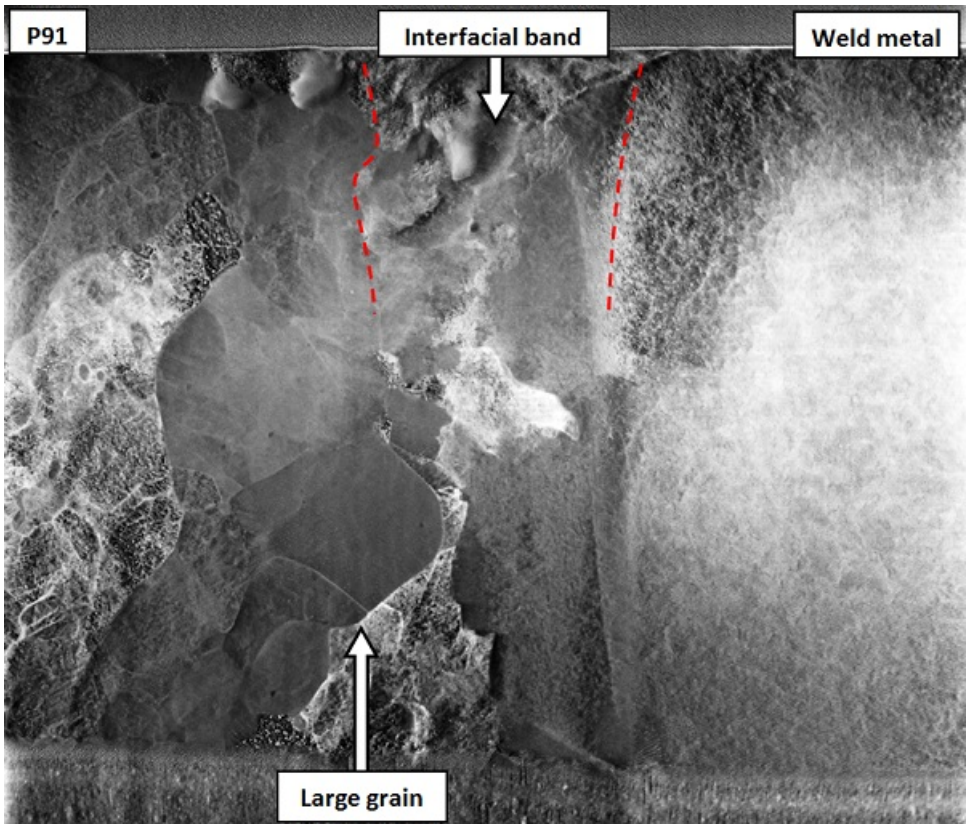

(b)

Figure 9.9: STEM images of the FIB specimen extracted from the P91 – P87 weld interface. Figure **(a)** was taken in bright field mode, **(b)** in HAADF mode.

and the ex-service P91 specimen was completely devoid of these particles.

A third distinct family of precipitates in the P91 can be seen at the top of the EDX maps, in the form of three large (400 – 500 nm) particles enriched in molybdenum and silicon. These are the same coarse type I particles that were previously observed by SEM. Conventional TEM analysis, the results of which are shown in figure 9.11, has been used to show that these particles are FCC in structure, with a lattice parameter most closely matching that of M_6C (though they may more accurately be described as M_6X, as they are found by EDX to contain nitrogen as well as carbon).

Careful examination of figure 9.10(d) reveals a fourth type of particle, in a set of niobium-rich particles close to the weld interface, of similar morphology to the V-rich MX particles; these may be an alternative form of MX. Like their V-rich counterpart, their small size inhibits identification by SADPs.

Table 9.1: Approximate compositions of the various types of particles and the interfacial band in the P91 – P87 weld, as measured by STEM-EDX. Note that the iron levels in the particles may be exaggerated due to beam interaction with the metal matrix. The levels of C and N are not quantified, and are instead categorised as strong (**S**) or weak (**W**) signals.

	Element (wt %)								
	C	Cr	Fe	Mo	N	Nb	Ni	Si	V
Cr-rich particles	**S**	63.4	27.1	5.9	**S**	< 0.5	1.5	< 0.5	0.6
Uncertainties (±)	-	3.5	1.7	3.5	-	0.0	0.4	0.2	0.3
V-rich particles	**W**	8.0	71.3	1.4	**S**	5.6	1.0	< 0.5	11.1
Uncertainties (±)	-	1.1	4.4	4.7	-	1.8	0.6	0.0	1.2
Mo-rich particles	**W**	9.1	29.5	39.8	**S**	2.9	8.8	6.0	3.0
Uncertainties (±)	-	0.1	0.2	0.5	-	0.2	0.1	0.1	0.1
Nb-rich particles	**W**	7.8	55.0	< 0.5	**S**	19.7	10.9	1.1	0.6
Uncertainties (±)	-	1.1	3.4	0.0	-	3.6	1.5	0.5	0.4
Interfacial band	**W**	8.7	78.1	1.0	**W**	< 0.5	16.7	< 0.5	< 0.5
Uncertainties (±)	-	0.1	0.5	0.5	-	0.0	0.2	0.1	0.1

The structures of the P87 weld metal and the interfacial band have been investigated in greater detail by conventional TEM analysis, the results of which are presented in figures 9.12 and 9.13. The P87 weld metal is found from SADPs to have an FCC crystal structure, as is to be expected.

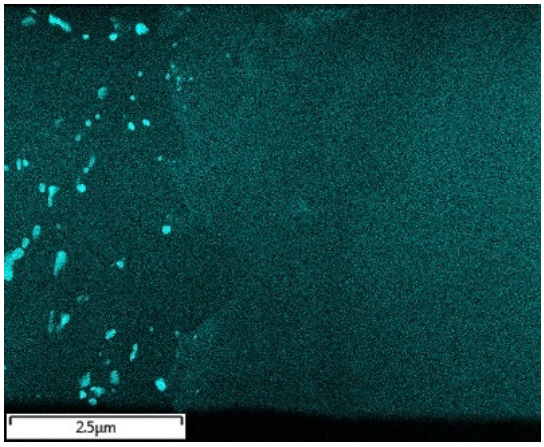

(a) Cr EDX map

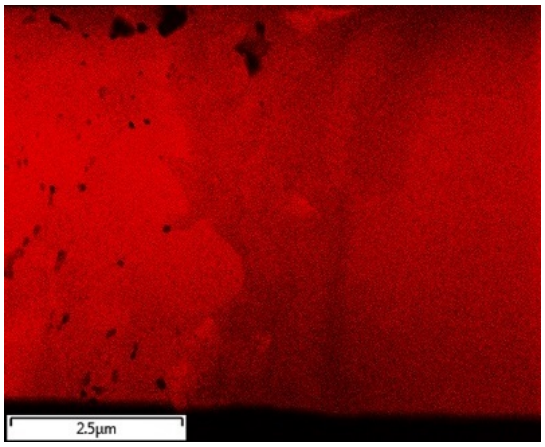

(b) Fe EDX map

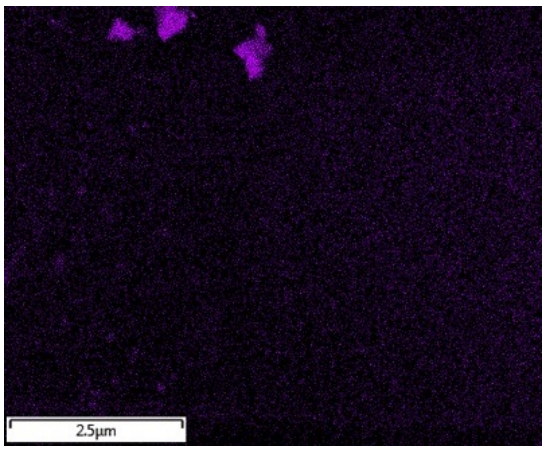

(c) Mo EDX map

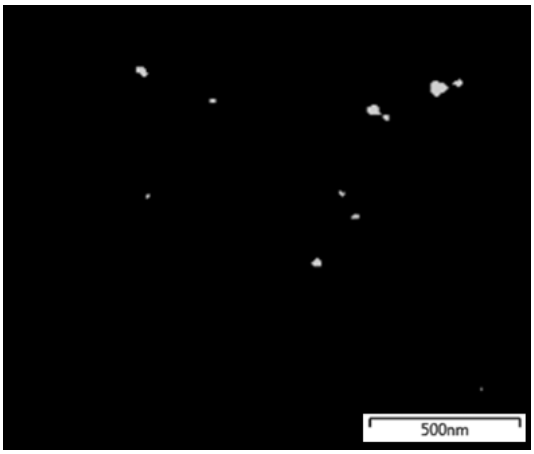

(d) Nb EDX map

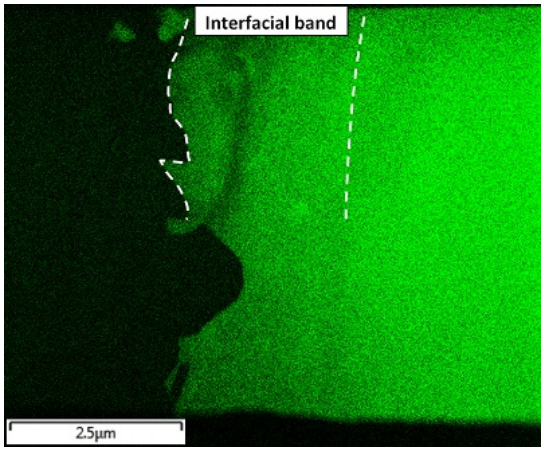

(e) Ni EDX map

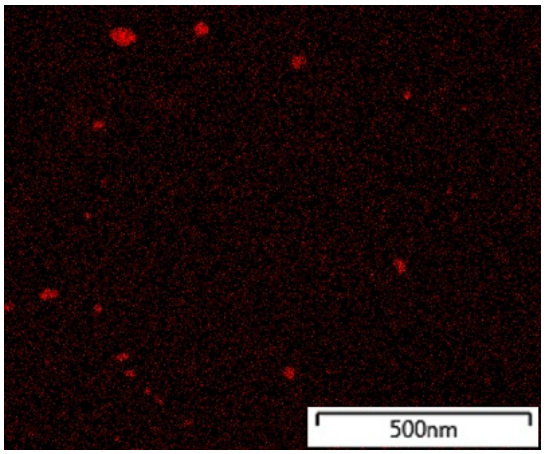

(f) V EDX map

Figure 9.10: STEM-EDX maps of the P91 – P87 weld interface. Map **(d)** is zoomed in on the area in the yellow box in figure 9.9(a), and **(f)** on the red box.

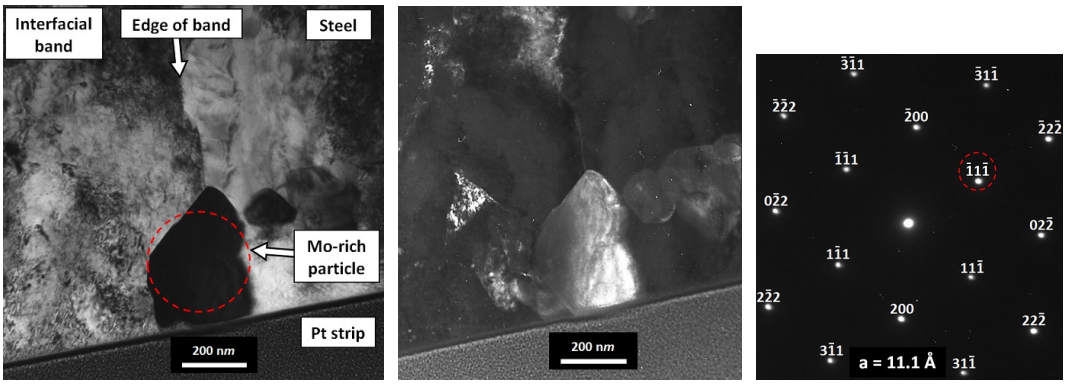

(a) **(b)** **(c)**

Figure 9.11: TEM analysis of a Mo-rich particle at the P91 – P87 interface, showing **(a)** a bright field image, **(b)** a dark field image, and **(c)** an indexed SADP of the FCC-[110] zone axis of the particle, corresponding most closely to M_6C carbide. The pattern in **(c)** was taken from the circled area in **(a)**, while the dark field image in **(b)** was formed from the circled diffraction spot in **(c)**.

The interfacial band, by contrast, is found to be BCC in structure, and of distinctly different orientation to either adjacent alloy. Comparison with the STEM-EDX maps reveals that it is enriched in nickel and chromium compared to the adjoining P91. Semi-quantitative point EDX analysis, the results of which are presented in table 9.1, confirms this enrichment.

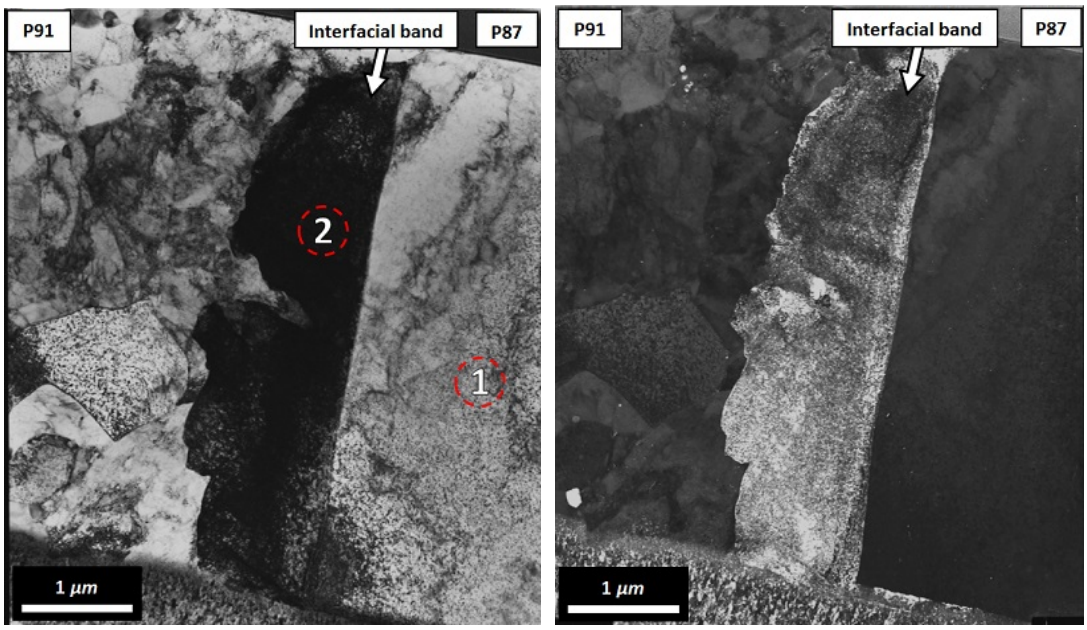

(a) **(b)**

Figure 9.12: TEM images from the P91 – P87 weld interface, at an orientation at which strong diffraction contrast was observed from the interfacial band. The figures are **(a)** a bright field image, and **(b)** a dark field image. The latter was formed using the circled diffraction spot in figure 9.13(b).

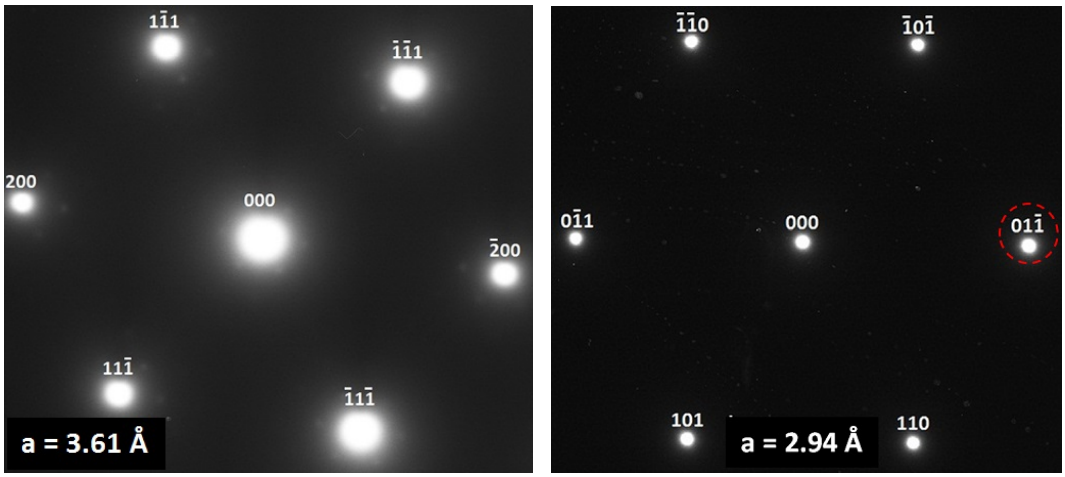

(a) **(b)**

Figure 9.13: TEM SADPs from the P91 – P87 weld interface, showing **(a)** an indexed SADP of the P87 FCC-[011] zone axis, taken from the circled area labelled '1' on figure 9.13(a), and **(b)** an indexed SADP from the interfacial band of the BCC-[111] zone axis, taken from circle '2' on figure 9.13(a). Pattern **(b)** was taken at the same tilt angle as the images in figure 9.12, while **(a)** was taken at a different tilt angle

9.6 Discussion

In this section the properties of these P87 welds, particularly with regards to performance in service environments, will be discussed, with reference to previously-discussed cases where appropriate. This will tie in with a consideration of possible weld failure modes and mechanisms, and how these may be mitigated based on the present findings.

9.6.1 Properties of the P87 Weld Metal

As the P87 weld metal has only been examined in a single aged condition, it is impossible to make any judgements on the time dependency of its evolution. However, the similarities between the intergranular particles in this material and the interdenritic particles in the ex-service Alloy 625 are unmistakeable, despite them being fewer in number; it is hence likely that they are δ-phase, a conclusion supported by the EDX data in figure 9.7. This is also supported by intuitive expectations, in that much of the niobium content of the P87 would segregate to grain boundaries during welding. However, the relatively low hardness of the P87 material (only 201 VHN_{50} on average, compared to 352 VHN_{100} in the second weld bead of the ex-service Alloy 625) may not be consistent with this conclusion, since δ-phase should cause precipitation hardening, even at this lower volume fraction than in the Alloy 625.

A phase fraction plot of nominal P87, as predicted by *Thermo-Calc* using the TCFE7 database, is shown in figure 9.14 (the same calculation was also performed in the SSOL5 database, with near-identical results). This shows that at 650 $°C$ (the temperature at which the observed sample was aged) the equilibrium phases are $M_{23}C_6$ carbide and δ-phase, in roughly equal proportions; SEM observation all but confirms the presence of the latter phase, while particles were observed which may have been of the former type. M_6C carbide is observed below 600 $°C$, at the

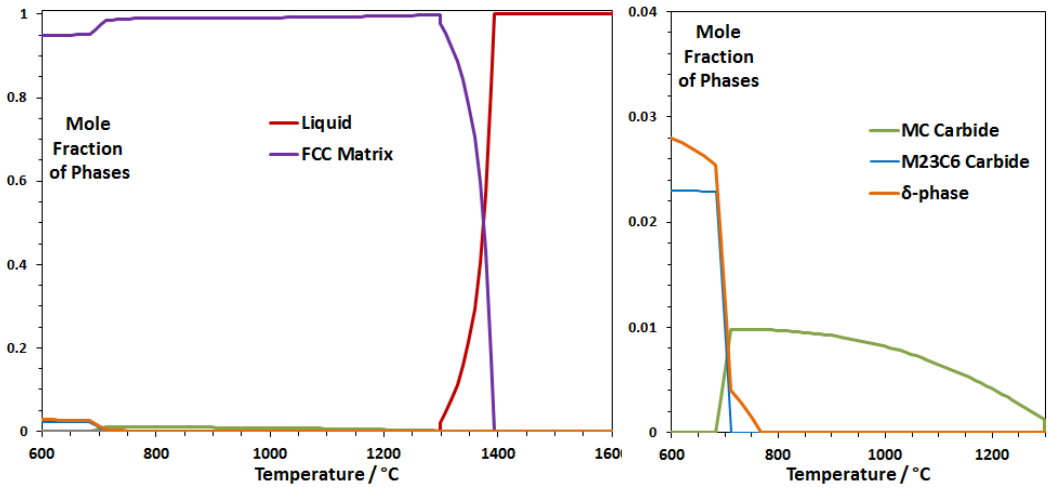

Figure 9.14: A plot of phase fraction as a function of temperature in nominal P87 weld metal, as calculated by *Thermo-Calc* using the TCFE7 database, showing **(a)** matrix and liquid phases, and **(b)** secondary phases.

expense of $M_{23}C_6$ carbide. At 740 $°C$ the $M_{23}C_6$ and δ phases begin to dissolve, being replaced by MC carbide, which in turn dissolves at 1215 $°C$. Melting begins at 1280 $°C$ and ends at 1385 $°C$.

Thermo-Calc has also be used to investigate the potential effectiveness of P87 in its aim of suppressing carbon diffusion at P91/P92 welds. Shown in figure 9.15 is a plot of the carbon activities as a function of temperature in nominal P91, P92, P87 and Alloy 625. This demonstrates that the activities in P91, P92 and P87 are closely matched, in comparison to that of Alloy 625, at all temperatures up to 830 $°C$ (which, not coincidentally, is the A_{e1} temperature of P91 and P92). Beyond this temperature, carbon activity is greater in the P87 metal, according to the SSOL5 database, which would create a driving force for diffusion into the steel. If predicted correctly, this would have an effect on P91/P92 – P87 weld joints that were given a full re-normalisation heat treatment (of the sort described in Appendix B), possibly leading to carbon enrichment in the steel; experimental investigation would be required to determine if this does in fact occur.

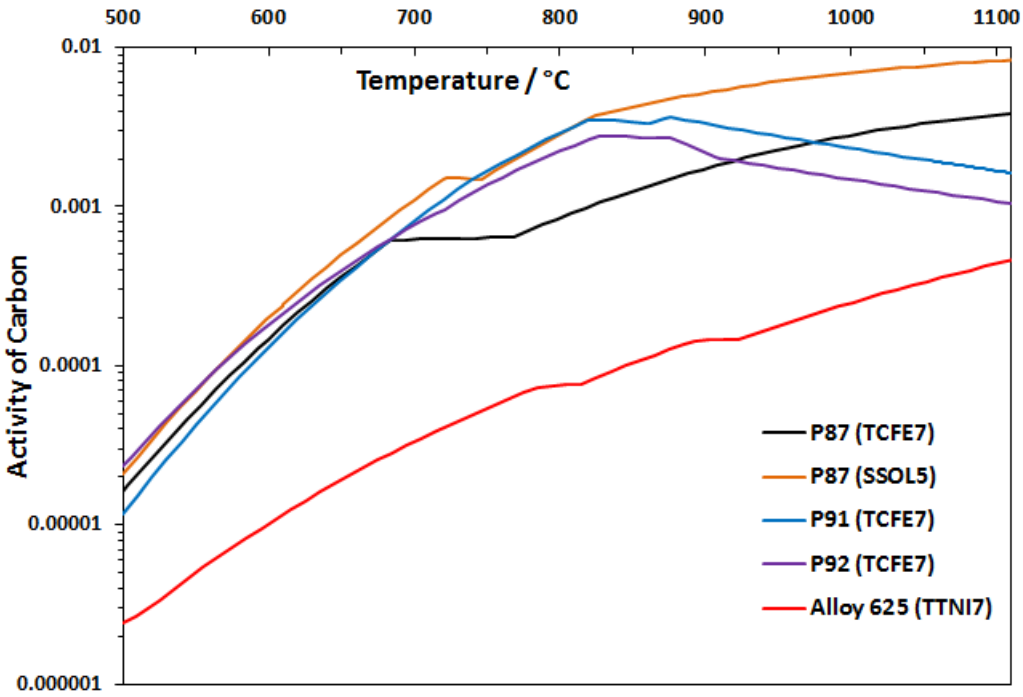

Figure 9.15: A plot of carbon activities as a function of temperature in nominal P91 steel, P92 steel, P87 weld metal and Alloy 625, as calculated by *Thermo-Calc* using the TCFE7, SSOL5 and TTNI7 databases.

9.6.2 Interdiffusion at P87 Welds

As demonstrated in figure 9.15, the P87 weld metal is predicted to be very closely matched to P91 and P92 steels in terms of carbon activity at temperatures below 830 $°C$, being no more than a factor of 1.5 different at any point in this range. This ought to negate the diffusion of carbon across the weld interface, as per the design criteria of this alloy. EDX measurements of carbon level across the P91 – P87 weld interface, as presented in figure 9.8, appear to support this conclusion, as they show only minimal variations in count rates from the mean base levels.

Whilst in each of the aged welds prepared with Alloy 625 there is some level of decarburisation/de-nitriding, the steel in the weld systems prepared with P87 filler metal, as shown in figure 9.2, do not show any observable CNDZ; the density and size of precipitates does not change near the weld line (with the exception

of the type I carbides). Additionally, the P87 weld metal in the areas adjacent to the interfaces, as shown in figure 9.5, does not show any evidence of vein-like features that characterised the CNEZ in previously-examined Alloy 625 welds. These facts are encouraging, as they provide further indication that relatively minimal diffusion is taking place at these welds, and that P87 is performing its intended role in preserving the microstructures around the weld line.

The effectiveness of the P87 weld metal in suppressing carbon diffusion has been investigated using the *DICTRA* software. The results of this simulation, alongside results of a simulation of the ex-service ageing condition, are shown in figure 9.16. These results confirm that far less diffusion of carbon should take place across the P91 – P87 weld, and that there should be no discernable CDZ/CNDZ in the steel. The small zone of carbon enrichment in the steel adjacent to the weld line in both cases results from diffusion of carbide-forming elements from the weld metal; in the Alloy 625 case, this is primarily caused by chromium diffusion, while in the P87 case it is primarily due to molybdenum diffusion.

The P91 – P87 weld system shows far fewer type I carbides in micrographs than the previous cases, critically than the P91 – Alloy 625 ex-service weld. While few in number, they are relatively coarse compared to those seen in other systems. By a combination of STEM-EDX data (which shows them to contain molybdenum, nitrogen and carbon) and SADPs, they are concluded to be M_6X carbonitrides. Their presence indicates that some limited diffusion of carbon and nitrogen across the interface may be taking place; this is supported by the small calculated activity differences between P91 and P87 at the temperature in question (650 $°C$) in figure 9.15 and the *DICTRA* results in figure 9.16.

The P92 – P87 weld, in contrast, shows no discernible type I carbides, possibly for the same reason that type I carbides are subdued in the P92 – Alloy 625 welds (which is believed to be the presence of boron, acting to limit carbide coarsening). Alternatively, it is possible that slightly less diffusion takes place at this interface

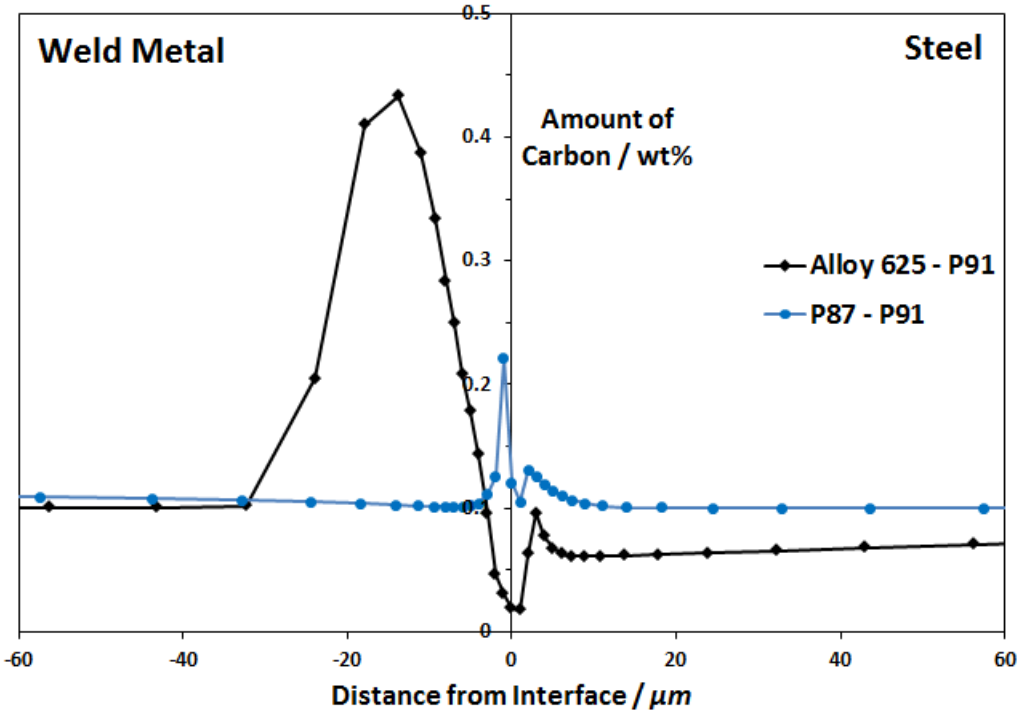

Figure 9.16: Results of simulations of carbon diffusion across the P91 – Alloy 625 (black) and P91 – P87 (blue) interfaces, performed using the *DICTRA* software. The P91 composition was simplified slightly by removing V and N. The former simulation was performed in much the same way as those in chapter 6, while the latter was performed using solely the TCFE7 database, and a step composition profile at the interface.

due to slight differences in chemical potential gradients, as illustrated in figure 9.15.

9.6.3 The Role of P87 in Mitigating DMW Failures

Based on the results presented here, P87 may be a more suitable weld metal than Alloy 625 when working with P91 and P92 steels. All of the experimental evidence that has been gathered indicates that welds between P87 and P91/92 contain no observable CNDZ or CNEZ. A near-ideal phase distribution is maintained, which ought to make P87 welds resistant to the manner of failure observed in the ex-service P91 – Alloy 625 welds by eliminating the creep-weak zone. Additionally, P87 has demonstrated less extensive age hardening than Alloy 625, which would minimise the effect of strain concentration in the steel.

However, P87 welds are not without issues. Perhaps the most apparent are the Mo-rich type I carbides that are observed to form at the P91 – P87 interface. While relatively infrequent, these particles are coarse, and could hence serve as sites for void formation in brittle creep failure. Using P92 as the base steel removes this issue.

There is also the issue of type IV damage to consider. This, as described in section 2.2.4, is creep failure in the FGHAZ and/or ICHAZ. It has not been directly observed in this thesis, as few stressed samples have been investigated, but it is nonetheless an important concern in DMW design. It can be assumed that the ex-service P91 - Alloy 625 weld that suffered failure (sample FP-C) did so at the point of least strength, which happened to be the weld interface/CNDZ. If this weakness were to be mitigated (by using P87 as the weld filler, for instance) then it is entirely possible that weld failure would shift to the type IV region. One problem would be traded for another, and DMWs may still pose a weakness.

Type IV failure would be suppressed by removing the HAZ, which could be achieved by performing a full normalisation and tempering heat treatment (as described in section 4.1.1). This is not performed on conventional ferritic-austenitic welds for a number of reasons, one of which being interdiffusion at the weld interface. As is shown in Appendix B, this treatment, while successful in removing the HAZ, causes excessive interdiffusion when applied to P92 – Alloy 625 welds. However, it may be more suitable in P91/92 – P87 welds, in which carbon and nitrogen activities are more closely matched. Were such a treatment to be successful, it might all but eliminate material weaknesses associated with the DMW.

9.7 Summary

Based on the analysis of this weld system, the following key points have been found:

- The aged P91 – P87 and P92 – P87 welds demonstrate far less significant diffusion of carbon and nitrogen across the weld interface than equivalent aged welds prepared with Alloy 625.

- Due to the lack of diffusion in these systems, there is no discernible CNDZ or CNEZ at these welds. A near-ideal phase balance is maintained in the two steels up to the weld interface.

- Type I particles near the weld line in the P91 – P87 system are found to be far fewer in number than in at the ex-service P91 – Alloy 625 weld. Like in previous cases, they are found to form at the edge of an interfacial band. The particles in this case are found to be Mo-rich M_6X carbonitrides.

- Due to the lack of a distinct CNDZ, welds of this type may be resistant to the manner of failure observed in the ex-service P91 – Alloy 625 system.

Chapter 10

Conclusions & Future Work

The main aim of this research was to investigate the nature and evolution of DMWs involving P91 and P92 steels and nickel-based weld metals, particularly with regards to diffusion behaviour, phase evolution, and microstructural phenomena such as the formation of an interfacial band and interfacial precipitates. This was done in the context of understanding points of mechanical weakness and potential high-temperature creep failure modes, by a combination of experimental characterisation and thermodynamic/kinetic modelling.

10.1 Conclusions

Based on the results presented and discussed in the preceding chapters, the conclusions can be summarised as follows:

- In the P92 – Alloy 625 system, the base P92 is found to have a tempered martensitic structure, with $M_{23}C_6$, MX and Laves phases all present after

ageing at 625 $^{\circ}C$. The Alloy 625 weld metal is found to have a typical dendritic structure, though strongly diluted in iron (up to 30 wt%). Intermetallic precipitates, believed to be γ'' or δ phase of form Ni_3Nb, precipitate in the weld metal during ageing, causing the material to harden. There is found to be a partially mixed zone (PMZ) at the weld interface, up to 50 μm in width, over which the material composition varies smoothly from that of the steel to that of the weld metal.

- FIB methods have been used successfully to produce site-specific cross-weld TEM specimens, which has proven highly useful in examining the nature and evolution of features at the weld interface too small for conventional SEM methods, such as the interfacial band and particularly fine precipitates (such as MX). Additionally, it has allowed phases to be identified by electron diffraction.

- During ageing, there is experimental evidence for diffusion of carbon across the weld interface, from the steel to the weld metal. This results in a carbon denuded zone (CDZ) in the steel, and a carbon enriched zone (CEZ) in the weld metal. The extent to which diffusion occurs is far less pronounced than in comparable 2.25Cr-1Mo steel systems, due to the lesser chemical potential gradient of carbon. Nitrogen has been found to diffuse in a similar manner to carbon. The extent of diffusion of substitutional elements, such as iron, chromium and nickel, is found to be much less significant due to the lower mobility of these elements in the present conditions.

- As a result of diffusion, secondary carbide/carbonitride phases ($M_{23}C_6$ and MX) in the CDZ in the steel dissolve to some degree. Laves phase particles are found to coarsen particularly rapidly in this area. Diffusion into the nickel-based weld metal appears to take place largely along grain boundaries, resulting in vein-like microstructural features. TEM analysis indicates that

grain boundaries in the CEZ contain coarse carbonitride particles, of type Nb(C,N), with smaller Mo-rich particles precipitating as satellites around them. The latter particles have not been identified conclusively.

- Particles are found to form in the steel adjacent to the weld interface after ageing at 625 $^{\circ}C$. These appear to be primarily $M_{23}C_6$ carbides, though some Laves phase particles may also have formed in this area. Precipitation happens along the edge of an 'interfacial band' which is a 1 – 2 μm wide feature that separates the steel from the weld metal. Its composition is intermediate between those of the steel and the PMZ, and it is of a different crystallographic orientation to either adjacent alloy. As such, it presents a grain boundary that diffusing elements must cross, which is an energetically favourable site for precipitate formation. This band is found to form as a result of the welding process, and it is present in all examined samples.

- The novel low-voltage EDX method has been used to demonstrate the enrichment of carbon in the weld metals as a result of high-temperature ageing, and the relative lack of enrichment in the as-welded system (indicating that diffusion cannot occur to any significant degree during the welding process).

- Similar diffusion and phase evolution phenomena have been observed at a P91 – Alloy 625 interface in an ex-service weld, though features are generally more pronounced. This is especially apparent in the CDZ, where the $M_{23}C_6$ and MX particles have disappeared entirely, being replaced by a band of coarse type I carbonitrides (either $M_{23}X_6$ or M_6X in structure, and of an unusual mixed chemistry). A few coarse particles of this type are found in the CDZ.

- Low-ductility creep failure has been observed in this weld system, with the tip of the crack propagating through the CDZ. This indicates that this area represents a mechanical weakness in the weld system, likely due to the lack

of precipitates to pin microstructural features (which allows for the accumulation of creep strain). This is exacerbated by extensive precipitation hardening of the weld metal, inhibiting its ability to accommodate creep strain and causing it to concentrate in the adjacent steel. The cracking appears to have started at the outer edge of the pipe, indicating that oxide notching may have been the initiating factor.

- The properties of the newly-developed EPRI P87 filler metal have been investigated at interfaces with P91 and P92 steel. In both cases, it is found to be effective at inhibiting the diffusion of carbon and nitrogen, due to closely-matched chemical activities. Near-ideal phase balances are maintained in the steels and the weld metal (i.e. there is no CDZ or CEZ). Some isolated type I carbides are present at the P91 – P87 interface, which are found to be Mo-rich particles of form M_6X. The lack of a CDZ in the P91/92 steels should preclude mechanical weakness in this area, hence making interfaces of this type less susceptible to the manner of failure observed in the ex-service P91 – Alloy 625 system.

- The computational modelling tools *Thermo-Calc* and *DICTRA* have been used to provide insight into the chemical and kinetic behaviour of dissimilar welds. Diffusion modelling has been performed using the 'homogenisation model' in *DICTRA*. The predicted trends, in terms of diffusion and phase behaviour, generally match those observed experimentally, demonstrating the usefulness of the methods. However, the microstructural complexity of real systems prevent the models from being completely accurate, in that features such as grain boundaries, interfacial band and the dendritic nature of the weld metal cannot be simulated.

10.2 Future Work

The results presented in this work present new areas highlight areas that warrant further investigation, such as:

- High-temperature creep testing of P92 - Alloy 625 welds should be carried out, so that failure modes may be linked with microstructural evolution at the weld interface. This would allow the potential suitability of welds of this type for service applications to be gauged.

- P91/92 – P87 welds should be investigated in a range of aged states, including a fully re-normalised and tempered post-weld heat treated condition. This may be combined with creep testing, so as to judge its suitability for service environments.

- Further developments should be made to the computational model, with the aim of properly simulating phenomena such as grain boundary diffusion and type I carbide formation. This may be further extended by linking diffusion results from *DICTRA* with a finite element model of creep, which would tie in with either of the aforementioned experimental tasks.

Bibliography

[1] R. Viswanathan, J. Henry, J. Tanzosh, G. Stanko, J. Shingledecker, B. Vitalis, and R. Purgert. U.S. program on materials technology for ultra-supercritical coal power plants. *Journal of Materials Engineering and Performance*, 14(3):281–292, 2005.

[2] C. Lundin. Dissimilar metal welds - transition joints literature review. *Welding Research Supplement*, pages 58–s – 63–s, 1982.

[3] W. Callister. *Materials Science and Engineering: An Introduction*. Wiley, 5 edition, 2000.

[4] H. Bhadeshia. *Bainite in Steels*. IOM Communications, 2 edition, 2001.

[5] H. Bhadeshia and R. Honeycombe. *Steels: Microstructure and Properties*. Elsevier, 3 edition, 2006.

[6] H. Beeghly. Behavior of nitrogen and some of its compounds in steel. *Analytical Chemistry*, 24(7):1095 – 1100, 1952.

[7] A. Beneteau, E. Aeby-Gautier, G. Geandier, P. Weisbecker, A. Redjaimia, and B. Appolaire. Tempering of a martensitic stainless steel: Investigation by in situ synchrotron x-ray diffraction. *Acta Materialia*, 81:30 – 40, 2014.

[8] A. Strang and V. Vodarek. Microstructural stability of creep resistant alloys for high temperature power plant applications. *The Institute of Materials*, pages 31 – 52, 1998.

[9] P. Bianchi, P. Bontempi, A. Benvenuti, and N. Ricci. Microstructural stability of creep resistant alloys for high temperature power plant applications. *The Institute of Materials*, pages 107 – 116, 1998.

[10] J. Olsson and B. Wallen. Experience with a high molybdenum stainless steel in saline environments. *Desalination*, 44:241 – 254, 1983.

[11] F. Abe. Bainitic and martensitic creep-resistant steels. *Current Opinion in Solid State and Materials Science*, 8:305 – 311, 2004.

[12] T. Fujita. Proceedings of the materials engineering in turbines and compressors conference. *The Institute of Materials*, pages 493 – 499, 1995.

[13] M. Taneike, K. Sawada, and J. Abe. Effect of carbon concentration on precipitation behavior of $M_{23}C_6$ carbides and MX carbonitrides in martensitic 9Cr steel during heat treatment. *Metallurgical and Materials Transactions A*, 35A:1255 – 1262, 2004.

[14] S. David, J. Siefert, and Z. Feng. Welding and weldability of candidate ferritic alloys for future advanced ultrasupercritical fossil power plants. *Science and Technology of Welding and Joining*, 18:631 – 651, 2013.

[15] S.-H. Song, J. Wu, X.-J. Wei, D. Kumar, S.-J. Liu, and L.-Q. Weng. Creep property evalutation of a 2.25Cr-1Mo low alloy steel. *Materials Science and Engineering A*, 527:2398 – 2403, 2010.

[16] W. Bendick, J. Gabrel, B. Hahn, and B. Vandenberghe. New low alloy heat resistant ferritic steels T/P23 and T/P24 for power plant application. *International Journal of Pressure Vessels and Piping*.

[17] N. Komai, F. Masuyama, I. Ishihara, T. Yokoyama (ed. by R. Viswanathan, and J. Nutting). *Advanced Heat Resistant Steels for Power Generation*. IOM Comminications, 1999.

[18] R. Klueh. Ferritic/martensitic steels for advanced nuclear reactors. *Transactions of the Indian Institute of Metals*, 62:81 – 87, 2009.

[19] H. Li and D. Mitchell. Microstructural characterization of P91 steel in the virgin, service exposed and post-service re-normalized conditions. *Steel Research International*, 84:1302 – 1308, 2013.

[20] B. Hahn, V. Baumhoff, and M. Zschau. Use of X10CrMoVNb 91 steel in power plant retrofitting: Experience and application potential. *VGB PowerTech*, 77:204 – 210, 1997.

[21] B. Silwal, L. Li, A. Deceuster, and B. Griffiths. Effect of postweld heat treatment on the toughness of heat-affected zone for grade 91 steel. *Welding Journal*, pages 80–s – 87–s, 2013.

[22] P. de Smet and H. van Wortel. Controlling heat treatment of welded P91. *Welding Journal*, pages 42 – 44, 2006.

[23] W. Newell Jr. Welding and postweld heat treatment of P91 steels. *Welding Journal*, pages 33 – 36, 2010.

[24] J. Parker and J. Siefert. Weld repair of grade 91 steel. *Metal 2012 Conference*, 2013.

[25] R. Viswanathan and W. Bakker. Materials for ultrasupercritical power plants–boiler materials: Part 1. *Journal of Materials Engineering and Performance*, 10:81 – 95, 2001.

[26] P. Ennis and A. Czyrska-Filemonowicz. Recent advances in creep-resistant steels for power plant applications. *Sadhana*, 28:709 – 730, 2003.

[27] J. Parker. Creep cavitation in CSEF steels. *Advances in Materials Technology for Fossil Power Plants*, pages 714 – 731, 2014.

[28] A. Zielinski, G. Golanski, A. Zielinska-Lipiec, J. Jasak, and C. Kolan. Influence of ageing process on microstructure and mechanical properties of 9% Cr cast steel. *10th Liege Conference: Materials for Advanced Power Engineering 2014*, pages 131 – 140, 2014.

[29] J. Hald. Microstructure and long-term creep properties of 9-12% Cr steels. *International Journal of Pressure Vessels and Piping*, 85:30 – 37, 2008.

[30] C. Panait, W. Bendick, A. Fuchsmann, A. Gourgues-Lorenzon, and J. Besson. Study of the microstructure of the grade 91 steel after more than 100000h of creep exposure at 600 C. *International Journal of Pressure Vessels and Piping*, 87:1 – 13, 2010.

[31] V. Sklenicka, K. Kucharova, M Svoboda, and A. Kroupa. Creep behaviour of advanced power plant steels after long-term isothermal ageing. *Advances in Materials Technology for Fossil Power Plants*, pages 516 – 529, 2011.

[32] H. Danielsen, J. Hald, F. Grumsen, and M. Somers. On the crystal structure of Z-phase Cr(V,Nb)N. *Metallurgical and Materials Transactions A*, 37A:2633 – 2640, 2006.

[33] H. Danielsen and J. Hald. Influence of Z-phase on long-term creep stability of martensitic 9 to 12 % Cr steels. *VGB PowerTech*, pages 68 – 73, 2009.

[34] M. Rashidi, F. Liu, and H-O. Andren. Microstructure characterization of two Z-phase strengthened 12% chromium steels. *10th Liege Conference: Materials for Advanced Power Engineering 2014*, pages 71 – 80, 2014.

[35] F. Abe. Precipitate design for creep strengthening of 9% Cr tempered martensitic steel for ultra-supercritical power plants. *Science and Technology of Advanced Materials*, 9:1 – 15, 2008.

[36] I. Shibli, S. Holdsworth, and G. Merckling. *Creep and Fracture in High Temperature Components: Design and Life Assessment Issues*. DEStech Publications, 2005.

[37] D. Laverde, T. Gomez-Acebo, and F. Castro. Continuous and cyclic oxidation of T91 ferritic steel under steam. *Corrosion Science*, 46:613 – 631, 2004.

[38] A. Shibli and F. Starr. Some aspects of plant and research experience in the use of new high strength martensitic steel P91. *International Journal of Pressure Vessels and Piping*, 84:114 – 122, 2007.

[39] S. Price, M. Walsh (ed. by R. Viswanathan, and J. Nutting). *Advanced Heat Resistant Steels for Power Generation*. IOM Comminications, 1999.

[40] P. Ennis, A. Zielinska-Lipiec, O. Wachter, and A. Czyrska-Filemonowicz. Microstructural stability and creep rupture strength of the martensitic steel P92 for advanced power plant. *Acta Metallurgica*, 45(12):4901 – 4907, 1997.

[41] A. Czyrska-Filemonowicz, A. Zielinska, and P. Ennis. Modified 9% Cr steels for advanced power generation: Microstructure and properties. *Journal of Advancements in Materials and Manufacturing Engineering*, 19(2):43 – 48, 2006.

[42] A. Vyrostkova, V. Homolova, J. Pecha, and M. Svoboda. Phase evolution in P92 and E911 weld metals during ageing. *Materials Science and Engineering A*, 480:289 – 298, 2008.

[43] P. Ennis, A. Zielinska-Lipiec, and A. Czyrska-Filemonowicz. Influence of heat treatments on microstructural parameters and mechanical properties of P92 steel. *Materials Science and Technology*, 18:1226 – 1232, 2000.

[44] K. Rodak, A. Hernas, and A. Kielbus. Substructure stability of highly alloyed martensitic steels for power industry. *Materials Chemistry and Physics*, 81:483 – 485, 2003.

[45] F. Kauffmann, K. Maile, S. Straub, K. Mayer, M. Bauer, and E. Roos. Optimisation of long-term creep strength of martensitic steels. *Transactions of The Indian Institute of Metals*, 63:357 – 361, 2010.

[46] M. Tabuchi, H. Hongo, and F. Abe. Creep strength of dissimilar welded joints using high B-9CR steel for a USC boiler. *10th Liege Conference: Materials for Advanced Power Engineering 2014*, pages 101 – 110, 2014.

[47] J. Brozda. New generation creep resistant steels, their weldability and properties of welded joints: T/P92 steel. *Welding International*, 19(1):5 – 13, 2005.

[48] P. Mathiazhagan and A. Sawroop Khanna. High temperature oxidation behavior of P91, P92 and E911 alloy steels in dry and wet atmospheres. *High Temperature Material Processes*, 1-2:43 – 50, 2011.

[49] V. Rivlin and G. Raynor. 1: Critical evaluation of constitution of chromium-iron-nickel system. *International Metals Reviews*, 25:21 – 38, 1980.

[50] H. Eiselstein and D. Tillack. The invention and definition of alloy 625. *Superalloys 718, 625 and Various Derivatives*, pages 1 – 14, 1991.

[51] J. Farrar. *The Alloy Tree: A Guide to Low-alloy Steels, Stainless Steels and Nickel-base Alloys*. CRC Press, 2004.

[52] G. Vander Voort, J. Bowman, and R. Frank. Microstructural characterization of custom age 625 PLUS alloy. *Superalloys 718, 625, 706 and Various Derivatives*, pages 489 – 498, 1994.

[53] J. DuPont and A. Marder. Dilution in single pass arc welds. *Metallurgical and Materials Transactions B*, 27B:481 – 489, 1996.

[54] R. Ayer, R. Mueller, D. Leta, and W. Sisak. Phase transformations at steel/IN625 clad interfaces. *Metallurgical Transactions A*, 20A:665 – 681, 1989.

[55] C. Jang, J. Lee, J. Sung Kim, and T. Eun Jin. Mechanical property variation within inconel 82/182 dissimilar metal weld between low alloy steel and 316 stainless steel. *International Journal of Pressure Vessels and Piping*, 85:635 – 646, 2008.

[56] M. Cieslak, G. Knorovsky, T. Headley, and A. Romig Jr. The solidification metallurgy of alloy 718 and other Nb-containing superalloys. *Superalloy 718-Metallurgy and Applications*, pages 59 – 68, 1989.

[57] M. Cieslak. The welding and solidification metallurgy of alloy 625. *Welding Research Supplement*, pages 49–s – 56–s, 1991.

[58] S. Floreen, G. Fuchs, and W. Yang. The metallurgy of alloy 625. *Superalloys 718, 625, 706 and Various Derivatives*, pages 13 – 37, 1994.

[59] J. Radavich and A. Fort. Effects of long-time exposure in alloy 625 at 1200 F, 1400 F, 1600 F. *Superalloys 718, 625, 706 and Various Derivatives*, pages 635 – 647, 1994.

[60] V. Shankar, K. Bhanu Sankara Rao, and S. Mannan. Microstructure and mechanical properties of inconel 625 superalloy. *Journal of Nuclear Materials*, 288:222 – 223, 2001.

[61] K. Coleman, D. Gandy, R. Viswanathan, and W. Newell. Weld filler for welding dissimilar alloy steels and method of using same, 11 2005.

[62] J. Tanzosh, W. Newell Jr., J. Siefert, J. Sanders, and J. Shingledecker. Development of EPRI P87 solid wire. *Materials at High Temperatures*, pages 243 – 252, 2010.

[63] M. Urzynicok, R. Jachym, K. Kwiecinski, P. Mariani, and Y. Minami. Application of EPRI P87 in dissimilar austenitic-martensitic welded joints of tempaloy AA-1 and T92 steel grades. *Advances in Materials Technology for Fossil Power Plants*, pages 992 – 1005, 2014.

[64] R. Messler. *Principles of Welding*. Wiley, 1999.

[65] P. Mayr. *Evolution of Microstructure and Mechanical Properties of the Heat Affected Zone in B containing 9% Cr Steel*. PhD thesis, Graz University of Technology, Graz, Austria, 2007.

[66] S. Banovic, J. DuPont, and A. Marder. Dilution control in gas-tungsten-arc welds involving superaustenitic stainless steels and nickel-based alloys. *Metallurgical and Materials Transactions B*, 32B:1171 – 1176, 2001.

[67] V. Kumar, C. Lee, G. Verhaeghe, and S. Raghunathan. CRA weld overlay - influence of welding process and parameters on dilution and corrosion resistance. *Stainless Steel World America*, 2010.

[68] J. DuPont and C. Kusko. Technical note: Martensite formation in austenitic/ferritic dissimilar alloy welds. *Welding Journal Supplement*, pages 51–s – 54–s, 2007.

[69] M. Gittos and T. Gooch. The interface below stainless steel and nickel-alloy claddings. *Welding Research Supplement*, pages 461–s – 472–s, 1992.

[70] K. Laha, K. Chandravathi, K. Bhanu Sankara Rao, S. Mannan, and D. Sastry. An assessment of creep deformation and fracture behavior of 2.25Cr-1Mo similar and dissimilar weld joints. *Metallurgical and Materials Transactions A*, 32A:115 – 124, 2001.

[71] A. Schaeffler. Constitution diagram for stainless steel weld metal. *Metal Progress*, 56(11):680 – 680B, 1949.

[72] T. Nelson, J. Lippold, and M. Mills. Nature and evolution of the fusion boundary in ferritic-austenitic dissimilar weld metals, part 1 – nucleation and growth. *Supplement to the Welding Journal*, pages 329–s – 337–s, 1999.

[73] T. Nelson, J. Lippold, and M. Mills. Nature and evolution of the fusion boundary in ferritic-austenitic dissimilar weld metals, part 2 – on-cooling transformations. *Supplement to the Welding Journal*, pages 267–s – 277–s, 2000.

[74] J. C. Lippold, J. DuPont, and S. D. Kiser. *Welding Metallurgy and Weldability of Nickel-Base Alloys*. John Wiley & Sons, 2009.

[75] B. Alexandrov, J. Lippold, J. Sowards, A. Hope, and D. Saltzmann. Fusion boundary microstructure evolution associated with embrittlement of ni-base alloy overlays applied to carbon steel. *Weld World*, 57:39 – 53, 2013.

[76] M, Divya, C. Das, S. Albert, S. Goyal, P. Ganesh, R. Kaul, J. Swaminathan, B. Murty, L. Kukreja, and A. Bhaduri. Influence of welding process on type IV cracking behavior of P91 steel. *Materials Science and Engineering A*, 613:148 – 158, 2014.

[77] V. Gaffard, A. Gourgues-Lorenzon, and J. Besson. High temperature creep flow and damage properties of the weakest area of 9Cr1Mo-NbV martensitic steel weldments. *ISIJ International*, 45(12):1915 – 1924, 2005.

[78] X. Xu, G. West, R. Thomson, and J. Parker. The effect of post weld heat treatment on the creep behaviour and microstructural evolution in grade 92 steel welds for steam pipe applications. *Advances in Materials Technology for Fossil Power Plants*, pages 615 – 626, 2014.

[79] S. Mannan and K. Laha. *Transactions of the Indian Institute of Metals*, 49:303 – 320, 1996.

[80] H. Cerjack and P. Mayr. *Conference on Welding Creep-Resistant Steels*, pages 472 – 508, 2007.

[81] K. Chandravathi, K. Laha, K. Bhanu Sankara Rao, and S. Mannan. Microstructure and tensile properties of modified 9Cr-1Mo steel (grade 91). *Materials Science and Technology*, 17:559 – 565, 2001.

[82] R. Nicholson. Effect of aging on interfacial structures of nickel-based transition joints. *Metals Technology*, 11:115 – 124, 1984.

[83] A. Bhaduri, V. Seetharaman, and S. Venkadesan. Effect of ageing on the interfacial microstructure and mechanical properties of a alloy 800/2.25 Cr-1 Mo steel joint. *Z. Metallkde*, 80:630 – 634, 1989.

[84] C. Pan and Z. Zhang. Morphologies of the transition region in dissimilar austenitic-ferrtic welds. *Materials Characterization*, 36:5 – 10, 2000.

[85] W. Savage, E. Nippes, and E. Szekeres. A study of weld interface phenomena in a low alloy steel. *Welding Journal Supplement*, 55:260–s – 268–s, 1976.

[86] L. Darken. Diffusion of carbon in austenite with a discontinuity in composition. *Trans. AIME*, 180:430 – 438, 1949.

[87] R. Christoffel and R. Curran. Carbon migration in welded joints at elevated temperatures. *Welding Research Supplement*, pages 457–s – 468–s, 1956.

[88] B. Buchmayr, H. Cerjak, M. Witwer, and J. Kirkaldy. Carbon diffusion and microstructure in dissimilar Cr-Mo-V welds and their influence on the mechanical properties. *Conference: Recent Trends in Welding Science and Technology, USA*, pages 237 – 244, 1989.

[89] Z. Liu, L. Wang, and L. Wang. Changing rule of carbon-enriched zone and diffusion behavior of carbon in aging 0Cr6Mn13Ni10MoTi/1Cr5Mo dissimilar welded joints. *Journal of Materials Science and Technology*, 20:307 – 310, 1982.

[90] B-C. Kim, H-S. Ann, and J-T. Song. Analysis of carbon migration with post-weld heat treatment in dissimilar metal weld. *International Trends in Welding Science and Technology*, pages 307 – 313, 1992.

[91] J. Pavlovský, B. Million, K. Ciha, and K. Stránský. Carbon redistribution between an austenitic cladding and a ferritic steel for pressure vessels of a nuclear reactor. *Materials Science and Engineering*, A149:105 – 111, 1991.

[92] B. Million, K. Bacilek, J. Kucera, P. Michalicka, A. Rek, and K. Stransky. Carbon diffusion and thermodynamic characteristics in chromium steels. *Z. Metallkd.*, 86(10):706 – 712, 1995.

[93] M. Huang and L. Wang. Carbon migration in 5cr-0.5mo/21cr-12ni dissimilar metal welds. *Metallurgical and Materials Transactions A*, 29A:3037 – 3046, 1998.

[94] R. Foret, B. Million, M. Svodoba, and K. Stránský. Structural stability of dissimilar weld joints of steel P91. *Science and Technology of Welding and Joining*, 6(6):405 – 411, 2001.

[95] R. Anand, C. Sudha, T. Karthikeyan, A. Terrance, S. Saroja, and M. Vijayalakshmi. Effectiveness of ni-based diffusion barriers in preventing hard zone formation in ferritic steel joints. *Journal of Materials Science*, 44:257 – 265, 2009.

[96] R. Anand, C. Sudha, V. Thomas Paul, S. Saroja, and M. Vijayalakshmi. Microstructural changes in grade 22 ferritic steel clad successively with ni-based and 9Cr filler metals. *Welding Journal Supplement*, pages 65–s – 74–s, 2010.

[97] R. Anand, C. Sudha, S. Saroja, and M. Vijayalakshmi. Experimental and thermokinetic simulation studies on the formation of deleterious zones in dissimilar ferritic steel weldments. *Metallurgical and Materials Transactions A*, 44A:2156 – 2170, 2013.

[98] J. Race. *Carbon Diffusion across Dissimilar Steel Welds*. PhD thesis, Department of Materials Science and Metallurgy, University of Cambridge, 1992.

[99] J. Race and H. Bhadeshia. Precipitation sequences during carburisation of Cr-Mo steel. *Materials Science and Technology*, 8:875 – 882, 1992.

[100] J. Race and H. Bhadeshia. Carbon migration across dissimilar steel welds. *International Trends in Welding Science and Technology*, pages 307 – 314, 1993.

[101] S. Albert, T. Gill, A. Tyagi, S. Mannan, S. Kulkarni, and P. Rodriguez. Soft zone formation in dissimilar welds between two Cr-Mo steels. *Welding Research Supplement*, pages 135 – 142, 1997.

[102] C. Sudha, A. Terrance, S. Albert, and M. Vijayalakshmi. Systematic study of formation of soft and hard zones in the dissimilar weldments of Cr-Mo steels. *Journal of Nuclear Materials*, 302:193 – 205, 2002.

[103] C. Sudha, V. Paul, A. Terrance, S. Saroja, and M. Vijayalakshmi. Microstructure and microchemistry of hard zone in dissimilar weldments of Cr-Mo steels. *Welding Journal Supplements*, pages 71–s – 80–s, 2006.

[104] M. Sireesha, S. Albert, and S. Sundaresan. Influence of high-temperature exposure on the microstructure and mechanical properties of dissimilar metal welds between modified 9Cr-1Mo steel and alloy 800. *Metallurgical and Materials Transactions A*, 36A:1495 – 1506, 2005.

[105] A. Bhaduri, T. Gill, G. Srinivasan, and S. Mannan. Effect of aging on the microstructure and tensile properties of an alloy 800/9Cr-1Mo steel joint. *International Journal of Pressure Vessels and Piping*, pages 25 – 33, 1995.

[106] B. López, I. Gutiérrez, and J. Urcola. Microstructural analysis of steel-nickel alloy clad interfaces. *Materials Science and Technology*, 12:45 – 55, 1996.

[107] R. Nicholson. Effect of post-weld heat treatment on development of interfacial structures in nickel-based transition joints. *Materials Science and Technology*, 1:227 – 233, 1985.

[108] R. Nicholson and C. Li. The effect of long term service on the interfacial structure and fracture of nickel-based dissimilar welds. *EPRI Report 1874 - Dissimilar Weld Failure Analysis and Development*, 1981.

[109] R. Gray, J. King, J. Leitmaker, and G. Slaughter. Examination of a failed transition weld joint and the associated base metals. *Report ORNL 5223, Oak Ridge National Laboratory*, 1977.

[110] J. Parker and G. Stratford. Characterisation of microstructures in nickel based transition joints. *Journal of Materials Science*, 35:4099 – 4107, 2000.

[111] R. Nicholson. Interfacial structures in nickel-based transition joints after long term service. *Report RD/M/N1131, Central Electricity Generating Board*, 1980.

[112] K. Laha, K. Chandravathi, P. Parameswaran, S. Goyal, and M. Matthew. A comparison of creep rupture strength of ferritic/austenitic dissimilar weld

joints of different grades of Cr-Mo ferritic steels. *Metallurgical and Materials Transactions A*, pages 1174 – 1186, 2011.

[113] J. Siefert and J. Shingledecker. Temperbead repair of T91 using EPRI P87 filler metal. *Trends in Welding Research*, pages 235 – 241, 2013.

[114] A. Celik and A. Alsaran. Mechanical and structural properties of similar and dissimilar steel joints. *Materials Characterisation*, 43:311 – 318, 1999.

[115] G. Reddy and K. Rao. Microstructure and mechanical properties of similar and dissimilar stainless steel electron beam and friction welds. *International Journal of Advanced Manufacturing Technology*, 45:875 – 888, 2009.

[116] K. Fang, G. Li, G. Li, W. Yang, M. Zhang, and Z. Sun. Microstructures and mechanical properties of dissimilar metal weld A508/52M/316L used in nuclear power plants. *Key Engineering Materials*, 479:40 – 47, 2011.

[117] M. Sireesha, S. Albert, and S. Sundaresan. Microstructure and mechanical properties of weld fusion zones in modified 9Cr-1Mo steel. *Journal of Materials Engineering and Performance*, 10(3):320 – 330, 2001.

[118] J. DuPont. Microstructural evolution and high temperature failure of ferritic to austenitic dissimilar welds. *International Materials Reviews*, 57:208 – 234, 2012.

[119] J. Williams and J. Parker. Effect of thermal cycling on creep behaviour of 2.25Cr-1Mo/type 316 steel dissimilar welds. *Materials Science and Technology*, 10:915 – 923, 1994.

[120] K. Sedman, J. Thornley, and R. Griffin. Type III creep cracking at main steam line welds. *Engineering Failure Analysis*, 4(2):210 – 216, 1997.

[121] P. Budden and I. Curbishley. Assessment of creep crack growth in dissimilar metal welds. *Nuclear Engineering and Design*, 197:13 – 23, 2000.

[122] R. Nicholson. Creep-rupture properties of austenitic and nickel-based transition joints. *Metals Technology*, 9:305 – 311, 1982.

[123] R. Nicholson and J. Williams. Failure and deformation modes in heavy section dissimilar welds subjected to accelerated thermal cycle: Creep loading. *International Journal of Pressure Vessels and Piping*, 20:239 – 274, 1985.

[124] R. Klueh and J. King. Austenitic stainless steel-ferritic steel weld joint failures. *Welding Research Supplement*, pages 302–s – 311–s, 1982.

[125] R. Ryder, C. Li, R. Viswanathan, and J Dimmer. Dissimilar metal weld failures in power plants - causes and remedies. *Trends in Electric Utility Research*, pages 137 – 147, 1984.

[126] D. Roberts, R. Ryder, and R. Viswanathan. Performance of dissimilar welds in service. *Journal of Pressure Vessel Technology*, 107:247 – 254, 1985.

[127] J. Parker and G. Stratford. Review of factors affecting condition assessment of nickel-based transition joints. *Science and Technology of Welding and Joining*, 4:29 – 39, 1999.

[128] J. Parker and G. Stratford. The high-temperature performance of nickel-based transition joints i: Deformation behaviour. *Materials Science and Engineering*, A299:164 – 173, 2001.

[129] J. Parker and G. Stratford. The high-temperature performance of nickel-based transition joints ii: Fracture behaviour. *Materials Science and Engineering*, A299:174 – 184, 2001.

[130] J. Parker. Type IV cracking in low alloy steel weldments. *ECF 9: Reliability and Structural Integrity of Advanced Materials*, pages 493 – 498, 1994.

[131] D. Smith, N. Walker, and S. Kimmins. Type IV creep cavity accumulation and failure in steel welds. *International Journal of Pressure Vessels and Piping*, 80:617 – 627, 2003.

[132] M. Abd El-Azim, A. Nasreldin, G. Zeis, and A. Klenk. Microstructural instability of a welded joint in P91 steel during creep at 600C. *Materials Science and Technology*, 21(7):779 – 790, 2005.

[133] J.-Q. Zhang, B.-Y. Yao, T.-J. Li, F.-G. Liu, and Y.-L. Zhang. Numerical simulation of mechanical controlling parameters for type IV cracking on the welding joints of martensitic heat-resistant steel. *Frontiers of Materials Science in China*, 4(2):210 – 216, 2010.

[134] K. Laha, K. Chandravathi, P. Parameswaran, K. Bhanu Sankara Rao, and S. Mannan. Characterization of microstructures across the heat-affected zone of the modified 9Cr-1Mo weld joint to understand its role in promoting

type IV cracking. *Metallurgical and Materials Transactions A*, 38A:58 – 68, 2007.

[135] J. Francis, W. Mazur, and H. Bhadeshia. Type IV cracking in ferritic power plant steels. *Materials Science and Technology*, 22(12):1387 – 1395, 2006.

[136] F. Abe, M. Tabuchi, and S. Tsukamoto. Alloy design for suppression of type IV fracture in 9Cr steel welds at 650 C. *10th Liege Conference: Materials for Advanced Power Engineering 2014*, pages 91 – 100, 2014.

[137] J. Andersson, T. Helander, L. Hoglund, F. Shi, and B. Sundman. Thermo-Calc and DICTRA, computational tools for materials science. *CALPHAD*, 26:273 – 312, 2002.

[138] T. Helander, J. Ågren, and J. Nilsson. An experimental and theoretical investigation of diffusion across a joint of two multicomponent steels. *ISIJ International*, 37(11):1139 – 1145, 1997.

[139] T. Helander and J. Ågren. Computer simulation of multicomponent diffusion in joints of dissimilar steels. *Metallurgical and Materials Transactions A*, 28A:303 – 308, 1997.

[140] A. Engstrom, L. Hoglund, and J. Agren. Computer simulation of diffusion in multiphase systems. *Metallurgical and Materials Transactions A*, 25A:1127 – 1134, 1994.

[141] H. Larsson and A. Engstrom. A homogenisation approach to diffusion simulations applied to alpha + gamma Fe-Cr-Ni diffusion couples. *Acta Materialia*, 54:2431 – 2439, 2006.

[142] H. Larsson and L. Hoglund. Multiphase diffusion simulations in 1D using the DICTRA homogenization model. *CALPHAD: Computer Coupling of Phase Diagrams and Thermochemistry*, 33:495 – 501, 2009.

[143] E. Kozeschnik, P. Polt, S. Brett, and B. Buchmayr. Dissimilar 2.25Cr/9Cr and 2Cr/0.5CrMoV steel welds part 1: Characterisation of weld zone and numerical simulation. *Science and Technology of Welding and Joining*, 7(2):63 – 68, 2002.

[144] E. Kozeschnik, P. Warbichler, I. Letofsky-Papst, S. Brett, and B. Buchmayr. Dissimilar 2.25Cr/9Cr and 2Cr/0.5CrMoV steel welds part 2: Identification

of precipitates. *Science and Technology of Welding and Joining*, 7(2):69 – 76, 2002.

[145] R. Foret, B. Zlamal, and J. Sopousek. Structural stability of dissimilar weld between two Cr-Mo-V steels. *Welding Journal*, 85(10):211–s – 217–s, 2006.

[146] N. Saunders and A. Miodownik. *CALPHAD (Calculation of Phase Diagrams)*. Pergamon, 1998.

[147] N. Gokcen and R. Reddy. *Thermodynamics*. Plenum Press, 2 edition, 1996.

[148] D. Porter and K. Easterling. *Phase Transformations in Metals and Alloys*. Chapman and Hall, 1981.

[149] R. Balluffi, S. Allen, and W. C. Carter. *Kinetics of Materials*. Wiley, 2005.

[150] L. Onsager. Reciprocal relations in irreversible processes, i. *Physical Review Letters*, 37:405 – 426, 1931.

[151] J. Agren. Computer simulations of diffusional reactions in complex steels. *ISIJ International*, 32(3):291 – 296, 1992.

[152] J. Andersson and J. Agren. Models for numerical treatment of multicomponent diffusion in simple phases. *Journal of Applied Physics*, 72(4):1350 – 1355, 1992.

[153] A. Borgenstam, A. Engstrom, L. Hoglund, and J. Agren. DICTRA, a tool for simulation of diffusional transformations in alloys. *Journal of Phase Equilibria*, 21(3):269 – 280, 2000.

[154] A. Engstrom. *PhD Dissertation*. PhD thesis, Division of Physical Metallurgy, Royal Institute of Technology, Stockholm, 1996.

[155] G. Smith. *Numerical Solution of Partial Differential Equations: Finite Difference Methods*. Clarendon Press, 3 edition, 1985.

[156] H. Strandlund and H. Larsson. Simulation of diffusion by direct solution in the lattice-fixed frame of reference. *Metallurgical and Materials Transactions A*, pages 1785 – 1789, 2006.

[157] T. Totemeier. Ex-service metallurgical examination, tttm-d9584. Technical report, Alstom Power, 2011.

[158] M. Atkins. *Scanning Electron Microscopy: Physics of Image Formation and Microanalysis*. Springer, 2 edition, 1998.

[159] M. de Graef. *Introduction to Conventional Transmission Electron Microscopy*. Cambridge University Press, 2003.

[160] D. B. Williams and C. B. Carter. *Transmission Electron Microscopy I: Basics*. Plenum Press, 1996.

[161] D. B. Williams and C. B. Carter. *Transmission Electron Microscopy III: Imaging*. Plenum Press, 1996.

[162] D. B. Williams and C. B. Carter. *Transmission Electron Microscopy II: Diffraction*. Plenum Press, 1996.

[163] S. Pennycook and P. Nellist. *Scanning Transmission Electron Microscopy*. Springer, 2011.

[164] J. Baek, S. Nam, B. Kong, and S. Ryu. The effect of delta-ferrite in P92 steel on the formation of laves phase and cavities for the reduction of low cycle fatigue and creep-fatigue life. *Key Engineering Materials*, 297 – 300:463 – 470, 2005.

[165] H. Saghafifar. *Microstructural stability of a nickel-based alloy overlay on a 2.25Cr1Mo steel substrate*. PhD thesis, University of Nottingham, 2011.

Appendix A

Data from a T22 – Alloy 625 Weld

In this chapter, data gathered from a T22 (2.25Cr-1Mo) steel – Alloy 625 spiral weld system will be presented, for the purposes of comparison with other cases. This particular system was previously investigated thoroughly in a thesis by Saghafifar [165].

The results presented here constitute work following on from that performed by Saghafifar. Presented are the following:

- EDX measurements of carbon variation across the weld interfaces in three aged states ('D0', an as-welded sample, and 'D16' and 'D64', aged at 650 $°C$ for 16 days and 64 days respectively) using the low-voltage method.
- *DICTRA* simulations of the diffusion behaviour across the interfaces in samples D16 and D64.
- TEM analysis of the area around the weld line in sample D64.

The work presented here forms part of a journal article which has been written and is under review.

EDX Measurements of Carbon Variation

Using the low-voltage EDX technique to measure local carbon variation around the weld line reveals evolution, as shown in figure A.1. In the as-welded case, there

is no measureable enrichment or depletion of carbon. In the D16 and D64 cases, significant CEZs are observed. In the former case, the zone is approximately 30-40 μm in width, with a peak count rate occurring 10 μm away from the weld line. In the latter case, the zone is larger still, having grown to 40-50 μm in width, and with its peak level having shifted to 15 μm from the weld. A CDZ is not directly observed in either of these samples by this method; this is likely because the base carbon level in the steel is close to the minimum detection limit.

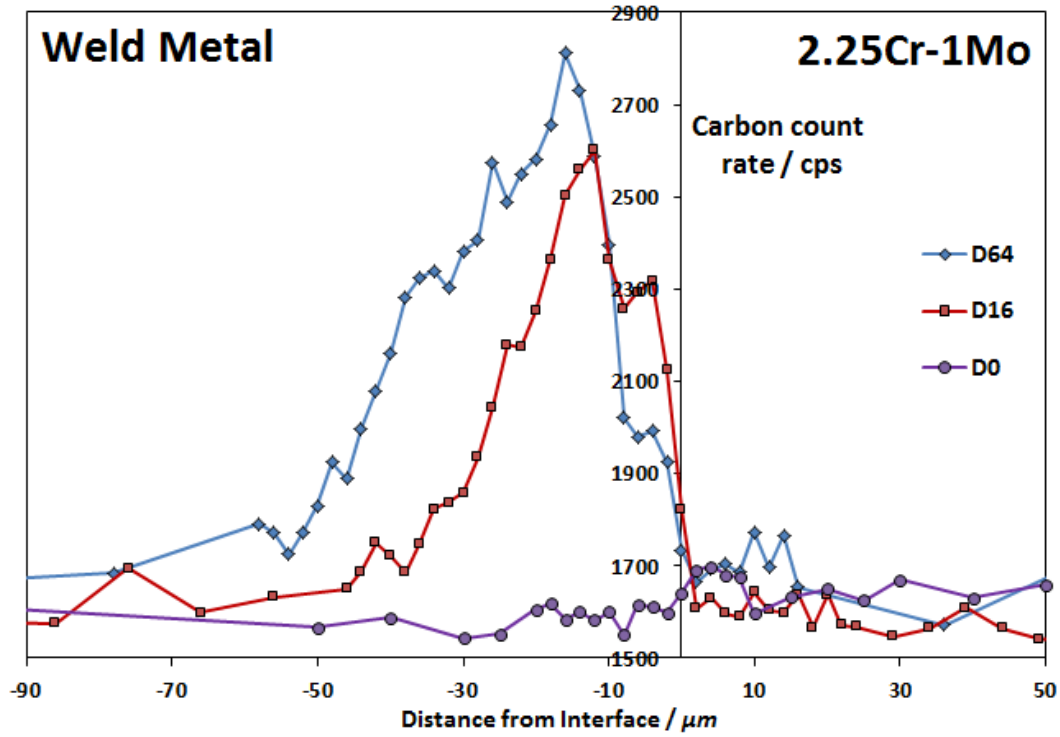

Figure A.1: EDX measurements of carbon count rate variation across the weld interfaces in samples D0, D16 and D64 using the low-voltage EDX method.

Diffusion Calculations

The simulated carbon concentration profiles, as calculated by the homogenisation model in *DICTRA*, across the weld interface in the D16 and D64 cases are shown in figure A.2. Simulations were performed using the homogenisation model and the upper Weiner bound, with a PMZ profile as an initial condition. Thermodynamic data for the BCC matrix and the $M_{23}C_6$ and M_6C carbide phases were

called from the TCFE7 database, while data for the FCC matrix, MC carbide and delta phase were called from the TTNI7 database. Kinetic data for both matrix phases were called from the MOB2 database.

These data show the evolution of the CEZ around the weld line. In the D16 case the CEZ extends 18 μm into the weld metal, with the peak concentration being 1.7 wt% at a distance of 10 μm from the weld line. The D64 case shows further evolution, with the zone now being approximately 30 μm wide, and the peak concentration of 1.8 wt% occurring 12 μm from the weld line.

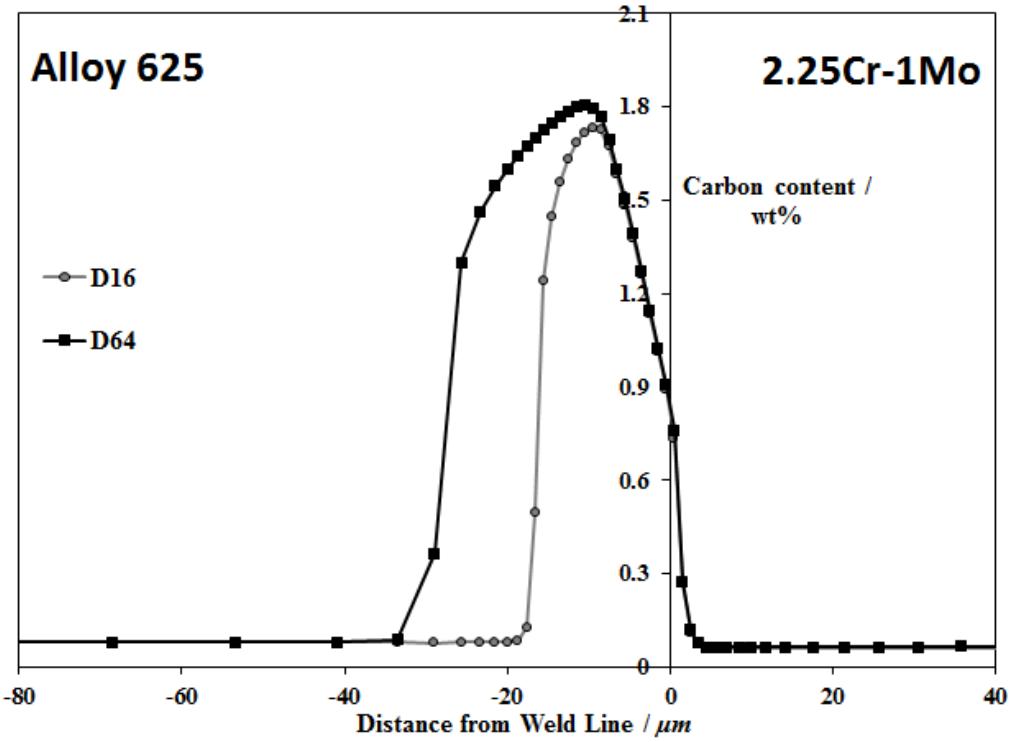

Figure A.2: Results of simulations of the 2.25Cr-1Mo – Alloy 625 system, as calculated by *DICTRA*, showing carbon concentration across the weld interface in cases D16 and D64.

TEM Examination of Sample D64

Analysis of the 64-day aged state reveals several new microstructural features, which are shown by way of STEM images and STEM-EDX maps in figure A.3. Type I carbides are visible here, present in a near-continuous band. They exhibit

an irregular, blocky morphology, with an average size of around 400 nm. The STEM-EDX maps reveal that they exist as two chemically distinct types: The more abundant Cr-rich particles, and the less common Mo-rich particles. The chemistries of these two particle families, as measured by STEM-EDX, are given in table A.1. The remainder of the steel is precipitate-free, consisting of plain ferrite.

Table A.1: Compositions of the two families of type I carbides and the interfacial band in sample D64, as measured by STEM-EDX.

	Element (wt %)							
	C	Cr	Fe	Mn	Mo	Nb	Ni	Si
Cr-rich particles	3.4	42.6	40.4	2.2	9.4	< 0.5	1.9	< 0.5
Uncertainties (±)	0.7	0.4	0.4	0.2	0.4	0.0	0.1	0.0
Mo-rich particles	3.6	4.9	33.3	< 0.5	1.2	0.8	4.9	3.3
Uncertainties (±)	1.4	0.2	0.8	0.1	1.2	0.4	0.2	0.2
Interfacial band	-	2.1	94.2	< 0.5	< 0.5	< 0.5	2.6	< 0.5
Uncertainties (±)	-	0.1	0.1	0.1	0.1	0.1	0.1	0.1

Electron diffraction has been used to identify the Cr-rich and Mo-rich particles as $M_{23}C_6$ and M_6C carbides respectively; indexed diffraction patterns are shown in figures A.4(a) and A.4(b). Both phases are of the FCC crystal structure, and both patterns are of the FCC-[112] zone axis; the patterns are distinguished by spacings (with diffraction spacings in the M_6C pattern being uniformly smaller than those of the $M_{23}C_6$ pattern by a factor of 0.97, in close alignment with the known difference in lattice parameter). The two diffraction patterns were taken with the FIB sample at the same tilt angle, indicating that the two particles in question are aligned.

To the left of the type I carbides is a narrow precipitate-free band, approximately 1 – 1.5 μm in width. It is seen best in figures A.3(a) and A.3(b). The diffraction contrast of this band is different to that of either adjoining region. This implies that there is no crystallographic alignment between these areas, and that this area is a distinct grain. This region is the interfacial band previously reported in similar systems [54] [105]. The composition of the band is given in table A.1.

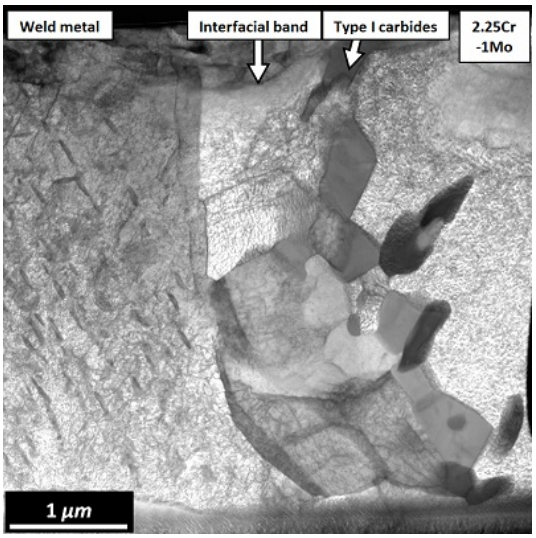

(a) STEM BF image

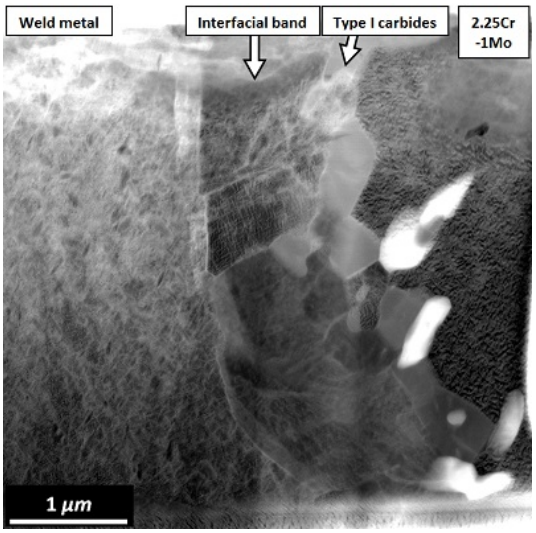

(b) STEM HAADF image

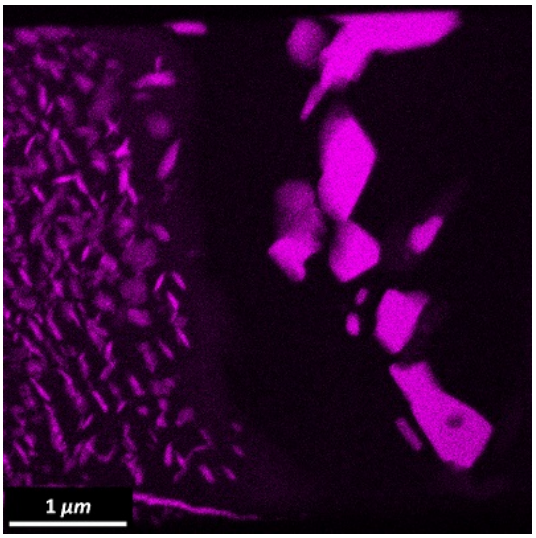

(c) Cr EDX map

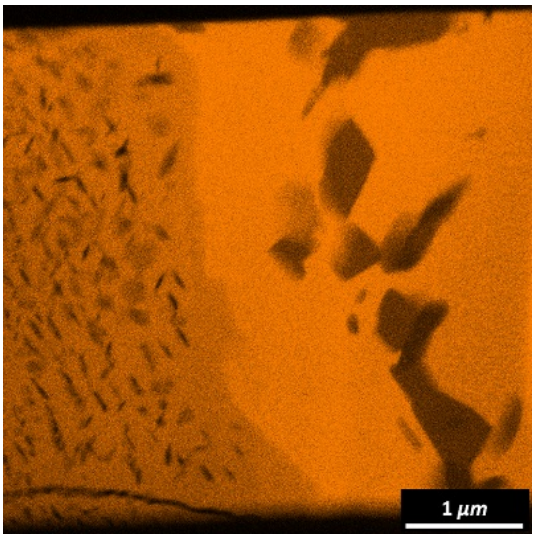

(d) Fe EDX map

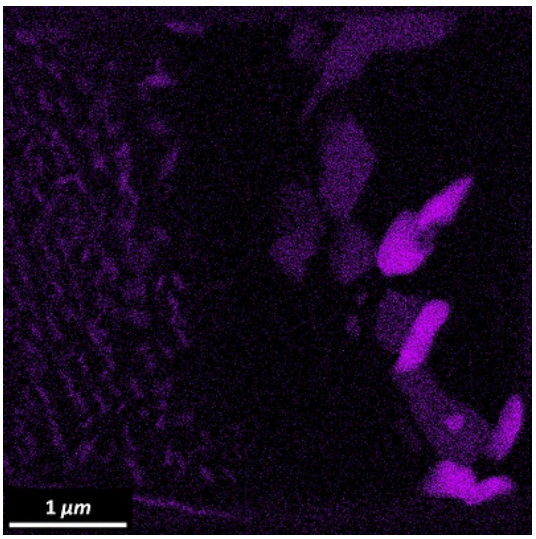

(e) Mo EDX map

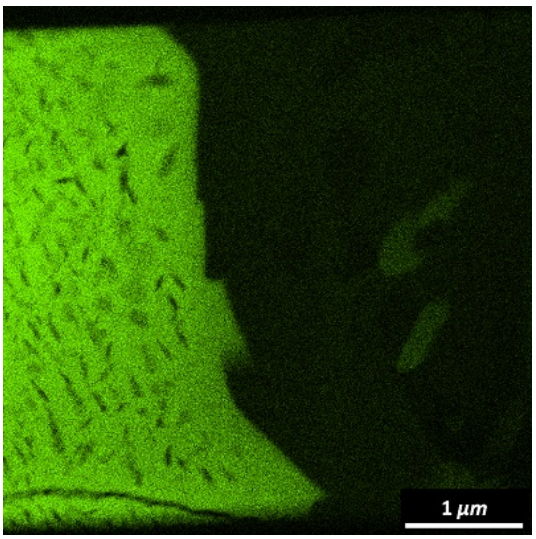

(f) Ni EDX map

Figure A.3: STEM-EDX data of the area around the weld line in sample D64.

The weld metal microstructure is characterised by large grains (c. 5 μm in diameter) containing a mesh of extremely fine-scale intra-granular particles, a small section of which is shown in figure A.4(c). They are also visible on the left side of all images in figure A.3. These particles exist along all of the electron-transparent weld metal (approximately 9 μm), and are slightly less abundant in the area visible in figure A.3 than in the rest of the sample. These particles appear to have irregular shapes, with some being circular and others elongated. The circular particles can be anywhere from 20 to 150 nm in diameter, while the elongated particles are up to 150 nm in length and usually around 40 nm across. The EDX maps in figures A.3 indicate that they are rich in chromium and molybdenum and depleted in nickel and iron relative to the surrounding matrix. Conventional TEM images and an SADP from these particles, shown in figure A.4(c), indicate that they may exist as families on certain crystallographic planes.

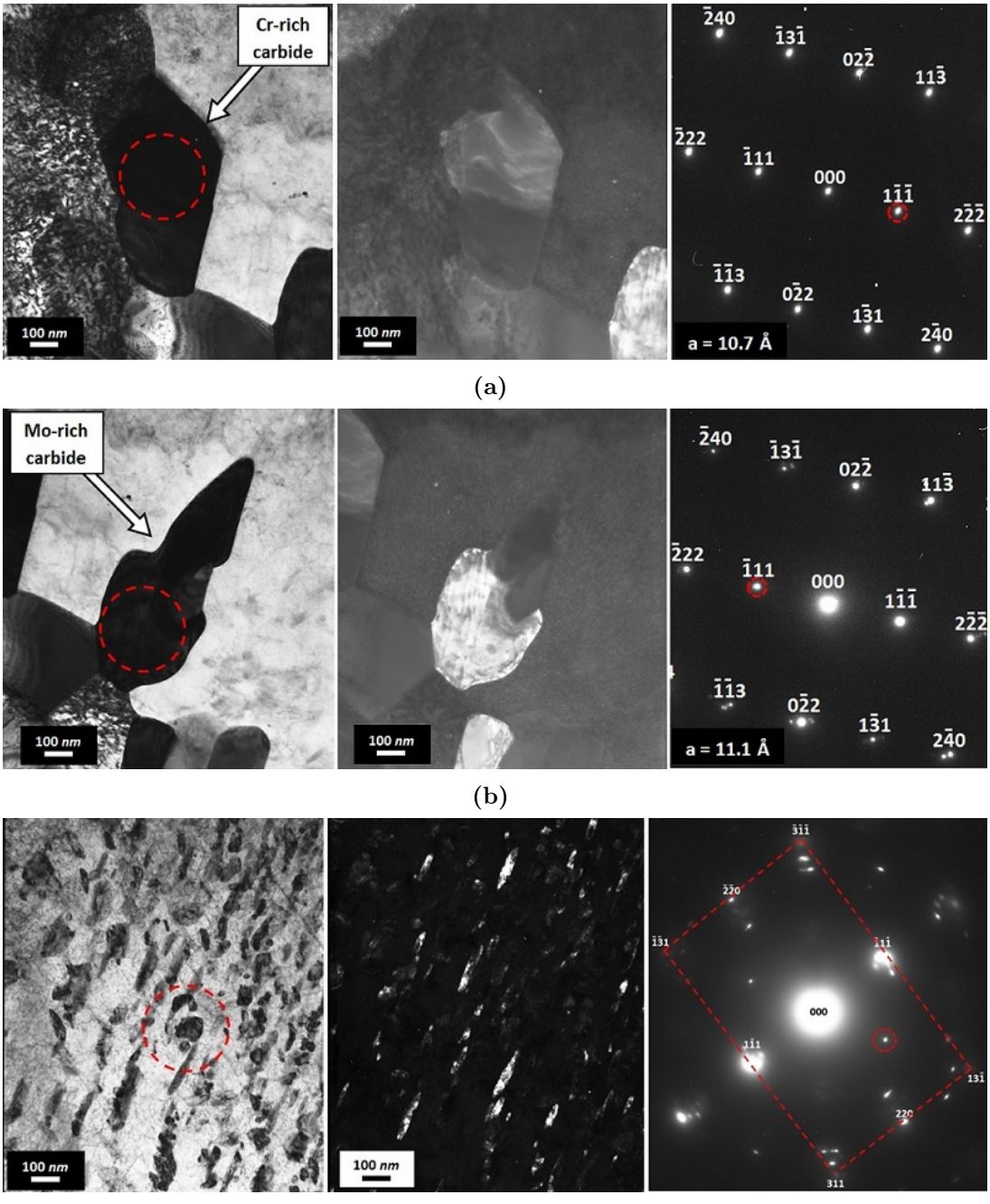

Figure A.4: TEM data from sample D64 showing (from left to right) a bright field image, a dark field image, and an SADP, from **(a)** a Cr-rich type I carbide, at the $M_{23}C_6$ FCC-$[11\bar{2}]$ zone axis, **(b)** an Mo-rich type I carbide, at the M_6C FCC-$[11\bar{2}]$ zone axis, **(c)** intragranular particles in the weld metal, with the background matrix (labelled) at the austenite FCC-$[11\bar{2}]$ zone axis. In all three cases, the dark field image was formed using the diffraction spot circled in red in the respective pattern, and the pattern formed from the area circled in the bright field image.

Appendix B

Re-normalising the P92 – Alloy 625 Weld

One proposed solution to the issue of type IV cracking in welds is to re-apply the steel manufacturing heat treatments (i.e. normalising and tempering) to the welded joint. This ought to eliminate the HAZ, restoring all areas of the steel to the ideal grain size and precipitate distribution by bringing the entire steel back into the austenite temperature range and quench cooling it to form fresh martensite.

Two P92 – Alloy 625 weld samples from the bead on plate system were hence prepared in this manner. One underwent the normalising treatment only (2 hours at 1050 $^{\circ}C$), while the other underwent the full normalising and tempering process (2 hours at 1050 $^{\circ}C$ followed by 2 hours at 760 $^{\circ}C$). These samples are named N and NT respectively. The effects of this normalisation heat treatment will be evaluated here.

Microhardness Profile

Automated microhardness profiles have been gathered from both of the samples. These are both shown in figure B.1. In sample N, the hardness of the steel away from the interface is around 450 $\pm$ 11 VHN_{100}, which indicates that fresh martensite has been formed. Around 1.2 mm away from the weld line the hardness starts to decrease, dropping to just under 400 VHN_{100} immediately adjacent to

the weld. There is no measurable soft zone, as is often found at the edge of a steel HAZ. The weld metal is soft by comparison, with the first pass being an average of 207 ± 7 VHN_{100}, and the second an average of 220 ± 6 VHN_{100}.

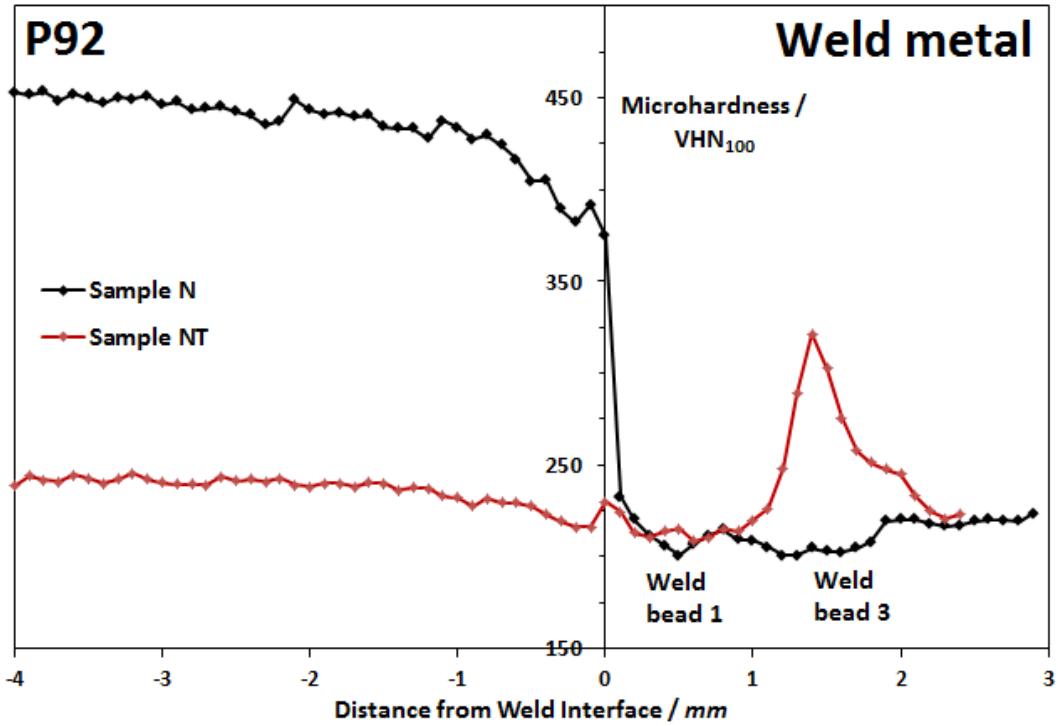

Figure B.1: Microhardness traces across the weld interfaces in samples N and NT, both representing the averages of 12 passes.

Sample NT shows dramatic differences to sample N. Firstly, the steel has been tempered, with its average hardness reduced to 242 ± 5 VHN_{100}. Like the tempered case, there is a reduction in hardness over a range of around 1.2 *mm* from the weld line, reaching a minimum of 216 VHN_{100} adjacent to the weld. As in sample N, no soft zone is observed. The first weld bead is relatively uniform, with an average hardness of 213 ± 9 VHN_{100}. There is then a sudden increase at the start of the second weld bead, with hardness peaking at around 340 VHN_{100}. There is then a steady decrease over the course of the second bead, reaching a minimum of 222 VHN_{100} at the edge of the scanned area.

Microstructure of the Steel

Microstructural analysis of the steel in samples N and NT indicates that the local average prior austenite grain size is approximately constant throughout both samples – it is between 10 and 20 μm, around the same as was observed in the as-manufactured steel from sample A-W. The CGHAZ, FGHAZ and ICHAZ, as shown in figure B.3, are now almost indistinguishable from one another, as their grain sizes and particle sizes are nearly identical. The only observable difference is in the form of a lower fraction of precipitates in the CGHAZ. This correlates with the lack of hard and soft areas normally associated with the HAZ in the hardness measurements.

While the areas away from the weld line in sample NT appear almost indistinguishable from as-manufactured P92, the local fraction of precipitates diminishes greatly towards the weld line. This is observed to some degree in the CGHAZ (figure B.3(a)), and is more apparent in the area immediately adjacent to the weld, as shown in figure B.4. Almost no precipitates are visible in this area, at PAGBs or on laths. This is likely to be indicative of decarburisation and/or de-nitriding. No type I or II carbides at the weld line can be discerned.

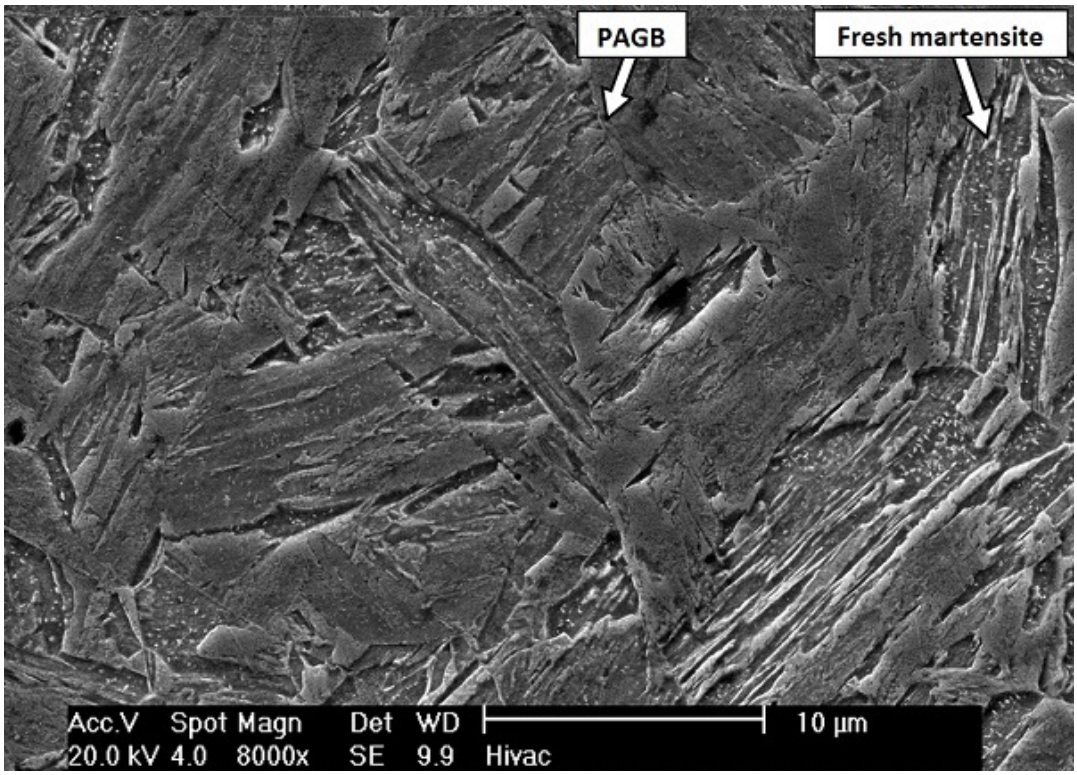

(a)

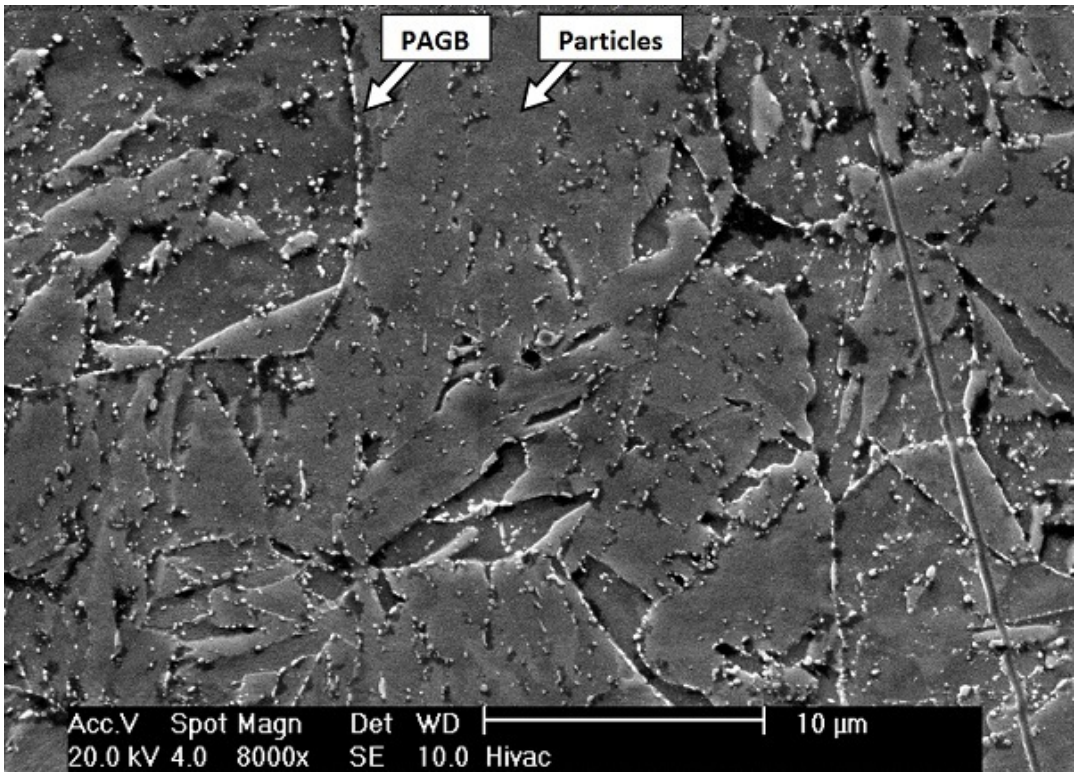

(b)

Figure B.2: Micrographs of the bulk P92 steel away from the weld interface after etching with Vilella's reagent, in **(a)** sample N, showing the fresh martensite, and **(b)** sample NT, showing tempered martensite.

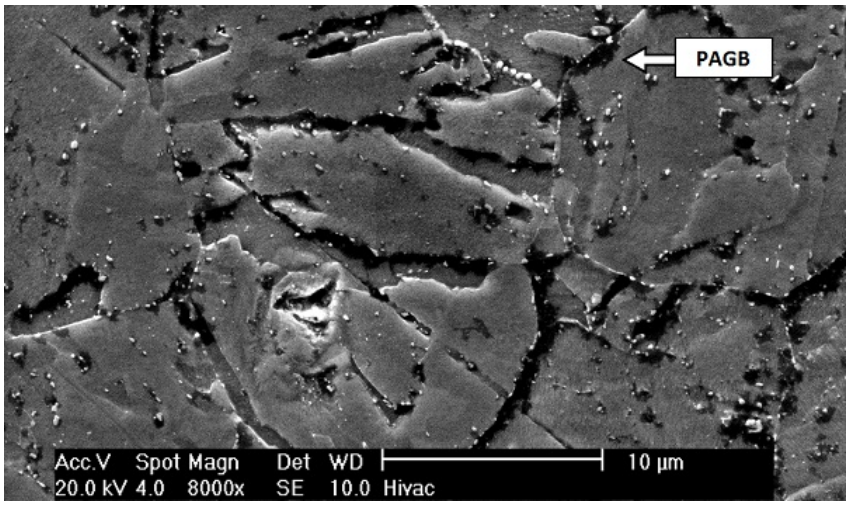

(a)

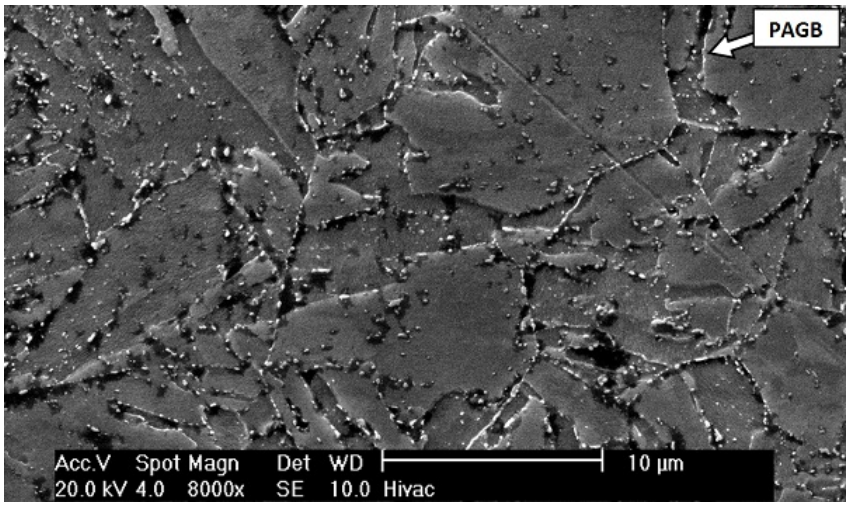

(b)

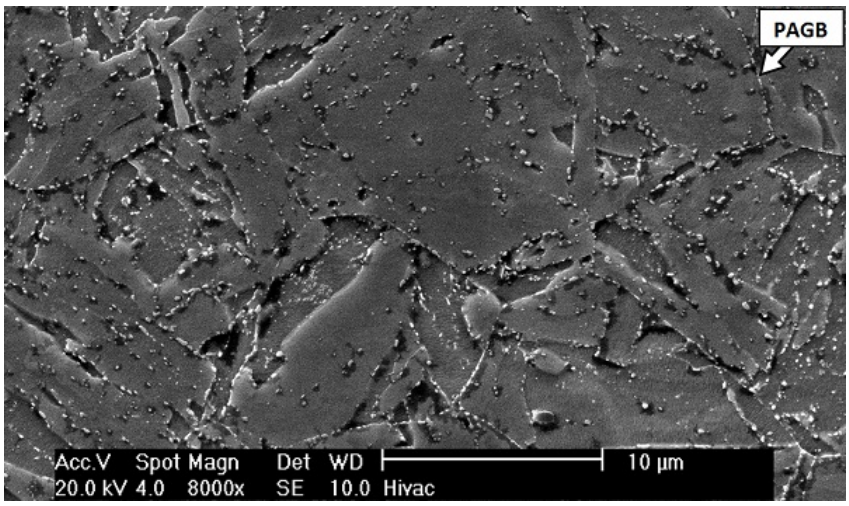

(c)

Figure B.3: SEM SE images of the HAZ in sample NT after etching with Vilella's reagent, showing **(a)** the CGHAZ, 300 μm from the weld line, **(b)** the FGHAZ, 700 μm from the weld line, and **(c)** the ICHAZ, 1300 μm from the weld line. The dark patches are due to the etching process, and do not correspond to microstructural features.

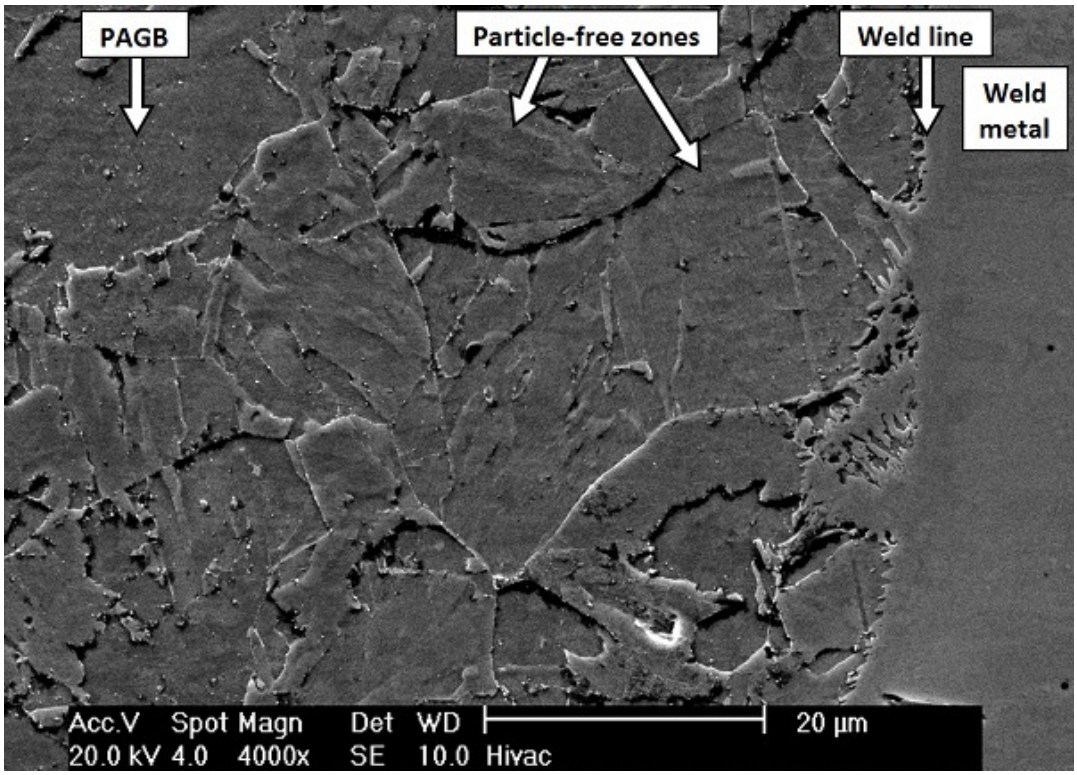

Figure B.4: An SEM micrograph of the area around the weld line in sample NT, after etching with aqua regia, showing the low fraction of precipitates when compared with figure B.2(b).

Microstructure of the Weld Metal

The weld metal near the fusion line in sample NT is shown in figure B.5. It appears rather different to the equivalent areas in samples A-W or T. It is still found that the second weld pass is more resistant to the etchant than the first, but there is little of the previously observed dendrite structure; grains are instead relatively featureless. Some vein-like features, of the type seen in sample T, are also observed in this case. The veins are much wider and more abundant than those seen in sample T, supporting the idea that they are related to diffusion phenomena (i.e. serving as pathways for diffusion of carbon and/or nitrogen).

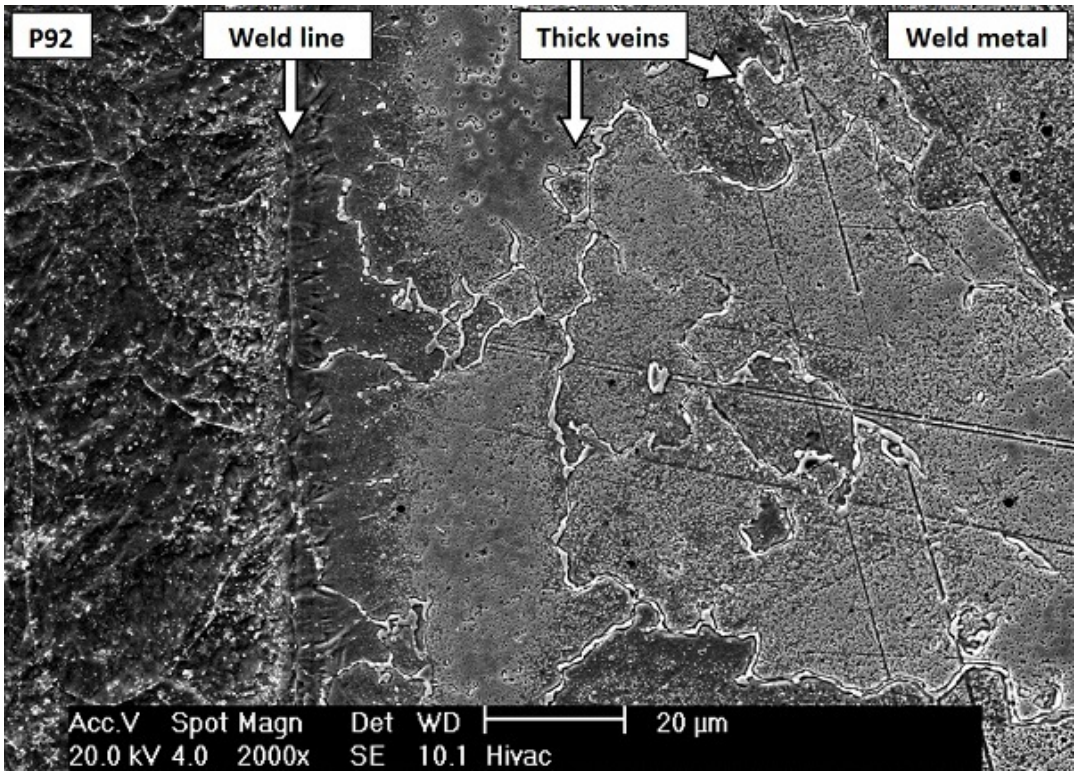

Figure B.5: An SEM micrograph of the Alloy 625 adjacent to the weld line in sample NT, after etching with aqua regia.

Oxidation Behaviour

The normalising and tempering procedure appears to result in aggressive oxidation of the steel. As figure B.6 shows, the oxide scale thickness immediately adjacent to the weld line in sample NT is around 140 μm. This same oxidation behaviour was observed at both edges of the sample. Additionally, pieces of oxide flaked off the steel surface after samples were removed from the furnace. These flakes were between 100 and 150 μm in thickness, and extremely brittle. As in other cases, the weld metal is largely unaffected by oxidation.

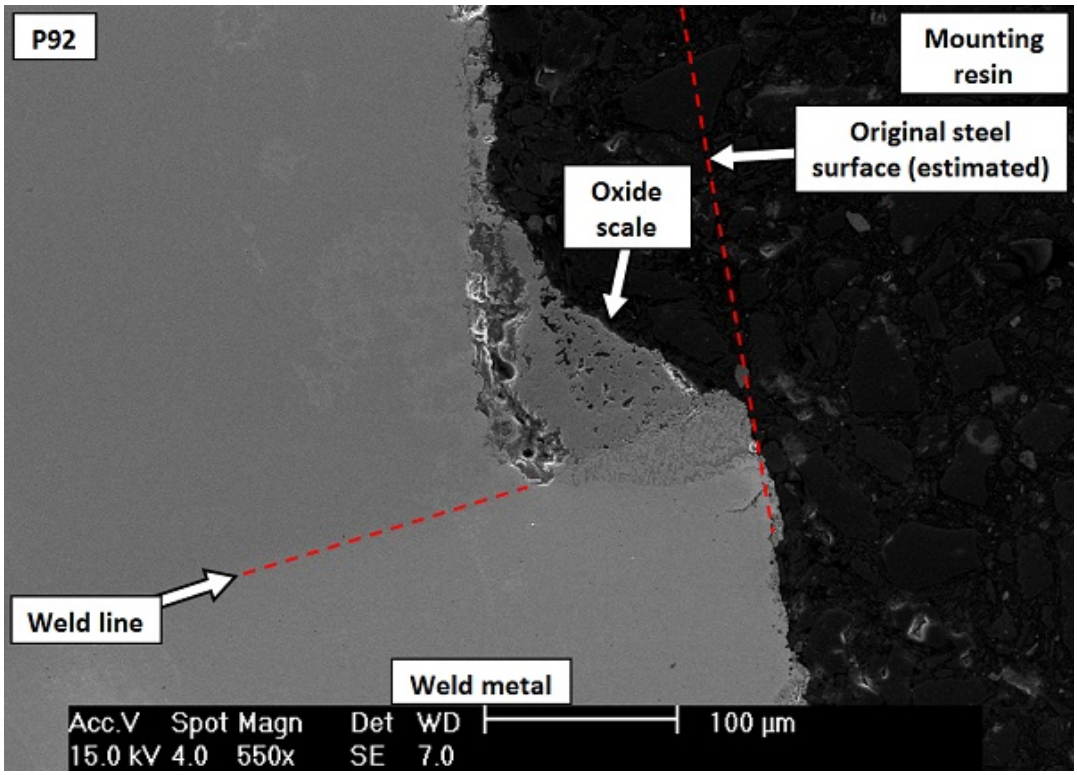

Figure B.6: An SEM micrograph of the oxide on the surface on the steel in sample NT, as viewed in the polished state in BSE mode. The scale thickness is estimated to be 140 μm at the weld line.

EDX Analysis of Carbon Diffusion

By the low-voltage EDX method, the concentration of carbon across the weld interface in sample N has been measured. The results of this are shown in figure B.7. These data show a distinct carbon denuded region in the steel, extending for at least 75 μm from the weld line. This is in contrast with the carbon enriched region in the weld metal, extending for at least 200 μm from the weld line. This confirms that significant diffusion of carbon across the weld line has occurred during the normalising treatment.

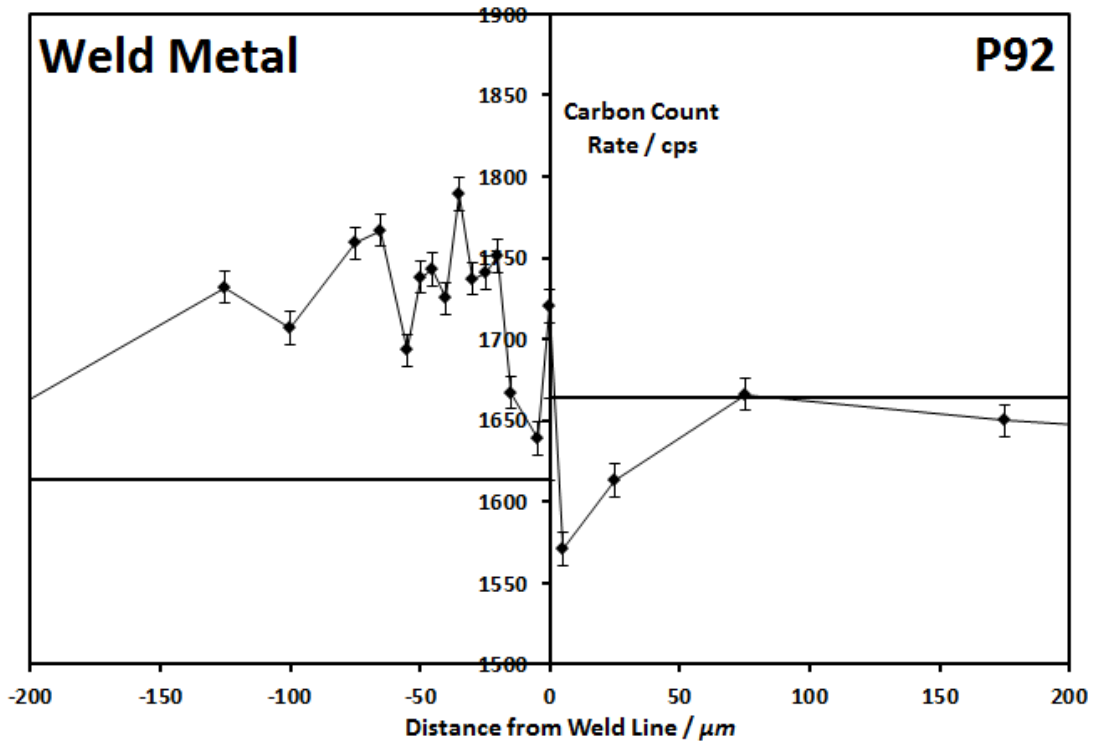

Figure B.7: Carbon concentration across the P92 – weld metal interface in sample N. The black horizontal lines represent the mean base level concentrations in the two alloys.

Discussion

The effectiveness of this heat treatment, in terms of removing the HAZ and the type IV zone, will be discussed here, as will other effects of the treatment, most significantly interdiffusion. The potential impacts of the treatment upon service performance will be evaluated.

The Heat Affected Zone

As is shown in figure B.3, the HAZ is almost completely removed by the normalising and tempering treatment, with all three sub-zones appearing indistinguishable from the bulk steel (with the exception of the CGHAZ, which has been affected slightly by decarburisation/de-nitriding). This is in strong contrast with the sample that was tempered only (sample T), as shown in figure 5.7, in which

the three sub-zones of the HAZ have distinct structures, making them weak relative to the base metal (especially the FGHAZ and ICHAZ). The normalising and tempering treatment should therefore be effective in supressing type IV weld failure.

Interdiffusion

There is strong evidence to suggest that significant migration of carbon and nitrogen from the steel to the weld metal has taken place during this heat treatment. The microstructure of the steel near the weld interface (i.e. the CNDZ) contains far fewer precipitates than the unaffected bulk. The extent of the CNDZ in this case is greater than in any of the other examined P92 – Alloy 625 samples, as it has visibly affected material at least 300 μm from the weld line; this serves to illustrate the strong temperature dependence of diffusion dynamics. Evidence for such diffusion is also seen in the microhardness trace (softening of the steel near the weld line) and in the EDX measurements of carbon count rate. Such excessive diffusion of carbon and nitrogen, and the resultant loss of secondary phases, will weaken this part of the steel, leaving it susceptible to mechanical failure in a stressed state.

While this level of diffusion is likely to be too great for welds of this type to be viable in a service environment, it is possible that welds prepared with P87 filler metal, such as those described in chapter 9, may not be as significantly affected by this process (assuming the chemical potentials in the steel and weld metal remain closely matched at the normalisation temperature). If such a treatment were to be successful, the resultant weld would be resistant to failure at the weld line (type II failure) and in the HAZ (type IV failure), and may hence have a service life comparable to those of the base materials.

Oxidation

Oxidation during the normalising process (maximum scale thickness c. 140 μm) is found to be extremely aggressive when compared to that which occurs during tempering or long-term heat treatments (maximum scale thickness c. 20 μm). This means that a re-normalised weld will lose a significant amount of load-bearing area before it even enters service. Additionally, oxide appears to have grown disproportionately rapidly at the weld line itself; while not sharing the characteristic appearance of oxide notching, this phenomenon would have the same effect of concentrating stress at the weld line. Protecting the steel from oxidation during this process would mitigate these issues, and may be necessary were this process to be performed in an industrial setting.

Conclusions

After analysing the effects of this re-normalisation PWHT, a number of conclusions can be reached:

- The treatment is successful in removing the microstructural features associated with the HAZ, and as such ought to suppress type IV weld failure.
- The diffusion of carbon and nitrogen across the weld interface is extreme, and has resulted in significant loss of precipitates from the steel.
- P91/92 – P87 welds may be more suited to heat treatments of this type, though further investigation is required to confirm this.
- Aggressive oxidation of the steel, particularly around the weld line, may leave welds of this type particularly vulnerable to oxide notch-assisted failure.

Appendix C

Published Diffraction Data

Given here are published diffraction data for crystal structures relevant to this thesis. This is used to verify the results of electron diffraction studies carried out by TEM.

Table C.1: A summary of published diffraction data from relevant crystal structures.

Crystal	**Chemistry**	**Structure**	**Lattice Parameter(s)**	**Space Group**	**PDF Number**
α/δ-ferrite	Fe	BCC	2.866 Å	Im3m	00-006-0696
γ-austenite	Fe,Ni,Cr	FCC	3.591 Å	Fm3m	00-033-0397
$M_{23}C_6$ carbide	$Cr_{23}C_6$	FCC	10.660 Å	Fm3m	00-035-0783
$M_6$6 carbide	Fe_3Mo_3C	FCC	11.136 Å	Fd3m	00-047-1191
MC carbide	NbC	FCC	4.470 Å	Fm3m	00-038-1364
MN nitride	NbN	FCC	4.394 Å	Fm3m	01-071-0162
MN nitride	VN	FCC	4.139 Å	Fm3m	00-035-0768
Laves phase	Fe_2W	Hexagonal	a = 4.727 Å c = 7.704 Å	P63/mmc	00-003-0920